

# Few-Femtosecond Nuclear Wave Packet Dynamics in Ozone

Dissertation

von

**Tobias Thomas Latka**





Fakultät für Physik  
Laser- und Röntgenphysik

# Few-Femtosecond Nuclear Wave Packet Dynamics in Ozone

Tobias Thomas Latka

Vollständiger Abdruck der von der Fakultät für Physik der Technischen Universität  
München zur Erlangung des akademischen Grades eines  
**Doktors der Naturwissenschaften**  
genehmigten Dissertation.

Vorsitzender: Prof. Dr. Andreas Weiler

Prüfer der Dissertation:

1. Prof. Dr. Reinhard Kienberger
2. Prof. Dr. Andreas Bausch

Die Dissertation wurde am 13.12.2017 bei der Technischen Universität München  
eingereicht und durch die Fakultät für Physik am 01.02.2018 angenommen.



# Abstract

The *ozone layer* of the Earth's atmosphere protects human beings and nature against mutagenic solar radiation in the deep ultraviolet (DUV) spectral domain between 200 nm and 300 nm. Ozone ( $\text{O}_3$ ), that is contained in this layer, thus absorbs DUV photons and gets promoted into an excited, dissociative electronic state. During this process, that is commonly known as ozone-photodissociation, optical energy is converted into kinetic energy of its photofragments (atomic (O) and diatomic ( $\text{O}_2$ ) oxygen). Although the photolysis of the ozone molecule, which is already completed after approximately 20 femtoseconds ( $1 \text{ fs} = 10^{-15} \text{ s}$ ), is very well described *theoretically*, it has evaded a *direct, time-resolved measurement* so far.

In order to reenact the process of ozone-photodissociation in the laboratory, two prerequisites have to be fulfilled: On the one hand a highly pure ozone source is indispensable, as ozone storage turns out to be difficult to implement and ozone itself can hardly be transported over long distances due to its high reactivity with the environment. On the other hand, a time-resolved measurement of the ozone-photolysis enforces the use of an intense DUV pump pulse to achieve a measurable population transfer between ground and excited state. Additionally, an extreme-ultraviolet (XUV) probe pulse is needed, that can be delayed relative to the DUV pump pulse and repeatedly interrogates the molecular dynamics at fixed times after DUV excitation. In general, femtosecond timescale temporal resolution can only be guaranteed by using short DUV pump and short XUV probe pulses. Within the scope of this thesis, two basic approaches concerning the generation of *short* and *intense* DUV pump pulses are discussed and compared to each other. Both are based on nonlinear frequency up-conversion of a femtosecond Kerr-lens-modelocked titanium-sapphire laser via *second* (SHG) or *third* (THG) harmonic generation.

As its primary result, the current thesis presents the *very first direct observation of the ozone-photodissociation* with the help of femtosecond time-resolved photoelectron spectroscopy (TR-PES). For this purpose, DUV pump pulses (sub-10 fs; 2  $\mu\text{J}$ ; 268 nm), generated via SHG, promote the ozone molecule into its excited state, while a short XUV probe pulse ( $\sim 1.7 \text{ fs}$ , 99.5 eV) is used for interrogation of the molecular dynamics. The experimental results show that ozone-photolysis is accompanied by 20 fs rapid molecular vibrations. The latter can be interpreted via quantum mechanical *multiconfigurational time-dependent Hartree* (MCTDH) simulations as a propagation of an excited state-related nuclear wave packet along closed trajectories in the space spanned by the molecular degrees of freedom. This may be considered as a manifestation of ultrafast coherent photochemistry.



# Kurzzusammenfassung

Die *Ozonschicht* der Erdatmosphäre schützt Mensch und Natur gegenüber der mutagen wirkenden Sonnenstrahlung im tiefen ultravioletten (*deep ultraviolett*, DUV) Spektralbereich zwischen 200 nm und 300 nm. Das in dieser Schicht enthaltene Ozon ( $O_3$ ) absorbiert dabei DUV-Photonen und geht in einen angeregten, dissoziativen elektronischen Zustand über. Bei diesem als Photodissoziation bekannten Prozess wird optische in kinetische Energie seiner Photofragmente (atomarer (O) und diatomarer ( $O_2$ ) Sauerstoff) umgewandelt. Obwohl die Photolyse des Ozon-Moleküls bereits nach ungefähr 20 Femtosekunden ( $1 \text{ fs} = 10^{-15} \text{ s}$ ) abgeschlossen und *theoretisch* sehr gut beschrieben ist, entzog sie sich bislang einer *direkten, zeitaufgelösten Messung*.

Zur experimentellen Nachstellung dieses Prozesses im Labor bedarf es der Erfüllung zweier Voraussetzungen: Zum einen eine hochreine Ozon-Quelle, da Ozon aufgrund seiner Reaktivität mit der Umgebung sowohl schwer zu lagern als auch über weite Strecken kaum zu transportieren ist. Zum anderen benötigt man zur zeitaufgelösten Messung der Ozon-Photolyse und für einen messbaren Populationstransfer zwischen Grund- und angeregtem Zustand einen intensiven DUV-Anregepuls. Zusätzlich ist ein extrem-ultravioletter (*extreme-ultraviolet*, XUV) Abfragepuls vonnöten, den man relativ zum DUV-Anregepuls verzögern kann und der die Moleküldynamik zu fixen Zeiten nach DUV-Anregung abfragt. Im Allgemeinen kann eine Femtosekunden-Auflösung nur mittels kurzer DUV-Anrege- und kurzer XUV-Abfragepulse gewährleistet werden. Im Rahmen dieser Arbeit werden daher zwei Ansätze zur Erzeugung solch *kurzer* sowie *intensiver* DUV-Anregepulse diskutiert und miteinander verglichen. Beide basieren auf nichtlinearer Erzeugung der *zweiten* bzw. *dritten* Harmonischen (*second/third harmonic generation*, SHG/THG) eines Femtosekunden Kerr-Linsen-modengekoppelten Titan-Saphir-Lasers.

Als primäres Ergebnis präsentiert die vorliegende Arbeit die *erste zeitaufgelöste Messung der Ozon-Photodissoziation* mittels zeitaufgelöster Photoelektronenspektroskopie (*time-resolved photoelectron spectroscopy*, TRPES). Zu diesem Zweck hebt ein via SHG erzeugter DUV-Puls (sub-10 fs; 2  $\mu\text{J}$ ; 268 nm) das Ozon-Molekül in seinen angeregten Zustand, während ein kurzer XUV-Puls ( $\sim 1.7 \text{ fs}$ ; 99.5 eV) die Moleküldynamik abfragt. Die experimentellen Ergebnisse zeigen, dass die Ozon-Photodissoziation durch 20 fs schnelle Molekülschwingungen begleitet wird. Letztere können mittels quantenmechanischer *multiconfigurational time-dependent Hartree* (MCTDH) Simulationen als Propagation des zum angeregten Zustand gehörigen Kernwellenpakets entlang geschlossener Trajektorien im Raum der Molekül-Freiheitsgrade interpretiert werden und stellen einen ultraschnellen Prozess kohärenter Photochemie dar.





# Contents

<b>1</b>	<b>Introduction</b>	<b>1</b>
<b>2</b>	<b>Theory</b>	<b>5</b>
2.1	Few-Cycle Femtosecond Laser Pulses . . . . .	5
2.2	Light-Matter Interaction . . . . .	11
2.2.1	Electromagnetic Wave Equation . . . . .	12
2.2.2	Linear Regime . . . . .	13
2.2.2.1	Isotropic Case . . . . .	15
2.2.2.2	Anisotropic Case - Uniaxial Crystal . . . . .	17
2.2.3	Nonlinear Regime . . . . .	20
2.2.3.1	Second-Order Nonlinear Effects . . . . .	21
2.2.3.2	Third-Order Nonlinear Effects . . . . .	24
2.2.4	Extreme Nonlinear Regime . . . . .	27
2.2.4.1	High Harmonic Generation . . . . .	28
2.2.4.2	Generation of Isolated Attosecond Pulses . . . . .	31
<b>3</b>	<b>Experimental Tools</b>	<b>33</b>
3.1	The FP3 Laser System . . . . .	33
3.1.1	Oscillator . . . . .	35
3.1.2	Multipass Regenerative Amplifiers . . . . .	35
3.1.3	DPHCF, Supercontinuum Generation and Final Compression . . . . .	38
3.1.4	CEP-Stabilization . . . . .	41
3.2	The Attosecond Beamline AS2 . . . . .	43
3.2.1	High Harmonic Generation Chamber . . . . .	43
3.2.2	Interferometer — Delay Chamber . . . . .	44
3.2.3	Experimental Chamber . . . . .	46
<b>4</b>	<b>Electronic and Nuclear Dynamics in Ozone</b>	<b>49</b>
4.1	Principle of the Experiment . . . . .	51
4.1.1	The Ozone Molecule . . . . .	51
4.1.2	Absorption Bands and Electronic States of Ozone . . . . .	52
4.1.3	Expected Molecular Dynamics . . . . .	54
4.2	Simulations of Electronic and Nuclear Dynamics in Ozone . . . . .	56

4.2.1	Theoretical Tools for Full Ab-Initio Simulations . . . . .	56
4.2.1.1	Electric Field-Perturbed Molecular Hamiltonian . . . . .	56
4.2.1.2	Local Electronic Population and Coherence at the FC point . . .	57
4.2.1.3	Dyson Orbitals and Photoionization Probabilities . . . . .	58
4.2.1.4	Theoretical Results . . . . .	59
4.2.2	Three-Level Simulation . . . . .	59
4.3	Group Theoretical Aspects . . . . .	62
4.3.1	The $C_{2v}$ Point Group . . . . .	62
4.3.2	Cation States of Ozone . . . . .	64
4.3.3	Angular Distribution of Photoelectron Emission . . . . .	65
4.4	Few-Femtosecond XUV Probe Pulse Generation . . . . .	69
4.4.1	Required XUV Probe Pulse Energy Resolution . . . . .	70
4.4.2	XUV Spectrum used in the Experiment . . . . .	71
4.5	Femtosecond DUV Pump Pulse Generation . . . . .	72
4.5.1	Early Attempt — THG Gas Phase Target . . . . .	74
4.5.2	Current Attempt — SHG Solid State Target . . . . .	76
4.5.3	Temporal Characterization of Ultrashort DUV Pulses — DUV-TG-FROG	82
4.5.4	Comparison between THG Gas Target and SHG Solid State Target . . .	87
4.5.5	Conclusion . . . . .	88
4.6	Synthesis of Highly Pure Ozone — Sample Preparation . . . . .	89
4.7	Ozone vs. Oxygen Photoelectron Spectra and Energy Domains . . . . .	91
4.8	Results and Discussion . . . . .	93
4.8.1	DUV–XUV Pump-Probe-Measurement of Ozone . . . . .	93
4.8.2	Multi-Level Data Analysis Scheme . . . . .	94
4.8.3	Temporal Evolution of Ground X State Depletion . . . . .	97
4.8.4	Temporal Evolution of Oxygen Build-Up . . . . .	97
4.8.5	Temporal Evolution of the Transiently Populated B State . . . . .	99
4.9	Interpretation . . . . .	100
4.9.1	X State-related Nuclear Wave Packet Motion . . . . .	102
4.9.2	B State-related Nuclear Wave Packet Motion . . . . .	103
4.10	Excited B State-Related Dyson Orbitals of $O_3$ and $O_2 + O$ . . . . .	104
<b>5</b>	<b>Conclusion</b>	<b>109</b>
<b>6</b>	<b>Outlook</b>	<b>111</b>
<b>Appendix A Pulse Characterization Techniques</b>		<b>113</b>
A.1	Attosecond Streaking . . . . .	113
A.2	FROG . . . . .	116
<b>Appendix B Group Theory and Group Representations</b>		<b>119</b>
B.1	Groups . . . . .	119
B.2	Classes . . . . .	120
B.3	Group Representations . . . . .	120

<b>Bibliography</b>	<b>125</b>
<b>Curriculum Vitae</b>	<b>135</b>
<b>Danksagung</b>	<b>139</b>



# Chapter 1

## Introduction

The origin of methods, striving to resolve processes which are fast with respect to timescales directly accessible by human beings, can be traced back to the pioneering work of *Eadweard Muybridge* in the 70s of the 19<sup>th</sup> century [1]. Back then, Muybridge adduced clear photographic evidence that there are instants of time during a horse's galloping motion, when its hooves do not touch the ground, but are airborne all at once. Thus, he solved a decades spanning controversy. The key to Muybridge's paramount achievement was the use of an array of very fast cameras, which are spatially displaced from each other along the direction of the galloping horse. Owing to the fact that the shutter of each camera along this line was released at the very moment the horse passed by it, Muybridge could take a series of pictures, each showing a different fraction of the entire motion. The crucial fact about Muybridge's new approach was to make use of shutters that allow for a short exposure time of their photosensitive films. The exposure time had to be much shorter than the timescale, on which the galloping motion of the horse evolves. If it had been too long, the images would have got blurred, which, in turn, would have rendered a decomposition of the entire motion into smaller subsets of motions impossible.

Nowadays, current state-of-the-art approaches, pioneered by *Ahmed H. Zewail* [2] and which led to the field called *femtochemistry*, rely on the very same principle that Muybridge used in his days. Compared to then, modern experiments gained an almost 18 orders of magnitude improvement in terms of temporal resolution [3]. Today, time-resolved investigation of the fastest processes in matter, which evolve on *femtosecond* or even *attosecond* timescales in, for example, *atoms* [4], *molecules* [5] or *solids* [6], became possible by the advent of modern ultrafast femtosecond lasers, which take over the role of Muybridge's cameras and are used in so-called pump-probe experiments. There, a pump pulse launches dynamics within a sample, while another time-delayed probe pulse queries the sample's momentary state. By repetition of this pump-probe-scheme for a set of delay times between pump and probe pulses, one can retrieve the entire evolution of the sample's underlying dynamics in a time-resolved manner. Always provided, that the duration of pump and probe pulse remains shorter than the inherent timescale of the dynamics themselves, just like in the case of Muybridge.

Besides a variety of different approaches, all promising to gain a deeper understanding of light-

matter interaction, they all depend on the availability of appropriate ultrafast radiation sources in a variety of spectral domains. Until today, such pump pulses are mainly available in the near-infrared (NIR) to far-infrared (FIR) part of the electromagnetic spectrum. Therefore and also for opening up the prospect of studying ultrafast dynamics in deep-ultraviolet- (DUV) sensitive samples, special emphasis should be placed on the generation of adequate DUV pump pulses. Unfortunately, these should be *short* and *intense*, and these conditions are technically hard to meet. Though many schemes regarding their creation have been developed and rely on, for example, third harmonic generation (THG) in neon-filled gas-cells [7], broadband chirped-pulse four-wave-mixing (BCP-FWM) [8], dispersive wave emission in gas-filled hollow-core photonic crystal fibers [9], and many more, they partially lack either of the aforementioned properties. Nevertheless, *short* and *intense* DUV pulses are an indispensable prerequisite for performing ultrafast time-resolved studies of DUV-absorbing molecules.

Regarding these molecules, ozone ( $O_3$ ) should be mentioned in particular, as it exhibits one of the most intense DUV absorption bands among all molecules. Apart from that, the Earth's stratospheric *ozone layer* is of vital importance for life on our planet. Therefore, it is not astonishing that the emergence of man-made *ozone depletion*, initially triggered by the emission of chlorofluorocarbons (CFCs), resulted in the internationally ratified *Montreal Protocol*. The latter tries to protect the ozone layer against potentially ozone-depleting substances (ODSs) by gaining control over their exhaust and production. Consequently, it is continuously amended by the inclusion of other chemical compounds, being substantially harmful to the ozone layer. For example, the impact of dichloromethane ( $CH_2Cl_2$ ), which is still not considered in the *Montreal Protocol*, on ozone depletion was revealed very recently [10]. Nevertheless, first hints grow stronger that the *Montreal Protocol* does take effect and the ozone layer slowly keeps recovering [11].

However, besides the impact of ODSs, the DUV-light-induced fragmentation of the ozone molecule into atomic (O) and diatomic ( $O_2$ ) oxygen is the primary ozone-depleting mechanism. It is mainly this process, commonly known as *photodissociation*, that is responsible for the protective property of the ozone layer against biologically hazardous DUV solar radiation. Upon absorption of a single DUV-photon ( $h\nu$ ), the ozone molecule undergoes a transition from its ground state ( $O_3$ ) into a dissociative, excited state ( $O_3^*$ ), before molecular fragmentation sets in, according to the reaction:  $O_3 \xrightarrow{h\nu} O_3^* \longrightarrow O + O_2$ . Despite a wealth of theoretical work on this issue [12–17], this process has evaded a direct, *time-resolved experimental* study for a long time, most likely owing to the lack of an appropriate DUV radiation source. As outlined before, this is required to be intense and particularly short, because the ozone photolysis is known to be completed approximately 20 fs after DUV excitation.

Therefore, the present thesis focuses on the development of such an ultrafast, pure-DUV radiation source, that is necessary for the *very first few-femtosecond experimental study* of the DUV-pump-pulse-induced molecular dynamics of ozone, evolving during its photodissociation.

## Outline of this Thesis

Following this introduction, chapter 2 will discuss the most fundamental concepts of few-cycle femtosecond pulses. This is continued by a review of the most important linear, nonlinear and extreme nonlinear effects during light–matter interaction. Special emphasis is laid on birefringent nonlinear crystals and symmetries, that can be exploited to ease numerical modeling of short and intense DUV pump pulse generation via nonlinear frequency up-conversion of few-cycle femtosecond pulses in beta-barium-borate (BBO) crystals. The fundamental concept of high harmonic generation (HHG), that is used for XUV probe pulse generation, is illuminated here as well.

Chapter 3 explains the setup of the *FP3 laser system* and introduces the *AS2 attosecond beamline* in general, where the pump–probe *time-resolved photoelectron spectroscopy* (TRPES) experiment on ozone is performed in.

Chapter 4 focuses on the ozone experiment itself. First, we will discuss the principle of the experiment, including the molecular structure, absorption bands and expected molecular dynamics of ozone, setting in after irradiation with a DUV pump pulse. We will explain the theoretical tools which are used by our colleagues *Ágnes Vibók*, *Gábor J. Halász*, *Piero Decleva* and *Fabien Gatti* to simulate TRPES-spectrograms of ozone, explicitly taking the angular distribution during photoemission into account. Following this discussion, we will present the cation states of ozone and deduce an experimental pump-probe-geometry via group theoretical arguments that is capable of rendering excited state dynamics of ozone measurable. Before digging into the experimental results themselves, experimental constraints regarding the XUV probe pulse generation are illuminated and a comparison between THG- and SHG-based DUV pump pulse generation schemes is given. The chapter ends with a discussion of the primary experimental results on ozone photodissociation and an interpretation in terms of nuclear wave packet motion as well as with an indication based upon Dyson orbitals, explaining why the experimental results are observable after all.

The thesis finishes with a conclusion of the main results as well as with an outlook.





## Chapter 2

# Theory

This chapter is intended to provide an introduction to the theoretical concepts of nonlinear optics, as far as they are relevant within the scope of this thesis.

Getting started, the first section is dedicated to the mathematical formalism of ultrashort, few-cycle laser pulses. Here special focus is laid on some peculiarities, occurring for few-cycle laser pulses as opposed to multi-cycle laser pulses. In section two, we will use the aforementioned formalism to describe light–matter interaction in greater detail, introducing new quantities and concentrating on both the linear and nonlinear regime. Special attention is paid to the last subsection of light–matter interaction, focusing on the application of intense, few-cycle laser pulses for the generation of attosecond *extreme-ultraviolet* (XUV) pulses via *high harmonic generation* (HHG). We will discuss the non-applicability of a perturbatory approach to describe this phenomenon and explain the underlying process.

### 2.1 Few-Cycle Femtosecond Laser Pulses

To put the subsequent treatment on an equal footing, we will introduce some quantities, which will be used in this thesis, partially following the notation of *R.W.Boyd* [18] when dealing with nonlinear optics. As far as it concerns the scope of this work, the electric field will be treated classically, as relativistic effects are negligible. Also magnetic effects are not dealt with as their strength even for strong electric fields and with respect to them are suppressed by a factor of  $1/c_0$ , where  $c_0 = 299792458 \frac{m}{s}$  denotes the vacuum speed of light. More information can be found in standard textbooks, for example in [19].

Consider the electric field vector of a laser pulse at time  $t$  and position  $\vec{r}$  in space

$$\vec{E}(t, \vec{r}) = \vec{e} \cdot \tilde{E}_0(t, \vec{r}) \cdot e^{i\Phi(t, \vec{r})} + c.c., \quad (2.1)$$

where  $\vec{e}$ ,  $\tilde{E}_0(t, \vec{r})$  and  $\Phi(t, \vec{r})$  denote the unit vector of polarization, scalar electric field envelope function and the total time- and space-dependent phase, respectively. The term *c.c.* stands

for "complex conjugate" and is necessary here, because the electric field is a real quantity. In general, the polarization vector  $\vec{e}$  is a three-component vector which does not have to consist of real numbers and reduces to a two-component *Jones vector*<sup>1</sup> in case of plane waves. The Jones vector describes the polarization state and is allowed to contain complex values as well. These are commonly used to represent circular or elliptical polarization ( $\vec{e}_{L,R} = \frac{1}{\sqrt{2}} \cdot (1, \pm i)^T$  for left- (*L*) / right- (*R*) polarized light) besides the linear polarization ( $\vec{e}_x = (1, 0)^T$  for x-polarized light), which we mainly deal with.

Up to now, the formalism does not exclusively apply to pulses, but to any wave that is decomposable in an envelope and phase function, respectively. In order to specialize the description for pulsed lasers, both phase and electric field envelope function can further be dismantled into

$$\Phi(t, \vec{r}) = \omega_0 \cdot t - \vec{k} \cdot \vec{r} + \phi(t) + \phi_{CEP} \quad (2.2)$$

$$\tilde{E}_0(t) = E_0 \cdot \exp\left(-\frac{t^2}{\sigma_t^2}\right) = E_0 \cdot \exp\left(-\frac{2 \ln(2)}{\Delta t^2} \cdot t^2\right). \quad (2.3)$$

Obviously, we have separated the total phase into a fast oscillating part  $\omega_0 \cdot t$ , where  $\omega_0$  is the laser's center angular frequency, and a space-dependent part  $\vec{k} \cdot \vec{r}$ , that takes the influence of the laser's propagation direction  $\vec{k}$  on the total phase into account. The modulus of  $\vec{k}$  is directly connected to the laser vacuum wavelength  $\lambda$  via  $k = \frac{2\pi}{\lambda}$ . The maximum phase contribution originating from the spatial part is expected to occur in directions  $\vec{r}$  that are parallel to  $\vec{k}$ . In directions perpendicular to  $\vec{k}$ , one does not obtain an additional phase shift, as the scalar product vanishes. Consequently, the so-called *wave-fronts*<sup>2</sup> extend in a plane, that is perpendicular to the vector  $\vec{k}$ .

Apart from these spatially and temporally very fast oscillating quantities, there are two residual terms in equation (2.2), that deserve special mention, because they play a dominant role for some highly nonlinear effects in case of few-cycle laser pulses. The first of the two latter terms in equation (2.2) is  $\phi(t)$  and symbolizes the time-dependent phase, describing higher-order chirps. In this context, *chirp* means a non-vanishing time-dependency of the *instantaneous angular frequency*

$$\omega(t) = \frac{d\Phi(t)}{dt} = \omega_0 + \frac{d\phi(t)}{dt}, \quad (2.4)$$

where we have ignored the spatial contribution for now.

In a perturbatory approach one would be tempted to expand the phase  $\phi(t)$  in a Taylor series, but, since it is less intuitive to interpret this in the time domain, it is usually performed in

<sup>1</sup>In the *Jones calculus* it is merely assumed that one deals with fully polarized electric fields, as we usually do for lasers, and was introduced in a series of papers [20–23].

<sup>2</sup>planes of constant phase in space.

the frequency domain and is postponed to the next section. The last term in equation (2.2) is  $\phi_{CEP}$  and denotes the so-called *carrier envelope phase*<sup>3</sup> (CEP), which is nothing less than the time-independent part of  $\phi(t)$ , but is tremendously important for the generation of isolated attosecond XUV pulses as will become apparent in subsection 2.2.4.1. This is why we have extracted it here explicitly.

Turning to the electric field envelope function  $\tilde{E}_0(t, \vec{r})$  in equation (2.3),  $E_0$  marks the electric field strength at the envelope's maximum value and  $\Delta t$  terms the *full-width-at-half-maximum* (FWHM) pulse duration<sup>4</sup>. Depending on the chosen convention, one could also define the pulse duration as 1/e-width  $\sigma_t$ . Since both quantities are related to each other via equation (2.5), they are equivalent:

$$\Delta t = \sqrt{2 \ln 2} \sigma_t. \quad (2.5)$$

Besides the time-domain picture of few-cycle laser pulses, there is another, but linked, frequency-domain picture, and one can freely choose between both, since they describe the same. The time- and space-related Fourier transform of the electric field (equation (2.1)) is defined as

$$\vec{E}(\omega, \vec{k}) = \int_{-\infty}^{\infty} dt \int_{\mathbb{R}^3} d^3 r \vec{E}(t, \vec{r}) e^{-i(\omega t - \vec{k} \cdot \vec{r})} \quad (2.6)$$

and the inverse Fourier Transform is defined accordingly, using

$$\vec{E}(t, \vec{r}) = (2\pi)^{-4} \int_{-\infty}^{\infty} d\omega \int_{\mathbb{R}^3} d^3 k \vec{E}(\omega, \vec{k}) e^{+i(\omega t - \vec{k} \cdot \vec{r})}, \quad (2.7)$$

where the additional term  $(2\pi)^{-4}$  occurs due to normalization constraints. If one applies equation (2.6) to equation (2.3), one will get the following spectral representation of the envelope function (omitting spatial integration)

$$\tilde{E}_0(\omega) = E_{0,\omega} \cdot \exp\left(-\frac{\omega^2}{\sigma_\omega^2}\right) = E_{0,\omega} \cdot \exp\left(-\frac{2 \ln(2)}{\Delta\omega^2} \cdot \omega^2\right), \quad (2.8)$$

where  $\sigma_\omega$ ,  $\Delta\omega$  are the 1/e-bandwidth and FWHM-bandwidth of the spectrum, respectively, and the latter can also be written in terms of  $\Delta t$  as

---

<sup>3</sup>The *carrier-envelope-phase* (CEP) is the phase difference between the peak position of the carrier wave and of the envelope.

<sup>4</sup>We assume a Gaussian shaped envelope function in equation (2.3), as it is directly related to our experimental condition, but other shapes are also conceivable, e.g., hyperbolic-secant-squared ( $\text{sech}^2$ ) shaped pulses etc.

$$\Delta\omega = \frac{4 \ln(2)}{\Delta t}. \quad (2.9)$$

It immediately occurs to the reader that the FWHM-duration and the FWHM-bandwidth show opposite behavior: *The shorter the pulse duration, the bigger the spectral bandwidth.* One can even prove that for a Fourier transform limited Gaussian pulse, their product (i.e. Time-Bandwidth-Product) cannot fall below a certain value. For a Gaussian pulse, one immediately obtains from the formula given above

$$\Delta t \cdot \Delta\nu = \Delta t \cdot \frac{\Delta\omega}{2\pi} = \frac{4 \ln(2)}{2\pi} \approx 0.441, \quad (2.10)$$

where  $\Delta\nu = \frac{\Delta\omega}{2\pi}$  is the frequency analog of the angular frequency, just extracting the radian measure. This equation illustrates the following fact: In order to obtain pretty short pulses, the need for a rather broad spectrum is indispensable. However, it should be mentioned that a broad spectrum does not directly imply a short pulse. For the time being, let us assume a pulse train, consisting of identical — down to their electric field shapes — and equidistantly separated pulses. If we calculate the associated Fourier Transform, we will get a spectrum, that contains equidistantly distributed delta peaks and another peak, that emerges at zero frequency, as shown in Figures 2.1 c),d). This is simply the frequency domain signature of the aforementioned identical pulse train. If we now made the first peak deviate from zero frequency, but maintain the relative spacing between adjacent modes, we would still receive a pulse train in the time domain picture, but with a constant pulse-to-pulse phase offset, as depicted in Figures 2.1 a),b). The first spectral spike is also referred to as the *carrier-envelope-offset* (CEO) frequency  $f_{CEO}$ , and the pulse train is commonly known as a Frequency Comb [24]. The CEO frequency directly relates to the CEP by using the following equation

$$f_{CEO} = \frac{\phi_{CEP}}{2\pi} \cdot f_{Rep}, \quad (2.11)$$

where  $\phi_{CEP}$  is defined within  $[0, 2\pi[$  and  $f_{Rep}$  represents the repetition rate of the pulse train, that is the inverse of the time difference between neighboring pulses.

Advancing the concept of pulse train formation from a frequency domain perspective, we can consider the pulse train as being formed by the coherent superposition of sinusoidal waves in integer multiples of a fundamental frequency difference  $\Delta f$ . If all of the wave crests were overlapped, they would add up constructively at times  $\Delta t$ , which are the inverse of  $\Delta f$ . At all other times, the waves would cancel each other out by destructive interference, thus forming pulses periodically. If we imagined for an instant that the phase relation between the waves was not rigid, but random, we would not get a well-defined pulse train, which is the more chaotic, the more waves contribute, because the moment of constructive interference would vary in an unpredictable manner. Therefore, a stiff phase relation between waves, contributing to the overall interference, is inevitable. One also calls this fixed phase relationship *phase-locking* or *mode-locking*. This has been tacitly assumed in the illustration of Figure 2.1.

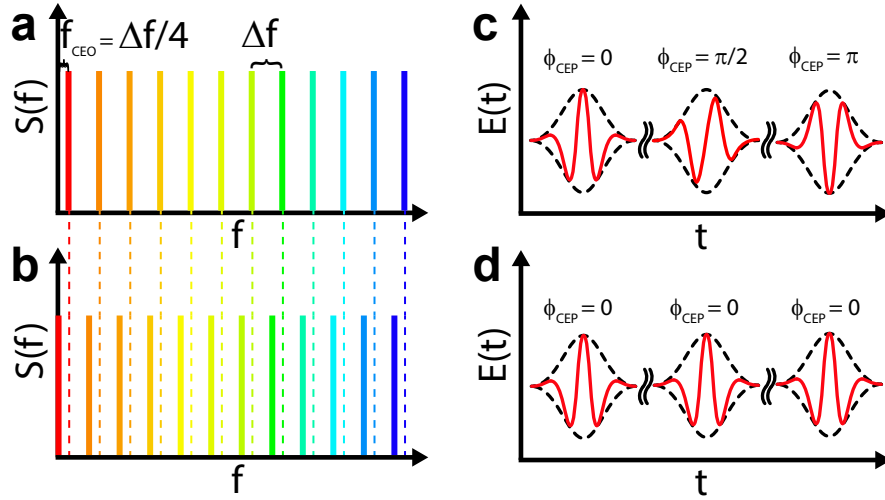


**Figure 2.1:** Shown is the equivalence between a comb-like spectrum and the time-domain pulse-train formation for two different carrier-envelope-offset frequencies **a),c)**  $f_{CEO} = \frac{\Delta f}{4}$ , **b),d)**  $f_{CEO} = 0$ , where  $\Delta f = f_{Rep}$  and  $f_{Rep}$  is the repetition rate of the pulse train. **d)** For vanishing  $f_{CEO}$ , the individual pulses are identical to one another. **c)** If  $f_{CEO}$  deviates from zero and is equal to  $\Delta f/4$ , for example, only every fourth pulse is identical, since every pulse accumulates an additional phase shift relative to its predecessor. Here, the carrier-envelope-phase is denoted by  $\phi_{CEP}$ .

Figure 2.2 illustrates the basic idea of mode-locking for four different cases. It is obvious from Figure 2.2 that the more frequencies or modes contribute, the shorter is the pulse in the time domain, provided that all modes are phase-locked to each other.

As attosecond experiments usually heavily rely on the control of the CEP, let us have a look at how the CEP influences the shape of the carrier wave under the field envelope for an identical set of CEP-values. Figure 2.3 a) illustrates the minor impact of the CEP for multi-cycle laser pulses, when changing the CEP from  $\phi_{CEP} = 0$  (black solid line) to  $\phi_{CEP} = \frac{\pi}{2}$  (blue dashed line). Here, the electric field drop can almost be neglected. Figure 2.3 b), instead, exemplifies the importance of the CEP on the electric field shape for few-cycle laser pulses. The reason for the now more pronounced drop of the carrier wave amplitude is the fast decrease of the pulse envelope to either side, whose width is comparable to the period of the carrier wave itself. Owing to this drastic change of electric field strength with CEP for few-cycle laser pulses, isolated attosecond XUV pulse generation became possible, showing that the control of the CEP is the key to their generation.

Anticipating part of the discussion considering isolated attosecond pulse generation as a highly nonlinear process we introduce the concept of *intensity* here. *Mode-locking* by itself does not lead to ultrashort pulses, but is also a good method to gain high intensities, as the available energy of all modes is bunched in narrow wave packets. If we once again identify ultrashort pulses with the coherent, phase-locked superposition of  $N$  waves with ascending frequencies, where each wave

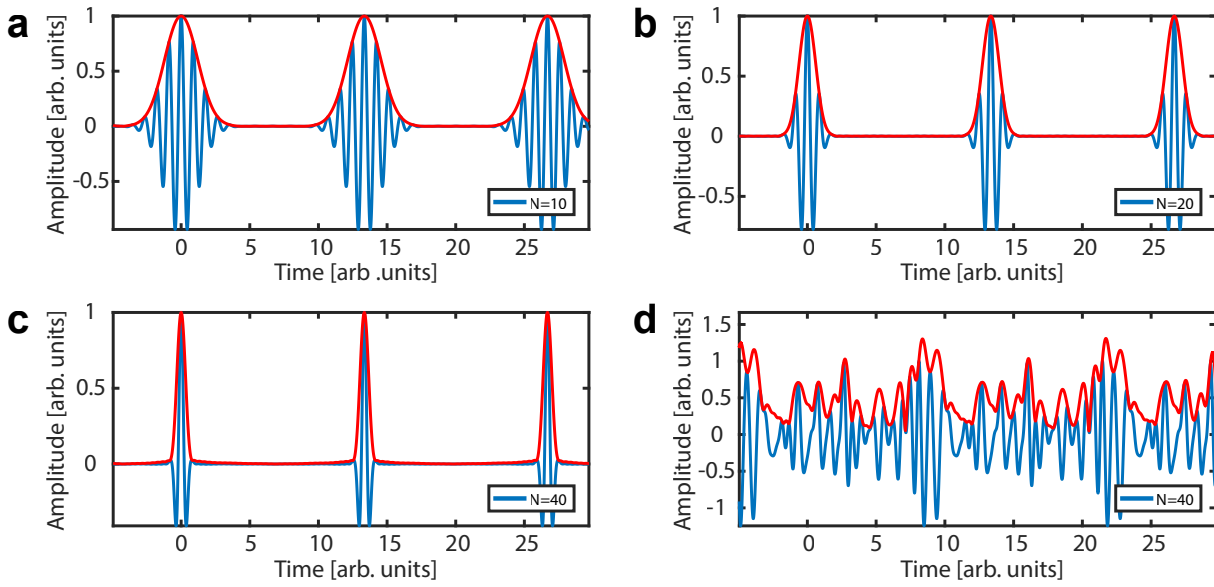


**Figure 2.2:** Pulse train formation for increasing bandwidth **a)-d)**: For better visualization, the ratio between the fundamental frequency and the free spectral range has been adapted accordingly. Time and electric field strength are given in arbitrary units. *Blue curve*: electric field carrier wave, *Red curve*: electric field envelope. **a)-c)** show the superposition of an increasing number of  $N$  coupled modes, whereas **d)** depicts the superposition of  $N=40$  uncoupled modes with random phase relation.

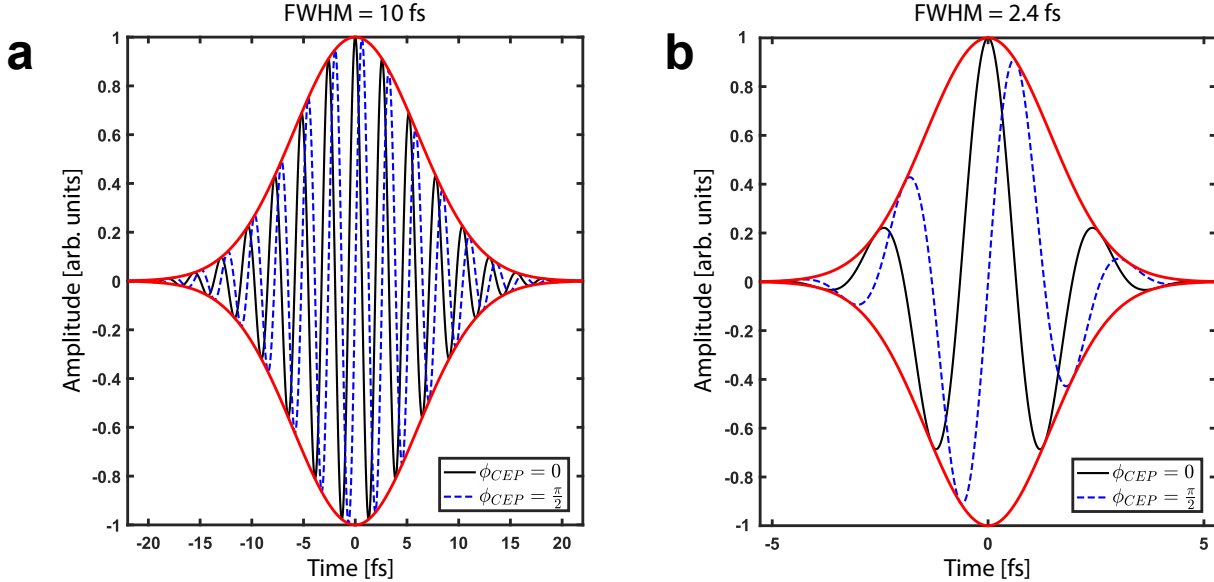


**Figure 2.3:** Impact of two different CEP-settings (*black solid line*:  $\phi_{CEP} = 0$  and *blue dashed line*:  $\phi_{CEP} = \frac{\pi}{2}$ ) on the shape of the carrier wave for **a)** a multi-cycle and **b)** for a few-cycle pulse. The change of the peak electric field as a function of the CEP is most striking in **b)**.

has an electric field strength  $E_0$ , we will find an  $N$ -fold amplitude amplification at the moment of constructive interference. Consequently, the resulting total electric field strength amounts to  $N \cdot E_0$ . This implies that the more modes contribute to the pulse formation, the higher the total instantaneous electric field strength becomes.

In order to quantify the *instantaneous intensity*  $I(t)$ <sup>5</sup> in a formal manner, it is usually defined as the absolute value of the so-called *Poynting-vector*  $\vec{S}(t)$  as

$$I(t) = \left| \vec{S}(t) \right| = nc_0 \epsilon_0 E_0^2(t) \cos^2(\omega_0 t), \quad (2.12)$$

where  $n$  denotes the refractive index of a material, that is penetrated by the electric field with envelope function  $E_0(t)$ . In section 2.2, we will relate the refractive index  $n$  to the *relative permittivity* of a material. The cycle-averaged intensity  $\bar{I}(t)$ , in turn, can be deduced from the above definition (equation (2.12)) via

$$\bar{I}(t) = \frac{1}{T} \int_{-\frac{T}{2}}^{\frac{T}{2}} I(t) dt \approx \frac{1}{2} nc_0 \epsilon_0 E_0^2(t), \quad (2.13)$$

if  $E_0(t)$  varies slowly and where  $T = \frac{2\pi}{\omega_0}$  is the duration of a single period.

For completeness of the current discussion, the *Poynting vector* itself is defined in *Poynting's theorem* [25] as

$$\vec{S}(t) = \vec{E}(t) \times \vec{H}(t), \quad (2.14)$$

where  $\vec{E}(t)$  and  $\vec{H}(t)$  are the electric and magnetic field strengths, respectively, and " $\times$ " is the *cross-product* between two vectorial quantities. The *Poynting vector* plays a special role in terms of birefringence, since it represents the flow of energy along a certain direction. In case of birefringent materials, there may be more than only one direction of energy flow, depending on the input polarization with respect to the optic axis of the birefringent material.

## 2.2 Light–Matter Interaction

In the last section we have learned about the basics that are necessary to describe electric fields in general and few-cycle pulses in particular. Nevertheless, these pulses are not studied for their own sake, but to gain a deeper insight into light–matter interaction on its very inherent timescale. Since the field of light–matter interaction is continuously increasing and still under intensive investigation, even the trial to gather all its facets is either impossible or at least incomplete. Therefore, we will simply give a short introduction into the concepts relevant to

<sup>5</sup>Intensity is defined as the optical power transmitted through a plane perpendicular to the propagation direction of light per unit area. The unit of intensity is thus given in  $W/m^2$ .

us from a phenomenological point of view, ranging from the linear regime over the perturbative nonlinear regime to the extreme nonlinear regime, that cannot be described anymore by a perturbative approach.

### 2.2.1 Electromagnetic Wave Equation

Maxwell's equations [26] as well as Schrödinger's equation [27] lie at the heart of the description of light-matter interplay. Neglecting Schrödinger's equation for now, Maxwell's equations take the matter's reaction on the electromagnetic fields into account and can be written as done in equations (2.15) – (2.19), where  $\vec{E}$  and  $\vec{B}$  denote as before the electric field and magnetic flux density, respectively.

$$\vec{\nabla} \cdot \vec{E} = \frac{\rho}{\epsilon_0} \quad (2.15)$$

$$\vec{\nabla} \cdot \vec{B} = 0 \quad (2.16)$$

$$\vec{\nabla} \times \vec{E} = -\frac{\partial \vec{B}}{\partial t} \quad (2.17)$$

$$\vec{\nabla} \times \vec{B} = \mu_0 \left( \vec{j} + \frac{\partial \vec{D}}{\partial t} \right) \quad (2.18)$$

$$\vec{D} = \epsilon_0 \vec{E} + \vec{P} \quad (2.19)$$

$\vec{D}$  is the so-called electric displacement field,  $\vec{P}$  symbolizes the polarization response of matter, that is irradiated by electromagnetic fields, and  $\vec{\nabla} = \left( \frac{\partial}{\partial x}, \frac{\partial}{\partial y}, \frac{\partial}{\partial z} \right)^T$  defines the *Nabla operator*. The physical constants  $\mu_0$  and  $\epsilon_0$  stand for the vacuum permeability and vacuum permittivity, respectively. Apart from these quantities,  $\rho$  and  $\vec{j}$  display the total charge and total current of the system under consideration, including the influence of bound and free electric charges, and are allowed to be functions of time and space. Those quantities can usually be described by additional equations, as for instance, by Schrödinger's equation. If we calculate the curl of equation (2.17) and insert equation (2.18) into the new equation, while we interconvert temporal and spatial differentiation and make use of equation (2.19), we will arrive for vanishing current density  $\vec{j}$  at the *electromagnetic wave equation*

$$\left[ \vec{\nabla} \times (\vec{\nabla} \times) + \frac{1}{c_0^2} \frac{\partial^2}{\partial t^2} \right] \vec{E}(t, \vec{r}) = -\mu_0 \frac{\partial^2 \vec{P}(t, \vec{r})}{\partial t^2}, \quad (2.20)$$

where the square bracket on the left-hand-side can be interpreted as an operator, that affects the electric field  $\vec{E}(t, \vec{r})$ , and the vacuum speed of light has been expressed in terms of  $\epsilon_0$  and  $\mu_0$ , according to  $c_0^{-2} = \epsilon_0 \mu_0$ .

This equation can be understood as follows: The left-hand-side (lhs) of equation (2.20) is responsible for the propagation of the electric wave through space and time, whereas the right-hand-side



(rhs) can be considered a source term, which influences the propagation. Since the rhs-term itself is either triggered or modified by the mere presence of the electric field equation (2.20), it can exhibit a wealth of dynamics, which can be split up into linear and nonlinear contributions, according to

$$\vec{P} = \vec{P}^L + \vec{P}^{NL}, \quad (2.21)$$

where  $\vec{P}^L$  and  $\vec{P}^{NL}$  are the components of the polarization term, which arise from linear and nonlinear effects, respectively, and will be discussed to some degree in the next subsections.

### 2.2.2 Linear Regime

The linear term  $\vec{P}^L$  in equation (2.21) is usually regarded as the leading order of the total polarization  $\vec{P}$ . In this sense, linearity refers to its linear dependence on the electric field vector  $\vec{E}$ , as opposed to nonlinear contributions, and can be expressed most generally as a convolution [19]

$$P_i^L(\vec{r}, t) = \epsilon_0 \int_{-\infty}^{\infty} d\tilde{t} \int_{\mathbb{R}^3} d^3\tilde{r} \chi_{ij}(\vec{r}, \vec{r}, t, \tilde{t}) E_j(\vec{r}, \tilde{t}), \quad (2.22)$$

where we have tacitly used *Einstein summation convention* [28] to sum across doubly occurring indices<sup>6</sup>. The index  $i$  can take on  $x, y, z$  and  $E_j$ ,  $P_i^L$  are the  $j$ -th and  $i$ -th component of  $\vec{E}$  and  $\vec{P}^L$ , respectively, and  $\chi_{ij}(\vec{r}, \vec{r}, t, \tilde{t})$  is known as the *dielectric susceptibility*. The shape of equation (2.22) permits the system under examination to possess two features:

- The temporal or spatial response of a material  $\chi_{ij}(\vec{r}, \vec{r}, t, \tilde{t})$  is allowed to be *non-local* and *non-instantaneous*, as its dependence on external variables is given explicitly and describes temporal and spatial dispersion properties. For instance, this will be the case, if the dipoles of a material cannot instantaneously follow the change of the electric field vector, either because they are too sluggish or because the irradiated electric field influences dipoles in the near vicinity.
- The direction of the matter response  $\chi_{ij}(\vec{r}, \vec{r}, t, \tilde{t})$  does not have to be parallel to the externally applied field, because the response  $\chi_{ij}$  can be thought of as a *second* order tensor, leading to the concept of *anisotropy*. It is this property that describes birefringence of matter, for example. This happens when the dipoles cannot freely follow the electric field, but are influenced by their surroundings. For instance, in a non-cubic crystal lattice the distances vary along different crystal axes.

As equation (2.22) looks quite complicated due to the occurrence of the convolution, it possesses a simple form, once it is Fourier transformed via equation (2.6). Then, it can be interpreted as a simple matrix product, when expressed in the reciprocal space:

<sup>6</sup>summation of  $j$  runs over the coordinates  $x, y, z$ .

$$P_i(\omega, \vec{k}) = \epsilon_0 \chi_{ij}(\omega, \vec{k}) E_j(\omega, \vec{k}) \quad (2.23)$$

Likewise, the electromagnetic wave equation can be expressed in Fourier space as

$$\vec{k} \times (\vec{k} \times \vec{E}(\omega, \vec{k})) + \frac{\omega^2}{c_0^2} \vec{E}(\omega, \vec{k}) = -\mu_0 \omega^2 \vec{P}(\omega, \vec{k}), \quad (2.24)$$

where we have explicitly written down the dependencies of the vectorial quantities on external variables.

Inserting equation (2.23) into equation (2.24) leads to an eigenvalue problem. These are also called *dispersion relations*,  $\omega(\vec{k})$ , or equivalently,  $\vec{k}(\omega)$ . Their corresponding eigenvectors are given as  $\vec{E}(\omega(\vec{k}), \vec{k})$ :

$$\left[ k^2 \delta_{ij} - k_i k_j - \frac{\omega^2}{c_0^2} (\delta_{ij} + \chi_{ij}(\omega, \vec{k})) \right] E_j(\omega, \vec{k}) = 0, \quad (2.25)$$

where  $k_i$  is the  $i$ -th component of the  $\vec{k}$ -vector,  $k^2$  is the square-modulus of  $\vec{k}$  and  $\delta_{ij}$  is the *Kronecker-delta*, that equals 1, if both indices are identical and 0 otherwise. In order to fulfill equation (2.25) for all angular frequencies  $\omega$  and  $\vec{k}$ -vectors the determinant of the left-hand-side square bracket has to vanish identically and one obtains in matrix notation

$$\det \left( k^2 \mathbb{1} - \vec{k} \vec{k}^T - \frac{\omega^2}{c_0^2} \hat{\epsilon}(\omega, \vec{k}) \right) = 0, \quad (2.26)$$

where  $\mathbb{1}$  symbolizes the identity matrix,  $T$  denotes the transpose and where we have introduced the *relative permittivity* tensor according to

$$\hat{\epsilon} = \epsilon_{ij}(\omega, \vec{k}) = \delta_{ij} + \chi_{ij}(\omega, \vec{k}). \quad (2.27)$$

Usually equation (2.26) constitutes an implicit equation, since the relative permittivity tensor depends formally on the  $\vec{k}$ -vector and angular frequency  $\omega$ .

Hereafter, we assume vanishing spatial dispersion of  $\epsilon_{ij}$ , which is equivalent to an independence of the external variable  $\vec{k}$ ,  $\epsilon_{ij}(\omega, \vec{k}) = \epsilon_{ij}(\omega)$ . Attributed to the fact that the relative permittivity tensor of dielectrics is symmetric with respect to its anisotropy indices, we can always find a coordinate system, in which  $\epsilon_{ij}$  emerges to be diagonal [29].

In order to ease the upcoming discussion, we will distinguish between two cases only and omit the case of highly anisotropic materials, like biaxial crystals. The first case is where  $\epsilon_{ij}$  describes an isotropic material and reduces to a multiple of the identity matrix  $\delta_{ij}$ . The second case is where the material exhibits a preferential axis with respect to light propagation, also called the *optic axis*. Here,  $\epsilon_{ij}$  possesses two nontrivial eigenvalues.

### 2.2.2.1 Isotropic Case

Isotropy describes a property, that is independent of the chosen direction, as all directions are equivalent to each other. This holds true for cubic crystal lattices (e.g. primitive cubic (*pc*), body-centered cubic (*bcc*) or face-centered cubic (*fcc*)), but is also applicable to liquids or gaseous media, which do not exhibit any long-range order. In those cases, the  $\omega$ - $\vec{k}$ -relation appears to be scalar-valued, since  $\epsilon_{ij}(\omega) = \epsilon(\omega)\delta_{ij}$ , and is given by

$$k(\omega) = \pm \frac{\omega}{c_0} \sqrt{\epsilon(\omega)} = \pm \frac{\omega}{c_0} n(\omega), \quad (2.28)$$

irrespective of direction and where we have considered either signs, as the *electromagnetic wave equation* (equation (2.20)) is a representative of a second order differential equation and thus supports two solutions, a forth and a backwards propagating wave. Additionally, we have introduced the refractive index  $n(\omega)$  as

$$n(\omega) = \sqrt{\epsilon(\omega)} = \tilde{n}(\omega) + i\kappa(\omega), \quad (2.29)$$

where  $\tilde{n}(\omega)$  and  $\kappa(\omega)$  denote the real and imaginary part of the refractive index, respectively. Both parts are not independent of each other, but rather connected by the *Kramers-Kronig-relations*, which can be found elsewhere [30]. The refractive index  $n(\omega)$  is a complex function of angular frequency in general. The real part  $\tilde{n}(\omega)$  describes both refraction and dispersion effects, while  $\kappa(\omega)$  is known as the *attenuation coefficient*, governing attenuation or gain of the electric field, depending on the sign.

In order to address *chromatic dispersion*, that is induced by the irradiated material, and to continue with the discussion of the *spectral phase* (section 2.1), we can expand equation (2.28) in a Taylor series about angular frequency  $\omega_0$ , according to

$$k(\omega) = \sum_{n=0}^{\infty} \frac{1}{n!} k^{(n)}(\omega_0) (\omega - \omega_0)^n, \quad (2.30)$$

where  $k^{(n)}(\omega_0)$  is the  $n$ -th derivative of  $k(\omega)$  with respect to angular frequency  $\omega$ , but evaluated at  $\omega_0$ . Because of the fact that this Taylor expansion is frequently used for the description of ultrashort pulses, the most important derivatives in equation (2.30) are linked in ascending order with the terms *group-delay* (GD), *group-delay dispersion* (GDD), *third-order dispersion* (TOD) and *fourth-order dispersion* (FOD). Figure 2.4 depicts their influence on an initially compressed ultrashort pulse (red and black dashed lines) that serves as a reference.

Consequently, the pulse can be delayed as an entity when exposed to a material which exhibits a group-delay, as displayed in Figure 2.4 a). It shall be stated that even the *CEP* of the delayed pulse has changed with respect to the *CEP* of the reference pulse. The situation changes, when the pulse is subjected to a material, that features group-delay-dispersion, as depicted in Figure

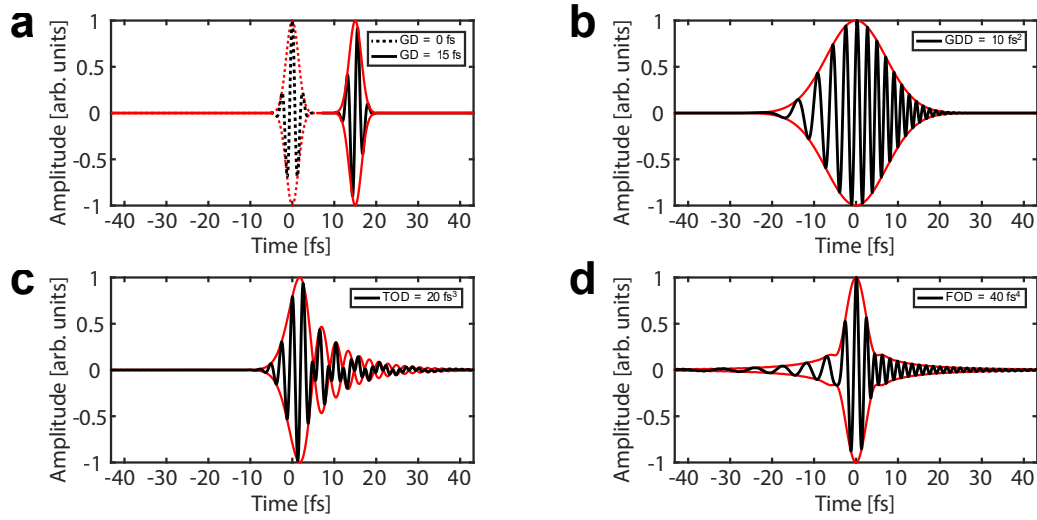


**Figure 2.4:** Influence of GD, GDD, TOD and FOD on an ultrashort reference pulse (dashed lines in **a**)), centered around  $\lambda = 780$  nm. *Black lines:* Electric field. *Red lines:* Pulse envelope. Initial FWHM pulse duration is assumed to be 2.4 fs. **a)** GD=15 fs, **b)** GDD=10 fs<sup>2</sup>, **c)** TOD=20 fs<sup>3</sup> and **d)** FOD=40 fs<sup>4</sup>.

2.4 b). The temporal spread is the most eye-catching difference besides an also present *up-chirp*<sup>7</sup> for positive GDD. In Figure 2.4 c), we introduce a non-vanishing third-order-dispersion and find the prior compressed pulse to form post-pulses on the trailing edge. Needless to say, that the occurrence of these secondary pulses depends on the magnitude and sign of the TOD and could also emerge on the rising edge. Since ultrashort pulses are extremely prone to dispersion effects, one also has to take fourth-order-dispersion into account, which usually manifest itself in the formation of symmetric pedestals, as illustrated in Figure 2.4 d).

In ultrafast optics, it often appears that one faces dispersion management in order to compress the entire pulse spectrum, i.e. to change the relative timing between different frequency components. For its description, a spectral approach in terms of the spectral phase  $\phi(\omega)$  of the pulse is most beneficial, because it provides an intuitive comprehension of which frequency components hurry ahead and which lag behind. This is not the case when dealing with the temporal phase  $\phi(t)$ . Apart from that, the response function of dispersive optical elements, like *gratings*, *prisms* or *chirped mirrors* used for dispersion management, are usually given in frequency domain. In order to explore their action on a certain pulse, one simply has to multiply their response functions by the pulse spectrum. This is why we postponed the discussion concerning  $\phi(t)$  of section 2.1 to here.

Owing to the presence of a dispersive medium, the speed, at which the pulse traverses it, deviates from the vacuum speed of light. Consequently, one distinguishes between the *phase-velocity* and the *group-velocity*. The phase-velocity refers to the speed at which a specific frequency

<sup>7</sup>the instantaneous frequency increases with time

component of the pulse propagates and is given as a function of angular frequency by [19]

$$v_p(\omega) = \frac{\omega(k)}{k} \stackrel{(2.28)}{=} \frac{c_0}{n(\omega)}, \quad (2.31)$$

where the second equality sign is only valid in the special case of equation (2.28). In contrast to the last quantity, the group-velocity describes the propagation speed of the envelope function and is defined as [19]

$$v_g(\omega) = \frac{\partial\omega(k)}{\partial k} \stackrel{(2.28)}{=} \frac{c_0}{n(\omega) + \omega \frac{\partial n(\omega)}{\partial \omega}}, \quad (2.32)$$

where again the second equality sign only holds true for equation (2.28), but may be adapted for other expressions of  $\omega(k)$ , too. In general the group-velocity does not have to be constant, but is allowed to vary with angular frequency and the terms *group-delay* and *group-delay-dispersion* derive from that expression.

### 2.2.2.2 Anisotropic Case - Uniaxial Crystal

If we drop the constraint of directional independence of the material response to electric fields, we will access the anisotropic domain. Here, the *dielectric permittivity* tensor can still be diagonalized, but in contrast to the previous case does not longer appear to be a multiple of the identity matrix. If we restrict ourselves to the case of an uniaxial crystal, we can write it down in its principal coordinate system with no loss of generality as

$$\hat{\epsilon} = \begin{pmatrix} \epsilon_o & 0 & 0 \\ 0 & \epsilon_o & 0 \\ 0 & 0 & \epsilon_e \end{pmatrix}, \quad (2.33)$$

where  $\epsilon_o$  (subscript *o*: ordinary) and  $\epsilon_e$  (subscript *e*: extraordinary) denote two distinct *dielectric permittivities* and are inextricably linked to *birefringence*. Their meaning will become obvious immediately. If one solves equation (2.26), using the above matrix, one will arrive at two nontrivial solutions of the eigenvalue problem (equation (2.26)) for the *dispersion relation*

$$\frac{\omega_o^2(\vec{k})}{c_0^2} = \frac{k_x^2}{\epsilon_o(\omega)} + \frac{k_y^2}{\epsilon_o(\omega)} + \frac{k_z^2}{\epsilon_o(\omega)}, \quad (2.34)$$

$$\frac{\omega_e^2(\vec{k})}{c_0^2} = \frac{k_x^2}{\epsilon_e(\omega)} + \frac{k_y^2}{\epsilon_e(\omega)} + \frac{k_z^2}{\epsilon_o(\omega)}, \quad (2.35)$$

depending on the chosen eigenvector  $\vec{E}(\omega, \vec{k})$ . If the eigenvector  $\vec{E}(\omega, \vec{k})$  has a component  $E_e$  parallel to the *optic axis*<sup>8</sup>, it is attributed to the *extraordinary* wave, whereas components  $E_o$ , perpendicular to the optic axis, are referred to as *ordinary* waves. The equations (2.34) – (2.35) are formally equivalent to each other and only differ in the first two terms on the right-hand-side. As the formulation of the *dispersion relation* in  $\vec{k}$ -space is quite cumbersome, we express the same relation in polar coordinates. There, we neglect the azimuthal angle, because the new equations do not depend particularly on it. Thus, the solution for the *dispersion relation* is supposed to be cylindrically symmetrical about the z-axis and handier equations are presented in the following

$$n_o(\theta, \omega) = n_o(\omega) \quad (2.36)$$

$$\frac{1}{n_e(\theta, \omega)} = \frac{\cos^2(\theta)}{n_o^2(\omega)} + \frac{\sin^2(\theta)}{n_e^2(\omega)}, \quad (2.37)$$

where we identify the *refractive indices*  $n_o$  and  $n_e$  with the square root of the *dielectric permittivities*  $\epsilon_o$  and  $\epsilon_e$ , respectively, according to equation (2.29). The symbol  $\theta$  denotes the polar angle between the optic axis (z-axis) and the direction of the  $\vec{k}$ -vector.

A graphical version of these equations is depicted in Figure 2.5 for two cases: a) an isotropic crystal and b) a negative ( $n_e - n_o < 0$ ), uniaxial birefringent crystal. The red and blue arrows in Figure 2.5 refer to the  $\vec{k}$ -vector of the ordinary and extraordinary wave, respectively, and belong to their correspondingly colored dispersion relations (red sphere: ordinary / blue spheroid: extraordinary).

Figure 2.5 a) shows only a single indicatrix (ordinary wave) and implies that the refractive index  $n_o(\theta, \omega)$ , determined by the distance between the origin of the coordinate system and the position on the corresponding surface pointed to by the electric displacement vector  $\vec{D}_o(\omega, \vec{k})$  (yellow arrow), depends neither on polarization nor on the direction of the  $\vec{k}_o$ -vector (red arrow). Figure 2.5 b) also covers the case of ordinary waves (red sphere, red and yellow arrows), but additionally describes the dependence of the extraordinary refractive index  $n_e(\theta, \omega)$  (blue spheroid) on the orientation of the electric displacement vector  $\vec{D}_e(\omega, \vec{k})$  (green arrow) and the direction of the  $\vec{k}_e$ -vector (blue arrow), respectively. Here,  $\vec{D}_e(\omega, \vec{k})$  lies in the plane spanned by the optic axis (z-axis) and the  $\vec{k}_e$ -vector of the extraordinary wave.

As mentioned before, the yellow (ordinary wave) and green (extraordinary wave) arrows in Figure 2.5 do not refer to the electric field eigenvectors  $\vec{E}_{o/e}(\omega, \vec{k})$ , but rather to their associated electric displacement eigenvectors  $\vec{D}_{o/e}(\omega, \vec{k})$ . If one prefers dealing with the electric field eigenvector  $\vec{E}$ , rather than with the electric displacement eigenvector  $\vec{D}$ , one could calculate the former by inverting the relation  $\vec{D} = \hat{\epsilon}\vec{E}$ . The vectors  $\vec{D}$  and  $\vec{E}$  need not necessarily be parallel to each other, if  $\hat{\epsilon}$  is not a multiple of the unity matrix. Since the  $\vec{D}$ - $\vec{E}$ -relation in Figure 2.5 a)

<sup>8</sup>In our case, the *optic axis* is the z-axis, as its assigned permittivity element  $\epsilon_e$  in equation (2.33) differs from the others.

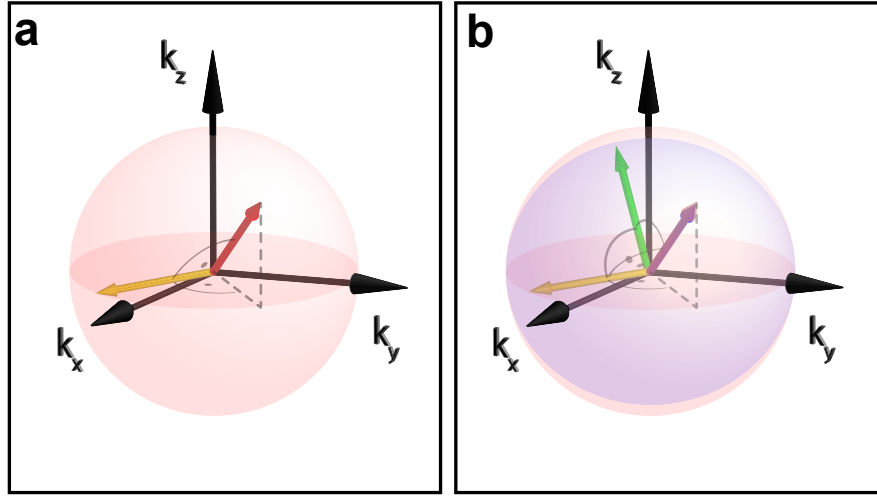


**Figure 2.5:** Comparison between the so-called *indicatrices* in  $\vec{k}$ -space of **a)** an isotropic and **b)** an anisotropic negative, uniaxial birefringent crystal. In **a),b)**, the  $\vec{k}$ -vector is represented either by a red arrow (ordinary) or by a blue arrow (extraordinary). The electric displacement vector  $\vec{D}(\omega, \vec{k})$  (yellow arrow) is perpendicular to the  $\vec{k}$ -vector. The dashed lines indicate the projection onto the  $k_x$ - $k_y$ -plane. While **a)** exhibits a single spherically symmetric indicatrix, that depends neither on polarization nor on the direction of the  $\vec{k}$ -vector (red sphere), **b)** shows two non-degenerate indicatrices, a spherical (ordinary,  $n_o(\theta, \omega)$ ) and another ellipsoidal (extraordinary,  $n_e(\theta, \omega)$ ) one. The refractive index that is associated with a certain indicatrix is determined by the position on the surface, pointed to by the  $\vec{D}(\omega, \vec{k})$ -vectors (yellow: ordinary / green: extraordinary), and its distance from the origin of the coordinate system.

is scalar valued, the electric field vector  $\vec{E}$  (not shown) and the electric displacement vector  $\vec{D}$  are parallel to each other,  $\vec{E} \parallel \vec{D}$ . Consequently, the Poynting vector  $\vec{S}$  is parallel to  $\vec{k}$ ,  $\vec{S} \parallel \vec{k}$ , because  $\vec{k} \perp \vec{E} \perp \vec{H}$  in nonmagnetic media. Now, if we turn to the extraordinary wave in Figure 2.5 b), this relation becomes invalid, since the scalar relation between  $\vec{E}$  and  $\vec{D}$  will be violated. Therefore,  $\vec{E}$  and  $\vec{D}$  basically meet at an angle,  $\vec{E} \not\parallel \vec{D}$ , just as the Poynting vector  $\vec{S}$  and the  $\vec{k}$ -vector themselves. This implies that the Poynting vector  $\vec{S}$  is parallel to the  $\vec{k}$ -vector in case of ordinary waves,  $\vec{S}_o \parallel \vec{k}_o$ , but not parallel in case of extraordinary waves,  $\vec{S}_e \not\parallel \vec{k}_e$ , except for selected points. In general, the Poynting vector is oriented perpendicularly to the dispersion-relations, explaining why there may be two separate beams, since the Poynting vector describes the direction of energy flow. For example, in an experiment where unpolarized light is incident normally at a vacuum-birefringent-crystal interface, it will lead to two separate beams, if the optic axis orientation of the birefringent crystal is neither perpendicular to nor in-plane with the interface. However, birefringence can be quite beneficial in terms of *second harmonic generation* (SHG), because it can help compensate chromatic dispersion, and will be discussed in the next subsection.

### 2.2.3 Nonlinear Regime

In this subsection, we want to extend our previous discussion, concerning light–matter interaction in terms of polarization  $\vec{P}$  to such an extent that we leave the linear domain, which is represented by  $\vec{P}^L$ , and focus on the nonlinear contribution  $\vec{P}^{NL}$  in equation (2.21). As we consider this contribution as a perturbation to the total polarization  $\vec{P}$ , we can expand it in a Taylor series in powers of the electric field strength  $E$ . Therefore, we expect that the Taylor series converges for moderate field strengths. Nevertheless, one should keep in mind that in general, the Taylor series need not converge [18], especially in cases, where the electric field strength is not negligible with respect to the atomic unit of the electric field  $E_{at}$ , given by

$$E_{at} = \frac{E_h}{ea_0} \approx 5.142 \dots \cdot 10^{11} \frac{V}{m}, \quad (2.38)$$

where  $e$  is the elementary charge,  $a_0$  is the Bohr radius and  $E_h$  is the Hartree energy. In the following, we assume that the electric field strength  $E$  is way less than  $E_{at}$ :  $E \ll E_{at}$ . The other case, in which  $E$  is comparable to  $E_{at}$ , will be dealt with in the subsection covering the generation of isolated attosecond pulses. Under the present condition, the nonlinear part  $\vec{P}^{NL}$  of the polarization term of equation (2.21) can be expressed in general and in the frequency domain as a sum of ever increasing nonlinear order. The two lowest orders are explicitly given below, but all other orders can be deduced accordingly as the scheme is quite apparent,

$$P_i^{(2)}(\omega) = \epsilon_0 \sum_{(nm)} \chi_{ijk}^{(2)}(\omega, \omega_n, \omega_m) E_j(\omega_n) E_k(\omega_m) \quad (2.39)$$

$$P_i^{(3)}(\omega) = \epsilon_0 \sum_{(mno)} \chi_{ijkl}^{(3)}(\omega, \omega_o, \omega_n, \omega_m) E_j(\omega_o) E_k(\omega_n) E_l(\omega_m) \quad (2.40)$$

⋮

and their forms are reminiscent of equation (2.23). As before, Einstein summation convention has been exploited for convenience and the summation across indices, encircled by parantheses (for example  $(nm)$ ), incorporates all frequencies, whose sum equals the frequency  $\omega$  on the left-hand-side<sup>9</sup>. This is simply a manifestation of conservation of energy. The tensors, which appear on the right-hand-side of equations (2.39) – (2.40), are classified by their orders — given as superscripts — as well as by their contribution of components  $ij \dots$  to the resulting nonlinear polarization. Here, we have omitted the  $NL$  superscript. The aforementioned equations have been adapted from [18]. Similar to the preceding discussion, equations (2.39) – (2.40) could also be expressed in the time domain as convolutions, but is omitted here, because the present equations are more compact.

---

<sup>9</sup>The resulting frequency  $\omega$  is allowed to be positive or negative, although both signs are connected via  $P_i^{(n)}(\omega) = P_i^{(n)*}(-\omega)$  and  $*$  stands for *complex conjugate*. This relation holds true, as the nonlinear polarization is supposed to be a real quantity. The very same argument is valid for the electric fields  $E(\omega)$  as well as the nonlinear susceptibilities  $\chi^{(n)}(\omega = \omega_m + \dots + \omega_n) = \chi^{(n)*}(-\omega = -\omega_m - \dots - \omega_n)$ .



### 2.2.3.1 Second-Order Nonlinear Effects

Now, we want to look into equation (2.39) a bit more deeply and we will briefly discuss nonlinear effects arising from it. Special attention is therefore paid to both symmetry considerations with respect to frequency constraints and index permutations, as they simplify the treatment of equation (2.39) enormously.

**Symmetry Considerations** Besides many more symmetry-related simplifications, we will solely mention the three relevant to us inasmuch as they have been applied for numerical simulations concerning DUV pulse generation, which are presented in chapter 4.

**Intrinsic Permutation Symmetry** The *intrinsic permutation symmetry* states that the coupling of the electric field components, emerging in equation (2.39), does not depend on the order in which they show up. Consequently, the index pairs  $(n, m)$  and also  $(j, k)$  can be interchanged simultaneously, leaving the resulting nonlinear polarization unchanged. This leads to the following identity, where as before  $\omega = \omega_n + \omega_m$

$$\chi_{ijk}^{(2)}(\omega, \omega_n, \omega_m) = \chi_{ikj}^{(2)}(\omega, \omega_m, \omega_n). \quad (2.41)$$

**Full Permutation Symmetry** The importance of the last equation can be seen when used in conjunction with lossless media, where the nonlinear susceptibilities  $\chi^{(2)}$  are real quantities [18]. Further, it can be shown that the permutation property is not solely restricted to the latter two components, but to any index permutation as long as the frequencies are interchanged as well. Here, special attention is necessary due to the condition that  $\omega = \omega_m + \omega_n$ , which may result in a sign change in the corresponding nonlinear susceptibilities. For example, one obtains the following relation

$$\chi_{ijk}^{(2)}(\omega, \omega_n, \omega_m) = \chi_{jki}^{(2)}(\omega_n, -\omega_m, \omega). \quad (2.42)$$

**Kleinman's symmetry** If we assume that the interaction takes place off-resonantly with a medium's transition, then one can expect the nonlinear susceptibilities to not depend on frequency explicitly. This suggests that we are allowed to freely interchange indices without the need to interchange the frequencies as well. One can imagine that *Kleinman's symmetry* [31] is capable of reducing the number of tensor elements  $\chi_{ij\dots}^{(n)}$  dramatically in a numerical simulation, if applicable. However, one always has to check, whether the application of any of the recently introduced symmetries is justified for a specific situation. For example, in some chiroptical systems the application of Kleinman's symmetry is questionable and a Kramers-Kronig approach seems to be more realistic [32]. Moreover, the exact expression of the nonlinear susceptibility also depends on the point group of a medium, because some of its principal axes can be considered equivalent.

**Second-Harmonic-Generation (SHG)** One of the very first nonlinear effects observed was *second harmonic generation* (SHG) [33] and offers a decisive means to generate laser radiation at wavelengths that are normally unobtainable in common materials due to a variety of reasons. For instance, one of these reasons is that lasers in the deep-ultraviolet spectral range are hard to build, because the rate of spontaneous emission scales with the third power of the optical frequency ( $\propto \omega^3$ ). This introduces a spurious contribution to the entire laser spectrum, that is temporally not coherent. Let us assume we have a monochromatic electric field at angular frequency  $\omega$  with a sufficiently high electric field strength to trigger second-order nonlinear effects. Then, we would receive a nonlinear polarization term according to equation (2.39) that reads

$$P_i^{(2)}(2\omega) = \epsilon_0 \chi_{ijk}^{(2)}(2\omega, \omega, \omega) E_j(\omega) E_k(\omega), \quad (2.43)$$

where we have already evaluated the summation across  $(nm)$  and did not restrict the input fields polarization term, that is provided by the indices  $(jk)$ . As this expression is simply the amplitude of the nonlinear contribution, we would expect it to oscillate at the very same frequency  $2\omega$ . Because of the fact that the polarization oscillates at twice the fundamental frequency, we know from classical electrodynamics [26] that oscillating dipoles<sup>10</sup> radiate electromagnetic waves at the very same frequency. Even from the viewpoint of light as consisting of particles (photons), one can think of second harmonic generation as the conversion of two photons at fundamental frequency  $\omega$  into a single photon of frequency  $2\omega$ . Because of the fact that those radiated waves also suffer from chromatic dispersion of the medium, which they travel in, one has to ensure that the wave driving the nonlinearity and the generated wave are properly phased to each other in order to make them exchange energy most efficiently along their propagation direction. This is commonly referred to as *phase-matching*. The idea behind phase-matching is to guarantee for an in-phase macroscopic built-up of the second harmonic. Only if all radiating dipoles oscillate in phase with the driving field, the emitted waves will add up constructively in the forward direction. With the help of equation (2.24), one derives that the SHG intensity  $I_2$  approximately scales with the input intensity  $I_1$  of the fundamental wave as

$$I_2 \propto \frac{d_{eff}^2 \omega_2^2 L^2}{n_1^2 n_2 \epsilon_0 c_0^2} I_1^2 \text{sinc}^2 \left( \frac{\Delta k L}{2} \right), \quad (2.44)$$

where  $d_{eff}$  is a measure of the nonlinearity pole strength and is related to the tensor elements of  $\chi^{(2)}$ .  $L$  and  $\Delta k$  are the length of the medium and the *wave vector-mismatch* quantity between the fundamental wave at frequency  $\omega$  and the second harmonic at frequency  $\omega_2 = 2\omega$ . The  $\text{sinc}^2$ -function abbreviates the term  $\sin(x)/x$  and comprises the phasing among all waves. The quantities  $n_1$  and  $n_2$  describe the refractive indices, evaluated at fundamental and second harmonic frequency, respectively. A rigorous derivation can be found in [18]. The wave vector-mismatch is usually defined as the wavenumber difference between SHG and fundamental wave according to

<sup>10</sup>The polarization density  $P$  has units of number of dipoles per volume ( $C/m^2$ ).

$$\Delta k = 2k_1 - k_2, \quad (2.45)$$

where  $k_1 = n_1\omega/c_0$  and  $k_2 = n_2\omega_2/c_0$  have already been defined previously in equation (2.28). It is noteworthy that the output intensity is quite sensitive to the argument of the sinc<sup>2</sup>-function. Although the output intensity increases quadratically with the length  $L$  of the medium, it becomes harder to maintain perfect phase-matching ( $\Delta k = 0$ ) with an argument close to zero. Apart from that, one could imagine that equation (2.45) can almost never be fulfilled in isotropic media, as those are prone to chromatic dispersion, usually leading to an increase of the refractive index with increasing frequency. Because equation (2.45) can be reformulated for SHG as

$$\Delta n = n(\omega) - n(2\omega). \quad (2.46)$$

It is obvious that  $\Delta n < 0$  for isotropic, normally dispersive media<sup>11</sup>. A way out is provided by the use of birefringent materials, because they exhibit two distinct refractive indices. One of them depends on the incident polarization. At this, the fundamental wave would be the ordinary wave and the second harmonic wave can be regarded as the extraordinary wave. This geometry is commonly called *Type-I-phase-matching* and refers to parallel input polarization, whereas *Type-II-phase-matching* is defined by orthogonal input polarization [34]. As these birefringent materials are meant to compensate for chromatic dispersion, we can sometimes find an angle  $\theta$ , following equation (2.37), so that equation (2.46) can be fulfilled and the angle is referred to as *phase-matching angle*. In terms of the indicatrices<sup>12</sup> depicted in Figure 2.5, it can be visualized as the intersection between a sphere constructed at frequency  $\omega$  and a spheroid constructed at frequency  $2\omega$ . Consequently, either waves share the same  $\vec{k}$ -vector, both in direction and magnitude. Getting back to equation (2.44), the behavior for different phase-mismatches is depicted in Figure 2.6 in terms of SHG intensity.

**Sum-/Difference-Frequency-Generation (SFG/DFG) and Optical Rectification (OR)** Up to here, we have dealt with SHG as the simplest nonlinear effect, but it has been mentioned in the beginning of this section, there is a cascade of second order nonlinearities. If we dropped the constraint of a single fundamental frequency, but allow two fundamental frequencies to be present, we would get a similar expression that is akin to equation (2.43). This leads us to *sum-frequency-generation* (SFG) and *difference-frequency-generation* (DFG). The main difference to the previous case is that the sum running across all unique combinations of  $(nm)$  is twice as big. It originates from the fact that we dropped the frequency degeneracy of the incident fields. Whether or not SFG or DFG are observable in an experiment depends on whether the phase-matching condition  $\Delta n = 0$  (equation (2.46)) can be satisfied. The generalized phase-matching requirement for noncollinear wave vectors can be written down as

<sup>11</sup>Normal dispersion refers to the situation, in which the refractive index grows with increasing angular frequency. Correspondingly, *anomalous dispersion* refers to the contrary behavior.

<sup>12</sup>This argument is only valid for negative uniaxial crystals ( $n_e < n_o$ ) and must be adapted for positive uniaxial crystals ( $n_e > n_o$ ) accordingly.

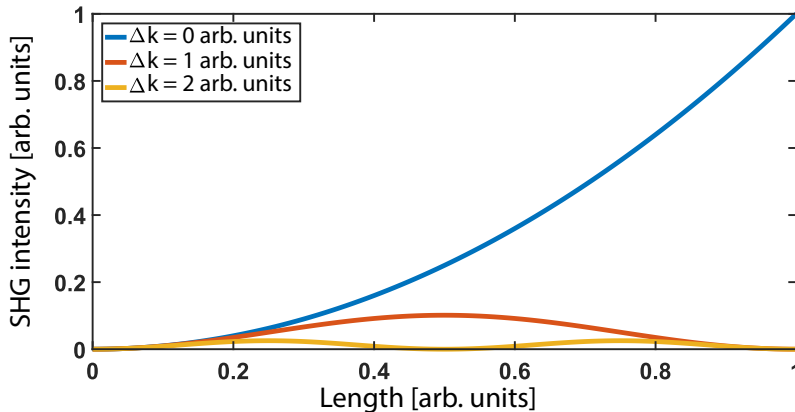


**Figure 2.6:** Dependence of SHG intensity on wave vector-mismatch  $\Delta k$  for three different values. All values are given in arbitrary units. For vanishing mismatch, there is a quadratic built-up of SHG intensity (*blue line*) with the length of the nonlinear material. For non-vanishing wave vector-mismatch, the maximally attainable SHG intensity decreases and starts oscillating (*red and yellow lines*).

$$\Delta \vec{k} = \vec{k}_1(\omega_1) \pm \vec{k}_2(\omega_2) - \vec{k}_3(\omega_3), \quad (2.47)$$

where  $\omega_1$ ,  $\omega_2$  and  $\omega_3$  are the incident and generated angular frequencies, fulfilling  $\omega_3 = \omega_1 \pm \omega_2$ , and  $\vec{k}_i$  ( $i = 1, 2, 3$ ) are their respective wave vectors. The sign in equation (2.47) depends on the chosen process (SFG(+)/DFG(-)). The importance of DFG and SFG must not be underestimated, because they pave the way for generating new frequencies in the infrared and ultraviolet range of the optical spectrum, which are normally unattainable via SHG due to a lack of appropriate laser sources. Above all, DFG provides a means to retrieve the carrier-envelope-offset frequency  $f_{CEO}$ , as will be discussed in chapter 3. A special case of DFG is *optical rectification* (OR), that is the difference frequency analog of SHG for degenerate input angular frequencies.

### 2.2.3.2 Third-Order Nonlinear Effects

Now, we would like to cast an eye on the effects originating from equation (2.40). In the beginning of this section, we noted that the perturbative expansion of the nonlinear polarization term is supposed to converge for certain conditions. This implies that the strength of those third order nonlinear effects is weaker than those arising from second order nonlinearities. Nevertheless, they are still strong enough not to be neglected, especially for ultrashort pulses. Therefore, we will focus on the most prominent features that are important to us, namely, third harmonic generation, Kerr effect and self-steepening. Depending on the presence of centrosymmetry<sup>13</sup>,

<sup>13</sup>Centrosymmetry means that a system possesses a center of inversion such that all system properties relative to this center do not change, when all coordinates  $\vec{r}$  are replaced by their corresponding counterparts  $-\vec{r}$ .

third order nonlinear effects might be the lowest nonlinear order, as second order effects only occur in noncentrosymmetric media.

**Third-Harmonic-Generation (THG)** The direct generalization of SHG, but for third order nonlinearity, is *third-harmonic-generation* (THG), where three photons at fundamental frequency  $\omega$  are mixed to one single photon at three times the fundamental frequency  $3\omega$  and was first observed by [35]. The corresponding nonlinear polarization term might be written as

$$P_i^{(3)}(3\omega) = \epsilon_0 \chi_{ijkl}^{(3)}(3\omega, \omega, \omega, \omega) E_j(\omega) E_k(\omega) E_l(\omega), \quad (2.48)$$

where, as before, the sum across  $(mno)$  has been evaluated to one, because there is only one permutation to create the third harmonic from a single field with angular frequency  $\omega$ . Apart from that, the incident polarization has not been specified to keep the discussion as general as possible. Once again: equation (2.48) refers exclusively to the one-atom response, not taking the constructive phasing between dipoles into account. However, obtaining a measurable, macroscopic signal requires the phase-matching condition to always be accomplished within the phase-matching bandwidth<sup>14</sup>.

**Optical Kerr-effect** Another very important third order nonlinear effect is the *Optical Kerr-effect*, describing the change of refractive index with intensity. Although one might be tempted to assume that the optical Kerr-effect is of minor importance, it plays a decisive role in the construction of ultrafast laser oscillators via *Kerr-Lens-Modelocking* and will be addressed later on. Let us write the nonlinear polarization expression for the optical Kerr-effect down as

$$P_i^{(3)}(\omega) = 3\epsilon_0 \chi_{ijkl}^{(3)}(\omega, \omega, -\omega, \omega) E_j(\omega) E_k^*(\omega) E_l(\omega), \quad (2.49)$$

where the polarization term oscillates at the fundamental frequency  $\omega$ , as opposed to the case of THG. If we assume to have an electric field that is linearly polarized along a certain direction and assume further that the nonlinear polarization term has the same polarization as the incident field, equation (2.49) will simplify to

$$P^{(3)}(\omega) = 3\epsilon_0 \chi^{(3)}(\omega, \omega, -\omega, \omega) |E(\omega)|^2 E(\omega), \quad (2.50)$$

where we have dropped the indices  $ij\dots$  and  $|\dots|^2$  defines the square of the absolute value. It is related up to constants to the optical intensity of the incident electric field at frequency  $\omega$ . Following the derivation of the optical Kerr-effect [18], one can define an effective susceptibility, including the linear contribution, as

<sup>14</sup>The phase-matching bandwidth refers to the width of the sinc<sup>2</sup>-function for which the argument  $\Delta kL$  takes on the value  $\pi/2$ .

$$\chi_{eff} = \chi^{(1)} + 3\chi^{(3)}|E(\omega)|^2, \quad (2.51)$$

where we have omitted the frequency dependency of  $\chi^{(3)}$ . This effective susceptibility can be related to the effective refractive index, which is modified by the intensity of the electric field. After some maths [18] one obtains

$$n_{eff} = n_0 + n_2 I, \quad (2.52)$$

where  $n_0$  is the low-intensity refractive index and  $n_2$  is the second order nonlinear refractive index. The latter is linked to the third order nonlinear susceptibility via

$$n_2 = \frac{3}{4n_0^2\epsilon_0c_0}\chi^{(3)}. \quad (2.53)$$

It is this relation that leads to an intensity-dependent refractive index and has far-reaching consequences for ultrashort pulses, because the intensity variation across an ultrashort pulse is huge.

**Self-Phase-Modulation (SPM)** One of the aforementioned consequences, emerging for ultrashort pulses, is *Self-Phase-Modulation* (SPM). Its notion is self-explanatory. It describes the phenomenon of an ultrashort pulse that modifies its own temporal phase  $\phi(t)$ , when it propagates through a nonlinear medium with third-order nonlinearity  $\chi^{(3)}$ . As we have seen in the last paragraph, the effective refractive index  $n_{eff}$  is a function of intensity  $I(t)$ . Since the intensity  $I(t)$  varies quite rapidly with time across the pulse, parts of it experience a bigger or smaller impact by the effective refractive index. In general, we can write down the instantaneous temporal phase  $\Phi(t)$  of the pulse (equation (2.2)) as

$$\Phi(t, L) = \omega_0 t - kL = \omega_0 t - \frac{n_{eff}(t)\omega_0 L}{c_0} = \omega_0 t - \frac{(n_0 + n_2 I(t))\omega_0 L}{c_0}, \quad (2.54)$$

where we have omitted the slowly varying phase  $\phi(t)$  and the carrier-envelope phase  $\phi_{CEP}$ .  $L$  denotes the length of the medium. We recognize the second term as an intensity dependent modification of the instantaneous phase, which translates to a spectral broadening of the original spectrum. The broadening is proportional to the first order time derivative of the intensity and is most prominent for ultrashort pulses, because the instantaneous frequency  $\omega(t)$  is related to the instantaneous temporal phase  $\Phi(t)$  via

$$\omega(t, L) = \frac{d\Phi(t, L)}{dt} = \omega_0 - \frac{n_2\omega_0 L}{c_0} \cdot \frac{dI(t)}{dt}. \quad (2.55)$$

In case of a Gaussian-shaped temporal pulse profile, we would expect the spectrum to be broadened symmetrically around  $\omega_0$ , because leading and trailing edge have identical slopes, but with opposite signs.

**Self-Steepening** One could go one step further and include not only the effect of the intensity-dependent refractive index  $n_2 I(t)$  onto the phase velocity  $v_p$  (equation (2.31)), but also on the group velocity  $v_g$  (equation (2.32)) of the pulse inside a medium. In the course of the pulse propagation through the nonlinear medium, the most intense part of the pulse will travel more slowly than the less intense wings of the pulse. Consequently, the envelope function will be influenced such that its shape gets more and more asymmetric. For positive  $n_2$ , the weak leading edge travels faster than the most intense part and will therefore become flatter, whereas the weak trailing edge will catch up with the most intense part, as it travels faster than it. Hence, it will make the trailing edge steeper. Following equation (2.55), this process results in an asymmetric spectral broadening due to the modified intensity profile and explains the term *Self-Steepening*.

**Self-Focusing** The optical Kerr-effect inside a third order nonlinear material does not merely influence the temporal evolution of an ultrashort pulse, but can also change its spatial propagation. For example, the more intense inner regions of a moderately intense pulse with radially slanting intensity profile experience a bigger effective refractive index due to the optical Kerr-effect. Thus, the optical path, that is the product between the length of the medium  $L$  and the effective refractive index  $n_{eff}(I)$ , has increased with regard to the outer, less intense regions. This, in turn, leads to a decreased phase velocity  $v_p$ , which implicates that the outer regions travel at a faster phase velocity  $v_p$  and can catch up with the inner regions and even overtake them. In total, the wavefront of the beam starts curving due to the nonlinearity-induced refractive index changes and is illustrated in Figure 2.7. As this phenomenon arises from the optical pulse itself, it is termed *Self-Focusing* (see for example [18, 36]). In general, self-focusing will only become important, if the optical power exceeds the *critical power* that is given by [37] as

$$P_{cr} = \alpha \frac{\lambda^2}{4\pi n_0 n_2}, \quad (2.56)$$

where  $\lambda$  is the optical wavelength and  $\alpha$  is a numerical constant on the order of one.

#### 2.2.4 Extreme Nonlinear Regime

It was pointed out in subsection 2.2.3 that the perturbative description loses its validity, once the electric field strength  $E$  approaches the atomic unit of the electric field  $E_{at}$ :  $E \approx E_{at}$ . This implies that the electric field is as intense as the inherent electric field inside a medium in such a way that it can compete with it. As will become evident in the course of this subsection, there is a fundamental difference between nonlinear optics and extreme nonlinear optics inasmuch as that the former can be described by bound and virtual states exclusively [18], while the treatment

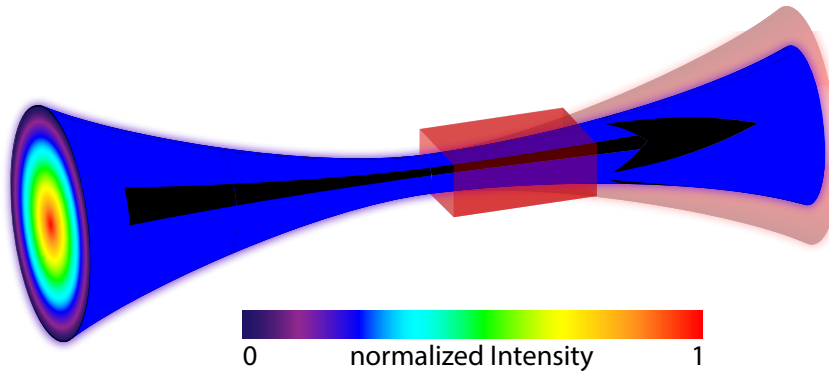


**Figure 2.7:** Illustration of Self-Focusing for an intense laser beam (blue object) with cylindrically symmetric, but radially dependent intensity distribution (false color plot on the left hand side of the blue object). The focused beam propagates from left to right along the black arrow. If an intense beam (blue object) is subjected to a third order nonlinear medium (red rectangular solid), it will experience a spatially dependent refractive index change that is linearly proportional to its optical intensity profile. These refractive index changes act as a focusing lens, such that the divergence angle of the beam diminishes after the nonlinear medium, compared to an unaltered beam (red object).

of the latter enforces the incorporation of continuum states [38]. Another indication for the invalidity of a perturbatory approach in case of extreme nonlinear optics is that the strength of certain individual harmonic orders needs not fall off with increasing harmonic order. This might have been expected from a perturbation theory point of view, but the strength of the harmonics remains nearly constant over a remarkably huge range [38]. The present subsection aims at giving a brief introduction to the underlying process of *high harmonic generation* in general and the *generation of isolated attosecond pulses* in particular, as they pave the way for pump-probe experiments with unprecedented time resolution. This time resolution can normally not be obtained with laser pulses in the infrared range of the optical spectrum, since their pulse duration is limited by the period of their center frequency. In order to generate even shorter pulses one has to increase the frequency, where high harmonic generation comes into play.

#### 2.2.4.1 High Harmonic Generation

The term *high harmonic generation* (HHG) usually refers to the production of harmonics, exceeding those that are producible by perturbative nonlinear optics and can be produced up to some hundredth harmonic order [39]. As for all harmonic generation schemes, phase-matching is the most important issue, which also applies to HHG [40]. Due to the extreme wavelengths, chromatic dispersion, re-absorption of radiation and some other effects render a solid-state ap-



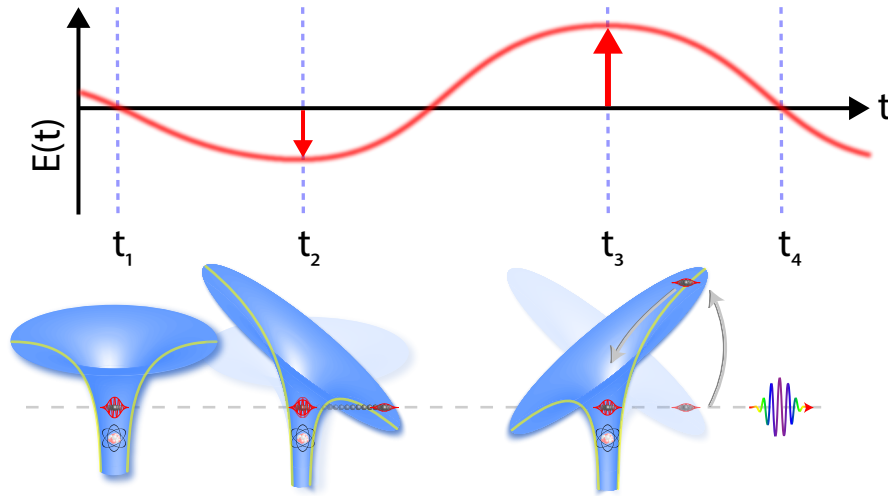


**Figure 2.8:** Illustration of the *Three-Step-Model* [38, 45]. The upper panel shows one cycle of the electric field of an ultrashort laser pulse. The lower panel depicts the associated modifications of the atomic potential at different times ( $t_1$ – $t_4$ ) (see main text for explanation).

proach challenging and is still under intense investigation [41–43]. Maybe, this is why HHG was first observed in rare gases [44]. A similar gas-phase approach is used for the experiment that is presented in this thesis.

In order to attain an intuitive understanding of the underlying process, it is worth looking at the response of a single atom which is exposed to an intense ultrashort laser pulse. An illustration of the following semi-classical *Three Step Model* [45] of HHG can be obtained by looking at Figure 2.8, whose validity even holds when comparing its predicted results to those retrieved from quantum mechanical calculations [38, 46] and only minor changes are necessary. The reason, why it is considered semi-classical, is that the first and last step are treated in a quantum mechanical way, while its intermediate step makes use of classical mechanics only. We will walk through this model step by step:

If we imagine to have a linearly polarized, ultrashort and intense laser pulse, shone on a single atom, its presence and its comparable strength relative to the intrinsic, atomic electric field will change the total atomic potential dramatically. At time  $t_1$  in Figure 2.8, the instantaneous electric field strength equals zero (upper panel / red line) and the atomic potential has not changed yet (lower panel / blue funnel). At a later time  $t_2$ , the field becomes as strong as to lower the atomic potential well and allows an electron to tunnel through the potential barrier (lower panel / green line) at zero velocity<sup>15</sup>. The effect of tunnel ionization is quite sensitive, because its probability scales exponentially with applied electric field strength [47, 48]. In the subsequent optical half-cycle ( $t_3$ ) the field direction is inverted and the electronic wave packet is

<sup>15</sup>More precisely: All freed electrons with a variety of initial velocities after tunnel ionization have to be taken into account, but it turns out that only those having no initial velocity and which do return to the ion contribute most strongly [38].

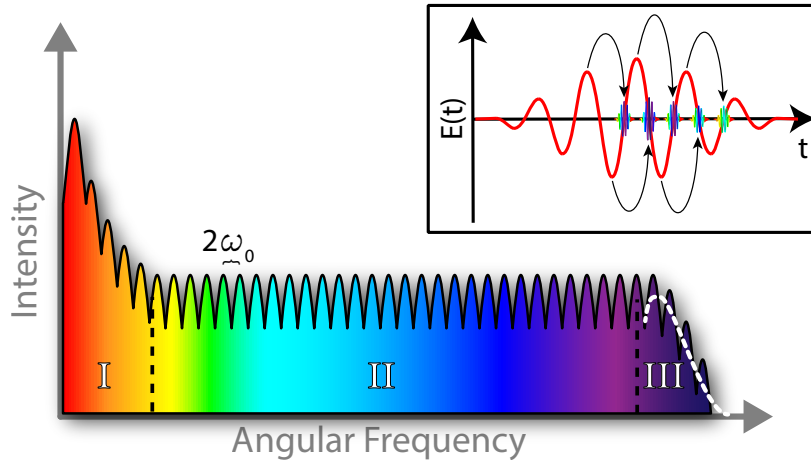


**Figure 2.9:** Schematic representation of a typical high harmonic spectrum. It basically consists of three areas. (I): perturbative regime. (II): plateau regime. (III): cutoff regime. In (III), we observe modulations in case of a sine-shaped ultrashort pulse, while for a cosine-shaped pulse (see inset) we get an unmodulated cutoff (white dashed line). The adumbrated electron trajectories in the inset are drawn for positively charged particles for clarity reasons. Every optical half-cycle an attosecond pulse is emitted with varying energy and color encoded in the plot.

accelerated back along a specific trajectory away from its parent ion in the continuum (indicated by the upright gray arrow in the lower panel). Consequently, it is directed backwards, thus gaining kinetic energy from the field and indicated by the gray arrow, pointing towards the ion core in the lower panel. Upon recombination between the continuum wave packet and the left part of the ground state at time  $t_4$ , the acquired kinetic energy gets released by emission of a high-energy XUV-photon. The prerequisite of linear polarization is of paramount importance here, because otherwise the continuum wave packet will be deflected to such an extent that it will miss its parent ion, effectively prohibiting recombination and emission.

The exact amount of kinetic energy, that is acquired by the wave packet in the continuum under the influence of the electric field, is a unique function of ionization time ( $t$ ) or recombination time ( $t'$ ), respectively, as both are linked to each other in an unambiguous way and is dictated by classical mechanics ( $t(t')$  or  $t'(t)$ ). The resulting spectrum of this so-called *attosecond pulse train* is shown in Figure 2.9. As the underlying process of HHG repeats every half optical cycle of the laser pulse, we get a train of XUV-photons of varying energy separated by half an optical cycle. The corresponding HHG spectrum can be decomposed into three areas:

The first area (I) in Figure 2.9 can be attributed to the perturbative regime, as indicated by their diminishing intensity with increasing harmonic order. Due to the presence of a center of inversion in case of atoms, only odd harmonics appear, which are separated by twice the fundamental frequency  $2\omega_0$ . The second area (II) is called the *plateau range*, in which all harmonic orders are of similar intensity. This is a clear manifestation of the continuum contribution to high harmonic generation. The modulation of the plateau is quite obvious and originates from the interference

of XUV-photons from adjacent half-cycles with nearly identical energy (inset in Figure 2.9). The third area of the spectrum (III) is characterized by an exponential decay in intensity and is commonly termed *cutoff*. Regarding attosecond pump-probe experiments, the cutoff domain is most interesting, because it can be provoked by a single attosecond pulse of highest energy for properly adjusted CEP [49]. It can be proven that the duration of this attosecond pulse decreases with decreasing pulse duration of the HHG-driving laser pulse [50]. The CEP-dependence was mentioned in the beginning of this chapter and its influence on the cutoff range is schematically depicted in area (III) of Figure 2.9. For a cosine-shaped electric field, there is only one electron trajectory that results in a highest energy XUV-photon, while for a sine-shaped electric field two adjacent electron trajectories lead to two XUV-photons of comparable energy. For the latter case we would expect to observe interference in the overall HHG-spectrum near the cutoff, while for the former case we would not expect any (dashed white line in Figure 2.9). The situation for a cosine-shaped pulse is illustrated in the inset of Figure 2.9, in which the electron following the trajectory just before the most intense crest of the pulse will return to the ion core with the highest kinetic energy. The adumbrated trajectories refer to positively charged particles for clarity reasons.

In order to express the cutoff energy of the emitted high harmonic spectrum, we have to introduce the *ponderomotive energy*  $U_p$  in terms of laser center angular frequency  $\omega_0$  and peak electric field strength  $E$  as

$$U_p = \frac{e^2 E^2}{4m_e \omega_0^2}, \quad (2.57)$$

where  $m_e$  and  $e$  are the electron mass and elementary charge, respectively. The ponderomotive energy describes the cycle-averaged quiver energy of an electron in an oscillating electric field. With the help of equation (2.57), we can express the cutoff energy  $E_{cut}$  [38] as

$$E_{cut} \approx 3.17U_p + I_p, \quad (2.58)$$

where  $I_p$  is the ionization potential of the neutral atom and the constant factor 3.17 results from the electron trajectory in the continuum, that results in the highest kinetic energy on its return to the parent ion.

#### 2.2.4.2 Generation of Isolated Attosecond Pulses

Up to now, we have solely discussed the single atom response, but in an experiment the total response comes from an atom ensemble. Therefore, phase-matching must not be neglected. There are basically four main contributions to phase-matching [51] with partly different signs and magnitudes [40], but are beyond the scope of this thesis. We will list them here for completeness:

- atomic dipole phase
- neutral atom dispersion

- plasma dispersion
- geometrical phase

The first item accounts for the phase shift between any generated harmonic and the external electric field amplitude of the fundamental wave and is identical with the intensity-dependent phase of the induced dipole moment [40]. The second and third items refer to chromatic dispersion effects, arising from neutral atoms and ions. The last term takes the position-dependent influence of the *Gouy-phase* [52] into account, since in an experiment the laser pulse is usually focused into a target for high harmonic generation. Assuming optimized phase-matching and in order to obtain an isolated attosecond pulse, one could simply apply spectral filtering of the cutoff range, since we know that it comprises a single attosecond pulse of highest energy for cosine-shaped, linearly polarized laser pulses. This is the preferred technique used for the experiment presented in this thesis<sup>16</sup>.

---

<sup>16</sup>Besides this technique many others exist, for instance *polarization-gating* [53] or *attosecond lighthouse* [54].

## Chapter 3

# Experimental Tools

After having discussed the theoretical concepts of ultrashort laser pulses and their interaction with matter, the present chapter is dedicated to their experimental realization. This includes tools needed to generate them, as well as all the components of the experimental infrastructure. In the first section of this chapter, we present the laser system FP3 and, as the demands on the aforementioned ultrashort pulses are high in terms of energy and stability, we are going to address all of its modules in greater detail and show how to satisfy these requirements. In section two, we introduce the attosecond beamline AS2, which the experiment is performed in. As the entire beamline is composed of vacuum chambers and is set up in a modular fashion, we will quickly summarize all their building blocks and point their versatility out, regarding the provided freedom and also the constraints that are related to this freedom.

### 3.1 The FP3 Laser System

The basis of the FP3 laser system is formed by a commercially available *Femtopower Compact Pro CE-Phase HP/HR*<sup>1</sup> by Femtolasers<sup>2</sup>. The laser system has been adapted to satisfy our needs for even shorter and more intense ultrashort pulses with respect to its factory-owned specifications. A schematic of the laser system is depicted in Figure 3.1 and more information about FP3 in general can be found in the PhD thesis of *W. Schweinberger* [55]. The entire FP3 laser system consists of an oscillator, two serialized chirped pulse amplification stages, a transmission-grating compressor prior to a rare gas hollow-core fiber-based supercontinuum generator and a final chirped mirror compressor. All these stages will be addressed in the course of this chapter.

---

<sup>1</sup>HP= High Power; HR = High Repetition Rate

<sup>2</sup>Femtolasers has completely been acquired by Spectra-Physics in the meantime.

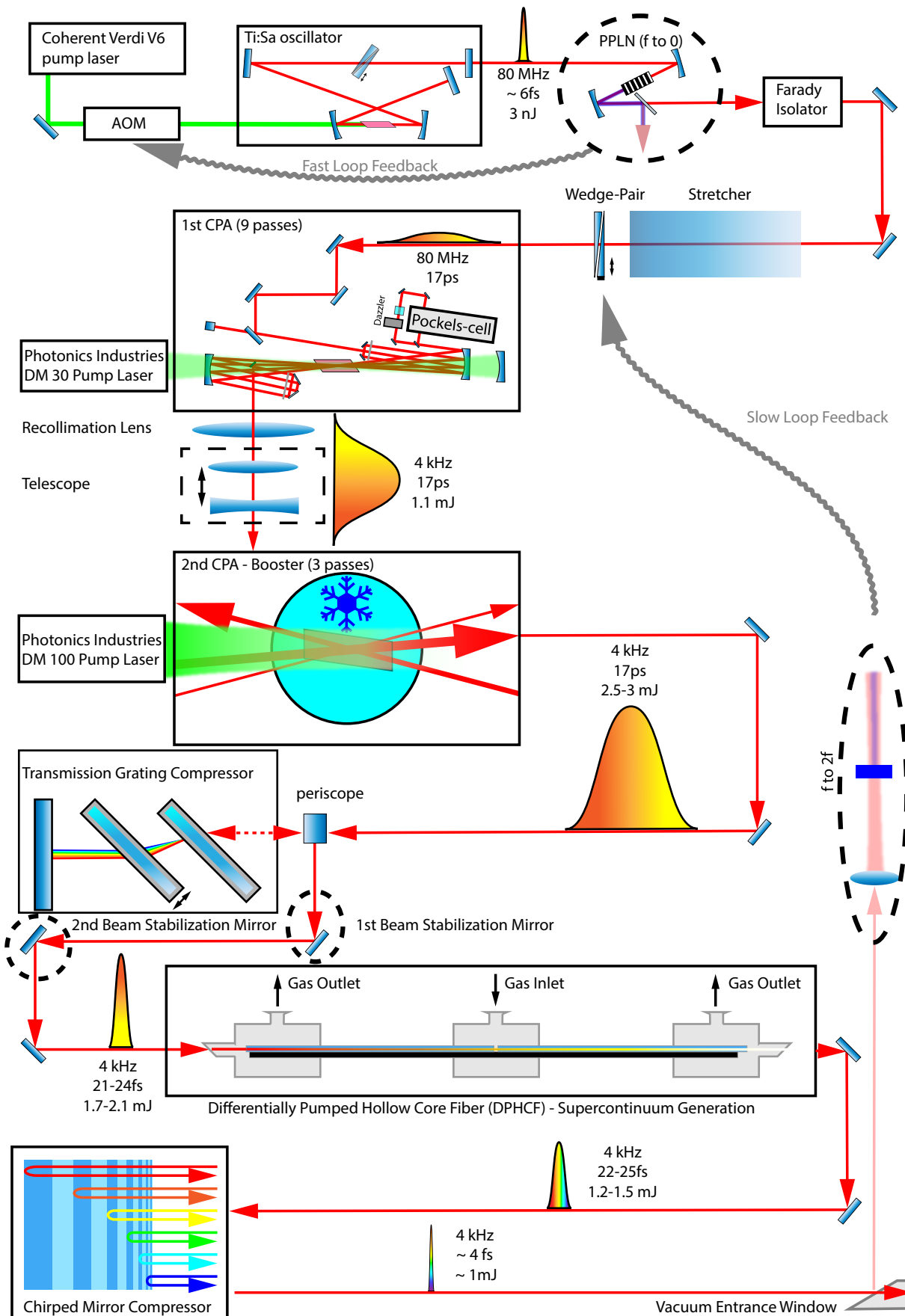


**Figure 3.1:** Schematic sketch of the FP3 laser system. For more information, see main text.

### 3.1.1 Oscillator

To start with, the ultrashort laser pulses are emitted from the oscillator at 80 MHz repetition rate and possess a pulse duration of  $\sim 6$  fs and a pulse energy of  $\sim 3$  nJ [56]. They are produced directly in a Kerr-lens mode-locked, *titanium-doped sapphire* (Ti:Sa) crystal-based femtosecond oscillator. An oscillator usually consists of a gain medium, a resonator, that is formed by at least two mirrors, and a pump source. In case of femtosecond oscillators, further requirements must be met. Therefore, the presented oscillator consists of several negatively double-chirped mirrors for compensation of chromatic dispersion, which is introduced by the Ti:Sa-crystal itself, and a pair of glass wedges, which are also located inside the oscillator. The Ti:Sa-crystal is cut at Brewster's angle to favor a well-defined polarization and to get rid of spurious polarization. The aforementioned glass-wedges serve as a chromatic dispersion fine-tuning tool to balance negative as well as positive chromatic dispersion contributions in order to maintain a short pulse. Moreover, they act as a lever to adjust the carrier-frequency-offset-frequency ( $f_{CEO}$ ) by adding or removing a variable amount of glass. The determination and experimental extraction of the CEP will be described soon. Ti:Sa-based solid state lasers provide an unprecedented broad emission band around 800 nm and a FWHM of  $\sim 200$  nm, that is not even met to some extent by other lasers. Actually the emission band extends from 670 nm up to 1050 nm and, hence, can support broad laser spectra in principle. As we have learned in chapter 2, a broad optical spectrum is indispensable in order to produce very short pulses and Ti:Sa-lasers fulfill this requirement extraordinarily well. Like every laser, the Ti:Sa-oscillator must be pumped and so it is done optically here, using a *Coherent Verdi V6* frequency-doubled cw Nd:YVO<sub>4</sub> laser emitting light around 532 nm and usually runs at  $\sim 3.9$  W pump power.

### 3.1.2 Multipass Regenerative Amplifiers

Although the pulse duration of the pulses leaving the oscillator is suited for femtosecond pump-probe experiments in principle, the pulse energy is still insufficient, as HHG calls for high electric field strengths. Hence, subsequent pulse amplification is indispensable and this is why we make use of two multipass regenerative amplifiers, which are discussed in the following and with which we increase the optical power by approximately five to six orders of magnitude.

#### 1st Multipass Regenerative Amplifier

The Femtopower Compact Pro is inherently equipped with a nine-pass Ti:Sa-crystal-based regenerative amplifier. It is pumped with a frequency-doubled, pulsed *Neodymium-doped Yttrium Lithium Fluoride* (Nd:YLF) solid state laser (*Photonics Industries DM30*) and is usually operated at 4 kHz repetition rate. The pump laser emits 527 nm nanosecond light pulses at 32 W pump power. Since the Ti:Sa-crystal of the oscillator strongly absorbs the 527 nm light and heats up, it is cooled down to  $\sim 176$  K, which also increases its heat conductance and decreases thermal lensing effects. Getting back to the nine-pass regenerative amplifier, the optical power gradually increases with every pass and, consequently, increases the risk of damaging amplifier components. Therefore, we have to ensure their integrity even when the last amplified pulse has made it through the last passage, since it carries the maximum amount of pulse energy

then. If we decided to use a femtosecond pulse in our amplifier, its accumulated pulse energy and huge peak electric field strength would easily exceed the damage threshold of the amplifier crystal. Therefore, the pulses are temporally spread on purpose in a 13.5 cm long SF57 glass block *stretcher*. It is located in front of the entrance to the amplifier and is traversed twice by the oscillator pulses (back and forth). Here, we make use of its excessive chromatic dispersion, that is exerted on the pulses which are heavily chirped from 7 fs to 17 ps. Right after the stretcher and prior to the second transit, there is another glass wedge pair, which will be used in the slow part of the CEP-feedback-loop (subsection 3.1.4).

The amplification works as follows: The chirped pulses pass the Ti:Sa-crystal four times, are then sent through a *Pockels cell*, which also acts as a pulse picker. The Pockels cell is necessary to reduce the repetition rate and to ensure more efficient pulse amplification for the remaining passes, because the temporarily stored energy in the Ti:Sa-crystal is not distributed among many pulses (80 MHz repetition rate), but among a few pulses (4 kHz repetition rate). After pulse picking, the pulse train traverses another optical device that is called *Dazzler* [57]. The Dazzler is a programmable dispersive filter, which can modify the spectral phase, amplitude and even the CEP of the amplified pulse, although it is introduced to counteract gain narrowing. The latter arises from the spectrally non-constant gain profile of the Ti:Sa-crystal. After the Dazzler, the pulse train is brought back to its original beam path through the amplifier and is further amplified in the remaining five passes. At the end of the amplification process, every pulse leaving the amplifier carries an energy of roughly  $\sim 1.1$  mJ, which is equivalent with an almost 6 orders of magnitude increase of pulse energy, compared to what the oscillator outputs.

## 2nd Multipass Regenerative Amplifier — The Booster

As pointed out in the introductory part of this chapter, we make use of an additional, but three-pass Ti:Sa-based amplification stage and is referred to as *the Booster*. It is pumped at 50 W with 532 nm nanosecond pulses from a single Q-switched, Nd:YAG frequency-doubled and diode-pumped solid-state laser (*Photonics Industries DM100*). However, the Booster was designed to increase the pulse energy by a factor of two to three such that the final pulse energy reaches 2.5 mJ to 3 mJ [55]. In contrast to the first amplifier, a loose focusing is chosen for the present one to prevent crystal damage to occur. Despite, there are some difficulties concomitant with this loose focusing, which can be understood from a Gaussian optics viewpoint. For that reason, we introduce the *Rayleigh length*  $z_R$  here, defined by

$$z_R = \frac{\pi w_0^2}{\lambda}, \quad (3.1)$$

where  $w_0$  is the  $1/e^2$  beam waist radius,  $\lambda$  the wavelength and the beam diameter  $2w_0$  of the pulse to be amplified, which is usually 1 mm. Accordingly, the focus of the pump beam must be matched to this and takes on the value  $2w_0 \approx 1.5$  mm. Due to this loose focusing and the huge Rayleigh length, the focusing as such follows rules that totally differ from those known from ray optics, if the focusing optics are placed within this Rayleigh length [19]. In this case, where the focusing optics are displaced to each other, the focus position will not move accordingly, but



altering the focal length of the focusing optics will do. Consequently, the focusing optics of the booster are deliberately selected such that they image the beam onto itself, effectively leaving the focus position and size of any subsequent pass unchanged with respect to its preceding one. This situation will hold true only, if the curvatures of the focusing optics and those of the Gaussian beam match. Since the focus position and size of any pass relies on those of its previous pass, we insert a telescope between the first and second amplifier, which allows us to adapt the focus size and position of the first pass nearly individually. Unfortunately, the high optical pump power causes thermal lensing in the Ti:Sa-crystal and, hence, makes the focusing of each pass deviate from what is expected from Gaussian optics. Therefore, proper adjustment of all three foci enforces intermediate realignment of all successive passes at full power. Due to the high pump power and energy deposition in the Ti:Sa-crystal and in order to reduce thermal lensing effects, the booster is operated at cryogenic temperatures around  $\sim 60$  K. These temperatures are produced by a customized *Gifford-McMahon Cryocooler* from *Cryotech* and even lead to an increasing thermal conductivity of the Ti:Sa-crystal, that can even approach that of copper for very low temperatures. Apart from this discomfort, the alignment need not be touched, once it is adjusted, and can be operated for months. Moreover, the output power behind both amplification stages does not vary substantially, since both amplifiers are run in the gain saturation limit and small changes of the input power convert into minor variations of the output power.

### Transmission Grating Compressor

After the booster, we end up with high-power pulses. Since these were previously stretched by excessive chromatic dispersion of a glass block, they need to be compressed to be useful for femtosecond-timescale pump-probe experiments. Therefore, we make use of a *Transmission Grating Compressor*. It consists of two optical gratings<sup>3</sup> which can be shifted freely to each other via a translation stage that is put below the first grating and which are impinged by the amplified and stretched laser pulses at an angle of roughly  $34^\circ$ . While the first grating disperses the beam into its spectral components, the second grating will collimate them again. After traversing both gratings for the first time, the spectrally dispersed beam will be redirected by two mirrors for a second transit through these gratings. In this way, the previously exerted spectral unfolding is undone. Since the short-wavelength components are diffracted less strongly by the grating than the long-wavelength components, the long-wavelength components travel more distance than their short-wavelength counterparts. This makes the short-wavelength components catch up with the long-wavelength components. This behavior reverses the chromatic dispersion that is caused by normally dispersive media. By changing the distance between the two gratings, one is able to vary the amount of negative dispersion. Moreover, this kind of compression turns out to be highly efficient and an overall transmission of roughly 86% has been measured [55]. Nevertheless, there is one drawback of the current scheme, namely, that a transmission grating compressor does not merely introduce second order dispersion, but also third and higher order dispersion (subsubsection 2.2.2.1). Fortunately, these can be satisfactorily compensated with the help of the Dazzler.

---

<sup>3</sup>*Fraunhofer Institute for Applied Optics* [55].

### 3.1.3 DPHCF, Supercontinuum Generation and Final Compression

Owing to the still narrow spectral width of the amplified pulses even after compression, the pulse duration does not fall below 21 fs. The latter is far apart from a few-cycle laser pulse. Here, we want to describe a device, which is capable of generating a so-called *supercontinuum* spectrum from the aforementioned Fourier-limited pulses so that intense few-cycle laser pulses come within reach. What we exactly mean by supercontinuum is explained soon. However, the only way to generate even shorter pulses from Fourier-limited pulses is to augment their spectrum by new spectral components and is a direct consequence of the time-bandwidth product, introduced in section 2.1.

#### Differentially Pumped Hollow Core Fiber (DPHCF) and Supercontinuum Generation

Practically, this extension of the optical spectrum by new spectral components is accomplished by SPM (paragraph 2.2.3.2) in a 1.3 m long, two-sided *differentially pumped hollow core fiber* (DPHCF), made of glass and filled with a gaseous, nonlinear medium such as helium<sup>4</sup>. The DPHCF-assembly is schematically sketched in Figure 3.1. The high intensity, required for SPM to occur, is realized by smooth focusing of the beam into the DPHCF by a telescope consisting of a set of mirrors and lenses (not shown in Figure 3.1). These offer some freedom to find the optimal focus size, shape and position for a decent degree of transmission and spectral broadening. For optimal fiber coupling, the focus diameter  $2w_0$  and inner fiber diameter  $a$  must obey the relation [58]

$$2w_0 \approx 0.64a. \quad (3.2)$$

The fiber diameter  $a$  is determined by balancing spectral broadening effects and fiber losses of the DPHCF. The latter scale proportionally to  $\lambda^2/a^3$ , where  $\lambda$  is the laser wavelength [59]. In our setup, we agreed on an inner diameter of 380  $\mu\text{m}$ . Additionally, it is experimentally found, that a couple of positively chirped mirrors behind the telescope could enhance the temporal pulse compression in front of the DPHCF, since spectral narrowing in the focusing lenses does not occur anymore. This is attributed to amplified pulses, which need to accumulate an increased negative frequency chirp before traversing the focusing lenses of the telescope in order to be compensated by the positively chirped mirrors. Consequently, the nonlinear effects, taking place in the focusing lenses, are negligible. The design of the DPHCF is based on the original, statically gas-filled *hollow core fiber* (HCF) [55,56] and is considered a refined version thereof [60], as will become apparent soon. Speaking of the original setup, the statically gas-filled HCF serves two purposes: First, it acts as a weak wave guide to keep the intensity high within the nonlinear medium and, second, as a container for the nonlinear medium, thus increasing the nonlinear interaction length dramatically. Nonetheless, unlike the HCF, the DPHCF is not

---

<sup>4</sup>One could claim that neon, instead of helium, is a much better option, because of its even bigger third order nonlinearity. Indeed, neon has been used for quite some time in our fiber, but there was an intermediate worldwide shortage, which entailed a price explosion and rendered it economically irrational for further usage.

flooded once a day with a static amount of a nonlinear medium, but is continuously refilled with it. The main advantage of the new DPHCF over the old HCF approach is that a continuous exchange of helium prevents the system from contamination with air, that might leak into the fiber and which could compromise SPM inside the fiber. Moreover, it minimizes the impact of undesired nonlinear effects at the entrance and exit part of the fiber, like self-focusing in helium, followed by filamentation<sup>5</sup>. Of course, both effects usually take place inside the fiber, but while these are desired to happen inside the DPHCF, they are not wanted to take place close to its entrance or exit. The reason is that self-focusing in front of the fiber modifies the focus in an unpredictable fashion and normally leads to degraded fiber coupling efficiency and, consequently, to less spectral broadening. At the exit, self-focusing in residual helium results in the formation of a very intense spot ("hotspot") in the otherwise homogeneous beam profile, since more intense parts of the fiber-exiting beam will experience more self-focusing than weaker areas [60]. This has the disadvantage of destroying subsequent optics due to the occurrence of this "hotspot" and, moreover, to additional nonlinearities taking place in the fiber exit window. However, in order to reduce these effects at the entrance and exit of the DPHCF, its setup is as follows:

The initially unbroken HCF is split into two equally long fiber pieces under consideration of its mutual rotation about the fiber axis. As the inner core of the HCF need not be perfectly concentric due to technical imperfections during its fabrication, their mutual orientation turns out to be crucial to produce a nice beam profile. After splitting of the HCF, the end facets of both fiber pieces are glued into three vacuum compatible housings to isolate the DPHCF from the environment. Two of them serve as gas outlets for the escaping, but continuously refilled nonlinear medium. Values for the residual gas pressure at either end of the fiber are on the order of a few mbar. As the gas is continuously removed, it explains why the new design is termed DPHCF. Additionally, the two housings are used as holders for the entrance and exit windows for the laser, respectively. The third one, instead, serves as an inlet system for the nonlinear medium, which is usually supplied in form of helium at a pressure of 1.5 bar – 2.3 bar. However, after splitting, the two inner facets of the two fiber pieces must be brought close to each other to ensure ideal optical coupling into one another at their juncture. Nonetheless, an unavoidable small gap between the two terminal facets proves beneficial to guarantee the gas to enter the inner core region of the DPHCF. Once the DPHCF is set up correctly, it delivers spectrally broad pulses of 1.2 mJ – 1.5 mJ pulse energy. Furthermore, special attention must be paid to the fiber suspension during its alignment, because it was proven to have a crucial impact on the overall transmission and beam profile, if the fiber is bent [59]. A typical broadened spectrum (red shading) and a reference spectrum (blue shading), taken in front of the fiber, are shown in Figure 3.2. Since the broadened spectrum spans more than an octave, it is commonly referred to as a supercontinuum. In our case, it extends from roughly 450 nm up to approximately 1000 nm.

---

<sup>5</sup>Filamentation describes the phenomenon of self-amplified self-focusing in nonlinear media due to high intensity, culminating in the ionization of the nonlinear medium. This usually modifies the refractive index such that the beam might break up in multiple beams or starts diverging again, as the plasma-related refractive index contribution is smaller than unity.

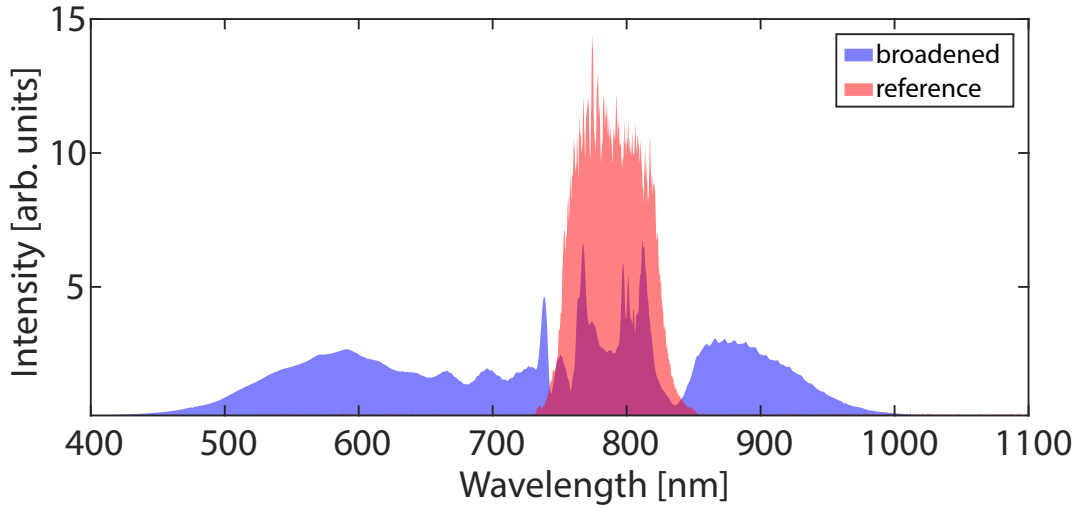


**Figure 3.2:** Typical spectrum that is spectrally broadened inside the DPHCF (*blue-shaded area*) and a typical unbroadened reference spectrum (*red-shaded area*). The broadened spectrum was recorded after the DPHCF with an inner core diameter of 380  $\mu\text{m}$  and at a helium backing pressure of 2.3 bar. Both spectra are normalized with respect to their integral.

### Chirped Mirror Compressor

As a result of the SPM-generated new frequencies on either side of the original spectrum (Figure 3.2), the pulse is not Fourier limited anymore. Hence, we need to compress the pulse once again and *chirped mirrors* turned out to be the method of choice for few-cycle femtosecond pulse compression, because they add little extra amount of material as opposed to prism or grating compressors and due to their rather high damage threshold. Chirped mirrors are based upon *Bragg reflectors*<sup>6</sup>. Unfortunately, Bragg reflectors are known to be too narrow-band to support the entire supercontinuum of the SPM-broadened pulse at once. Fortunately, one can drastically extend their reflectivity bandwidth by means of a simple trick, that also results in the capability of the mirror to compress SPM-broadened pulses. The idea is to concatenate a series of Bragg reflectors, each optimized for a certain wavelength. Consequently, each wavelength is reflected as efficiently as possible across most of the supercontinuum, making use of the high reflectivity of individual Bragg reflectors and of the fact that different wavelengths penetrate to a various extent into the mirror. When properly designed, shorter wavelengths can be forced to penetrate the mirror less deeply than long wavelengths do. This in turn can be identified with a negative GDD (subsubsection 2.2.2.1) and effectively compresses the SPM-broadened laser pulse. In our case, we achieve a pulse compression down to  $\sim 4$  fs, while maintaining a pulse energy of  $\sim 1$  mJ by using six pairs of chirped mirrors in a double-angle design. Their total reflectivity profile spans 400 nm to 950 nm, nearly supporting the entire spectrum. The high number of chirped

<sup>6</sup>Bragg reflectors are a periodic structure of high- and low-index materials for a given wavelength  $\lambda$ , where the optical path length for each material equals a quarter of the wavelength, at which one wants the Bragg reflector to reflect light, i.e.  $n_i \cdot d_i = \lambda/4$ , where  $n_i$  is the refractive index of the  $i$ -th material and  $d_i$  is its thickness.

mirrors is necessary to compensate the 2 mm amount of glass of the entrance window to the vacuum system of the AS2-beamline (section 3.2), as shown in the lower right corner of Figure 3.1.

### 3.1.4 CEP-Stabilization

As we saw in chapter 2, the CEP of ultrashort laser pulses plays a crucial role for the generation of isolated attosecond pulses. Therefore, we discuss two techniques now, which enable us to stabilize and control this quantity and both of them are required, as short- and long-term CEP-drifts arise during laser operation. The former is coped with by the *Fast Loop*, whereas the latter long-term drifts are compensated by the *Slow Loop*.

#### Fast Loop — CEP-stabilization scheme for short-term drifts

Let us start with the description of the fast loop. Between the incoupling of the pump beam into the oscillator and the Verdi V6 laser head, an *acousto-optic modulator* (AOM) is inserted into the beam path, that is used to modulate the pump laser intensity. It makes use of the refractive index of the Ti:Sa-crystal, which depends on the instantaneous intensity of the pump pulse compliant with the optical Kerr effect (subsubsection 2.2.3.2). Since the optical Kerr effect impacts the phase and group velocity of a pulse in the crystal, this can be exploited to vary the carrier-envelope-offset frequency  $f_{CEO}$  of the emitted pulse train. As stated above, it is suited to stabilize it against possible fast CEP-drifts, which might arise from nonlinearities. In order to accomplish a full feedback system, which is able to compensate these fast CEP-drifts, we first need to extract the  $f_{CEO}$  frequency of the pulse train and this is usually performed with the *f-0-technique*. Why it is named like this, will become apparent soon. The idea of the *f-0-technique* is to generate a down-converted pulse train from the fundamental wave (emitted pulse train from the oscillator) via DFG (subsection 2.2.3) in a *periodically-poled-lithium-niobate* (PPLN)-crystal, which removes  $f_{CEO}$  according to

$$f_{mn} = (f_m + f_{CEO}) - (f_n + f_{CEO}) = f_m - f_n, \quad (3.3)$$

where  $f_m, f_n$  denote two longitudinal modes of the spectrum of the fundamental pulse train and  $f_{mn}$  labels the difference frequency. As a consequence, we have gained a well-defined "ruler", starting from  $\tilde{f}_{CEO} = 0$  ( $0$  in *f-0-technique*), and which we use to measure the  $f_{CEO}$  ( $f$  in *f-0-technique*) of the fundamental pulse train, that did not undergo DFG in the PPLN-crystal. This is achieved via extraction of their beating frequency  $f_{Beat}$  by spectral interference and low-frequency filtering. Anyway, one prerequisite must be fulfilled, namely, the initial spectrum must be as broad as to extend down to the newly generated difference frequency  $f_{mn}$  for spectral interference to occur, in accord with

$$f_{Beat} = (f_k + f_{CEO}) - f_{mn} = (f_k - f_{mn}) + f_{CEO} \stackrel{f_k=f_{mn}}{=} f_{CEO}, \quad (3.4)$$

where  $f_k$  is another longitudinal mode in the long-wavelength range of the spectrum, matching the DFG-signal, and thus providing the extracted  $f_{CEO}$ -frequency. Fortunately, the fundamental pulses are spectrally broadened inside the PPLN-crystal by SPM. The corresponding setup of the *f-0-technique*, just described, is usually located behind the oscillator and outputs a signal that is proportional to the  $f_{CEO}$ -offset from a target value. However, the fast loop is usually locked to a quarter of the repetition rate, i.e. 20 MHz. This implies that the CEP of only every fourth pulse is identical. Since the Pockels cell of the first multipass regenerative amplifier (subsection 3.1.2) lets only every fourth pulse pass, it ensures that all pulses leaving the Pockels cell have identical CEPs. This is why the repetition rate is reduced by a factor that is a multiple of four.

### Slow Loop — CEP-stabilization scheme for long-term drifts

Now, that we know how the f-0-technique works, we would like to finish this subsection with the discussion of the *Slow Loop*. Like the fast loop, the slow loop is another CEP-stabilization, that tries to cope with CEP-drifts, that take place on a longer timescale, and can be used to vary the CEP-value in an arbitrary fashion, as it is necessary for HHG. In contrast to the f-0-technique, the slow loop makes use of the so-called *f-2f-technique*. Therefore, we pick off the reflection from the Brewster window to the vacuum system of the AS2-beamline and steer it into a f-2f-setup (right-hand-side of Figure 3.1). It consists of a  $\lambda/2$ -waveplate, a focusing lens, a beta-barium-borate (BBO) nonlinear crystal, suitable for SHG, another lens to focus the beam into a Thorlabs HR-spectrometer and a polarizer. The waveplate is needed to align the laser polarization perpendicularly to the optic axis of the BBO for proper type-I phase-matching. The idea behind the f-2f-method is to generate the *second harmonic* (SH) of the laser and to make it interfere with its fundamental, i.e. the very same SH wavelength from the laser spectrum that does not originate from SHG. The polarizer is necessary to project the SH and the fundamental onto a common axis to make both beams interfere. From the spectral interference pattern one can deduce  $f_{CEO}$  via the beat frequency  $f_{Beat}$  according to

$$f_{Beat} = 2 \cdot (f_n + f_{CEO}) - (f_m + f_{CEO}) = (2f_n - f_m) + f_{CEO} = f_{CEO}. \quad (3.5)$$

Here,  $f_n$  is the laser wavelength of the fundamental wave and  $f_m$  is the SH wavelength from the SPM-broadened laser spectrum that does not arise from SHG and the last equality will hold, if  $2f_n = f_m$ . The slow loop feedback signal stems from the displacement of the spectral interference fringe pattern and is fed back to a piezoelectric transducer, that is attached to one of the wedges behind the glass block stretcher, as schematically sketched in Figure 3.1. Small changes on a few- $\mu\text{m}$  scale in the amount of glass, which is inserted into the beam path, leads to a shift of the CEP due to an induced phase-shift  $\Delta\phi = \frac{2\pi n \Delta L}{\lambda}$ . Here,  $n$  is the refractive index of the wedge material,  $\lambda$  the center wavelength of the laser pulse and  $\Delta L$  denotes the change of the material thickness. The beam-pointing and temporal pulse profile remain unaffected by those small changes, but do have a big impact on the CEP.

## 3.2 The Attosecond Beamline AS2

Once the ultrashort pulse generation is accomplished, one has to ensure that the ultrashort pulse remains short until it arrives at the experiment. We learned in chapter 2 that an ultrashort pulse tends to disperse temporally when exposed to dispersive media. Since the experiment covers two floors at the *Max Planck Institute of Quantum Optics* (MPQ)<sup>7</sup>, pulse propagation in air is prohibited, because its dispersive character is already enough in terms of pulse spreading. Therefore, quickly after the final pulse compression, it enters a vacuum system as already mentioned in the last section and is called the *AS2-beamline*. The entire beamline is based upon a modular design, which allows us to vent and modify each vacuum chamber in the beamline separately. We will introduce the vacuum chambers one by one in this section.

### 3.2.1 High Harmonic Generation Chamber

The first step in every pump-probe TRPES-experiment consists in the generation of the probe pulse by means of HHG, as explained in subsection 2.2.4.1, and takes place in the *High Harmonic Generation chamber*. A schematic sketch of the corresponding chamber is depicted in Figure 3.3 a).

The laser beam comes from the second floor and is guided through another chamber — the *Switchbox*<sup>8</sup> — and finally enters the HHG-chamber with a pulse energy of approximately 650  $\mu\text{J}$  – 900  $\mu\text{J}$ , owing to the non-perfect reflectivity of several silver mirrors between the laser upstairs and the HHG-chamber downstairs. In order to facilitate beam alignment, we placed several motorized apertures (MA) in the beam path, which are adjustable from the outside. These apertures are necessary to ensure reproducible alignment into the experimental setup by steering the beam concentrically onto the aperture. Moreover, it is used to vary the intensity for HHG by clipping the beam on purpose, in this way reducing the optical intensity. In front of the motorized aperture we inserted a glass wedge pair (not shown) at Brewster’s angle for final pulse compression, since the last chirped mirror compressor stage overcompensates the chromatic dispersion a bit. Only after the glass wedge pair, the pulse is fully compressed down to roughly 4 fs. Subsequently, the beam is loosely focused by a concave focusing mirror (FM) into the *high harmonic target* (HHT) (Figure 3.3 b)). With the help of two motorized mirrors (MM1/MM2), we are given some freedom to steer the beam through the HHT until the incoupling into the next chamber (subsection 3.2.2) is sufficiently good. Furthermore the HHT is placed onto a one-dimensional translation stage to move the HHT along the beam path through the laser focus and to meet the HHG-related phase-matching condition (subsection 2.2.4.2). The high harmonics are generated in a collinear fashion with the fundamental laser beam in a quasi-static gas cell. It is formed by a 3 mm thick ceramics tube, where one end is sealed with *Torr Seal*<sup>®</sup> *Low Vapor Pressure Epoxy*, whereas the other is used for neon gas supply as nonlinear medium. Two 300  $\mu\text{m}$  holes are pre-drilled perpendicularly to the tube axis and in line with the laser to

<sup>7</sup>The laser system FP3 is located on the second floor, whereas the beamlines are placed on the first floor.

<sup>8</sup>As the laser facility itself consists of several lasers and beamlines, one basically has the possibility to use different lasers for different experiments. Therefore, the *Switchbox* acts as a distributor unit to assign a certain laser to a particular experiment.

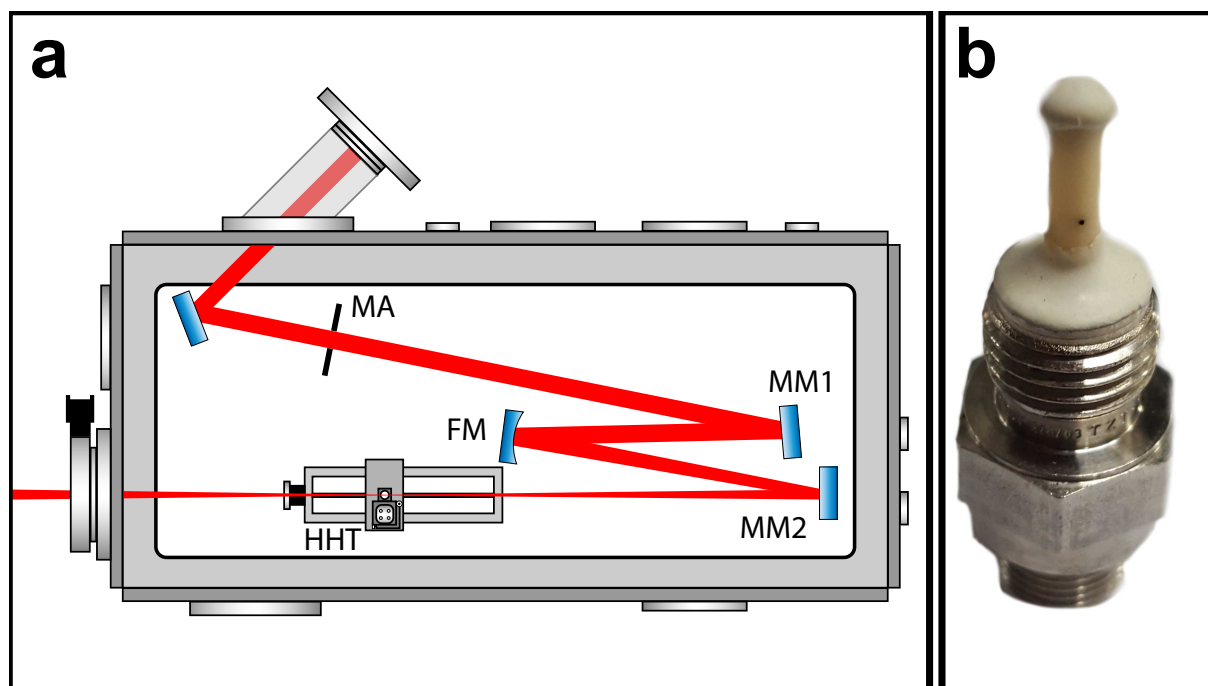


**Figure 3.3:** a) Schematic sketch of the HHG chamber. *MA*: motorized aperture; *MM1/MM2*: motorized plane mirrors; *FM*: focusing mirror; *HHT*: high harmonic target. The laser polarization is out-of-plane. b) closeup view of a typical ceramics high harmonic target with predrilled holes on either side of the ceramics target (dark spot).

allow the pulse to interact with the nonlinear medium. The advantage of ceramics targets over stainless steel targets, which have been used quite frequently in the past, is that the former survive the high laser intensity more easily than the latter and need not be replaced that often. By adjustment of the applied neon gas pressure (usually 100 mbar – 130 mbar), the position of the high harmonic target and the amount of inserted glass, one can optimize the high harmonic generation in terms of phase-matching (subsubsection 2.2.4.2). Despite the gas load, the backing pressure inside the HHG chamber remains below  $1 \times 10^{-2}$  mbar. This pressure is low enough not to suffer from high harmonics being reabsorbed by residual background neon atoms. This low pressure is achieved by use of two *Alcatel Adixen ATH 300 Hybrid Turbomolecular Pumps*, developed for high gas load.

### 3.2.2 Interferometer — Delay Chamber

The High Harmonic Generation chamber is followed by the *Delay-Chamber* and a schematic sketch is displayed in Figure 3.4. The purpose of this chamber is to provide space to manipulate the pump pulse (chapter 4). Moreover, it is employed to delay the probe pulse with respect to the pump pulse, effectively forming a Mach–Zehnder interferometer. This enables us to perform pump–probe TRPES-experiments on ozone, in particular, as it is the topic of this thesis. The



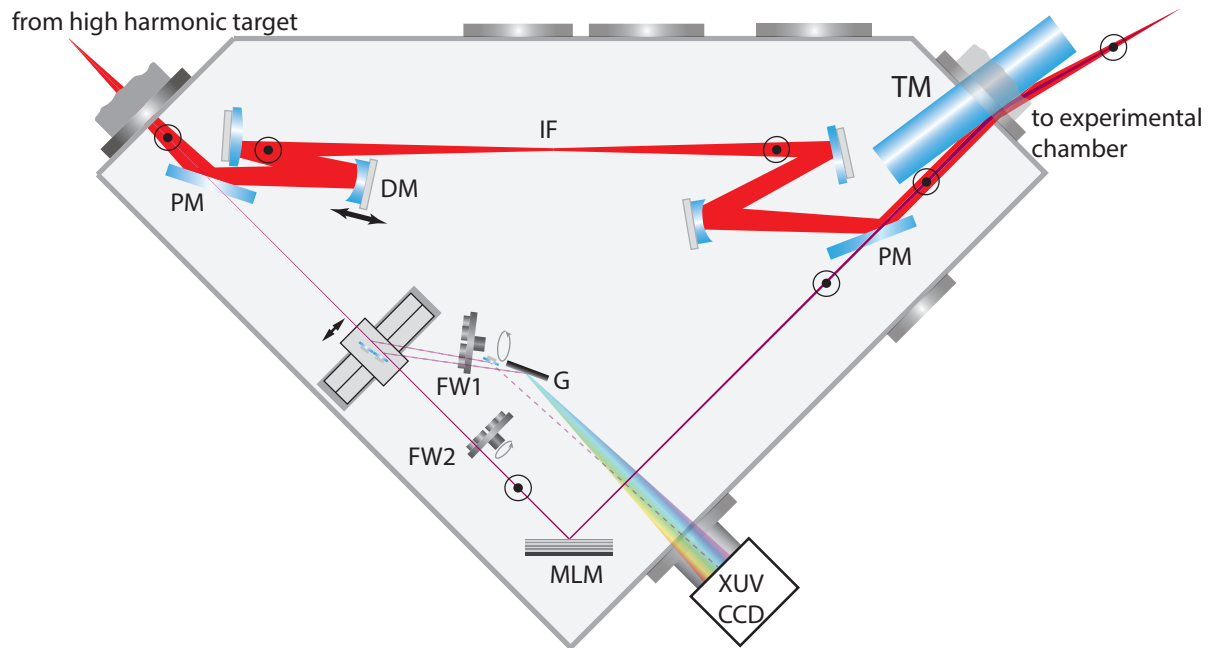


**Figure 3.4:** Schematic sketch of the delay-chamber, providing a lot of freedom due to its size and which serves as a Mach–Zehnder interferometer in order to delay the pump pulse (upper arm) with respect to the probe pulse (lower arm). For a description of various components, see main text.

setup is as follows: The fundamental pulse and the high harmonics (in the remainder of this chapter called NIR and XUV, respectively) enter the delay-chamber in a collinear way that is enforced by the HHG process. Due to the deviating divergence angles of NIR and XUV, respectively, which originate from its photon energy scaling (NIR:  $\sim 1.5$  eV, XUV:  $\sim 100$  eV), the XUV diverges less strongly than the NIR does. Consequently, as both beams propagate, they differ in size at the position of the first *perforated mirror* (PM). If we want to separate both beams, we will not be allowed to insert a common beamsplitter to two major reasons: First, the additional chromatic dispersion of a beamsplitter may lead to temporal broadening and second, what is more severe, any material would simply absorb the XUV, which must be prevented.

This is the reason why a silver-coated perforated mirror is used instead, that has a 1 mm hole and which lets the XUV pass, while the NIR is reflected due to its bigger beam size (relative to the XUV) at  $45^\circ$  (upper left corner in Figure 3.4). While both beams are separated, they propagate along the two arms of the interferometer. On the one hand, the XUV travels along the lower arm and optionally traverses very thin and freestanding metal filters mounted on a motorized filter wheel (FW2) for spectral filtering of the cutoff range of the HHG spectrum. Subsequently, it is reflected by a *multilayer mirror* (MLM), exclusively designed to meet experimental constraints, like photon energy, reflectivity, spectral phase and bandwidth. The combination of freestanding

metal filters<sup>9</sup> and MLM lead to the generation of isolated attosecond pulses and serve in the following as probe pulses for our experiment. On the other hand, the NIR propagates along the upper arm of the interferometer and is focused via appropriate mirrors of the first "Z" — formed by two opposing mirrors — into an *intermediate focus* (IF). The first of these mirrors is mounted on top of a translation stage for coarse balancing of the interferometer and, additionally, on top of a one-dimensional piezoelectric nanopositioning stage from *Piezosystem Jena*. The latter is used for delaying the pump pulse with regard to the probe pulse with attosecond precision and with a span of several hundred femtoseconds (DM in Figure 3.4).

Getting back to the intermediate focus, it can be used for pump pulse modification, nonlinear conversion or experiments themselves. After the intermediate focus, the NIR is reflected by two suitable mirrors in the second "Z" and the divergence of the NIR is adapted to that of the XUV. Both beams, NIR and XUV, are then recombined on a second perforated mirror in a collinear way again (PM in upper right corner of Figure 3.4). Since their divergence is identical behind the second perforated mirror, they will be focused on the very same spot via a grazing incidence, nickel-coated *toroidal mirror* (TM). Despite the huge amount of space, which enables the chamber to be used versatilely, there are a few constraints to be fulfilled for performing pump–probe TRPES-experiments successfully. First, the two arms have to be equally long, down to a few microns. This sometimes proves to be quite difficult to achieve without destroying the spatial overlap in the focal plane after the toroidal mirror and maintaining a nice NIR focus, as each arm has a length of roughly 2 m. Second, the size of the interferometer calls for special attention concerning the overall pointing and timing stability, which would make pump–probe experiments impossible, if they were not fulfilled. Apart from the interferometer, the delay-chamber provides lots of diagnostic tools to monitor the beam profile, beam-pointing and spectrum of the high harmonics by means of an additional filter wheel (FW1), filled with various freestanding metal filters, an unprotected rhodium mirror or, optionally, an imaging XUV-grating<sup>10</sup> (G). The XUV radiation is detected with a *Princeton Instruments SX-400* CCD camera. In order to prevent its absorption by residual gas, the backing pressure inside the delay-chamber is kept well below  $1 \times 10^{-4}$  mbar.

### 3.2.3 Experimental Chamber

The *Experimental Chamber* constitutes the back end of the AS2-beamline and a graphical illustration can be found in Figure 3.5. In this chamber, streaking measurements are usually performed in either parallel or perpendicular configuration (section A.1 in the appendix). The two-color, collinear NIR-XUV-beam, as it leaves the delay-chamber, enters the experimental chamber from the left. Both beams have a common spot underneath the *electron time-of-flight* (TOF) detector<sup>11</sup>. Any sample is placed right underneath the TOF in the gas phase and is provided through a glass nozzle target (N) from the outside. The nozzle is coated with graphite for reduction of charging effects and is aligned perpendicularly to the TOF axis. For pump–probe

<sup>9</sup>We use commercially available freestanding metal filters from *Lebow Company*, that are 150 nm up to 1500 nm thin, depending on the experimental demands and which must be treated carefully.

<sup>10</sup>We use a trapezoidal high reflectivity XUV-grating (2105 lines/mm; HORIBA Jobin Yvon).

<sup>11</sup>We use an ETF10 electron TOF from *Stefan Kaesdorf - Geräte für Forschung und Industrie*.

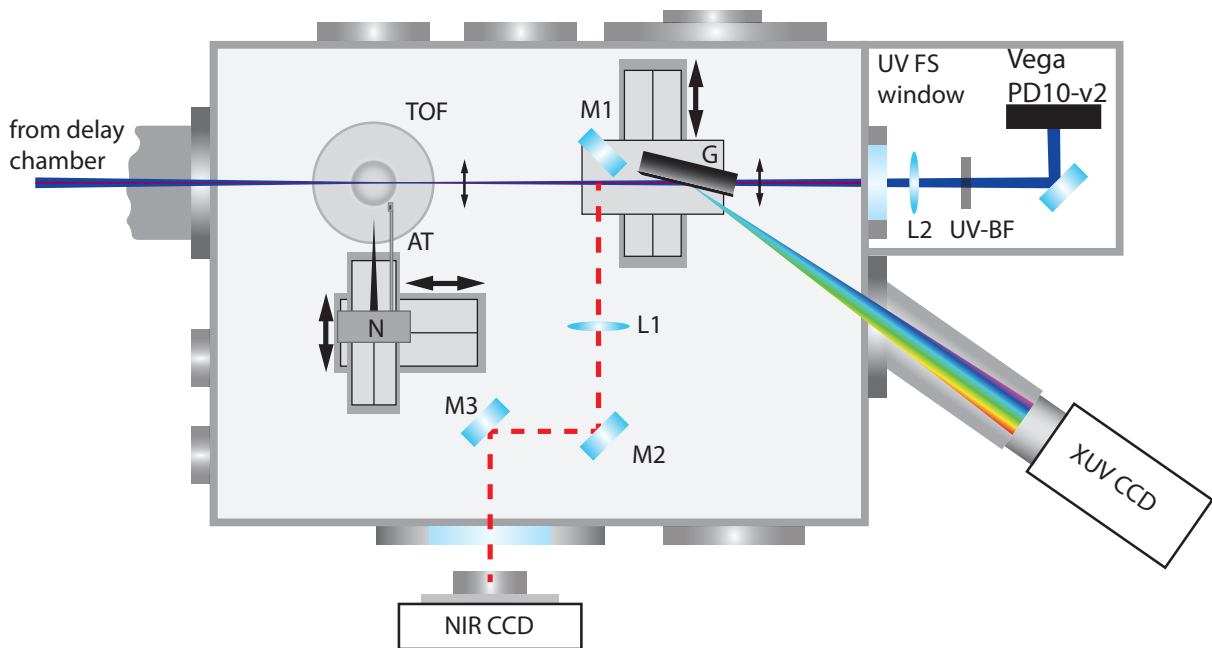


**Figure 3.5:** Schematic sketch of the experimental chamber in which pump–probe experiments are conducted. TOF: electron time-of-flight detector; N: gas nozzle for sample supply; AT: alignment tool for spatial overlap; M1–M3: mirrors; L1–L2: focusing lenses; NIR CCD: camera for validation of spatial and temporal overlap; G: XUV-grating; XUV CCD: XUV radiation sensitive CCD camera for XUV beam profile and spectrum measurements; UV-BF: deep ultraviolet bandwidth filter for UV pulse measurement (adapted to meet experimental conditions presented in chapter 4).

experiments, proper spatial overlap between XUV and NIR at the place of the experiment is stringently required. Therefore, an *alignment tool* (AT) is installed close to the nozzle. Basically, it is a thin copper foil with a 100  $\mu\text{m}$  small hole inside. The alignment procedure works as follows: Both beams are steered through this hole and their transmission can be monitored via various diagnostic tools, that are sensitive to either NIR, XUV or even DUV radiation (chapter 4). Since the AT can be moved along the beam propagation axis, optimal transmission is likely to be found at the focus. Afterwards, the nozzle as well as the TOF are placed at this point where spatial overlap is assured. For temporal overlap between XUV and NIR, both beams are imaged onto an NIR CCD camera. Looking at the interference fringes originating solely from the NIR part, that propagates along both arms of the interferometer, one adjusts the temporal overlap by maximizing those interference fringes via displacement of the nanopositioning stage of the delay-chamber.

Getting back to the detection scheme for the pump–probe experiment: The TOF collects XUV-ejected photoelectrons, emerging from the sample, and steers them onto a *multichannel plate* (MCP) detector. The latter amplifies the detected signal to a measurable amount. Then, its output signal is further processed and discerned by the particles’ time of arrival at the detector.

From this quantity one can deduce the kinetic energy of the photoelectrons quite easily by means of the following equation:

$$E_{kin} = \frac{m_e L^2}{2(t - t_0)^2} = E_{XUV} + I_p, \quad (3.6)$$

where  $E_{kin}$  is the kinetic energy of the photoelectron,  $m_e$  its mass,  $L$  is the effective length of the TOF and  $t - t_0$  labels the time of arrival ( $t$ ), measured from the time of ionization ( $t_0$ ), that is the position of the so-called *light peak*.

Knowledge of the XUV photon energy  $E_{XUV}$  enables one to make a statement about the binding energy or work function of a sample, respectively, represented in the above equation by  $I_p$ . Additionally, if electron dynamics are triggered by the NIR or, in case of ozone by a DUV pump pulse, one will also be able to monitor this impact onto the photoelectron spectrum as a function of delay between pump (NIR) and probe (XUV) pulse. These impacts onto the photoelectron spectrum manifest themselves as chemical shifts or as emergence of new spectral lines. This forms the basis for the ozone-experiment being discussed in chapter 4. Since the MCP detector, that is usually biased with 2.15 kV, will be prone to damage, if the backing pressure inside the experimental chamber is too high, the pressure at the MCP detector is kept below  $4 \times 10^{-6}$  mbar when the sample is guided into the experimental chamber.

## Chapter 4

# Electronic and Nuclear Dynamics in Ozone

The current chapter is dedicated to the femtosecond-timescale investigation of the electronic–nuclear dynamics in ozone. These are triggered by absorption of a single DUV-photon, followed by the photodissociation of ozone. Besides the excited state-related *potential energy surface* (PES), whose topology dictates the evolution of the DUV-induced photodissociation, ozone possesses many more excited state-associated PESs with quite different topographies. Among these, multiple *conical intersections* (CIs) [61] with adjacent PESs appear and usually serve as funnels for the nuclear wave packet to release previously absorbed energy in a radiationless manner along different pathways. They occur quite frequently in polyatomic, especially biologically important molecules like peptides [62], proteins [63] or DNA [64–66]. It is exactly this phenomenon that makes DNA robust against ultraviolet radiation. Since ozone is one of the most strongly DUV-absorbing molecules, it is therefore predestined to push few-femtosecond or even attosecond timescale pump–probe experiments from the NIR into the DUV spectral domain. However, a prerequisite that must be met before scrutinizing nonadiabatic phenomena in ozone is the observation of its photolysis, indicating the successful promotion of the ozone molecule into its dissociative excited state. Yet, the ozone photodissociation is known to happen on a few tens of femtoseconds, hence enforcing few-femtosecond temporal resolution in pump–probe TRPES-experiments. Although the ozone photolysis is successfully described by post-Hartree-Fock methods, it has never been measured in a time-resolved fashion. Since its direct observation has evaded experimental access so far due to the unavailability of intense and ultrashort DUV laser pulses, we undertook efforts to close this gap.

The chapter is structured as follows:

First, we will start with a description of the principle of the ozone experiment. We will introduce the ozone molecule along with its most important absorption bands and electronic states. Then, we adumbrate its expected molecular dynamics, that are kicked off by the absorption of a DUV-photon.

Second, we will focus on the theoretical treatment that is necessary for the description of the

ozone photodissociation. Here, we make use of a simple three-level simulation, in which we restrict ourselves to two levels — one for the ground and another for the excited state — in order to quickly estimate the ozone excitation probability without the need for highly sophisticated *ab-initio* quantum chemical calculations like multiconfigurational time dependent Hartree (MCTDH). Nonetheless, the latter are inevitable to describe the experimental results to a very high degree. At this point, we will further introduce — besides other quantities — the concept of *Dyson orbitals* and their consequences in the estimation of the angular distribution of photoelectron emission in the molecular frame and their derived photoionization probabilities upon XUV probe pulse irradiation.

Third, before we turn our attention to the direct experimental observation of the ozone photodissociation, we first need to cast an eye on group theoretical aspects regarding molecular selection rules for photoionization. These apply to transitions that are driven between any initial and final state of neutral ozone and its cation, respectively, and are also influenced by the ionizing XUV probe pulse polarization in the molecular frame. To an even bigger extent than in the case of atoms, the observability of photoelectron emission from different states into the continuum is highly dependent on the symmetry of these states and on the molecular orientation relative to the chosen laboratory coordinate system. Therefore, we will shed some light on these contributions and focus on how the experiment has to be designed geometrically to render excited state dynamics in ozone observable. In order to do so, we will exemplify this circumstance by looking at the molecular-frame angular distribution of photoelectron emission after introduction of the most important cation states of ozone.

Fourth, following the statements made in the previous section, we will address the relative positions of the ground and the dissociative excited states in terms of energy. Their energy spacing naturally imposes constraints considering the experimentally achievable time and energy resolution, which is required to maintain their discriminability. At the end of the fourth section, we depict the XUV spectrum that is used in the experiment to ionize and probe the electronic–nuclear dynamics of ozone.

Fifth, after having addressed the XUV probe pulse generation, we will discuss two attempts that have been tested for the generation of short and intense DUV pulses. Both are based upon the concept of nonlinear frequency up-conversion of an intense NIR few-cycle laser pulse. Here, we make use of the concepts introduced in chapter 2. To be more precise, we investigate a THG approach in a rare gas target and an SHG approach in a solid. The section ends with a comparison of both approaches and provides a short conclusion.

Sixth, as we need highly pure ozone for our experiment, we will explain the employed ozone distillation setup in more detail.

Seventh, we will quickly compare photoelectron spectra of ozone and diatomic oxygen. We define energy domains being used for the evaluation of the experimental data.

The experimental results of the few-femtosecond pump–probe TRPES-measurement on ozone are the subject of sections eight and nine of this chapter. There, we describe our multi-stage data analysis scheme that is used to unveil the molecular dynamics from the data and, finally, we discuss and interpret our findings before we compare them to calculated TRPES-spectra obtained by sophisticated MCTDH-simulations.

The chapter ends with a presentation of Dyson orbitals for both undissociated and dissoci-

ated ozone and, finally, with their interpretation in terms of photoionization cross sections for both nuclear geometries. The latter provide an indication for why the experimental results are detectable after all.

## 4.1 Principle of the Experiment

As outlined in the introduction of this chapter, we perform TRPES-experiments on the ozone photodissociation, which permanently happens in the stratosphere, and monitor this process in real-time. These experiments rely on a few-femtosecond timescale DUV-pump / XUV-probe scheme, applied to a gaseous, highly pure ozone sample (section 4.6). The idea behind this approach is to optically excite the molecule with a single DUV-photon (4.6 eV or 268 nm), which leads to less tightly bound valence electrons due to charge redistribution, that is a sequitur of molecular orbital population transfer, as opposed to those remaining in the ground state (subsection 4.1.2). Thereby, electronic charge redistribution triggers nuclear motion within the ozone molecule through the interplay of electrostatic forces. The entire action can be probed successively for arbitrary time steps relative to when the entire dynamics started. By collecting these photoelectrons with a TOF (subsection 3.2.3), we can discern the photoelectrons with respect to their arrival time at the detector and is equivalent to the photoelectron kinetic energy. The latter allows us to deduce the instantaneous binding energy of an electron within the molecule and, consequently, any population transfer between electronic states and structural changes. Repeating the DUV-pump / XUV-probe measurement for different instants of time yields a spectrogram consisting of individual spectra, one per pump-probe delay time.

### 4.1.1 The Ozone Molecule

Now, let us have a look at the ozone molecule,  $O_3$ , and its geometrical structure. It consists of three angled oxygen atoms, O. The *Lewis structure* [67] or *resonance structure* is depicted in Figure 4.1 and indicates this issue. The three spheres indicate oxygen atoms, that are equidistantly arranged ( $R = 2.42$  a.u.), where the two terminal oxygen atoms form an angle of  $116.8^\circ$  with the central oxygen atom. Solid lines signify doubly occupied orbitals and dashed lines illustrate the fact that residual bonding electrons are delocalized across the molecule in the sense of quantum mechanical superposition of orbitals. It is a simplified illustration of the circumstance that two mesomeric Lewis structures of ozone exist, where a single and a double bond can occur on either side of the central oxygen atom. This is due to the indistinguishability of the two terminal oxygen atoms, effectively rendering them equivalent. Nevertheless, we choose the Lewis structure on purpose to illustrate the structure of the ozone molecule, as it facilitates its assignment to a certain point group, i.e.  $C_{2v}$  in this case (section 4.3). Regarding this point group and whenever we discuss any implications arising from group theoretical discussions, it is inevitable to define the orientation of the molecular frame coordinate axes. Usually, the x-axis is perpendicular to the molecular plane, while the z-axis is the principal rotation axis, as illustrated in Figure 4.1. This will become important when dealing with the angular distribution of photoelectron emission in section 4.3.

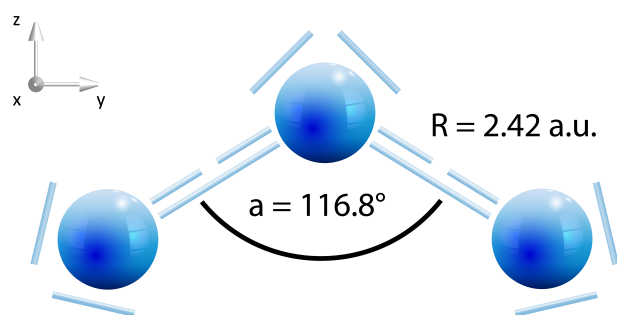


**Figure 4.1:** *Lewis structure or resonance structure* of ozone at its equilibrium configuration. It consists of two equidistantly arranged oxygen atoms (blue spheres,  $R = 2.42$  a.u.) to either side, measured from the central oxygen atom, and form an angle of  $116.8^\circ$  with the central O-atom. Solid and dashed lines indicate doubly occupied bonds and those, respectively, that are delocalized across the molecule, since the electrons can either reside on its left or right bond. The ozone body-fixed coordinate system is shown in the upper left corner.

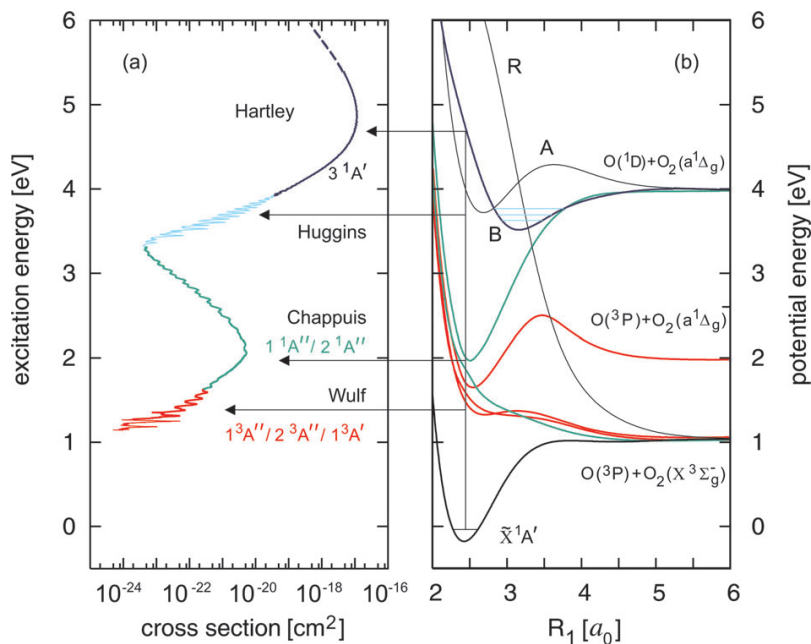
#### 4.1.2 Absorption Bands and Electronic States of Ozone

Figure 4.2 a) depicts the four major absorption bands of ozone, including their corresponding absorption cross sections, whereas Figure 4.2 b), in addition, relates these bands to certain optical transitions, where the latter start at the ground X state ( $\tilde{X}^1A'$ ). Further, Figure 4.2 b) depicts a one-dimensional cut through the PESs of ozone as a function of the dissociation coordinate, while the remaining two degrees of freedom are kept fixed ( $R_2 = 2.43$  a.u.;  $\alpha = 117^\circ$ ). The state labeling in Figure 4.2 a) refers to ozone in  $C_s$  point group symmetry<sup>1</sup>, in which the two terminal oxygen atoms are not necessarily arranged equidistantly around the central oxygen atom. Nonetheless, in the following discussion we will mainly refer to state labeling in terms of  $C_{2v}$  point group symmetry, anticipating the discussion in section 4.3. The special topography of these PESs is essential for the efficient and highly protective effect of the ozone molecule against biologically harmful, solar DUV radiation. Obviously, the Hartley band (B state in Figure 4.2 b)) in the DUV spectral domain (6.2 eV – 4.1 eV or 200 nm – 300 nm) is the most intense, centered around  $\sim 4.86$  eV (254 nm), and is approximately three orders of magnitude stronger than the Chappuis band absorption in the NIR spectral domain (3.1 eV – 1.8 eV or 400 nm – 700 nm). Electronic structure calculations refer the Hartley band to the electronic transition at the *Franck-Condon* (FC) point<sup>2</sup> from the ground X state ( $C_{2v}$ :  $1^1A_1$  /  $C_s$ :  $\tilde{X}^1A'$ ) to the aforementioned excited B state ( $C_{2v}$ :  $1^1B_2$  /  $C_s$ :  $3^1A'$ ). Moreover, and in contrast to the Chappuis band, the Hartley band is strongly dissociative and weakly binding, as can be deduced from the topography of the one-dimensional cut through the PES of ozone (Figure 4.2 b)).

<sup>1</sup>The  $C_s$  point group consists of only two elements: The identity transform  $E$ , that leaves the molecule unchanged, and the molecular in-plane reflection  $\sigma$ .

<sup>2</sup>The *Franck-Condon* (FC) point describes the ground state equilibrium configuration of ozone in terms of nuclear coordinates, as illustrated in Figure 4.1, and follows the Franck-Condon principle. The latter states that vibronic transitions between two electronic states are the more likely, the more their vibrational wavefunctions overlap spatially for a given configuration (vertical transition in nuclear coordinate space).





**Figure 4.2:** **a)** The measured absorption cross section (in  $cm^2$ ; logarithmic scale) of ozone as function of the excitation energy. **b)** One-dimensional cuts through the potential energy surfaces relevant for the photodissociation of ozone.  $R_1$  is one of the OO bond lengths; the other one is fixed at  $R_2 = 2.43 a_0$  and the bond angle is  $\alpha = 117^\circ$ .  $E=0$  corresponds to  $O_3(\tilde{X})$  in the ground vibrational state (zero point energy). A, B, and R indicate the three (diabatic)  $^1A'$  states relevant for the Hartley and Huggins bands. The horizontal arrows illustrate the electronic assignments of the absorption bands. Color coding in **a)** and **b)** stresses the relation between the absorption bands and the underlying electronic states. Figure and Caption reproduced from [17] with permission of the *PCCP Owner Societies*.

Apart from these two most prominent absorption bands, there are two more, but weaker absorption bands which are termed the Huggins (4.1 eV – 3.1 eV or 300 nm – 400 nm) and Wulf (> 700 nm or < 1.8 eV) bands. These refer to transitions between the ground X state and other excited electronic states, which will neither be taken into account in the discussion nor in numerical simulations regarding the intramolecular dynamics of ozone due to their obviously negligible contribution [17]. They are only mentioned here for the sake of completeness. Moreover, Figure 4.2 b) depicts multiple crossings of diabatic electronic states. These are the CIs, that are mentioned above. As brought up before, they act as funnels for molecules to release excess energy after optical excitation into kinetic energy. They even allow the population of electronic states via internal conversion or intersystem crossing, respectively, thus opening up the possibility to populate electronic states like  $^1A_2$ , which are dipole-forbidden and cannot be reached via optical excitation from the ground X state due to symmetry reasons (section 4.3). Nonetheless, on the timescale on which we monitor molecular dynamics, these CIs are negligible, but may become important in future research.

### 4.1.3 Expected Molecular Dynamics

Since DUV absorption of ozone triggers its subsequent photodissociation and finally leads to its fragmentation into atomic and diatomic oxygen and because the Hartley absorption band directly connects to the transition between the ground X and excited B state, we want to cast an eye on the shape of their PESs. They are the solutions of the electronic Schrödinger equation, that is part of the full molecular Schrödinger equation for fixed nuclei. They can be understood as the potential that the nuclei of the ozone molecule experience and which steers their motion. This can be compared to a sphere rolling down a hill due to the action of the gravitational field and which can be influenced by surface irregularities of the hill. Nonetheless, unlike the gravitational field, there is a great number of potential energy surfaces with different topographies and nonadiabatic coupling terms between them. Their topography depends on the electronic state of the molecule and, indeed, they get classified by so-called point group-related *irreducible representations* of these states (appendix B). Let us have a look at Figure 4.3, showing both the PES of the a) ground X state and b) excited B state in its full dimensionality and as a function of the three degrees of freedom. The color scale refers to the potential height in units of electronvolts. Concerning the ground X state PES (Figure 4.3 a)), there is a rather well-defined potential minimum (FC point) with little extent to neither bond lengths nor angle and which is symmetric with respect to the two terminal bond lengths. In contrast, regarding the three-dimensional B state PES (Figure 4.3 b)), there are also two well-defined, but asymmetric minima around ( $R_{1,2} = 3.2$  a.u. and  $R_{2,3} = 2.3$  a.u. and vice versa) and an increasing potential barrier along the diagonal of the coordinate space. The occurrence of this barrier and that of the two asymmetric minima explains, why ozone does not decay into three single oxygen atoms, but into atomic and diatomic oxygen. Due to the presence of this barrier and the presence of the two minima to either side of the diagonal, a saddle point structure is identifiable, that will play a crucial role during the molecular dynamics ( $R_{1,2} = R_{2,3} \approx 2.7$  a.u.). To facilitate the understanding of ozone photodynamics, the two-dimensional reduced PESs of the ground X state (Figure 4.3 c)) and excited B state (Figure 4.3 d)) are added for  $\alpha = 116.8^\circ$ . The white dots mark the position of the FC point on either PES and the white arrows indicate the expected *nuclear wave packet* (NWP) motion on the B state PES after DUV-induced excitation from the ground X state. Since we assume a vertical transition from X to B, following the Franck-Condon principle, the motion of the NWP starts at the FC point. It is steered by the topography of the B state PES towards the valley-ridge inflection point, midway between the two minima and close to the increasing potential barrier, at which the NWP trifurcates. Two parts will move towards bigger bond lengths and lead to molecular dissociation (splitting of one white arrow into two white arrows in Figure 4.3 d)). What might happen after NWP segregation has to be determined either by experiment or quantum dynamical calculations and is the subject of this thesis. In advance of the upcoming discussion, we will find evidence in TRPES-experiments that the NWP partly returns to the FC point periodically due to the attracting character of the two B state minima. Moreover, Figure 4.3 c) does not suggest any X state-associated NWP motion, as the NWP is trapped inside the symmetrically arranged minimum. Nonetheless, as we will see later on, there might be a ground X state-related NWP motion in this potential minimum that cannot be resolved experimentally, but is predicted in the simulations. The reason for that will be discussed in subsection 4.9.1.

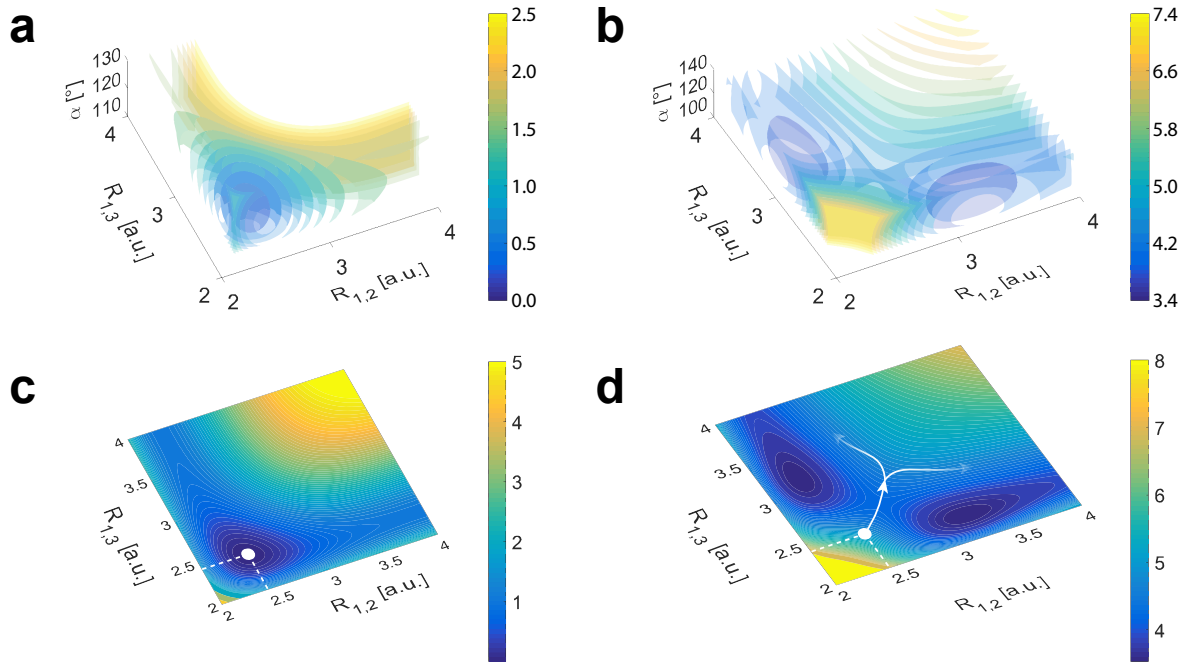


**Figure 4.3:** Illustration of **a)** the ground X and **b)** the excited B state-associated PESs of ozone, that are involved in the photodissociation process. **a)** color-coded X ground state PES as a function of the ozone degrees of freedom.  $R_{1,2}$  and  $R_{1,3}$  denote the two bonding lengths between the central oxygen atom and either of the two terminal oxygen atoms, respectively, whereas  $\alpha$  stands for the opening angle of the triatomic molecule. **b)** The same as in **a)**, but for the excited B state PES. **c),d)** Projections of the corresponding PES for fixed opening angle  $\alpha = 116.8^\circ$ . The FC point ( $R_{1,2} = R_{1,3} = 2.42 \text{ a.u.}$ ;  $\alpha = 116.8^\circ$ ) is indicated for **c)** the ground X state and **d)** also for the excited B state as a white dot. Arrows in **d)** indicate the onset of nuclear motion during ozone photodissociation and its bifurcation at a valley-ridge-inflection point. Color bars in **a)** – **d)** refer to potential energy values given in electronvolts with respect to the value on the X state PES at the FC point. All PESs were plotted using the fit functions of [68].

## 4.2 Simulations of Electronic and Nuclear Dynamics in Ozone

As pointed out at the end of the previous section, numerical simulations are indispensable for the full understanding of the ozone photodissociation. Apparently, since ozone possesses many electrons, which are correlated to each other and as the resonance Lewis structure in Figure 4.1 already suggests, the computations are expected to be computationally highly demanding. Therefore, this section is dedicated to the full quantum dynamical treatment of the nuclear and electronic motion in the ozone molecule after being excited by a 10 fs short DUV pulse at  $1 \times 10^{12} \text{ W cm}^{-2}$  and which are performed by our colleagues affiliating with the groups of *Ágnes Vibók*, *Gábor J. Halász*, *Piero Decleva* and *Fabien Gatti*. We will quickly review the underlying formalism of their simulations. Nonetheless, due to the complexity arising from a correlated multi-electron system, these quantum chemical simulations take a long time until their temporal propagation has been completed. Hence, we introduce a simplified simulation that can be run within fractions of a second and that estimates the expected population transfer from the ground X state to the excited B state. It is based upon Bloch equations [69], commonly used for the description of a two-level system. It delivers reasonable results with regard to the very first few femtosecond outcomes of the *ab-initio* simulations before nuclear motion starts and provides an estimate of the B state population probability.

### 4.2.1 Theoretical Tools for Full Ab-Initio Simulations

#### 4.2.1.1 Electric Field-Perturbed Molecular Hamiltonian

Let us start with introducing the underlying total Hamiltonian, that governs the entire dynamics in ozone and includes its interaction with an external electric field. As we have already learned in subsection 4.1.2, ozone possesses several electronic states, whose energy levels change with nuclear coordinates and are summarized as PESs for each electronic state. Thus, the presented calculations strive for solving the total molecular Schrödinger equation [27] as accurately as possible. It exclusively takes light-matter interaction into account and neglects possible non-adiabatic coupling terms between the two involved X and B electronic states of ozone (in atomic units and adapted from [70])

$$\hat{H}(\vec{r}, \vec{R}, t)\Psi(\vec{r}, \vec{R}, t) = i\hbar \frac{\partial \Psi(\vec{r}, \vec{R}, t)}{\partial t}, \quad (4.1)$$

where  $\Psi(\vec{r}, \vec{R}, t)$  denotes the total molecular wave packet and the total Hamiltonian,  $\hat{H}(\vec{r}, \vec{R}, t)$ , itself is given by

$$\hat{H}(\vec{r}, \vec{R}, t) = \hat{T}_{nuc}(\vec{R}) + \hat{H}_{el}(\vec{r}; \vec{R}) - \hat{\mu}(\vec{r}, \vec{R}) \cdot \vec{E}(t). \quad (4.2)$$

Here,  $\hat{T}_{nuc}$ ,  $\hat{H}_{el}(\vec{r}; \vec{R})$ ,  $\hat{\mu}(\vec{r}, \vec{R})$  and  $\vec{E}(t)$  designate the kinetic energy operator of the nuclei, the electronic Hamiltonian, the nuclear coordinate-sensitive dipole moment and an external electric

field, respectively. The two latter terms form the light–matter interaction term. The terms  $\vec{r}$  and  $\vec{R}$  stand, once again, for the set of electronic and nuclear degrees of freedom, respectively. In order to receive the electronic Hamiltonian from the total Hamiltonian, we merely separate the nuclear kinetic energy operator from it. Since the nuclear motion evolves on a slower timescale as compared to that of the electrons, the nuclear coordinates  $\vec{R}$  can be thought of contributing only parametrically to the electronic Hamiltonian<sup>3</sup>. Therefore, the electronic Hamiltonian consists of the repulsive electrostatic potential between nuclei, the attractive potential between positively charged nuclei and negatively charged electrons, and the kinetic energy operator of the electrons themselves. The molecular wave packet  $\Psi(\vec{r}, \vec{R}, t)$  from equation (4.1) is represented as a superposition of products between an electronic wave function  $\Phi_i(\vec{r}; \vec{R})$  and a nuclear wave packet  $\psi_i(\vec{R}, t)$ . These belong to certain electronic states,  $i = X, B$ , according to

$$\Psi(\vec{r}, \vec{R}, t) = \sum_{i=X,B} \psi_i(\vec{R}, t) \Phi_i(\vec{r}; \vec{R}). \quad (4.3)$$

In order to solve equation (4.1), it enforces the treatment of electronic and nuclear motion on an equal footing. Among a variety of theoretical approximations, the MCTDH approach is considered state of the art [71–73] and is implemented in the *MOLPRO quantum chemistry software* package [74] and used for the approximate solution of the nuclear wave packet.

#### 4.2.1.2 Local Electronic Population and Coherence at the FC point

Besides the most fundamental quantities in quantum dynamics calculations, like the molecular wave function or total electric-field perturbed molecular Hamiltonian, there are some other quantities which should at least be mentioned here. They can directly be deduced from the molecular wave packet and are absolutely essential for the proper understanding of the coherent photochemical wave packet dynamics. Moreover, their knowledge proves to be beneficial in the simulation of TRPES-spectrograms, which in turn can be used to compare them to experimentally measured ones. These items, to which we will return in the next subsection 4.2.1.3, are the local electronic population  $\rho_{ii}(t)$  and the local electronic coherences  $\rho_{ij}(t)$ , ( $i \neq j$ ) around the Franck-Condon point  $\vec{R}_{FC}$  and are given by

$$\rho_{ij}(t) = \frac{\psi_i^*(\vec{R}_{FC}, t) \psi_j(\vec{R}_{FC}, t)}{\sum_{l=X,B} |\psi_{(l)}(\vec{R}_{FC}, t)|^2}. \quad (4.4)$$

With these quantities at hand, it is possible to keep track of the nuclear wave packet density at the FC point on both the X and B state-related PESs. As we will see later on (section 4.8), they already carry most of the necessary information for interpretation of the experimental results to a very high degree. Yet, as the experimental results are based upon photoionization, we need to

---

<sup>3</sup>The separation of the nuclear kinetic energy operator is only justified at nuclear coordinates far away from CIs, as electronic and nuclear degrees can be considered independent. Obviously, this does not hold true in the vicinity of CIs, where the electronic and nuclear dynamics are strongly coupled.

know the ionization probabilities before being able to derive theoretical TRPES-spectrograms. These are introduced next.

### 4.2.1.3 Dyson Orbitals and Photoionization Probabilities

The ionization probabilities  $I_{jk}$  are proportional to the squared norm of the so-called *Dyson orbitals*, according to

$$I_{ik} \propto \langle \phi_{i,k}^{Dyson} | \phi_{i,k}^{Dyson} \rangle, \quad (4.5)$$

which, in turn, are expressed by

$$\phi_{i,k}^{Dyson}(\vec{r}; \vec{R}) = \sqrt{N} \int d\vec{r}_2 \dots d\vec{r}_N \phi_i^{el}(\vec{r} = \vec{r}_1, \vec{r}_2, \dots, \vec{r}_N; \vec{R}) \times \phi_k^{cat*}(\vec{r}_2, \dots, \vec{r}_N; \vec{R}). \quad (4.6)$$

Here,  $\phi_i^{el}$  and  $\phi_k^{cat}$  denote the  $N$ -electron electronic wave function of the neutral ozone molecule in any state  $i$  and the  $N - 1$ -electron electronic wave function of its cation in any state  $k$ , respectively, after removal of a single electron. Just like the electronic multi-electron wave function, the Dyson orbitals depend parametrically on the nuclear coordinates  $\vec{R}$  and can be understood as an effective one-electron *molecular orbital* (MO), from which an electron has been removed during photoionization, i.e. the wave function of the hole that is created within the neutral molecule. This picture is only valid for an uncorrelated Hartree-Fock wave function of the neutral and becomes more complicated in cases, where more than one configuration<sup>4</sup> contribute to the total wave function of the neutral molecule or its cation and are usually expressed in terms of Slater determinants.

For the time being and for the sake of the current discussion, we are primarily interested to obtain an approximate photoelectron spectrogram  $I_{ik}(\epsilon, \tau)$ , that is a function of delay time  $\tau$  after  $X \rightarrow B$  transition and of photoelectron kinetic energy  $\epsilon = \epsilon_{ik} = E_{photon} - (E_k - E_i)$ . Here,  $E_{photon}$ ,  $E_k$  and  $E_i$  denote the photon energy of the ionizing XUV probe photon, the energy of the final state of the cation and the initial state of the neutral molecule, respectively. Including the angle dependence  $\theta$  on photoelectron emission, measured to the ionizing XUV polarization, it is given by (see [70, 75, 76] for more detailed information regarding the calculation of these quantities and references therein)

$$I_{ik}(\epsilon, \theta, \tau) = \sum_k \rho_{kk}(\tau) I_k(\epsilon, \theta), \quad (4.7)$$

$$I_k(\epsilon, \theta) = \sum_j G_{jk}(\epsilon_{jk}) \frac{\sigma_{ik}(\epsilon_{jk})}{4\pi} [1 + \beta_{jk}(\epsilon_{jk}) P_2(\cos \theta)]. \quad (4.8)$$

---

<sup>4</sup>In this context, *configuration* refers to a certain set of populated MOs. Such a configuration does not need to consist of the lowest few, energy-ordered MOs, but is also allowed to possess higher-lying MOs at the expense of lower-lying MOs in the sense of electron-hole excitation or multiples thereof.

In equation (4.8),  $G_{jk}(\epsilon_{jk})$  refers to a Gaussian function mimicking the XUV probe pulse spectral bandwidth that is used to ionize a randomly oriented sample.  $\sigma_{ik}(\epsilon_{jk})$  and  $\beta_{jk}$  stand for the ionization cross section and ionization asymmetry parameter, respectively.  $P_2(\cos\theta) = \frac{1}{2}(3\cos^2\theta - 1)$  is the second order Legendre-polynomial.

#### 4.2.1.4 Theoretical Results

Now, we quickly present the most important results of our colleagues *Ágnes Vibók, Gábor J. Halász, Piero Decleva* and *Fabien Gatti* and their colleagues and which rely on the previously defined quantities. Figure 4.4 a) shows the simulated temporal evolution of the B state population, taking a 10 fs FWHM DUV pump pulse into account, that is centered around 268 nm and carries a pulse energy of  $(2.0 \pm 0.5) \mu\text{J}$ . Thus, it should be possible to achieve a 40% excitation probability for the B state, although this value strictly applies to ozone molecules only whose transition dipole moment is parallel to the DUV pump pulse polarization. Figure 4.4 b), instead, shows the local coherence as a function of delay time and around the FC point between the part of the nuclear wave packet that is left in the ground X state and the part that is promoted into the B state. It clearly reveals that the coherence builds up within 20 fs, because shortly after excitation both nuclear wave packets share identical positions in nuclear coordinate space before nuclear motion sets in. Around 0 fs delay time, the coherence decreases and pauses temporarily at a constant value between 10 fs and 20 fs before it keeps dropping down to zero coherence and is followed by a small transient increase around 40 fs. We will learn about this evolution in more detail in section 4.8 and give a physical interpretation for this behavior in terms of nuclear wave packet trajectories on the excited B state PES. Figure 4.4 c), in turn, displays the B state-related nuclear wave packet density. It is obtained by integrating out the angle and vibrational degrees of freedom, reducing it to a function of the dissociative coordinate only. Apparently, the majority of the excited B state nuclear wave packet density remains localized around the FC point for nearly all delay times, although by 20 fs part of it has already left the FC point region, proving successful ozone photodissociation.

#### 4.2.2 Three-Level Simulation

Without the need to approach our colleagues every time, we implemented a simulation of a simple three-level quantum system, where the levels are assumed to represent the ground  $X$  ( $^1A_1$ ), the excited  $B$  ( $^1B_2$ ) and, optionally, the bright Chappuis 1 state  $C1$  ( $^1B_1$ ). The latter exclusively absorbs light in the NIR spectral domain and is therefore neglected for the interaction of the three-level quantum system with a pure DUV pump pulse. The three-level simulation does not call for supercomputers or computer clusters, which are necessary for the previously described and more elaborate full quantum mechanical approach (subsection 4.2.1), but can be evaluated rather quickly within fractions of a second. As mentioned, it relies on the temporal propagation of a three-level quantum system under the influence of electric fields in the DUV or NIR spectral domain, which are either resonant with the  $X \rightarrow B$  or  $X \rightarrow C1$  transition. Nonetheless, the three-level-simulation already provides — at least within the very first few femtoseconds, where negligence of nuclear motion is legitimate — quite useful information on the expected probability

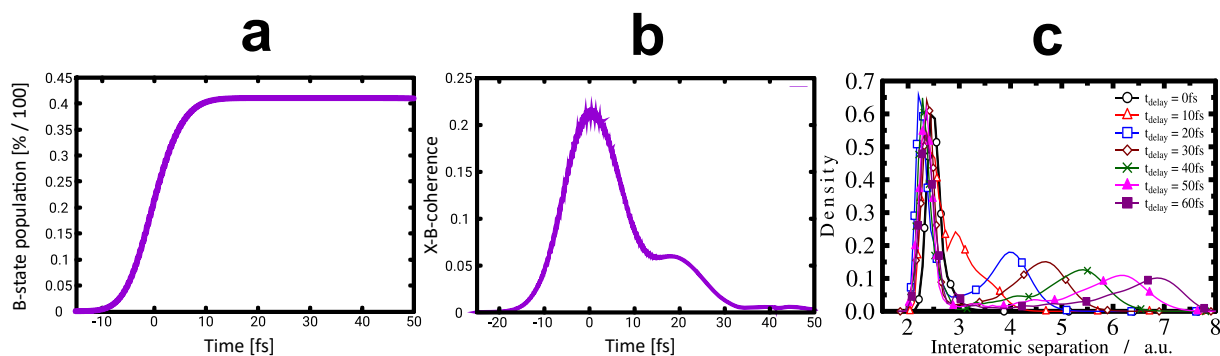


**Figure 4.4:** **a)** Simulated temporal evolution of the B state population of ozone for interaction with a 268 nm, 10 fs FWHM DUV pulse, carrying  $(2.0 \pm 0.5) \mu\text{J}$  pulse energy. 40% population of the B state is achievable for aligned ozone molecules. **b)** Local coherence between the ground X state and excited B state electronic–nuclear wave packet at the FC point. **c)** Angle and vibrational coordinate integrated B state-related nuclear wave packet density as a function of the dissociative coordinate. At around 20 fs after maximum excitation, a significant part has already left the FC region, indicating completed ozone photodissociation. *Adapted with courtesy of Ágnes Vibók and Gábor J. Halász.*

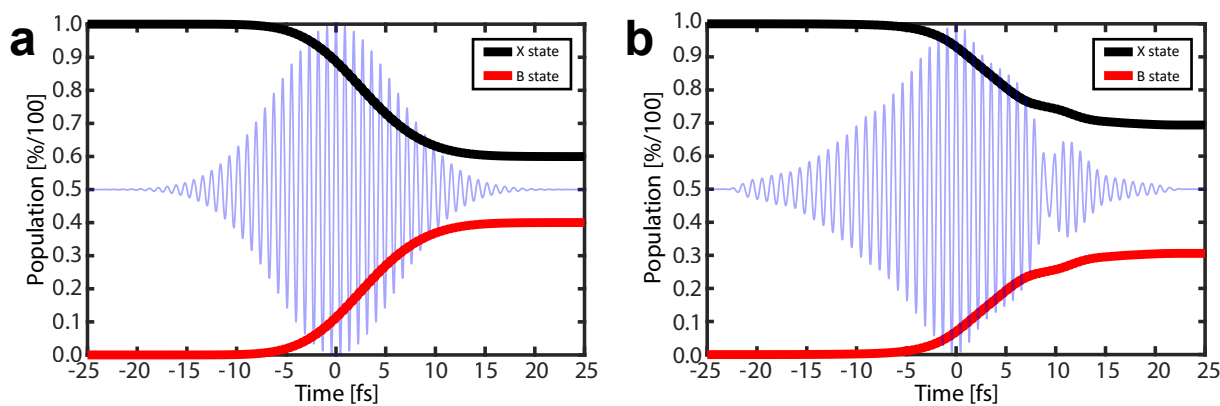


**Figure 4.5:** Simulated temporal evolution of X (black solid line) and B (red solid line) state-associated population probability, using a three-level simulation for **a)** a 10 fs FWHM DUV pulse and **b)** the experimental DUV pulse (blue solid lines) as retrieved from a DUV-TG-FROG measurement (subsection 4.5.3). In both cases, the pulse parameters are identical, although their exact pulse shapes differ from each other. For more information on the computational details, see main text.



of the B state population for varying DUV pulse energy and pulse shape, although it neglects nuclear motion completely. However, it allows us to estimate the population probabilities, if the experimental parameters are supposed to change and we want to know how these relate to the experimental observable.

Formally, the unperturbed Hamiltonian of the three-level-system  $\hat{H}_0$  and the light-matter interaction term  $\hat{V}(t)$  are written down as

$$\hat{H}_0 = \hbar \begin{pmatrix} 0 & 0 & 0 \\ 0 & \omega_{NIR} & 0 \\ 0 & 0 & \omega_{UV} \end{pmatrix}, \quad (4.9)$$

$$\hat{V}(t) = -\hat{\vec{d}} \cdot \hat{\vec{E}}(t) = - \begin{pmatrix} 0 & \vec{d}_{01} \cdot \vec{E}(t) & \vec{d}_{02} \cdot \vec{E}(t) \\ \vec{d}_{10} \cdot \vec{E}(t) & 0 & \vec{d}_{12} \cdot \vec{E}(t) \\ \vec{d}_{20} \cdot \vec{E}(t) & \vec{d}_{21} \cdot \vec{E}(t) & 0 \end{pmatrix}, \quad (4.10)$$

where  $\vec{d}_{ij} = \vec{d}_{ji}^*$  are the dipole moments between states  $i$  and  $j$ , and  $\vec{E}(t)$  denotes the electric field that may be comprised of a superposition of an NIR and a DUV pulse. The former quantities, i.e. the dipole moments, were adjusted manually to match the results obtained from the more elaborate calculations of our colleagues [77,78]. Therefore, the dipole moment  $\hat{d}_{02}$  for the Hartley band transition amounts to 1.6 Debye. Moreover, the level indexing is chosen such that  $i = 0$  refers to the ground X state,  $i = 1$  to the Chappuis 1 C1 state and  $i = 2$  to the Hartley B state.

With these operators at hand, we solve the *Lindblad*-equation, using the density matrix  $\rho$  instead of simple wave functions. Further, we neglect relaxation and loss terms and the equation of motion is defined by

$$\dot{\rho} = -\frac{i}{\hbar} [\hat{H}(t), \rho], \quad (4.11)$$

where  $[\cdot, \cdot]$  symbolizes the quantum mechanical commutator. The output of the three-level simulation in terms of the temporal evolution of the X/B state-related population is shown in Figure 4.5. The simulation assumes a DUV pump pulse, centered around 268 nm, and carries a pulse energy of approximately 2  $\mu$ J. It is further assumed to be focused down to a beam waist radius of  $w_0 = 50 \mu\text{m}$ . Figure 4.5 a) displays the  $X \rightarrow B$  population transfer of a pure 10 fs Gaussian DUV pulse, while Figure 4.5 b) depicts the same for the experimental DUV pulse of comparable pulse duration, as it is retrieved from a DUV-TG-FROG trace (subsection 4.5.3). The experimental generation and characterization of the latter is explained in more detail in section 4.5. Apparently, the simulations suggest that the population transfer behaves similarly in both cases, with the pulse in b) showing a 10% smaller  $X \rightarrow B$  population transfer. Once again, we would like to point out that the population transfer refers to fully aligned ozone molecules. Consequently, the B state population has to be multiplied by a factor of 1/3 when referring this value to randomly aligned ozone molecules. The latter case reflects our experimental condition and yields a maximum B state population of roughly 10% in case of Figure 4.5 b).

## 4.3 Group Theoretical Aspects

Apart from the mere optimization of the B state population, there is another important detail that must not be forgotten and without which the time-resolved excited state dynamics in ozone would hardly be detectable, that is the angular distribution of photoelectron emission. It is dictated by the molecular symmetry and in general by molecular selection rules regarding optical transitions. Moreover, the exact molecular symmetry governs the symmetry and shape of molecular orbitals with regard to the molecular frame and is a consequence of the fact that they have to reflect the molecular symmetry itself. These molecular orbitals even get classified after so-called *irreducible representations* of the point group that the molecule is assigned to (for more information on groups, classes, and irreducible representations refer to the appendix B). The following discussion strives for deriving qualitative arguments on how the experiment has to be designed geometrically in order to maximize the emission yield of photoelectrons in pump-probe TRPES-experiments. Basically, the photoelectrons emanate from either the ground or excited state of ozone, but also from states of photodissociation products, like atomic or diatomic oxygen. Specifically, the current approach borrows lessons learned from group theory.

The current section is structured as follows:

In the first subsection we will quickly review the  $C_{2v}$  point group, which the ozone molecule belongs to for equal bond lengths.

The second subsection will briefly discuss the cation states of ozone and the role, they play in photoionization events.

This discussion is followed by a description of the angular distribution of photoelectron emission for certain transitions. Finally, we will conclude with a derivation of an experimental geometry in terms of DUV-/XUV-polarization that is capable of detecting excited state dynamics in ozone. On these grounds, we will exemplify the procedure by looking at two scenarios. The very same approach can be transferred to other molecules, but the exact molecular point group must explicitly be taken into account.

### 4.3.1 The $C_{2v}$ Point Group

As pointed out in the introductory paragraph of this chapter, the  $C_{2v}$  point group reflects the symmetry of the ozone molecule. Unfortunately, we have not given a definition of it yet. This is why we make up for it here. Based upon the group theoretical concepts presented in appendix B, we would like to illustrate their application to the  $C_{2v}$  point group. Let us have a look at the ozone molecule in its molecular-frame coordinate system, where the x-axis is perpendicular to and the z-axis lies *in* the molecular plane, where the latter bisects the opening angle of the ozone molecule, as depicted in Figure 4.6.

By symmetry operations we mean those transforming the molecule in such a way that the molecule is mapped onto itself and so that it is indistinguishable from its former arrangement as an entity, although some atoms might interchange positions. Obviously, in the case of the ozone molecule in  $C_{2v}$  symmetry, the set of possible symmetry operations consists of 4 elements:  $G = \{E, C_2, \sigma_v, \sigma'_v\}$ . Here,  $E$  denotes the identity transform, leaving the molecule and all its atoms unchanged. The symbols  $\sigma_v$  and  $\sigma'_v$  denote the two mirror planes from which the former

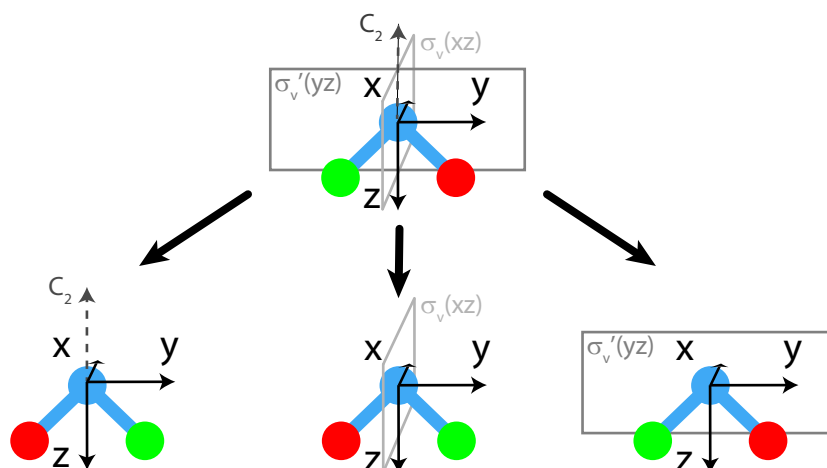


**Figure 4.6:** Illustration of the action of the  $C_{2v}$  point group symmetry operations  $G = \{E, C_2, \sigma_v, \sigma'_v\}$  on the ozone molecule in its molecular frame coordinate system. *Topmost subplot:* identity operation  $E$  serves as a reference. *Bottommost subplots:* principal rotation axis  $C_2$  (*left*) and mirror planes  $\sigma_v$  (*middle*) and  $\sigma'_v$  (*right*). All oxygen atoms are assumed to be distinguishable and color-coded (blue, green and red circles) in order to keep track of their positions.

bisects the molecule and which is perpendicular to the molecular plane and the latter lies in the molecular plane. The operation  $C_2$  symbolizes the principal twofold ( $180^\circ$ ) rotation about the z-axis. One can easily prove that this set of elements forms a group in a mathematical sense, which is identical with the statement that the consecutive execution of any number of symmetry operations can be replaced by the execution of a single symmetry operation, i.e. an element of the group  $G$  itself. Moreover, each element in the  $C_{2v}$  point group generates a *class* by itself, because every element is only conjugated to itself. In addition to the present point group, there exists a vast number of other groups with different symmetry operations. For an overview, see for example [79].

The consecutive application of group elements (i.e. symmetry operations) does not necessarily have to be commutative, but are allowed to depend on the order in which they are applied. This immediately becomes clear when recognizing that the group operation is represented here by a matrix multiplication, which is generally non-commutative. The ordered output is usually summarized in form of a *group multiplication table*, like the one shown in Table 4.1.

Since it is often hard to find an explicit matrix representation of an arbitrary group, one is often content with the *characters* of group elements  $R \in G$ , that is just a number. These characters are summarized for all these classes (columns) in the so-called *character table* and attributed to certain irreducible representations (rows), similar to the group multiplication table. It is depicted in Table 4.2. In subsection 4.3.3, we will show how we will take advantage of this character table in order to deduce the angular distribution of photoelectron emission.

$C_{2v}$	$E$	$C_2$	$\sigma_v$	$\sigma'_v$
$E$	$E$	$C_2$	$\sigma_v$	$\sigma'_v$
$C_2$	$C_2$	$E$	$\sigma'_v$	$\sigma_v$
$\sigma_v$	$\sigma_v$	$\sigma'_v$	$E$	$C_2$
$\sigma'_v$	$\sigma'_v$	$\sigma_v$	$C_2$	$E$

**Table 4.1:**  $C_{2v}$  point group multiplication table. The result of the consecutive execution of symmetry operations refers to the case where these operations, shown as columns, are applied prior to those from the rows. In this particular case the order does not matter, as the group is commutative, but needs not to apply in general.

$C_{2v}$	$1E$	$1C_2$	$1\sigma_v$	$1\sigma'_v$		
$A_1$	1	1	1	1	$z$	$x^2, y^2, z^2$
$A_2$	1	1	-1	-1	$R_z$	$xy$
$B_1$	1	-1	1	-1	$x, R_y$	$xz$
$B_2$	1	-1	-1	1	$y, R_x$	$yz$

**Table 4.2:**  $C_{2v}$  point group character table. The set of irreducible representations (rows) of all groups always contains the so-called *totally-symmetric representation*  $A_1$  and exclusively carries "1"s. The labelling of irreducible representations follows the *Schoenflies*-nomenclature [80]. The number of group elements per class (columns) is given in the header of the table. Each class is represented by a class representative.  $C_{2v}$  is an *Abelian* group, so every group element forms a class by itself. The impact of symmetry operations on rotations  $R_{x,y,z}$  and coordinate axes  $x, y, z$  (two rightmost columns) are attributed to specific irreducible representations.

### 4.3.2 Cation States of Ozone

Owing to the circumstance that the B state-related dynamics cannot be probed directly, but rather indirectly, by ejection of a photoelectron through XUV probe pulse induced photoionization, we have to cast an eye on the set of B state-related cation states  $E_j$  numbered by an index  $j$ . These are the energy eigenstates of the positively and singly charged ozone molecule after removal of an electron and are also characterized by their irreducible representation. If the ground X and excited B states, respectively, are considered as the initial states in the process of photoionization, the cation states can be thought of as final states. A list of the 19 lowest cation states of ozone, which were calculated by our colleagues *Piero Decleva*, *Ágnes Vibók* and colleagues [70], is shown in increasing order of their ionization potential (except for 14<sup>th</sup> and 15<sup>th</sup> cation states) in Table 4.3. It includes their irreducible representation, their ionization potentials  $E_j - E_{X/B}$ , measured from either the ground X state or excited B state of the neutral molecule, and their ionization probabilities  $I_{jk}(X/B)$ , as introduced in subsection 4.2.1.3. As pointed out above, we are primarily interested in detecting excited state-related photoelectrons from the B state. Obviously, by looking at Table 4.3, the third cation state (B-3 ( $1^2A_2$ )) is supposed to contribute most strongly to the photoionization signal, that belongs to the excited B state. So, we will especially focus on this one when deriving an experimental setup for the

pump-probe experiment in order to render its angular distribution in photoelectron emission events detectable.

	cation states (j)	$E_j - E_X$ (eV)	$I_{jk}(X)$	$E_j - E_B$ (eV)	$I_{jk}(B)$
1	( $1^2A_1$ )	12.38	0.72	6.59	0.08
2	( $1^2B_2$ )	12.51	0.69	6.72	0.09
3	( $1^2A_2$ )	13.20	0.71	7.42	0.41
4	( $1^2B_1$ )	14.14	0.00	8.36	0.00
5	( $2^2A_2$ )	14.45	0.00	8.66	0.00
6	( $2^2B_2$ )	15.18	0.01	9.40	0.01
7	( $2^2A_1$ )	15.58	0.00	9.80	0.02
8	( $2^2B_1$ )	16.35	0.29	10.56	0.24
9	( $3^2A_2$ )	16.50	0.00	10.72	0.00
10	( $3^2B_1$ )	17.10	0.06	11.32	0.02
11	( $3^2A_1$ )	17.33	0.27	11.54	0.32
12	( $3^2B_2$ )	17.65	0.13	11.87	0.41
13	( $4^2B_2$ )	18.18	0.01	12.41	0.03
14	( $4^2A_2$ )	18.64	0.00	12.85	0.00
15	( $4^2B_1$ )	18.61	0.00	12.83	0.00
16	( $4^2A_1$ )	19.07	0.01	13.29	0.01
17	( $5^2B_2$ )	19.61	0.04	13.83	0.02
18	( $5^2A_1$ )	19.48	0.26	13.70	0.11
19	( $6^2B_2$ )	19.94	0.42	14.16	0.04

**Table 4.3:** Calculated *ab-initio* ionization potentials in MRCI-SD(Q) level of theory. The 19 lowest-lying cation states with respect to either the ground state ( $X$ ) or the Hartley band ( $B$ ) at the FC point. The quantity  $I_{jk}$  denotes the square of the Dyson norms, using CASSCF/aug-cc-pVQZ level of theory. Adapted from [70].

### 4.3.3 Angular Distribution of Photoelectron Emission

Although the previous discussion is kept mainly formal, we would like to explicitly apply group theoretical tools to determine whether the photoelectron continuum wave function for a specific photoionization process might be detectable. The tools used here are based upon those in [81]. This approach is particularly important in the case of ozone, as the strength of the photoionization process is to some extent proportional to the norm of the Dyson orbital between some initial and any final state and its angular distribution. Moreover, the continuum wave function of the ionized photoelectron needs not be totally symmetric, but is allowed to be a nonuniform function of angle, exhibiting nodal lines or nodal planes. For the latter the knowledge of the molecular symmetry is indispensable. The Dyson orbital, that is represented here as  $\phi_{IF}^D$ , between an  $N$ -electron initial state ( $I$ ) with wave function  $\phi_I^{(N)}$  and an  $N - 1$ -electron final state ( $F$ ) with wave function  $\phi_F^{(N-1)}$  is defined as their overlap integral, just like in equation (4.6). There, the integration runs across  $N - 1$  electronic space and spin degrees of freedom (subsub-

section 4.2.1.3). Now, the objective of the current discussion can be reduced to the calculation of the *photoionization cross section*  $\sigma_{IFf}(E_k)$ , using a certain polarization for the ionizing XUV probe pulse  $\hat{\epsilon}$  under photoelectron emission, the latter represented in form of a continuum wave packet by  $\phi_{kf}^{(1)}$ . It is defined by a momentum quantum number  $k$  and another quantum number  $f$ , that is necessary to disentangle degenerate states associated with  $k$ , which in turn relates to a kinetic energy  $E_k = \frac{\hbar^2 k^2}{2m_e}$ . It is known [82, 83] that the photoionization cross section  $\sigma_{IFf}(E_k)$  in the single-active-electron approximation and in the sudden ionization limit is proportional to

$$\sigma_{IFf}(E_k) \propto \left| \langle \phi_{F,kf}^{(N)} | \vec{\mu} \cdot \hat{\epsilon} | \phi_I^{(N)} \rangle_N \right|^2 \propto \left| \langle \phi_{kf}^{(1)} | \vec{r} \cdot \hat{\epsilon} | \phi_{IF}^D \rangle_{\vec{r}} \right|^2, \quad (4.12)$$

where  $\vec{\mu}$  is the dipole moment of the sample and  $\vec{r}$  is again the electronic space coordinate.  $\phi_{F,kf}^{(N)}$  summarizes the total wave function consisting of both the cationic final state  $F$  and the continuum wave function  $\phi_{kf}^{(1)}$  of the photoelectron with quantum numbers  $k$  and  $f$ . Integration is performed over the set of all  $N$  electronic coordinates  $\vec{r}$ .

Additionally, if one is interested in the angular distribution and not in the total photoionization cross section, one could simply restrict the integration in equation (4.12) to the radial coordinate  $r = \sqrt{\vec{r}^2}$  and write the photoionization cross section down in terms of polar coordinates  $(\theta, \phi)$  in the following way [82]

$$\sigma_{IFf}(E_k, \theta, \phi) \propto \left| D_{kf}^{IF}(\theta, \phi) \right|^2, \quad (4.13)$$

$$D_{kf}^{IF}(\theta, \phi) = \langle \phi_{kf}^{(1)} | \vec{r} \cdot \hat{\epsilon} | \phi_{IF}^D(r, \theta, \phi) \rangle_r, \quad (4.14)$$

where we have expressed the angular part of the photoionization cross section in equation (4.13) as the modulus square of the angular part of the so-called *photoelectron matrix element*  $D_{kf}^{IF}(r, \theta, \phi)$ . The latter contains all the information to derive the angular distribution of photoelectron emission.

Now, we want to fully devote ourselves to the observability of this photoelectron continuum wave function in pump-probe TRPES-experiments along certain directions in the molecule-fixed coordinate system. In order not to make the photoionization cross section  $\sigma_{IFf}(E_k)$  (equation (4.12)) vanish at all, it must contain — in the language of group theory — the *totally symmetric irreducible representation*  $A_1$  (Table 4.2). Consequently, this would yield a photoelectron continuum wave function  $\phi_{kf}^{(1)}$  that is more likely to be detected [81] and relates to a certain angular distribution of photoelectron emission, compliant with equations (4.13) – (4.14).

As of now, we do not want to calculate the integrals in equations (4.13) – (4.14) explicitly, but take advantage of the strengths of group theory in predicting the irreducible representation of the Dyson orbital. Knowing its irreducible representation allows us to determine the irreducible representation of the photoelectron continuum wave function, which we are interested in to observe

excited state dynamics in ozone. The irreducible representation of the Dyson orbital is simply given by the row-wise and column-after-column multiplication of the corresponding characters from Table 4.2 of its composing initial state and final state wave functions. For example, if the initial wave function of the neutral  $I$  was characterized by the irreducible representation  $A_2$  and the final wave function of its cation  $F$  by the irreducible representation  $B_1$ , we would multiply their characters (Table 4.2) element-wise, i.e.  $(1, 1, -1, -1) \odot (1, -1, 1, -1) = (1, -1, -1, 1)$ , where " $\odot$ " stands for the entrywise *Hadamard*-product [84]. The result must usually be decomposed into a linear combination of character vectors (equation (B.6) of appendix B), associated with an irreducible representation, but in the case of  $C_{2v}$  point group, it reduces to a character vector of a single irreducible representation. Here, the result  $(1, -1, -1, 1)$  refers to the characters of the  $B_2$  irreducible representation and is commonly written in form of a direct product, like  $A_2 \otimes B_1 = B_2$ , where " $\otimes$ " symbolizes the direct product, as defined in equation (B.7) of appendix B.3. It should be stated that for the current point group, the direct product of any irreducible representation with itself yields the totally symmetric irreducible representation  $A_1 = A_{1/2} \otimes A_{1/2} = B_{1/2} \otimes B_{1/2}$ .

Regarding our aspiration of finding an experimental design, that is capable of rendering photoelectron continuum wave function detectable, and for the sake of the upcoming discussion, we want to keep our mind on the three lowest B state-related cation states from Table 4.3. In particular, we want to focus on the third cation state B-3 ( $1^2A_2$ ), because it is expected to contribute the strongest, based upon its huge squared Dyson norm ( $I_{jk} = 0.41$ ), as compared to the remaining B state-associated cation states.

Similarly, in order to optically excite the ozone molecule from its ground X ( $1^1A_1$ ) state into the excited B ( $1^1B_2$ ) state via a DUV pump photon, the dipole transition matrix element  $\langle X | \vec{\mu} \cdot \vec{\epsilon} | B \rangle$  for this process must not vanish either. Therefore, in order to make this integral contain the  $A_1$  irreducible representation, the product of the transition dipole moment and the DUV laser polarization  $\vec{\mu} \cdot \vec{\epsilon}$  has to belong to the  $B_2$  irreducible representation so that  $\langle X | \vec{\mu} \cdot \vec{\epsilon} | B \rangle \cong A_1 \otimes B_2 \otimes B_2 = A_1 \otimes A_1 = A_1$ . Consequently, the B state can *exclusively* be excited via a DUV pump pulse polarization pointing in y-direction of the molecular frame. Following the same argument, it is impossible to populate a state from the ground X state ( $1^1A_1$ ) that belongs to the  $A_2$  irreducible representation, since the possible laser polarization refers to either x ( $B_1$ ), y ( $B_2$ ) or z ( $A_1$ ), respectively. Hence, the resulting dipole integral never contains the  $A_1$  irreducible representation and is therefore dipole-forbidden. Only magnetic dipole transitions ( $R_z$ ) or electric quadrupole transitions ( $xy$ ), all attributed to the  $A_2$  irreducible representation, can drive this particular transition (Table 4.2).

In advance of the subsequent discussion, let us first have a look at what the experimental setup is going to look like (Figure 4.7). The pulse train, consisting of DUV pump pulse (blue solid line) and XUV probe pulse (purple solid line), enters the interaction region along the laboratory x-axis from the upper right corner. A randomly oriented ensemble of ozone molecules is released into the interaction region along the laboratory y-axis through a graphite-coated glass nozzle. The ionized photoelectrons, which carry information on the entire molecular dynamics in ozone, are collected along the laboratory z-axis by a TOF detector (subsection 3.2.3).

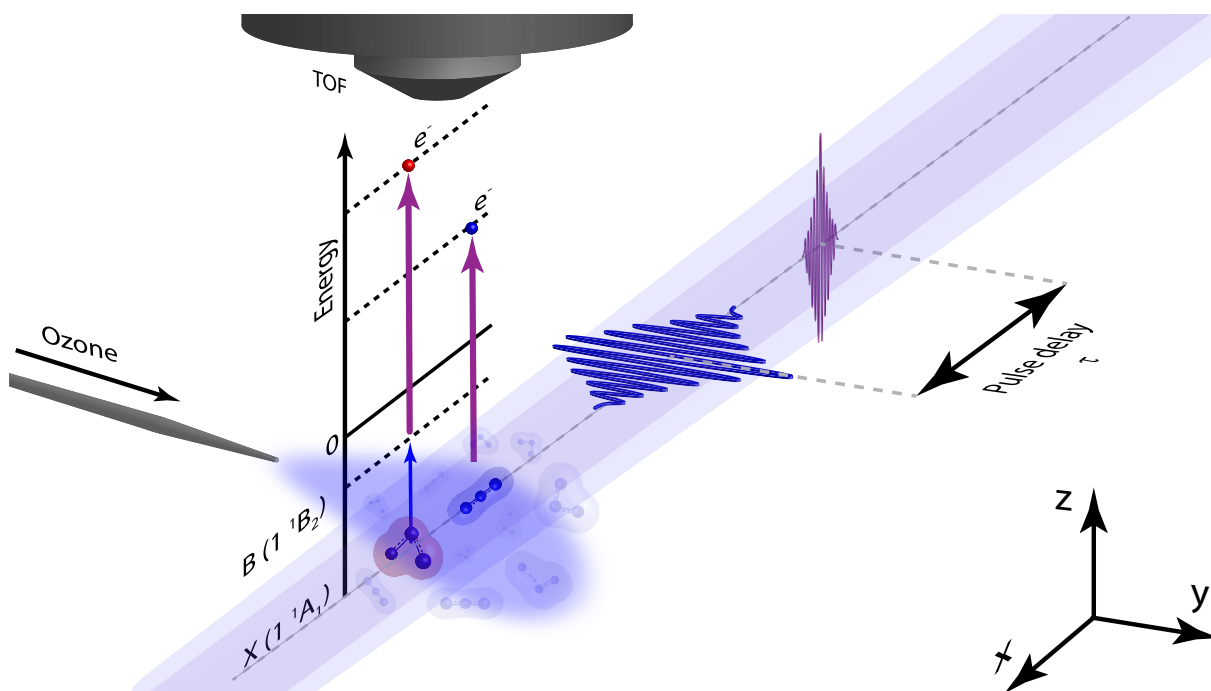


**Figure 4.7:** Experimental geometry as used for the pump–probe TRPES-measurements on ozone. The pulse train, consisting of the DUV pump pulse (blue solid line) and the XUV probe pulse (purple solid line), comes from the upper right corner (x-axis) and interacts with the ozone sample. The latter exits a graphite-coated glass nozzle (y-axis) in a randomly oriented fashion, as we forgo molecular alignment. The entire molecular dynamics are detected by an electron time-of-flight (TOF) detector (z-axis).

From now on, we always require that detection of ozone-related electronic and molecular dynamics has to take place perpendicular to the DUV pump pulse polarization in order not to compete with laser-induced photoelectron momentum shifts by parallel *attosecond streaking* (section A.1 of appendix A). If these streaking-shifts were not prohibited, our measurements would otherwise be compromised by them and it would be impossible to discriminate between momentum shifts induced by molecular dynamics or streaking. Considering the constraints with regard to the used polarization of the XUV probe and the DUV pump pulses, only two possible experimental designs come into consideration:

The first option (I) features a parallel polarization of the ionizing XUV and the DUV pulses ( $XUV \parallel DUV$ ). There, one measures the released photoelectrons in a plane that is perpendicular to the laser polarization. The second possibility (II) comprises a detection of the ejected photoelectrons alongside the XUV polarization, while being perpendicular to the DUV polarization ( $XUV \perp DUV$ ). As we will see soon, only the second option (II) of crossed XUV–DUV polarization — indicated in Figure 4.7 — proves itself promising in detecting B state-related electronic and nuclear dynamics, whilst streaking-induced momentum shifts are minimized.

Let us start with the discussion of option (I), i.e. parallel XUV–DUV polarization. Since the



ozone molecule gets excited via a  $y$ -polarized DUV pump photon (in the molecular frame) and is probed by a  $y$ -polarized XUV-photon and as we are mainly interested in excited ozone molecules, we *always* need to detect the photoelectrons along any direction within the molecular  $x$ - $z$ -plane. Because the molecular and laboratory frames need not coincide, regarding their orientation, they do coincide for ozone molecules, which are accidentally aligned like the red molecule (except for a rotation about the common  $y$ -axis in Figure 4.7) and to which we restrict our discussion here. As stated above, even a rotation about the molecular  $y$ -axis (identical with the laboratory  $y$ -axis) does not change much in terms of the arguments of the current discussion, because orientation of the  $x$ - $z$ -plane is maintained.

Getting back to the current discussion of the first case (I), Figure 4.8 a) tells us that the continuum wave function for the most intense, excited state-related photoionization process  $B(1^1B_2) \xrightarrow{y-pol.} B^+(1^2A_2)$  (cation state B-3 in Table 4.3) belongs to the  $A_2$  irreducible representation (column "y-pol.", lowermost row). Generally, the continuum wave function of the ejected photoelectron is expanded in a Taylor series of partial waves. Figure 4.8 b) depicts their angular distribution as a function of angular momentum quantum number (columns) and depending on their irreducible representation (rows). In case of the  $A_2$  irreducible representation, we conclude that the  $x$ - $z$ -plane is a nodal plane, effectively reducing the detection yield of photoelectrons along directions within this plane. Consequently and due to low photoelectron yield, we discard the experimental geometry (I) of parallel XUV–DUV polarization, i.e.  $y$ -polarization.

The situation changes when looking at the second case (II) of crossed XUV–DUV polarization. As the DUV polarization is always assumed to point along the molecular  $y$ -axis, the XUV polarization is allowed to point along any direction within the  $x$ - $z$ -plane, which is identical with the TOF-axis orientation in the laboratory frame. Now, Figure 4.8 a) predicts either the  $A_1$  or the  $B_1$  irreducible representation for the photoionization process  $B(1^1B_2) \xrightarrow{x/z-pol.} B^+(1^2A_2)$  (columns "x-pol."/"z-pol."). By comparison with Figure 4.8 b), we conclude that some of the angular distributions referring to either  $A_1$  or  $B_1$  lack nodal lines or nodal planes within the  $x$ - $z$ -plane. This shows that we found an experimental geometry in which the photoelectron yield is inherently higher than compared to the first geometry (I). This derivation of an experimental configuration was possible by exploiting group theoretical means without the exact knowledge of the photoelectron continuum wave function and solely results from symmetry considerations.

## 4.4 Few-Femtosecond XUV Probe Pulse Generation

After having discussed the detection of photoelectrons emerging from the excited B state of neutral ozone by means of group theoretical arguments, we now want to concentrate our attention on the required energy resolution, given by the bandwidth of the XUV probe pulse spectrum. Although some of the X and B state-associated cation states (in particular: X-1 to X-3 and B-3; Table 4.3) are well separated from each other in terms of energy, the XUV bandwidth cannot be chosen arbitrarily due to the following reason: Measuring the fastest processes in molecules or solids and trying to unveil their femtosecond or even attosecond dynamics is at the heart of pump–probe experiments. For retaining a decent spectral and temporal resolution of these

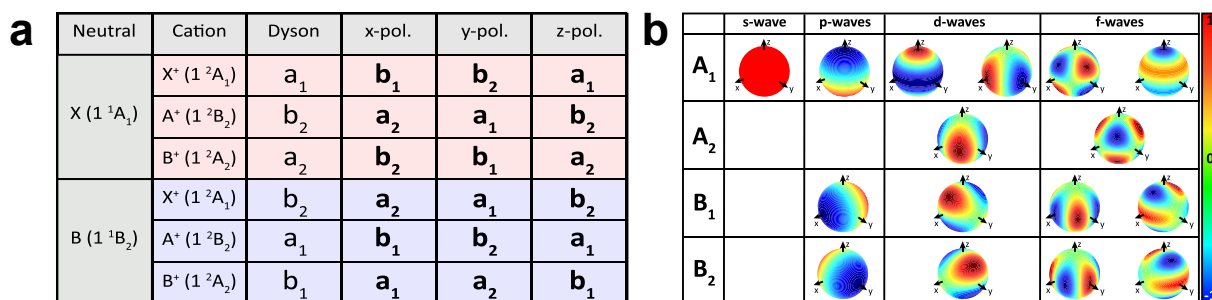


**Figure 4.8:** **a)** Irreducible representations of continuum wave functions (bold characters), dependent on the state which the XUV pulse ionizes photoelectrons from (first column), cation channels (second column) and XUV-polarization in the molecular frame (three rightmost columns). **b)** Angular distribution of photoelectron continuum wave functions, represented by surface spherical harmonics and as a function of angular momentum (columns) and sorted by irreducible representations (rows). Adapted from [81].

dynamics without smearing out any of them, both must be chosen accordingly. The concept of the time–bandwidth product was already introduced in section 2.1 when we dealt with few-cycle laser pulses. The main message conveyed was that the shorter a pulse (temporal resolution), the broader its spectrum (spectral resolution) and vice versa. This statement can directly be transferred to our current situation when realizing that the temporal resolution is directly linked to the duration of the ionizing XUV probe pulse. It implies that the energy separation between the dynamics-involved states limits the maximally acceptable bandwidth and determines the minimal XUV pulse duration. Regarding the current situation, where we try to unravel the temporal evolution of the transiently populated B state during ozone photodissociation, we try to discern it unambiguously from the ground X state dynamics. Therefore, we ran numerical simulations trying to mimic a photoelectron spectrum of ozone for a specific spectral bandwidth of the XUV probe pulse and are introduced and explained in the first subsection. The second subsection finally presents the XUV spectrum, as it is used in the experiment.

#### 4.4.1 Required XUV Probe Pulse Energy Resolution

Figure 4.9 displays the cation states from Table 4.3 graphically, neglecting their rovibrational-structure such that they appear as peaks in a *sticky spectrum* at well-defined energies. The blue and red vertical lines refer to the ground X state- and excited B state-associated cation states, respectively. Moreover, this illustration neglects any angular dependence, that might vary with the irreducible representation, and detection issues, as they would occur in TRPES-experiments (section 4.3). Now, we try to derive a reasonable XUV spectral bandwidth so that the X state-related cation states remain distinguishable from the third cation state (B-3 in Table 4.3). The latter state is chosen, since it exhibits the highest photoionization probability and, additionally, is characterized by a distinct energy separation from the X state-associated cation states (X-1 to X-3 in Table 4.3). Aside from this, photoelectrons that are associated with oxygen and which get produced after completion of ozone photodissociation will show up in the gap between the two

primary peaks of the ozone photoelectron spectrum (Figure 4.9). If the XUV bandwidth had been chosen too broad, their observation would have been hampered by reasons similar to those mentioned above. The green solid line in Figure 4.9 shows the result of a convolution between X and B state-related cation states (blue and red vertical lines) and a Gaussian of 1.1 eV bandwidth FWHM. Apparently, it allows for the unambiguous assignment of photoelectrons to either X or B state-associated cation states and to oxygen-related cation states in the gap between the two primary peaks (X-1 to X-3 and X-16 to X-19).

Consequently, Figure 4.9 further displays a typical photoelectron spectrum, measured with an XUV probe pulse that has a FWHM bandwidth of 1.1 eV and that is centered around 99.5 eV (light gray shaded area). The dark gray solid line depicts another simulated ozone photoelectron spectrum considering X state-related cation states only. These states belong to different irreducible representations and, consequently, refer to different angular distributions upon photoemission. Further, they are weighted by fit to the experimentally obtained ozone photoelectron spectrum (light gray shaded area). This is necessary to account for issues regarding the observability of certain cation states at least qualitatively. Moreover, it performs a convolution of all these weighted states with the experimental XUV spectrum (central photon energy: 99.5 eV / 1.1 eV bandwidth FWHM; subsection 4.4.2). Additionally, it is convolved with another Gaussian of 1.5 eV bandwidth FWHM. The latter, however, is needed to take the limited relative temporal resolution of the TOF detector into account and amounts to  $T/\Delta T \approx 100$ . Here,  $T$  and  $\Delta T$  refer to the time of flight of an electron and temporal measurement uncertainty, respectively. This value is equivalent to an energy resolution of roughly 2 eV around 99.5 eV and shows very good agreement with the measured photoelectron spectrum of ozone (light gray shaded area), except for very low photoelectron kinetic energies. The deviation is due to missing information on cation states in this energy range. On the whole, such a narrow-bandwidth XUV spectrum (1.1 eV bandwidth FWHM; 1.7 fs XUV pulse duration Fourier limit) allows for the uncompromised distinction between photoelectron wave packets emerging from the ground X state, the excited B state or even from oxygen associated cation states.

#### 4.4.2 XUV Spectrum used in the Experiment

Regarding the XUV pulse generation, explained in section 3.2, we generate a train of XUV probe pulses via HHG in a quasi-static gas cell, filled with neon at approximately 165 mbar backing pressure. This target is then subjected to our CEP-controlled few-cycle NIR pulse (1.2 mJ, 3.9 fs). Spectral filtering, that fulfills the temporal and spectral constraints discussed previously, takes place via a suitably designed dielectric multilayer XUV bandpass mirror, whose reflectivity profile is shown in Figure 4.10 a) as a function of XUV photon energy. It is based upon a *molybdenum-silicon* (MoSi) system, in which the silicon absorbs high-energy photons above 100 eV and which has a central energy of 99.6 eV at the position of the highest reflectivity value. Moreover, it is characterized by a rather narrow spectral bandwidth of approximately 1.75 eV FWHM. It is the silicon that enables the 1.1 eV narrow bandwidth of the XUV mirror. Using it together with a combination of a 500 nm silicon filter and a 150 nm molybdenum metallic filter (Figure 4.10 b)), both being used in transmission, completes the spectral filtering of our original XUV spectrum (Figure 4.10 b)). In total, their application gives rise to a spectrally narrow

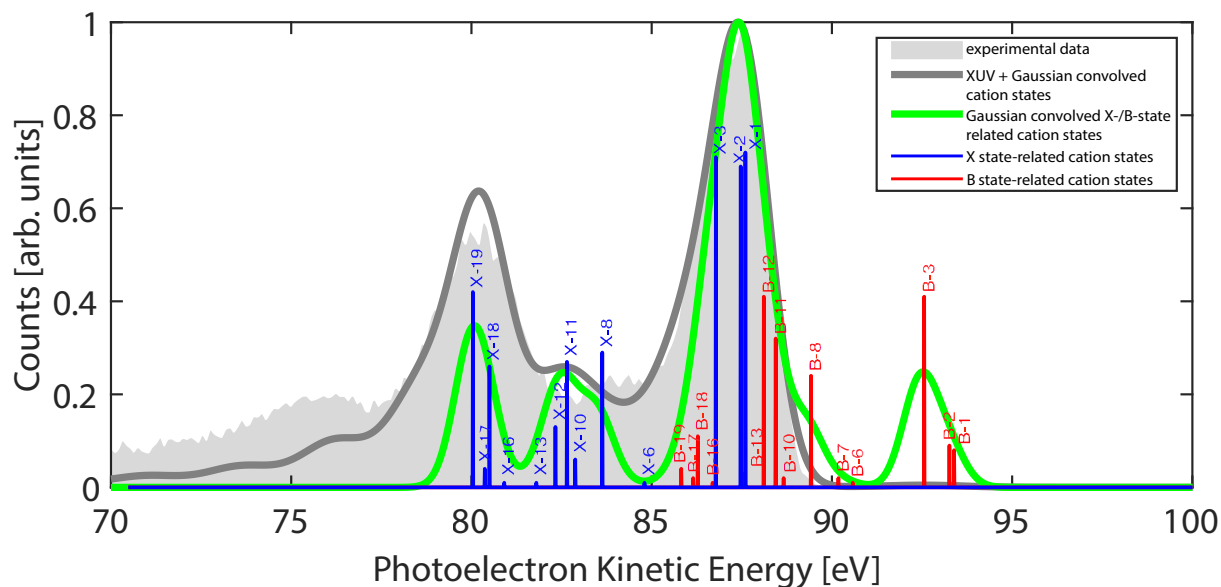


**Figure 4.9:** Typical ozone photoelectron spectrum (light gray shaded area), recorded with an XUV probe pulse spectrum centered around 99.5 eV and with 1.1 eV bandwidth FWHM. The ground X (blue vertical lines) and B (red vertical lines) state-related cation states are shown as well. The dark gray solid line illustrates a simulated photoelectron spectrum for X state-associated cation states, convolved with both the XUV spectrum (1.1 eV bandwidth FWHM) and with an additional Gaussian function of 1.5 eV bandwidth FWHM. The latter accounts for the energy resolution of the TOF detector. Moreover, the pole strength of X state-related cation states belonging to different irreducible representations are scaled with respect to those of other irreducible representations in order to find the best accordance with the measured ozone photoelectron spectrum (light gray shaded area). The green solid line shows both X and B state-related cation states convolved with the Gaussian XUV bandwidth only (1.1 eV FWHM).

XUV probe pulse with roughly 1.7 fs FWHM duration and is displayed in Figure 4.10 d). The resulting XUV spectrum is centered around 99.5 eV with a 1.1 eV bandwidth, showing a rather clean high-photon-energy side as compared to the unfiltered, calibrated XUV spectrum. The XUV spectrum itself is usually recorded after transmission through a 3  $\mu\text{m}$  thick zirconium filter. It is necessary to protect the XUV-CCD camera against NIR radiation, that would otherwise damage the camera. In total, we achieve an XUV pulse energy of roughly 1 pJ on target, that is equivalent to  $1 \times 10^{12} \text{ W cm}^{-2}$  at a focal beam waist of roughly 15  $\mu\text{m}$ .

## 4.5 Femtosecond DUV Pump Pulse Generation

The first subsection of this section deals with two approaches concerning the generation of ultrashort DUV pulses. In order to motivate these attempts, it is quite helpful to recapitulate the necessary features which our radiation source has to fulfill. On the one hand, we aim at

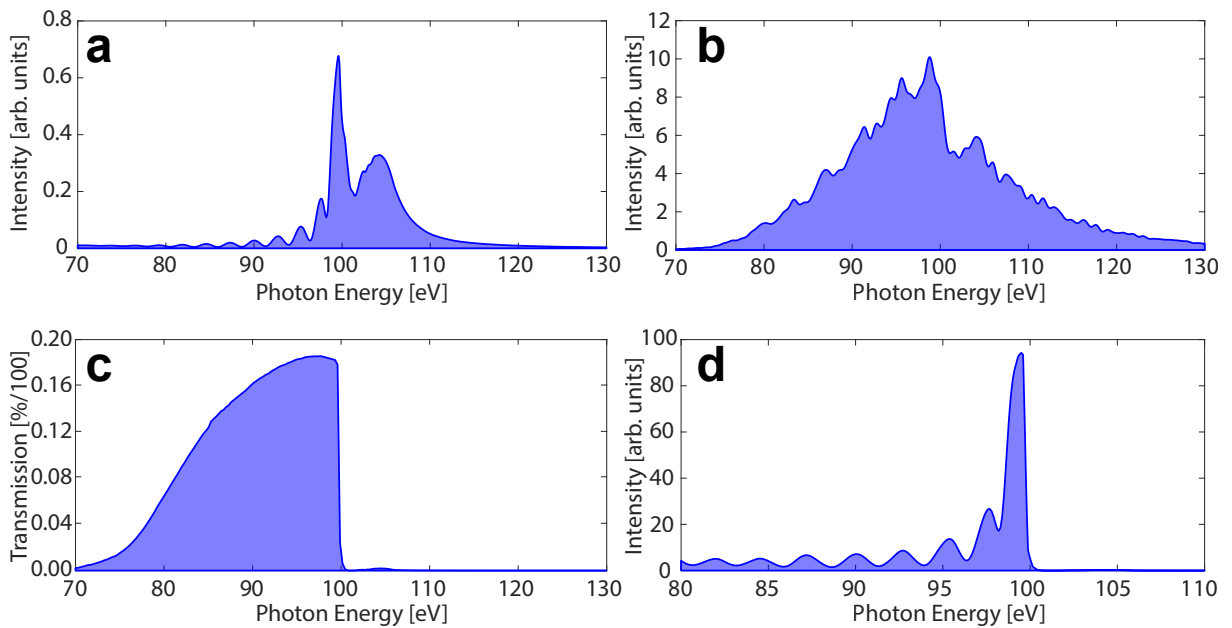


**Figure 4.10:** **a)** Reflectivity of the 1.75 eV-bandwidth, *molybdenum-silicon* (MoSi) multilayer XUV mirror as a function of XUV photon energy and without additional metallic filters. **b)** Typical calibrated XUV spectrum, taken after transmission through a 3  $\mu\text{m}$  thick zirconium filter. **c)** Total transmission function of the set of metallic filters used (150 nm Mo and 500 nm Si). **d)** Simulated XUV spectrum with 1.1 eV bandwidth FWHM, as used on target, taking all mirror reflections (MoSi-multilayer XUV mirror and Ni-coated grazing incidence toroidal mirror of the AS2-interferometer) and filter transmission factors from **c)** into account. Please notice that the x-axis in **d)** deviates from those in **a)** – **c)** for clarity.

kicking off the photodissociation of ozone. It is known to happen on a few tens of femtoseconds and, hence, calls for short DUV pulses to enable its experimental observation. On the other hand, relatively high intensities in the DUV spectral range on the order of  $1 \times 10^{12} \text{ W cm}^{-2}$  –  $1 \times 10^{13} \text{ W cm}^{-2}$  are a prerequisite for launching the photolysis of ozone to a measurable extent. Since the DUV pulse generation rests on nonlinear frequency up-conversion, we know from chapter 2 that the conversion efficiency usually increases with the length of the nonlinear material, but chromatic dispersion also does. The latter leads to temporal spreading of the generated harmonic. Apparently, short and intense pulses are usually mutually exclusive. Moreover, the fact that the third harmonic of our laser spectrum accidentally coincides quite well with the position of the Hartley absorption band between 200 nm and 300 nm, our very first attempt is to generate the required DUV pulses via THG in neon. Because gases usually exhibit less chromatic dispersion than solids, this approach is predestined to solve this problem in the first place. Nonetheless, we will see in the course of this section that ultrathin BBOs perform better due to a bunch of reasons.

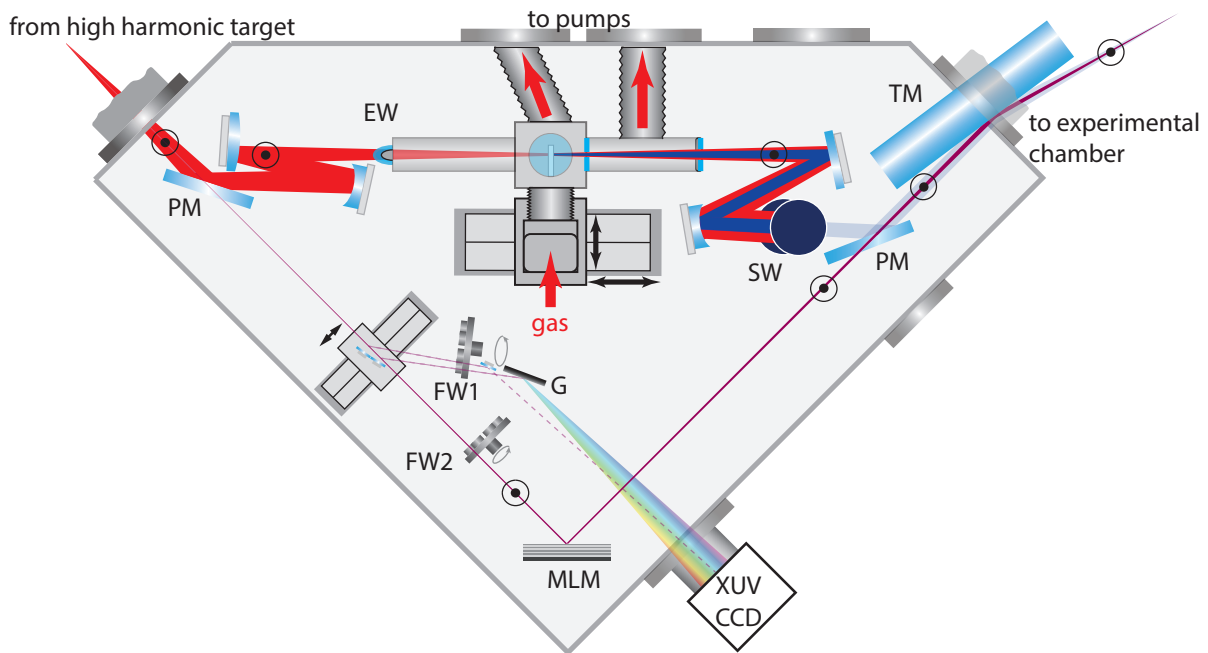


**Figure 4.11:** Schematic illustration of the THG setup for the generation of ultrashort DUV pulses, as used in the AS2-beamline at MPQ before DUV source revision. For explanation of the various components, see main text.

#### 4.5.1 Early Attempt — THG Gas Phase Target

As atoms possess an inversion symmetry center, their lowest order of nonlinearity is three<sup>5</sup>. Among all rare gas atoms, neon has proved to perform best for THG, whilst introducing little chromatic dispersion, and that it is possible to generate 3 fs short DUV pulses [7, 85]. A sketch of the adapted experimental setup, as implemented in the AS2-delay chamber together with Michael Jobst [56], is illustrated in Figure 4.11.

The heart of this setup is formed by a quasi-static neon gas cell. It is basically realized by a ceramic tube with 300  $\mu\text{m}$  small holes on either side, which are predrilled perpendicularly to the tube axis. These are similar to the ones already employed for HHG (Figure 3.3). The predrilled holes enable the fundamental NIR laser pulse to traverse and interact with the nonlinear medium. The NIR pulse in front of the THG target usually has a pulse energy of roughly 540  $\mu\text{J}$  [56]. The targets are put close to the intermediate focus of the delay chamber and are encased in an additional vacuum system for differential pumping, which, in turn, is embedded in the delay chamber itself. A one-dimensional translation stage put underneath the entire assembly offers us the possibility to move the THG target along the focus and allows us to find the point of best operation in terms of optimal phase-matching. Another degree of freedom for proper phase-matching emerges from the neon gas pressure and is adjusted by a highly sensitive dosing valve from outside the chamber. It usually runs at 9 bar for nearly optimal phase-matching.

<sup>5</sup>Only materials lacking centrosymmetry exhibit second order nonlinearities (chapter 2).

Because of the vast amount of exhausting gas from the ceramic target, one has to prevent it from getting into the delay chamber by the already mentioned, target-encasing two-stage differentially pumped vacuum system, as indicated by the big red arrows in Figure 4.11 and which is presented in more detail in the following:

The first stage of the differential pumping assembly removes most of the gas spilling out of the target, whereas the second stage, right after the first one, turned out to be essential to remove residual amount of gas. If the neon was not removed, it would hamper the experiment otherwise, due to residual neon atoms reabsorbing XUV-photons on their passage through the delay chamber. In order to retain enough gas within the first as well as in the second stage, we added extra predrilled sinter filters at the junctures between the first and second stage, and also at the transition from the second stage into the delay chamber (sketched as light blue rectangles inside of the differential pumping scheme in Figure 4.11). Both effectively act as a flow resistance for the exhausting gas. In order to lock up the first stage on the entrance side and to further reduce the residual gas load inside the delay chamber, we used a rather thin (approximately 50  $\mu\text{m}$ ) fused silica entrance platelet (abbreviated as *EW* in Figure 4.11). Unfortunately, we could not simply use another fused silica platelet as exit window due to a more dramatic impact of chromatic dispersion, that is imposed on the DUV pulse in contrast to the NIR pulse. With this setup, we are able to keep the residual backing pressure of the delay chamber below  $6 \times 10^{-3}$  mbar when the THG target is run at 9 bar neon backing pressure. In this way, the setup is shown to deliver DUV pulses around 266 nm and even down to shorter-wavelengths, having an energy per pulse of 7  $\mu\text{J}$  at 7 bar of neon [56].

Despite these extraordinary good performance, we now want to turn to its drawbacks, as we could not use all of its power, once it arrives at the interaction zone of the experimental chamber. The first drawback can be sought in the following: Governed by the nature of the THG process in an atomic vapor, the polarization of the third harmonic (DUV) was identical with that of the fundamental pulse (NIR). This issue is indicated by an encircled black dot ( $\odot$ ) in Figure 4.11 and refers to a polarization that is out of plane with the chamber. As outlined in subsection 4.3.3, the uncompromised measurement of the ozone photodissociation dynamics requires to get rid of the NIR almost completely in order to avoid momentum shifts induced by *streaking* (appendix A.1). This is quite a challenging task, because the third harmonic is collinearly generated with the NIR and the overall THG conversion efficiency is rather poor (approximately 1%). Since transversal streaking scales quadratically with increasing wavelength<sup>6</sup> the overall attenuation of the fundamental needs to be on the order of  $10^4$  or better.

In our case, the spectral filtering of DUV and NIR relies on the following approach: A combination of two NIR suppressing, but DUV reflecting dielectric mirrors (Figure 4.12 a)) and two silicon wafers (SW in Figure 4.11) put at Brewster's angle for the NIR (Figure 4.12 b)) lead to a sufficiently good NIR reduction at the expense of a 90% loss of DUV radiation, solely in the latter case. We have to use the silicon chicane anyway, since the dielectric mirrors (Figure 4.12 a)) only suppress the NIR between 700 nm and 900 nm by a factor of approximately 10, while they reflect DUV radiation around 266 nm up to 95% (DUV mirror reflectivity curve is

<sup>6</sup>due to its linear dependence on the ponderomotive potential  $U_p$  (equation (A.2b) in appendix A.1)

shown in Figure 4.12 a)). Regarding the silicon chicane, the reason for why they transmit DUV radiation so poorly lies in their 30% reflectivity in the DUV spectral range when applied at Brewster's angle (red solid line in Figure 4.12 b)). Consequently, we lose more than 90% of the DUV radiation after two reflections (roughly 10% overall reflection efficiency). The situation would change, if the DUV polarization was rotated by  $90^\circ$  with regard to the NIR polarization. Then, we would keep approximately 83% after traversal through the silicon wafer chicane (blue solid line in Figure 4.12 b)). It is this property that will make us use the silicon wafer chicane in this configuration, once the DUV generation setup has been revised (subsection 4.5.2) and finally makes the ozone experiment work due to better DUV / NIR separation and improved DUV transmission into the experimental chamber. The second drawback refers to the long-term pointing stability, necessary to run the ozone experiment: As stated above, the DUV generation takes place in an interaction region whose profile is on the order of  $300\ \mu\text{m}$  in diameter. This circumstance enforces a highly reliable beam pointing stability over a very long time. Experimentally, we found that — in spite of exploiting a beam pointing stabilizing feedback loop — recording even a single measurement on ozone easily exceeds a three-quarter hour. Still, evolving long-term drifts turned out to be hard to compensate for, as the beam stabilizer follows the motion of the chamber, which it resides in. Only short to moderate drifts could be coped with. In the sequel, the DUV flux could not be maintained over the course of a single measurement, but deteriorates to a noteworthy extent so that the collected data is useless. We attribute this to the sheer fact of having such a small THG target aperture of  $300\ \mu\text{m}$ , making the NIR beam leave its aperture. A third drawback — basically of economical character — but must not be neglected, came into play when the Ukraine crisis culminated in 2014. Back then, the neon price has kept increasing for quite some time and finally peaked at a maximum of 30.000 per bottle. For comparison, in former years a single Ne bottle could be purchased for approximately 1.000 . Owing to this market development, retention to this kind of DUV generation was rendered unreasonable and in combination with the aforementioned scientific reasons involved a revision of our DUV generation scheme.

#### 4.5.2 Current Attempt — SHG Solid State Target

Before reviewing our DUV radiation source, we should be aware of its required features first, making up for the disadvantages of the former approach. Preferably, the new DUV radiation source has to be . . .

- minimally dispersive and should provide short and intense DUV pulses *on target*
- easy to implement
- long-term stable with respect to minor beam pointing instabilities
- long-term stable in terms of DUV flux
- tunable to some extent in terms of wavelength
- separable from NIR without losing too much DUV
- cross-polarized with respect to the XUV.



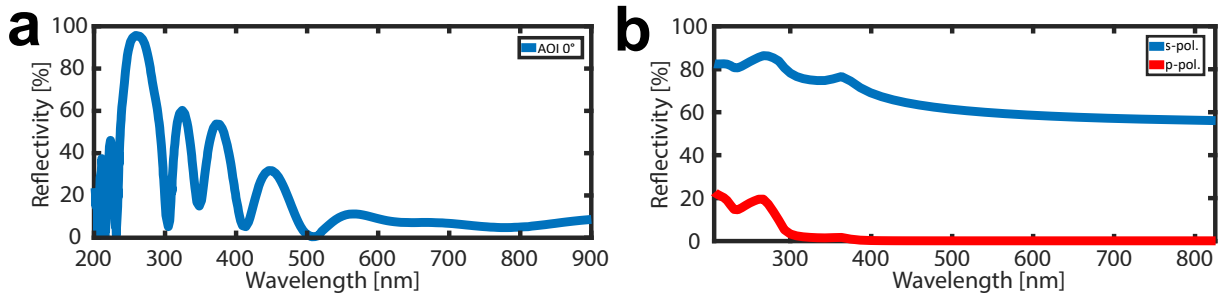


**Figure 4.12:** **a)** Reflectivity of a single DUV reflecting / NIR attenuating, specially designed dielectric bandpass mirror at normal incidence ( $0^\circ$ ). **b)** Total reflectivity of p-polarized (red solid line) and s-polarized (blue solid line) light at a two-stage silicon wafer chicane, both set at  $75^\circ$  angle of incidence with regard to the wafer's normal. If the DUV light was s-polarized relative to the wafer's plane of incidence, we would maintain more than 83% after traversal through the silicon wafer chicane. However, the NIR part should still be p-polarized in order to make the silicon wafer chicane work as a DUV–NIR filtering stage.

In principle, one could have thought of a setup, that satisfies each of the aforementioned features to a very high degree, which, in turn, would commonly cause tremendous amount of space and complexity. Unfortunately, the spatial extension of the delay chamber limits the intricacy of our revised DUV radiation source, as it should fit into the AS2-interferometer, placing approximately two meters of space at our disposal to accomplish these tasks. It is not an uncommon step, deliberating the rather simple THG setup used previously. So we sought a compact replacement for it and strove for an SHG scheme that is supposed to be even more efficient than THG and that already satisfies the first condition. If the crystal thickness was chosen reasonably, it would even satisfy the prerequisite of delivering short and intense DUV pulses. This issue is addressed individually in the next subsection.

However, exploiting second order nonlinear effects, like SHG, implies the usage of materials that lack a center of inversion, unlike in the case of THG. This is the case for birefringent crystals, like BBO. Usually the size of their aperture (roughly 3 mm in diameter as opposed to  $300\ \mu\text{m}$  in case of THG targets) renders the second and third feature achievable, because small beam pointing instabilities do not lead to a total loss of DUV radiation as long as the beam traverses the crystal. The fourth feature is supposed to be fulfilled automatically, because the amount of DUV generating material does not change with time and is supposed to deliver a temporally stable DUV flux. This has to be contrasted with the gas-based THG approach, where the temporal stability directly depends on the amount of provided gas. As we learned in chapter 2, when we dealt with second order nonlinear effects in particular, phase-matching must be fulfilled for efficient second harmonic generation (paragraph 2.2.3.1). Wavelength tunability can to some extent be considered as a by-product of the phase-matching condition and merely depends on the bandwidth of the DUV generating spectrum. The most important and most beneficial features of the revised DUV setup are summarized by the last two items in the above list. As stated previously, efficient DUV separability from the NIR radiation is a prerequisite for the ozone experiment, and so is a cross-polarized DUV–XUV pulse train. In subsection 4.3.3 we explicitly

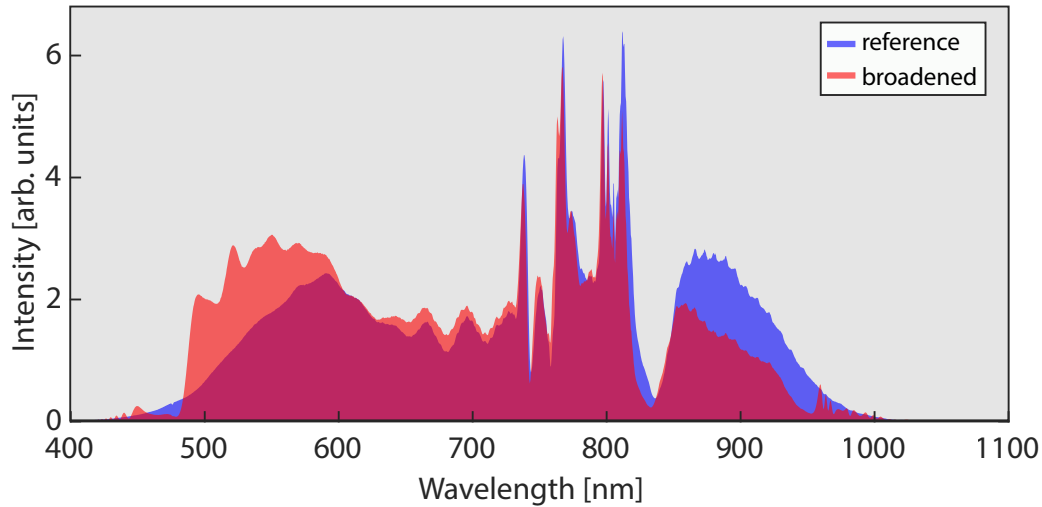


**Figure 4.13:** Illustration of a spectrally broadened NIR spectrum, concomitant with HHG at 140 mbar backing pressure of neon (red) and an unbroadened NIR spectrum without accompanying HHG at 0 mbar backing pressure of neon (blue) are shown for comparison. A substantial increase of spectral components between 500 nm and 600 nm is visible and turns out to be responsible for 90% of the subsequent DUV yield.

deal with the angular distribution of photoelectrons emanating from different states and from the B state in particular, using a picture that is motivated by group theory. There, we conclude that the observability of photoelectrons tremendously depends on the symmetry of the involved states during photoelectron emission, the polarization of the ionizing XUV probe pulse and on the orientation of the ozone molecule relative to the detector in the laboratory frame (equations (4.13) – (4.14)). Regarding the efficient separation of DUV and NIR, we have found a way out of this dilemma, that even allows us to retain the two-stage silicon wafer chicane and benefit from its full filtering capability (NIR suppression factor:  $10^4$ ), when using crossed DUV–NIR polarization. Because type-I SHG inherently rotates the polarization of the generated DUV with respect to that of the NIR, our goal is reached automatically. Thus, subsequent rotation of the DUV polarization is superfluous.

Still, an overall problem consists in the lack of appropriate spectral components in the range between 500 nm and 600 nm of the NIR spectrum in order to efficiently generate DUV via SHG. In the former setup we make use of the fact that the spectral range of the ozone Hartley band accidentally overlapped with the third harmonic of our laser spectrum. Unfortunately, this is not the case regarding an SHG approach. Up to now, we do not have a sufficient amount of spectral components between 500 nm and 600 nm (Figure 3.2), that is a prerequisite to produce light between 250 nm and 300 nm. One way out is to exploit HHG-accompanying nonlinear effects, like plasma-induced blue-shifting [86] of the optical NIR spectrum, as well as SPM [87] (paragraph 2.2.3.2), effectively producing new spectral components in the desired spectral domain. It is experimentally proven that one can find a compromise between HHG and

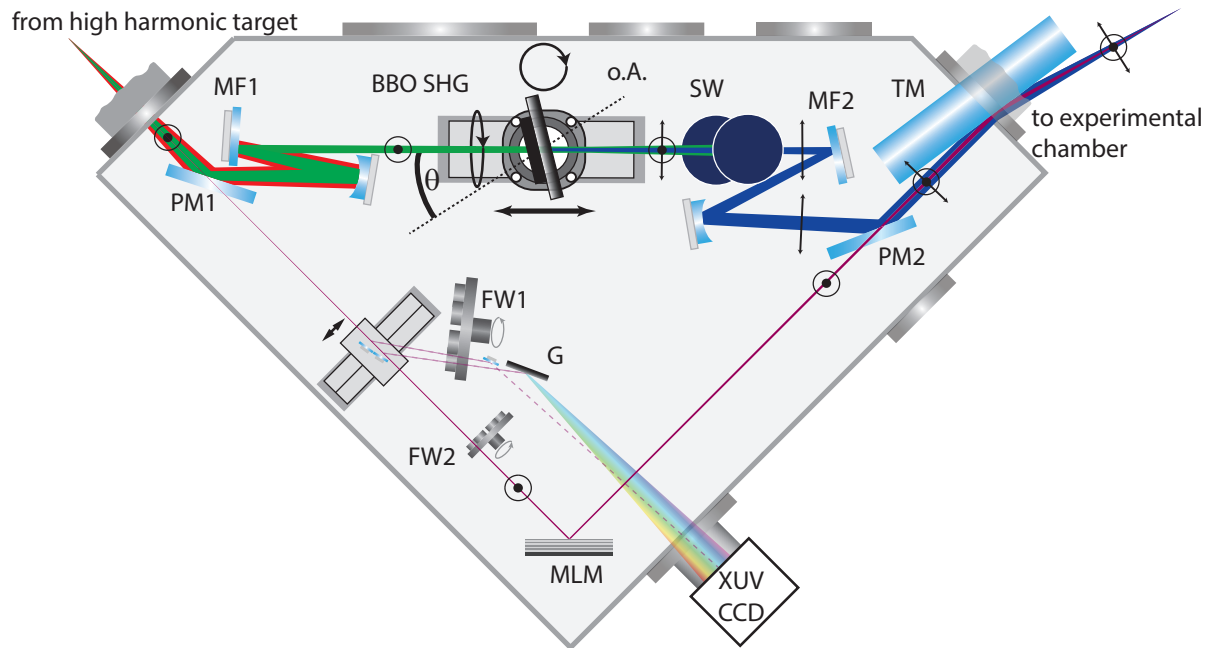


**Figure 4.14:** Schematic illustration of the SHG setup for the generation of ultrashort DUV pulses, as used in the AS2-beamline at MPQ after revision of the DUV source. For explanation, see main text.

spectral broadening of the NIR spectrum so that DUV generation becomes more efficient without spoiling our XUV yield to a noteworthy extent. Spectrally broadened (red shaded area) and unbroadened (blue shaded area) NIR spectra are shown in Figure 4.13. The oscillatory pattern on the high frequency / short wavelength side of the optical spectrum is a clear indication for plasma contributions as explained for example in [86,88].

A schematic illustration of our revised DUV generation setup is depicted in Figure 4.14. The HHG-accompanying spectral broadening of the NIR spectrum is illustrated as a red-green-shaded beam, entering the Mach-Zehnder interferometer of the AS2-delay chamber at its *first perforated mirror* (PM1). There, the XUV–NIR pulse train gets separated and the spectrally broadened NIR pulse is focused into the intermediate focus of the NIR-arm of the AS2-interferometer. As we go along our revised DUV setup, we implement a sequence of NIR-only attenuating elements. The first attenuating device is a specially designed broadband dielectric attenuating mirror (MF1 in Figure 4.14) that reflects light around 536 nm with a bandwidth of 210 nm FWHM. Its reflectivity curve is displayed in Figure 4.15.

Regarding the BBO holder (BBO SHG in Figure 4.14), two motorized rotation stages allow us to rotate the crystal about two axes<sup>7</sup> in order to satisfy the phase-matching condition (indicated by two arrowed circles next to and above the BBO). Now, since we exploit type-I SHG for DUV generation, its polarization is crossed with regard to that of the NIR. As our second filtering

<sup>7</sup>one along the propagation axis and another about an out-of-plane axis

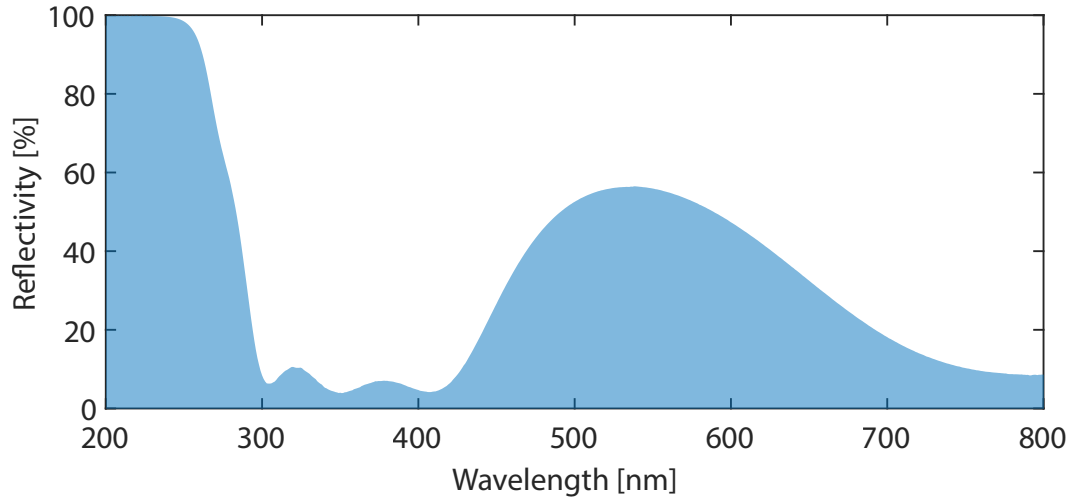


**Figure 4.15:** Reflectivity of the first NIR-only attenuating dielectric bandpass mirror (MF1 in Figure 4.14). It mainly reflects up to roughly 56% of green spectral components around 536 nm (FWHM bandwidth: 210 nm). Only 10% of 800 nm radiation are reflected.

stage, we once again apply the silicon wafer (SW) chicane (subsection 4.5.1). In contrast to the former THG setup, we do not lose as much DUV as before, owing to the s-like polarization with respect to the plane of incidence of the silicon wafer chicane. This fact is the key, since more than 83% make it through the second filtering stage, while the NIR is attenuated by more than four orders ( $> 10^4$ ) of magnitude. After the silicon chicane, we are basically supplied with a pure DUV beam. Residual NIR contributions could be got rid of by a set of identical NIR-attenuating dielectric mirrors (MF2 in Figure 4.14), as they are already used in the THG approach. They usually reflect more than 95% of the DUV with negligible phase distortions (Figure 4.12 a)). The polarization of our pure DUV beam is illustrated by a two-sided arrow, that is oriented perpendicularly to the DUV beam (blue beam in Figure 4.14). As we recombine the XUV and the DUV (purple and blue beams in Figure 4.14, respectively) on the *second perforated mirror* (PM2), we end up with a collinear, NIR-free, cross-polarized and pure XUV–DUV pulse train. Both beams are then — as always — focused by a nickel-coated grazing-incidence toroidal mirror (TM) into the experimental chamber onto a common spot underneath the TOF.

### Simulation of Ultrashort DUV Pulses in Ultrathin BBO Platelets

Before implementing a revised SHG-based DUV setup, we performed numerical calculations to find the more or less optimal BBO crystal thickness. The simulation assumes a one-dimensional propagation through such a crystal and is based upon the spatially propagated *unidirectional pulse propagation equation* (z-UPPE) [89], whose equation of motion is written down as

$$\frac{\partial}{\partial z} E_{o/e}(\omega, z) = ik_z E_{o/e}(\omega, z) + \frac{i\omega^2}{2\epsilon_0 c_0^2 k_z} P_{o/e}(\omega, z). \quad (4.15)$$

Here, we neglect contributions arising from electric or magnetic currents and momentum components along the remaining x- and y-axes as well as any back-propagating waves.  $E_{o/e}(\omega, z)$  is the Fourier transform of the ordinary (o) or extraordinary (e) electric field vector, respectively, and is defined relative to the orientation of the crystal optic axis.  $k_z = k_z(\omega, \theta) = \frac{\omega}{c_0} \sqrt{n_{o/e}(\omega, \theta)}$  is the momentum vector along the propagated z-axis and depends on the angle between the crystal optic axis and the z-axis for the extraordinary beam only. The term  $P_{o/e}(\omega, z)$  is the Fourier transform of the polarization vector for either the ordinary or extraordinary ray and comprises linear and nonlinear contributions. While the former expression is calculated using the linear susceptibility tensor in the spectral domain according to equation (2.23) and following a Sellmeier equation approach, the latter is calculated using a time domain version of equations (2.39) – (2.40) up to third order. Since any order of nonlinearity is assumed to follow the driving electric field instantaneously, we neglect dispersion effects, concomitant with the nonlinear susceptibility. To some extent, this is a reasonable and legitimate approximation as long as one is far away from resonances. On that account, i.e. calculating the nonlinearity in the time domain, the simulation benefits from covering all second (SHG, SFG/DFG and OR; subsection 2.2.3.1) and third (THG and SPM; subsection 2.2.3.2) order nonlinearities at once in the time-domain picture. Moreover, we take the tensor nature of the linear and nonlinear susceptibilities in their full dimensionality explicitly into account and, hence, the influence of the crystal orientation with regard to the incident pulse via a coordinate transformation from the reference frame into the crystal frame [34]. As the pulse propagates at the speed of light through the crystal, it would leave the computation window rather quickly, if we did not choose a reference frame that travels at the same speed along with the pulse.

Concerning the nonlinear coefficients, we assumed intrinsic permutation symmetry, Kleinman's symmetry and full permutation symmetry to be applicable (paragraph 2.2.3.1). The applicability of these approximations seems to be justified, since we simulate DUV generation far from resonance and in such a narrow spectral domain that nonlinear coefficients can be regarded frequency-independent. The simulation is numerically propagated using a *Runge-Kutta algorithm of fourth order* at reasonably small steps [90].

In order to obtain realistic results that compare to the experiment, we use the broadened spectrum from Figure 4.13 as input to our simulation. We further assume it to possess a flat spectral phase. Since the NIR is expected to contribute negligibly to the overall SHG process due to improper phase-matching, we forgo removing the NIR before running the simulation. Moreover, we estimate an input peak intensity for the green spectral components of the NIR spectrum of  $I_{peak} \approx 2 \times 10^{13} \text{ W cm}^{-2}$  via  $I_{peak} = 0.94 \cdot \frac{E_p}{\pi \cdot w_0^2 \cdot \tau_p}$ . Here,  $E_p = 0.30 \cdot 300 \mu\text{J} = 90 \mu\text{J}$ ,  $w_0 = 180 \mu\text{m}$  and  $\tau_p = 4 \text{ fs}$  are used and the 300  $\mu\text{J}$  refer to the overall pulse energy of the NIR in front of the BBO. We calculate that 30% of this energy comes from spectral components between 500 nm and 600 nm after spectral broadening in the HHG target. The numerical calculations propose to make use of approximately 20  $\mu\text{m}$  thin and freestanding BBO platelets as nonlinear medium,

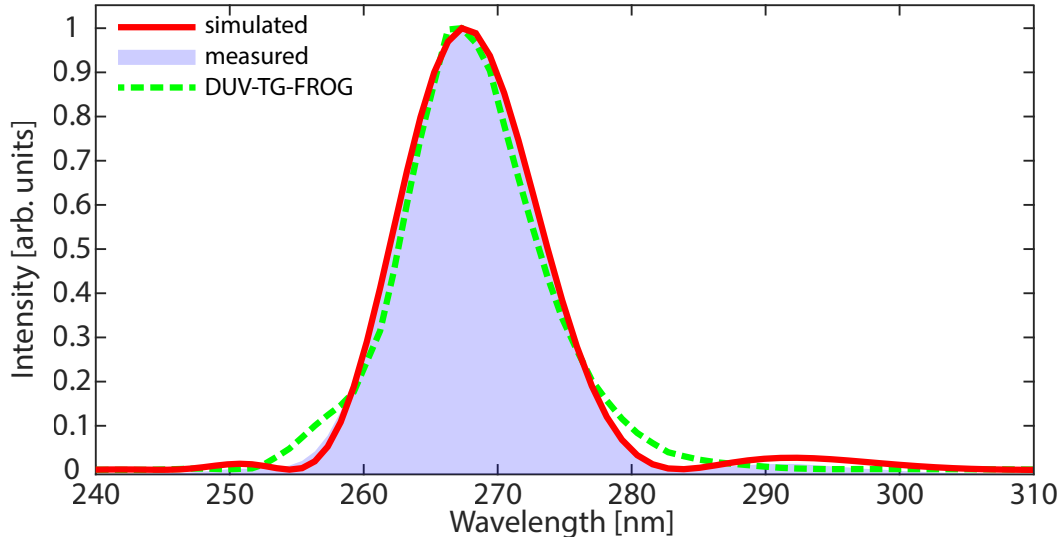


**Figure 4.16:** Comparison of DUV spectra, obtained from a direct measurement (blue shaded area), from the z-UPPE simulation, taking the broadened spectrum from Figure 4.13 as input and assuming a flat spectral phase (red solid line), and from a reconstructed DUV-TG-FROG spectrogram (green dashed line). In order to ease comparison, the simulated and retrieved spectra are multiplied by the DUV transmission profile (Figure 4.17), used for measuring the DUV spectrum.

which are cut at  $\theta = 44.3^\circ$  and  $\phi = 90^\circ$  for suitable SHG around 536 nm. Thus, Figure 4.16 shows a comparison between spectra obtained in various ways: The blue shaded area illustrates a measured DUV spectrum for a  $\sim 20\mu\text{m}$  thin and freestanding BBO crystal, while the solid red line depicts a simulated spectrum from the aforementioned z-UPPE simulation, assuming an identical crystal. The dashed blue line, instead, is a spectrum received from a reconstructed DUV-TG-FROG spectrogram. For more information on the temporal characterization of the DUV pulse, see subsection 4.5.3. All these spectra are made comparable to each other by multiplying the transmission profile of a DUV-bandpass filter<sup>8</sup> to them. The DUV filter is used to prevent the spectrometer from being saturated by NIR contributions during the measurement of the DUV spectrum. Its transmission profile is shown separately in Figure 4.17. Obviously, by comparison with the spectra shown in Figure 4.16, we hardly falsify the real spectrum by its application, because the width of the DUV-bandpass filter exceeds that of the DUV spectrum.

### 4.5.3 Temporal Characterization of Ultrashort DUV Pulses — DUV-TG-FROG

Full knowledge of our DUV pulses requires a characterization of their pulse duration. An attosecond streaking measurement (appendix A.1), conducted with DUV pump and XUV probe

<sup>8</sup>*Edmund Optics 254 nm CWL, 40 nm FWHM, 25 mm Mounted Diameter*

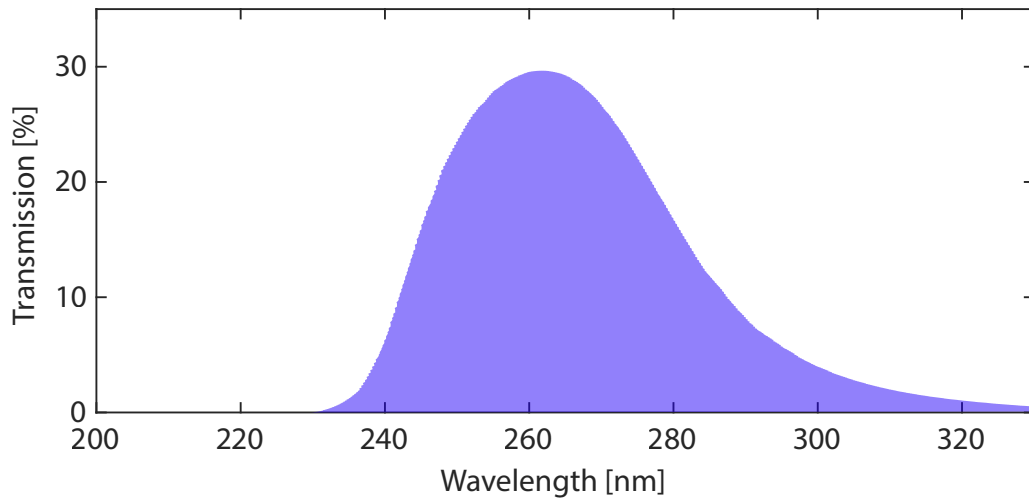


**Figure 4.17:** Transmission profile of the Edmund Optics DUV-bandpass filter (CWL 254 nm; FWHM: 40 nm) as a function of wavelength, that is multiplied to the data shown in Figure 4.16.

pulses, would have been desirable, since it would yield their temporal information directly. However, an insufficient DUV intensity had rendered this approach impossible, owing to the circumstance that the required intensity for streaking scales linearly with wavelength. This means that, as the DUV wavelength (266 nm) is a third of that of the NIR (800 nm), we need a DUV intensity that must be three times as high as for the NIR to result in an identical streaking shift. Anyway, a DUV streaking has never been performed yet and in order to circumvent this problem, we agreed on a DUV capable, vacuum version of a *transient grating frequency resolved optical gating* (TG-FROG) approach, instead. The entire FROG must be encased in a vacuum chamber, because DUV pulse propagation through air poses a source for falsified temporal pulse characterization due to increased chromatic dispersion in this spectral range. Nonetheless, it is even more important to prevent the DUV pulse from propagating through any kind of material (for example a UV fused silica exit window) before its pulse duration can be measured. With the help of the TG-FROG, we will show that the DUV pulse duration is different for both DUV generation schemes (THG gas target and SHG solid state target). For more information on FROG and TG-FROG in particular, refer to the appendix A.2.

A picture of a self-built version of a vacuum TG-FROG, that is explicitly designed for DUV pulse characterization, is visualized in Figure 4.18. Most of the optomechanical components (mirrors and apertures are controllable from the outside via a hand key pad) are necessary to align the incoupled DUV beam in a reproducible fashion into the FROG setup (red shaded area in Figure 4.18). Special emphasis was put on its compact design, as it has originally been intended to be attached to the back-end of the AS2 experimental chamber. Due to limited space, it does not allow for an arbitrarily big TG-FROG. The original idea was to characterize the DUV pulse duration as close as possible to where the ozone experiment is performed later on, namely, in the vicinity of the experimental chamber. Nonetheless, we were forced to flange the TG-FROG

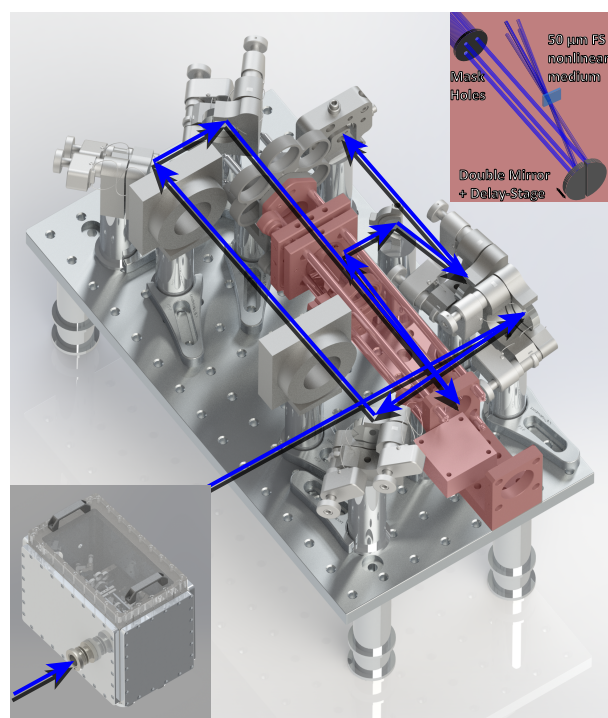


**Figure 4.18:** Illustration of the vacuum-compatible DUV-TG-FROG. Blue arrows indicate the beam path of the DUV beam entering the FROG from the lower left corner. *Lower left inset:* DUV-TG-FROG encasing vacuum chamber. *Upper right inset:* Close-up view of the red-shaded area: It shows the hole mask, cutting out three DUV beam replicas in a so-called *BOXCARS*-geometry, and the double-mirror arrangement for time delay control between the three replicas. All three DUV beams are focused into a nonlinear medium ( $50\ \mu\text{m}$  UV-grade fused silica platelet), where the nonlinear signal is generated before it is sent into a spectrometer for characterization.

to one side of the delay chamber, because the DUV losses — in case of the THG approach — between the delay chamber and the experimental chamber turned out to be extraordinarily high and ruled a DUV pulse characterization at the back-end of the AS2-beamline out (subsection 4.5.1).

Exemplary DUV-TG-FROG traces are depicted in Figure 4.19. Subplots a) and c) give the result for the gas phase THG target being run at 3 bar neon backing pressure relative to atmosphere. The pressure is optimized for maximum DUV yield, while forgoing NIR attenuation. Figures 4.19 b) and d), by contrast, display a FROG trace associated with the solid-state SHG target for DUV generation in  $20\ \mu\text{m}$  thin BBO platelets ( $\theta = 44.3^\circ$ ;  $\phi = 90^\circ$ ), but with NIR attenuation. The upper row shows the experimentally measured traces, while the lower row illustrates their reconstructed counterparts, respectively. It should be stated that performing FROG-measurements in the DUV spectral range are quite challenging due to the following reasons: First, the DUV beam is invisible to the human eye and trying to align the DUV beam



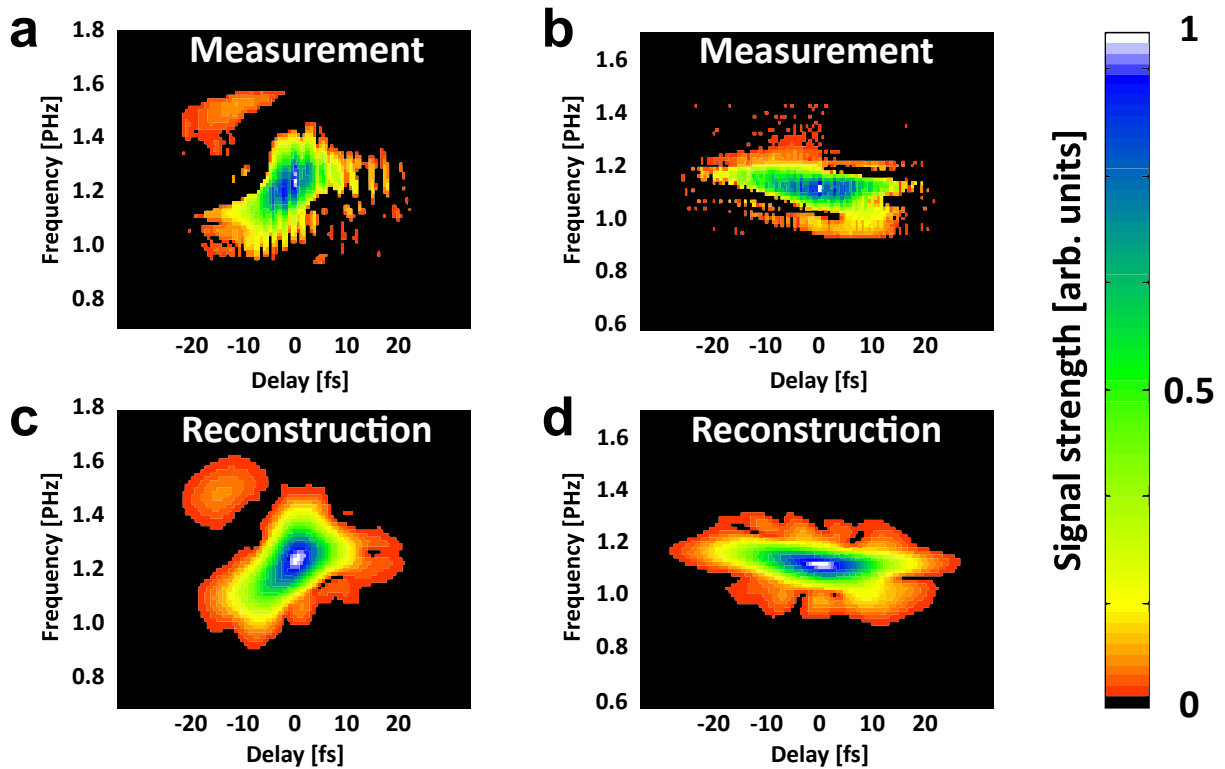


**Figure 4.19:** Measured DUV-TG-FROG traces in case of **a)** the THG target and **b)** for the SHG target. Reconstructed FROG traces are shown in **c)** and **d)**. The intensity of the recorded nonlinear signal is color-coded and shown on the right.

from outside the vacuum chamber is a rather demanding task. Actually, this is not really tragic, as this argument holds true for the invisible part of the NIR spectral domain as well. Nonetheless, the second reason is different: As FROG generally relies on nonlinear effects, high DUV intensities are indispensable, but hard to achieve in the DUV spectral domain, in contrast to the NIR spectral range. Moreover, the increased contribution of chromatic dispersion in the DUV spectral range, as opposed to the NIR, enforces an evacuated TG-FROG for uncompromised pulse characterization, which is not the case for the NIR. Obviously, the sheer fact that we work in the DUV spectral range complicates an experimental access to their pulse characterization.

From the FROG traces (Figure 4.19) we can now retrieve the temporal shape and duration of our DUV pulses. The retrievals are presented in Figure 4.20, obtained by an algorithm<sup>9</sup>, introduced in [91] and improved by [92]. The exemplary DUV pulse created via THG has a pulse duration of roughly 5.8 fs FWHM at 240 nm (Figure 4.20 a)). In turn, the SHG-associated DUV pulse is almost twice as long as its THG-related pendant, namely 11.7 fs FWHM at 268 nm (Figure 4.20 b)). Here, we assume that the nonlinear signal, from which we deduce the FROG traces and

<sup>9</sup>The retrievals are obtained with a software package, encompassing the *binner* and *frogger* programs, that is distributed by *R. Trebino* at <http://frog.gatech.edu/code.html>.

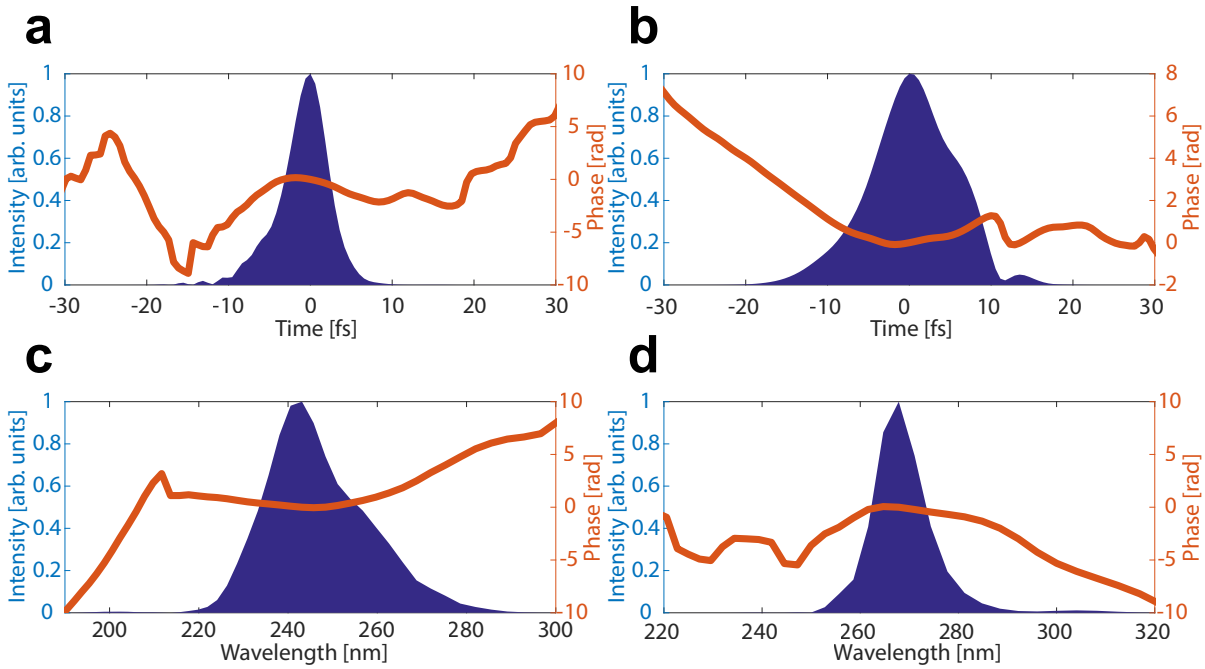


**Figure 4.20:** a),b) Temporal and c),d) spectral shape of the DUV pulses, retrieved from the FROG traces shown in Figure 4.19. a),c) refer to DUV generation via THG, while b),d) relate to DUV generation via SHG. It is assumed that the nonlinear signal within the UV-grade fused silica sample is generated in its front facet such that the pulse characterization is not compromised by chromatic dispersion effects during pulse propagation.

subsequently the DUV pulse duration, is generated at the front facet of the FROG's nonlinear medium (50  $\mu\text{m}$  UV-grade fused silica platelet). The above behavior in terms of generated DUV pulse duration for the two differing approaches is expected, since a solid-state target introduces more chromatic dispersion than a gaseous target like neon does. Consequently, it leads to a narrower phase-matching bandwidth, limiting the achievable pulse duration. Despite this fact, the gas in the THG approach can actually contribute negative dispersion through laser-induced plasma formation. Indeed, the results suggest that the THG approach tends to produce negatively chirped DUV pulses (Figures 4.19 a) and c)), while those generated via the SHG method carry a positive chirp (Figures 4.19 b) and d)). In both setups, we do not have the possibility to temporally compress them to the full extent after their generation, unless one is willing to employ specially designed chirped mirrors which are currently not available. Nonetheless, we determined the DUV pulse duration in either case as part of the full DUV pulse characterization in terms of polarization, pulse energy, temporal shape and spectrum.

	$E_{gen}$ [ $\mu J$ ]	$E_{target}$ [ $\mu J$ ]	$\tau$ [fs]	CWL [nm]	$\Delta\lambda$ [nm]	pol.	LTS
THG	2.3	0.9 <sup>†</sup>	5.8	246.0	24.1	"  "	–
SHG	5.2	2.0	11.7	268.5	11.2	"⊥"	+

**Table 4.4:** Tabulated properties of DUV pulses, generated either via THG or SHG, respectively. Here, we provide the set of values measured in both approaches and for which the DUV pulse duration was known through TG-FROG measurements. The listed values mean the following: DUV pulse energy at the place of generation ( $E_{gen}$ ) and on target ( $E_{target}$ ). Measured FWHM pulse duration ( $\tau$ ). Center wavelength (CWL) and spectral FWHM bandwidth ( $\Delta\lambda$ ). The DUV polarization (*pol.*) is given with respect to that of the NIR. Long-term stability (LTS) in terms of DUV flux are indicated *qualitatively* via + or –. The symbol <sup>†</sup> refers to the situation where NIR attenuation is neglected. In order to make this value comparable to the SHG associated value, one would have to consider the influence of the silicon wafer chicane on the total transmission factor, yielding 0.15  $\mu J$ .

#### 4.5.4 Comparison between THG Gas Target and SHG Solid State Target

Next, we compare the two DUV pulse generation schemes in terms of their usability for the ozone experiment. It should be mentioned that a general comparison between the SHG and THG approach proves difficult due to different prerequisites and varying performance of the laser at the time, when these measurements were carried out. Yet, big differences among the set of generated DUV pulses and between corresponding values are not expected to occur and, indeed, are not observed. On the whole, the *pros* and *cons* of both approaches are summarized in Table 4.4, giving an overview of typical performance values. Here, they refer to DUV pulses whose pulse duration is determined aside from other quantities. Among those, the pulse energy and duration, the spectrum-associated *center wavelength* (CWL) and its FWHM bandwidth should be mentioned, as these are, by far, the most important quantities regarding the feasibility of the ozone experiment. The pulse energy  $E_{gen}$  is retrieved by measuring the pulse energy with a powermeter<sup>10</sup> and the result is corrected for reflection and transmission factors of optical devices in between the places of generation and detection, respectively. The amount of energy, that a pulse carries when arriving at the target  $E_{target}$ , is derived in the same way, but is recorded at the back-end of the experimental chamber.

With respect to the amount of DUV pulse energy, we obviously do not generate that much more DUV via SHG than compared to THG in neon-filled gas cells (first column in Table 4.4). In erstwhile approaches, it was actually possible to generate even more DUV pulse energy up to 7  $\mu J$  and, in the first place, seemed to be more promising than SHG [56]. We attribute this to the fundamental NIR laser spectrum carrying the biggest amount of energy around 800 nm. Moreover, THG partly relies on plasma formation due to its benefits on fulfilling the phase-matching condition and it is thus not necessary to limit the NIR intensity prior to THG, e.g. by an aperture in front of the gas target. Compared to the maximum producible DUV pulse energy via SHG, THG was shown to perform better. Nonetheless, regarding the amount of DUV pulse

<sup>10</sup>We use an *Ophir Photonic Vega PD10-v2* powermeter

energy (second column in Table 4.4), that is transmitted onto the target, the situation is different. In case of THG, we report a value for  $E_{target} = 0.9 \mu\text{J}$ , that refers to DUV transmission from the delay chamber into the experimental chamber *without* NIR attenuation. In order to render this value comparable to its SHG-associated analogue ( $E_{target} = 2.0 \mu\text{J}$ ), where NIR attenuation is fully accounted for, one would have to consider the influence of the silicon wafer chicane on the resulting total DUV transmission. Special emphasis must be laid on the DUV polarization that is identical with that of the NIR. Because the DUV is shone on the silicon wafers at Brewster's angle of the NIR and in a p-polarized fashion with respect to the plane of incidence of the silicon wafer chicane, it is reflected very inefficiently (Figure 4.12). Consequently, this would yield an  $E_{target}$ -value that is approximately 14%<sup>11</sup> as big as the value given in Table 4.4. As a matter of fact, in case of SHG, we get roughly one order of magnitude ( $\approx 15\times$ ) more DUV on target, while still retaining the NIR-attenuating property of the silicon chicane, and experience little losses between the delay and experimental chamber ( $E_{target} = 0.9 \mu\text{J}$  (THG) vs.  $E_{target} = 2.0 \mu\text{J}$  (SHG)). This circumstance can be ascribed to the efficient separation of DUV from non-DUV spectral components.

Apart from a pulse energy viewpoint, the THG approach was initially believed to be more promising than its SHG counterpart, since it delivers shorter DUV pulses ( $\tau = 5.8 \text{ fs}$ ) than the SHG approach does ( $\tau = 11.7 \text{ fs}$ ). With regard to the ozone experiment, shorter DUV pulses would be highly advantageous in unraveling the fundamental molecular dynamics, while suffering less from temporal smearing. Nonetheless, this is only half the truth, since the experiment heavily relies on a *long-term stability* (LTS in rightmost column of Table 4.4) with regard to the DUV flux. This is equivalent to saying that a longer measurement-related integration time is necessary, compared to a laser with higher repetition rate. The former condition concerning the long-term stability is way easier to fulfill, because BBOs have a much larger aperture (3 mm in diameter) in the case of SHG, than in the case of THG (300  $\mu\text{m}$  THG target hole diameter). The latter makes the NIR beam leave the THG target quickly and leads to a total loss of DUV yield for minor long-term beam instabilities. Even the application of a two-stage beam stabilization feedback loop cannot get rid of this problem (subsection 4.5.1). Despite this, these long-term beam deviations are less crucial regarding the much bigger aperture of the BBO crystals, for the laser keeps interacting with the medium and delivers more or less stable DUV pulses over a long period of time. Another advantage of SHG over THG is that the polarization of the DUV with respect to the XUV is crucial (pol. in Table 4.4) and is addressed in section 4.3. Moreover, the DUV polarization is inherently rotated by the type-I SHG process and therefore perpendicularly polarized to the XUV, which makes successive rotation superfluous.

#### 4.5.5 Conclusion

Let us conclude: We have presented two compact DUV-generating as well as NIR-filtering schemes, which are investigated in the course of the present thesis. On the one hand, we focus on THG-based DUV generation in quasi-static gas-cells filled with neon. This approach has initially promised to be successful, as the wavelength of the DUV fits quite well to the third harmonic

<sup>11</sup>Reflectivity at a single silicon wafer for  $75^\circ$  angle of incidence is  $R_{Si} = 0.38$  at  $\lambda = 241 \text{ nm}$

of our fundamental NIR laser wavelength. On the other hand, we make use of solid-state based type-I SHG scheme in ultrathin (20  $\mu\text{m}$ ) BBO crystals and in single pass configuration. This attempt is less obvious, since our laser spectrum lacks components at wavelengths between 500 nm and 600 nm, essential for efficient second harmonic generation. In both cases, we conduct experiments on their long-term stability regarding DUV photon flux, on their reliability due to experimental insufficiencies and on their overall suitability with regard to a direct measurement of the ozone-photodissociation via pump–probe TRPES-experiments. Further, we performed a full characterization of the DUV pulses with regard to their pulse energy content at the place of their generation and after arrival at the ozone target. The pulse duration, spectrum and polarization is also looked at explicitly. Moreover, we find a way of eradicating the fundamental NIR pulse as well as possible, while not losing much of the DUV. The former is indispensable to get rid of NIR contributions which otherwise tend to compromise the results of the ozone-experiment, as one could not easily discern between DUV-induced chemical shifts and NIR contributions via attosecond streaking. On the whole, we conclude that the SHG-based DUV generation setup performs better and is advantageous over the gas-based THG target, because it directly delivers the right DUV polarization and results in a more efficient DUV separation from NIR (attenuation factor:  $> 10^4$ ). Despite the great number of advantages, the SHG-DUV scheme exhibits some drawbacks originating from the thinness of the BBO crystals. Under the thermal load, exerted by the green spectral components of the NIR radiation, the crystals usually bend. After several heating and cooling cycles<sup>12</sup> the crystals eventually break due to insufficient mechanical stability. Thicker crystals should get rid of this problem.

## 4.6 Synthesis of Highly Pure Ozone — Sample Preparation

Before we discuss our results considering the electronic and nuclear dynamics of ozone after DUV excitation, the sample preparation shall be discussed, as investigation of its photodynamics enforces the presence of a highly-pure sample thereof. Unfortunately, ozone is a metastable and volatile substance that cannot be stored in gas bottles for an arbitrarily long time. Illumination with light, high temperature, reaction with organic compounds or even vibrations could trigger exothermic fragmentation of ozone into atomic and diatomic oxygen which, in turn, would cause further fragmentation of surrounding ozone molecules in an uncontrollable fashion and usually leads to explosion. One way out of this dilemma is provided by our ozone distillation setup, depicted in Figure 4.21, and shows an assembly that is capable of producing a sufficient amount of highly pure ozone [56]. We will explain its functionality from left to right: Starting substance is bottled, pure oxygen, which is fed into a high-voltage gas discharge unit (subsequently termed ozonizer<sup>13</sup>) at low pressure around 0.05 bar between inlet and outlet and with a flux of 200 Nl/h. The gas-discharge leads to fission of diatomic into atomic oxygen. The latter forms ozone molecules by bonding to other diatomic oxygen molecules. Finally, an  $\text{O}_2/\text{O}_3$ -mixture with a low concentration of ozone leaves the ozonizer. The next part is essential to generate a highly pure

<sup>12</sup>due to unblocking and blocking of the laser in front of the BBOs

<sup>13</sup>*Sander Labor-Ozonisator 301.19.*

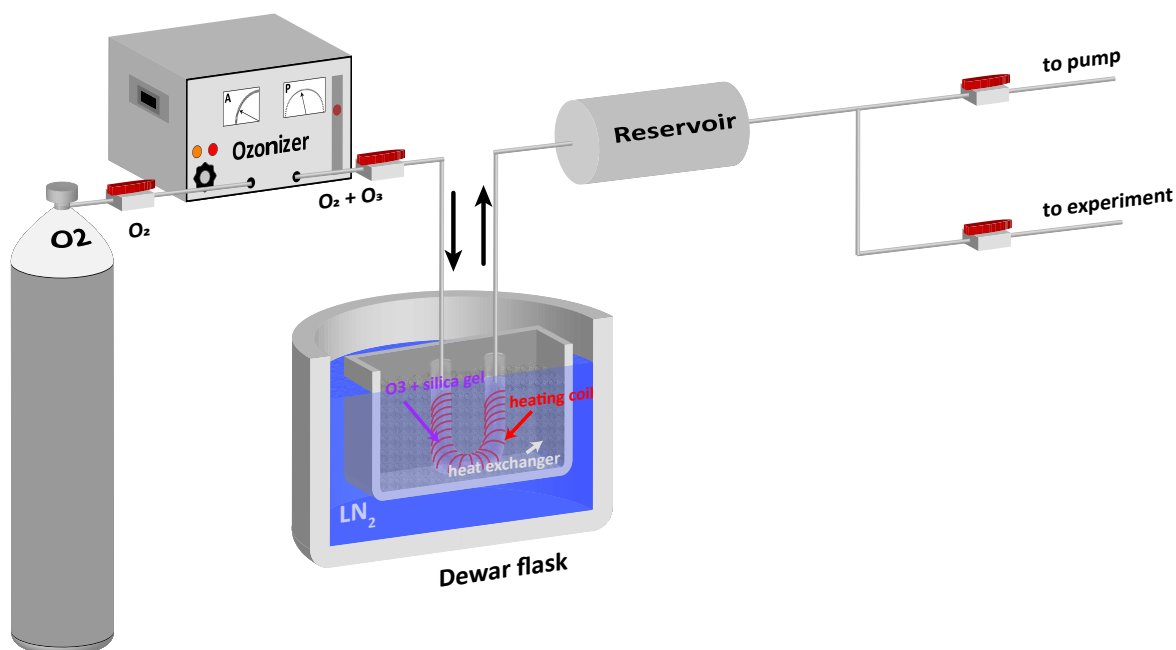


**Figure 4.21:** Schematic sketch of the high-purity ozone distillation setup. See main text for a detailed description.

ozone sample and serves as a filtering stage to get rid of parasitic oxygen, while it accumulates desirable ozone. It consists of a Dewar flask filled with *liquid nitrogen* ( $LN_2$ ;  $T = 77\text{ K}$ ). Into the  $LN_2$  we dipped another container made from steel, which itself contains a U-shaped silica and is surrounded by metal washers. The latter serve as heat exchanger, serving to establish a thermal contact between the U-shaped silica pipe and the surrounding  $LN_2$  thermal bath. A heating coil wrapped around the U-shaped silica pipe allows us to tune its temperature via a computer-controlled feedback loop. The U-shaped silica pipe is filled with silica gel, traversed by the  $O_2/O_3$ -mixture and is only connected to stainless steel tubes before and after it. Silica gel is used here to hamper the sudden conversion of ozone into oxygen. The use of stainless steel tubes is indispensable, because ozone turns out to be inert only against a few materials. Among those are Teflon<sup>®</sup>, silica and stainless steel. The separation of ozone from oxygen works as follows: We cool the U-shaped silica pipe down to  $-90\text{ °C}$  forming a cold trap for ozone and keep it constant throughout distillation. At this temperature, ozone and oxygen do not liquefy, but remain gaseous. Owing to the higher vapor pressure and smaller surface area of oxygen than compared to those of ozone, it does not get trapped and leaves the cold trap, in contrast to ozone. Ozone itself adsorbs to the silica gel and accumulates within the cold trap. Once, we have created a sufficient amount of ozone, the entire assembly gets flushed with oxygen, while the ozonizer has been shut off in the meantime. Then, the oxygen supply will be stopped via valves before and after the ozonizer in order not to damage it and the ozone distillation setup is pumped down to a few mbars to get rid of residual oxygen. After this step,

all valves are closed (valves labeled as "to pump" and "to experiment" as well as the valve at the ozonizer outlet) and we gradually heat our ozone-containing U-shaped silica pipe. Meanwhile adsorbed ozone desorbs from the silica gel and collects itself in another container serving as a sample reservoir. The reservoir pressure is permanently monitored and stabilized by a computer program, effectively supplying the experiment with a constant flow of ozone molecules. The purity of ozone is determined separately in the following way: Once we have temporarily stored a certain amount of ozone inside our reservoir, we measure its pressure, while it is isolated from the rest of our distillation setup. Then, we keep heating it up until the  $O_2/O_3$ -mixture converts into oxygen, according to the reaction



If we stored pure ozone in our reservoir, we would expect the pressure to have increased by 50% when measured at identical temperatures and by using equation (4.16). The following formula yields the purity  $C(O_3)$  of desorbed ozone [56]

$$C(O_3) = 2 \frac{p_e - p_s}{p_s - p_0}, \quad (4.17)$$

where  $p_s$ ,  $p_e$  and  $p_0$  stand for the reservoir pressure before and after conversion as well as for its residual pressure after pumping down. In that way, we determine a purity of 99% for desorbed gas. The purity usually deteriorates insignificantly with time and even after hours we measure concentrations exceeding 95%.

## 4.7 Ozone vs. Oxygen Photoelectron Spectra and Energy Domains

In the current section, we will eventually discuss the experimental results concerning the photodissociation dynamics in ozone, which are obtained by few-femtosecond XUV probe pulses and intense ultrashort DUV pump pulses, as explained in sections 4.4 and 4.5. Nonetheless, before being able to discriminate between ozone and oxygen related dynamics, some preliminary considerations are inevitable. They are necessary for the definition of distinct energy domains of our DUV-XUV-spectrograms, which can be unambiguously identified with either the ground X or excited B state dynamics of ozone or, alternatively, with oxygen dynamics. The latter indicate successful ozone photodissociation. Consequently, we recorded photoelectron spectra of pure ozone and pure oxygen one after another on the same day and under identical conditions with the XUV probe pulse present only (1.7 fs Fourier limit FWHM pulse duration, 99.5 eV central photon energy, 1.1 eV FWHM bandwidth). The result is depicted in Figure 4.22 as a function of photoelectron kinetic energy. Both spectra are normalized to their inelastically scattered background between 50 eV and 70 eV.

The blue solid line stands for the ozone-related, while the red solid line represents the oxygen-related photoelectron spectrum. Obviously, the ozone photoelectron spectrum comes along with

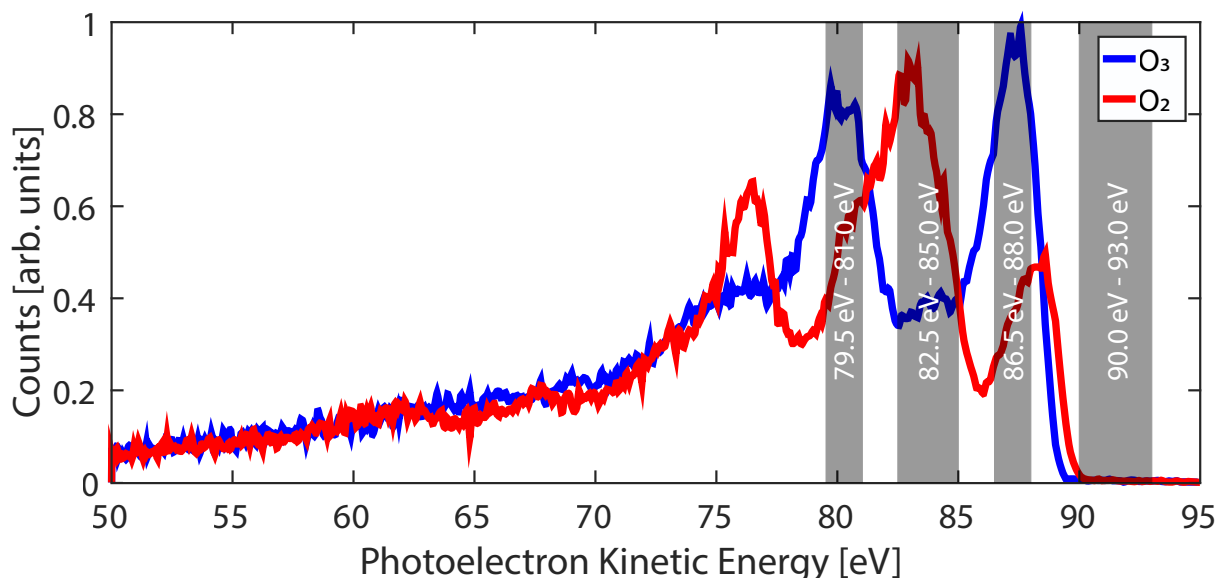


**Figure 4.22:** Exemplary photoelectron spectra of ozone (blue solid line) and oxygen (red solid line), recorded with our XUV probe pulse present only (1.7 fs Fourier limit FWHM pulse duration, 99.5 eV central photon energy, 1.1 eV FWHM bandwidth). Both spectra are normalized with regard to their inelastic background (50 eV – 70 eV). The gray shaded areas determine the four most important energy domains used in the analysis of molecular dynamics in ozone.

a two-peaked structure, which we have already related to certain, energy-bunched cation states, in conjunction with their convolution with the XUV spectrum (subsection 4.3.2), whereas the oxygen-related photoelectron spectrum exhibits a three-peaked structure. Thus, both spectra can be well distinguished from each other. Moreover, the most prominent peak of the oxygen spectrum (82.5 eV – 85 eV), accidentally falling in the energy region midway between the two outer peaks of the ozone photoelectron spectrum (79.5 eV – 81 eV and 86.5 eV – 88 eV) in a time-resolved measurement. Probably, it would show up at the expense of ozone-related peaks and this is exactly what we are going to see (subsection 4.8.1). However, for the time being, we have just determined the energy domains relating to cation states of the ground X state of ozone and to cation states of oxygen, which are not described in more detail. Anyway, we are mainly interested in the excited B state dynamics and therefore expect — by comparison with the cation states discussed in subsection 4.3.2 — them to fall within the energy domain between 90 eV and 93 eV. Choosing 90 eV as lower bound for the B state energy domain ensures oxygen-related photoelectrons to not contribute to dynamics that are linked to excited B state dynamics.

To conclude, by comparison between the photoelectron spectra of ozone and oxygen, respectively, and with the help of the cation states of ozone, we have defined dynamics-related energy domains.



These are going to be used in the subsequent discussion regarding the temporal evolution of the ground X state and excited B state of ozone as well as dynamics corresponding to the buildup of oxygen, following ozone photodissociation. They are listed below again, including the cation states of ozone, as listed in Table 4.3. Although the cation states of oxygen are not known, they can be related to ionization from specific orbitals, which are also given below and are taken from [93] and [94], respectively:

- (I): 79.5 eV – 81.0 eV ( $O_3$ : X-16 to X-19)
- (II): 82.5 eV – 85.0 eV ( $O_2$ :  $1\pi_u$  and  $2\sigma_g$ )
- (III): 86.5 eV – 88.0 eV ( $O_3$ : X-1 to X-3)
- (IV): 90.0 eV – 93.0 eV ( $O_3$ : B-1 to B-3)

## 4.8 Results and Discussion

Now, that we have defined the oxygen and ozone dynamics-related energy domains, we use these to retrieve the temporal evolution of the three species-associated dynamics:

1. ozone in the ground state,
2. ozone in the excited state,
3. oxygen.

Therefore, we will present in the next subsection a DUV-XUV-spectrogram of ozone recorded in few-femtosecond timescale TRPES-experiments and is composed of all collected scans. Following this, we finally turn our attention to the temporal evolution of the involved species, as brought up above. The experimental results are deduced from the DUV-XUV-spectrogram and are compared to simulated traces with regard to the temporal evolution of the excited B state. Qualitative agreement between theory and experiment allows us to interpret the results in terms of nuclear wave packet motion on the excited B state PES by comparison to nuclear wave packet density plots simulated via the MCTDH approach (subsection 4.2.1).

### 4.8.1 DUV–XUV Pump-Probe-Measurement of Ozone

Figure 4.23 depicts the combined, all measurements-comprising ozone DUV-XUV-spectrogram, that is recorded in cross-polarized DUV–XUV pulse train geometry (section 4.3). The question of how we combine the individual spectrograms to the resulting one (Figure 4.23) is subject of subsection 4.8.2. In addition to the mere spectrogram, an exemplary ozone photoelectron spectrum together with the energy domains, defined in section 4.7, is depicted on the left-hand side of Figure 4.23 for orientation. Please note that the spectrogram is plotted, using a logarithmic color scale for better visibility of the evolving molecular dynamics. Moreover, all measurements are performed at an MCP voltage of 2.15 kV and at a voltage of 600 V at the electron electrostatic lens of the TOF detector. The backing pressure in the ozone reservoir is stabilized to roughly 100 mbar and the TOF backing pressure is held below  $2 \times 10^{-6}$  mbar

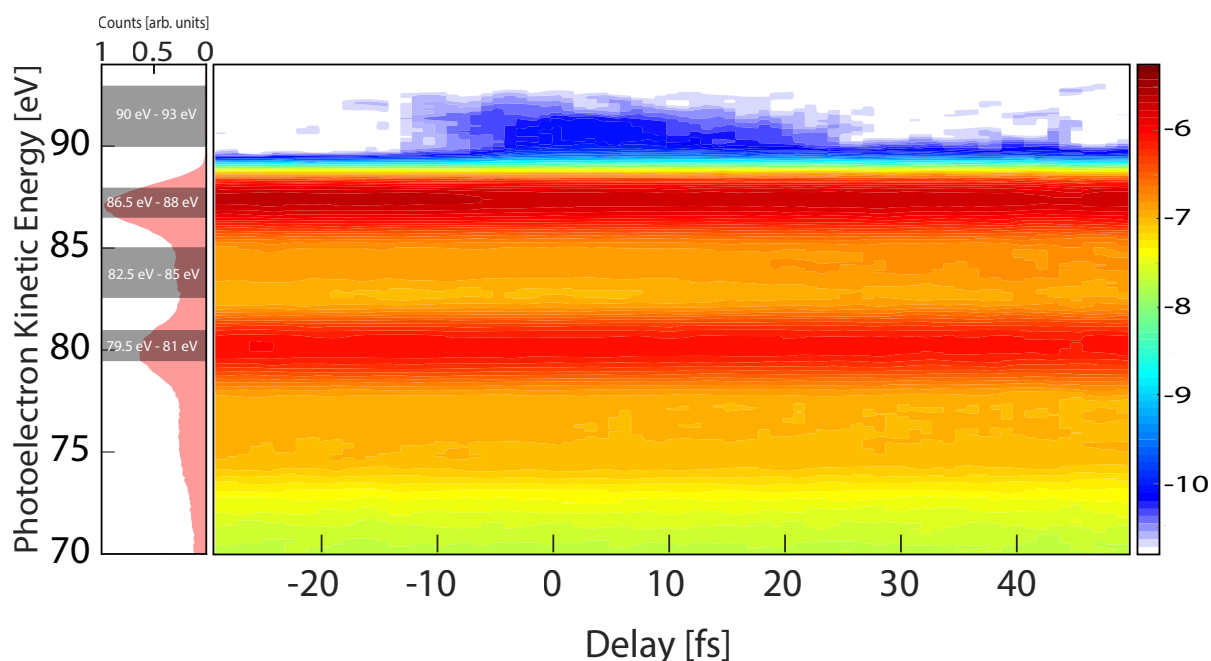


**Figure 4.23:** *Right:* DUV-XUV-spectrogram of ozone. Negative delay refers to the situation where the XUV probe pulse precedes the DUV pump pulse. Data is shown, using a logarithmic color scale (right bar). *Left:* A typical ozone photoelectron spectrum — together with the energy domains defined in section 4.7 — is plotted for orientation.

throughout our measurements in order to neither damage the MCP nor to falsify our data via MCP-related saturation effects. We further mention that all individual measurements are recorded on different days, but under otherwise identical conditions. Without going to much into detail, we recognize some transient changes showing up in Figure 4.23. Especially, the clear high-energy edge (90 eV – 93 eV) along the photoelectron kinetic energy axis (for negative delay times) is most striking and lasts for 40 fs only. This feature can be identified with the B state dynamics of ozone and will be discussed separately in subsection 4.8.5.

## 4.8.2 Multi-Level Data Analysis Scheme

To make up for the missing methodological strategy leading to the presented spectrogram (Figure 4.23), we are making good for this right here. The method is presented next and explicitly exemplified for the example of all six individual measurements, which the overall spectrogram is composed of: Once we have measured a single spectrogram, we convert in a first step each of its spectra individually from photoelectron time of arrival at the MCP detector into absolute values of photoelectron kinetic energy. An XUV photon, being scattered off the sample instead of ionizing another electron upon contact, needs negligible time to reach the MCP detector, because it travels at the speed of light along the TOF-axis towards the detector. Within the MCP material, it releases electrons at the time, that is defined as time "zero" here, since these ejected

electrons did not have to travel the distance between the actual sample and the MCP detector. The thus created signal can then be used as a timing reference and is referred to as the *lightpeak* and is reminiscent of time "zero" of a stop watch. All photoelectron arrival times, being measured with respect to the lightpeak, can then unambiguously converted to absolute photoelectron kinetic energy values due to the well-defined reference time. In a second step, potentially residual momentum shifts, that are linked to NIR-induced parallel streaking, are removed from the spectrogram for every delay time step. Subsequently, the resulting spectrum is normalized to its background between 50 eV to 75 eV. Normalization is required, because different spectra may contain a varying number of photoelectrons depending on which measurement they belong to. The third step is the most crucial for the entire analysis of the ozone-related molecular dynamics and relies on a fitting procedure (fit function is given in equation (4.18)). The idea behind this step is to establish a common delay time scale among all individual measurements. Therefore, we need to define a moment in time  $t_0$ , that is the same for all measurements and which every single data point can be related to. Since we assume that our DUV pulses are all similar to each other, even when employed on different days, it seems to be reasonable to define that very moment, by when the B state population takes on its maximum value<sup>14</sup>. Beyond this, our approach proves itself legitimate, because the rise time in the temporal evolution of the B state population is more or less the same for all measurements (Figure 4.24). Now, determination of this moment is accomplished by adding up all the B state-related photoelectrons between 90 eV and 93 eV as a function of delay time. Then, we adjust the total fit function (equations (4.18) – (4.22)) so that it represents the data as well as possible. Except for the mere fitting of the B state temporal evolution, the very same function is also used to describe those of the ground X state and oxygen. The results for the six individual scans are displayed in Figure 4.24, where they are already centered around the maximum value of the fit function, i.e. where the maximum coincides with  $t = 0$ . The total fit function is given as:

$$F(\{b\}, t) = G(\{b\}, t) * [H(\{b\}, t) \cdot (E(\{b\}, t) + C(\{b\}, t))] + \text{offset}, \quad (4.18)$$

$$G(\{b\}, t) = A_G \cdot \exp\left(-\left(\frac{t-t_0}{t_G}\right)^2\right), \quad (4.19)$$

$$H(\{b\}, t) = \begin{cases} 1 & \text{for } t \geq t_0 \\ 0 & \text{otherwise} \end{cases} \quad (4.20)$$

$$E(\{b\}, t) = A_E \cdot \exp\left(-\frac{t-t_0}{t_D}\right), \quad (4.21)$$

$$C(\{b\}, t) = A_C \cdot \cos(\omega \cdot (t-t_0)), \quad (4.22)$$

<sup>14</sup>Actually we will use the instant of time as reference, where the fit function (equation (4.18)) takes on its maximum value, owing to the fact that our measurement points are coarsely sampled in time and the sought moment may lie between two such delay time steps.

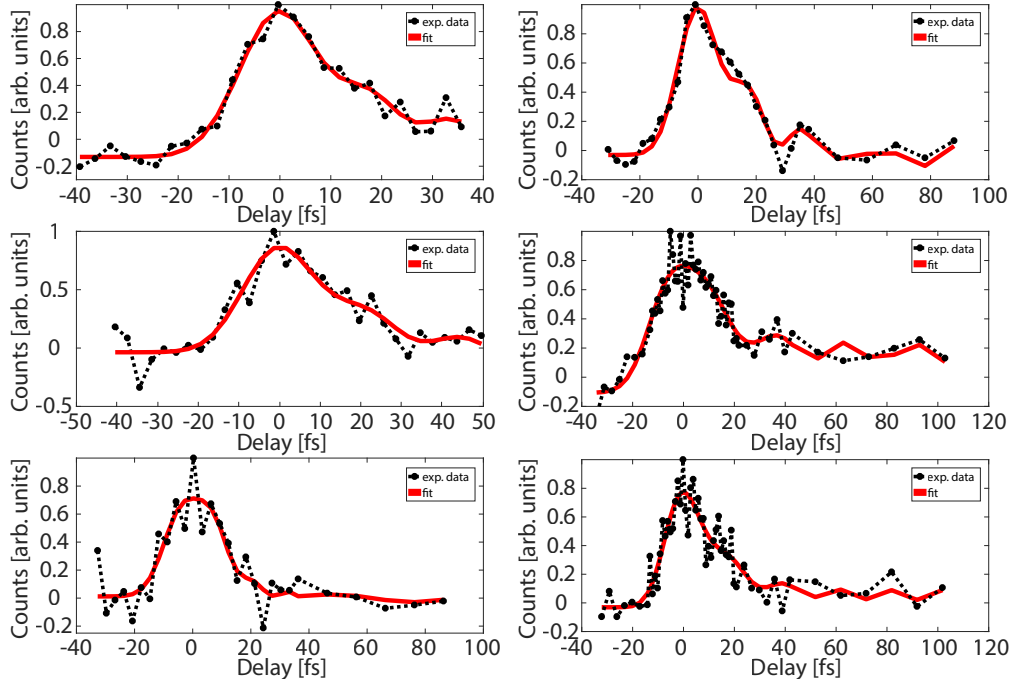


**Figure 4.24:** Energy-integrated photoelectron yield between 90 eV and 93 eV as a function of delay time in order to find  $t_0$ , as explained in the main text (already centered about time  $t = 0$ ). Black dots stand for experimental data. Red solid curve depicts the fit to the data via equations (4.18) – (4.22)). Please note the different time axes and that the rise time of the B state population is identical for all plots.

where  $\{b\}$  denotes the set of fit parameters.

Some remarks on the total fit function: As the excitation is usually a step-like process (one-photon transition), that is represented by a Heaviside-function (equation (4.20)),  $H(\{b\}, t)$ , we need to account for the temporal blur on the measurement, introduced by the non-vanishing DUV pump and XUV probe pulse duration. This is realized in form of a convolution between the Heaviside function and a Gaussian function,  $G(\{b\}, t)$  (equation (4.19)). Additionally, for the residual part of equation (4.18), we need to add another part taking the temporal evolution of the B state-related dynamics into account. The latter are represented by equations (4.21) – (4.22). There, we presume their temporal evolution to be optimally described by a sum of an exponential decay function  $E(\{b\}, t)$  and a cosine function  $C(\{b\}, t)$ , where both are multiplied with a Heaviside function, as their dynamics cannot start evolving before excitation takes place ( $t \geq t_0$ ). The exponential decay function itself considers the transient character of the B state population, which inevitably leads to ozone photodissociation. The cosine function, instead, anticipates an oscillatory behavior in the measured number of B state-related photoelectrons. The reason for this oscillation is subject of the discussion in section 4.9. By now, we have fitted the time-dependent B state-related photoelectron yield (Figure 4.24) employing equations (4.18) – (4.22). We have determined the moment  $t_0$  of maximum B state population individually for

all scans and shift all these scans such that their maximum coincides with  $t = 0$ , rendering all traces comparable. In the last step, we simply concatenate all spectra from all measurements in ascending order of delay time, since we know their exact timing with respect to the maximum B state population now. With this procedure, we arrive at the resulting spectrogram, shown in Figure 4.23.

### 4.8.3 Temporal Evolution of Ground X State Depletion

After having discussed our multi-level data analysis scheme, we make use of it in determining the temporal evolution of the number of ground X state-related photoelectrons in particular, according to the above scheme. Therefore, every data point in Figure 4.25 a) is obtained by binning together those spectra that fall within one femtosecond before the resulting spectrum is integrated over the respective X state-associated energy domains (79.5 eV – 81 eV and 86.5 eV – 88 eV). The vertical error bars and the red-shaded area refer to the 95% confidence interval of the data (black dots) and the fit (red solid line), respectively.

Figure 4.25 a) clearly shows depletion of the ground X state of ozone, starting at  $-10$  fs and lasting until 10 fs. Although one would expect the X state dynamics to be completed, once the DUV pump pulse has interacted with the ozone molecule, the measurements suggest that there is an intermediate recovery of the ground X state population between 10 fs and 40 fs. However, we believe this temporary rise to be partially attributable to a simultaneous build-up of oxygen, following ozone photodissociation. Since we added all the photoelectrons up that fall in the energy range between 79.5 eV – 81.0 eV as well as 86.5 eV – 88 eV, we know from section 4.7 that the ozone- and oxygen-related photoelectron spectra partially overlap spectrally (Figure 4.22). This, in turn, leads to ground X state-related data, that is compromised by oxygen-related data. Unfortunately, it turns out to be very hard to disentangle these two contributions from each other, even when using a global fit routine like implemented in *GLOTARAN* [95] and is most likely caused by insufficient changes with regard to the state populations. Nonetheless, Figure 4.25 b) presents simulated traces of the temporal evolution concerning the number of photoelectrons for certain photoelectron kinetic energy values (solid lines), as they would be detected along the XUV probe pulse polarization for a similar configuration as ours. Although it resembles the experimental data qualitatively well (especially for 80 eV (black solid line), 86 eV (brown solid line) and 88 eV (green solid line)) with exception for a small temporal offset between the experimental and theoretical curves towards greater delay times, our measurement does not resolve the predicted oscillations (Figure 4.25 b)). The discussion and interpretation of these oscillations is postponed to subsection 4.9.1.

### 4.8.4 Temporal Evolution of Oxygen Build-Up

Figure 4.26 illustrates the temporal evolution of the number of  $O_2$ -related photoelectrons (82.5 eV – 85 eV) in the same way, as explained in subsection 4.8.3. It is interesting that the onset of  $O_2$ -formation, following ozone photodissociation, takes place only 10 fs after the ground X state has partially been depleted under the impact of the DUV pump pulse. Precisely, it starts at 10 fs and lasts until 20 fs, but the entire dynamics is not over yet, but it rather seems, as if there

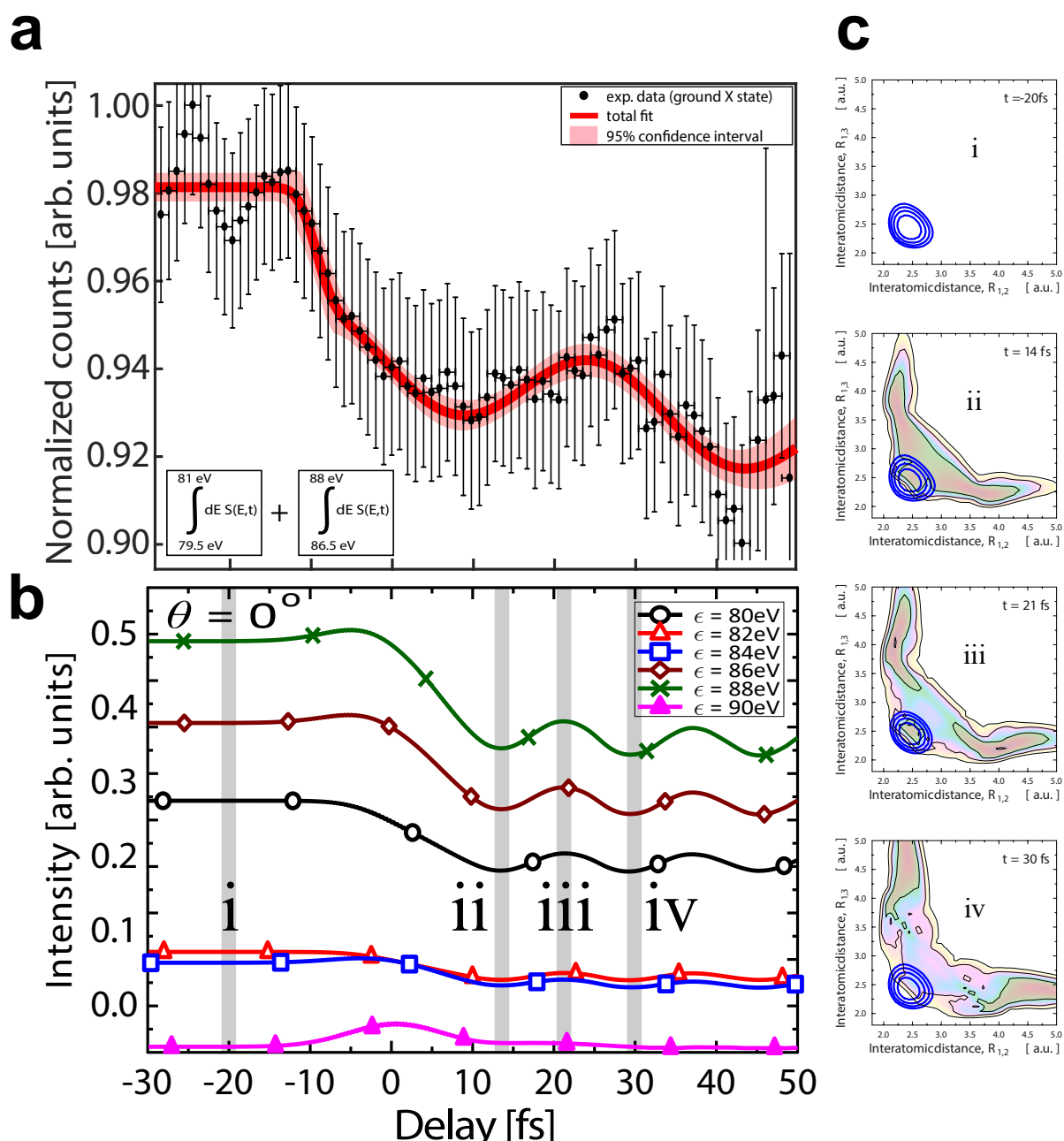


**Figure 4.25:** a) Experimentally attained temporal evolution of the integrated number of X state-related photoelectrons from the spectrogram  $S(E, t)$  as a function of delay time  $t$ , where integration is performed over their respective energy domains (79.5 eV – 81 eV and 86.5 eV – 88 eV). Horizontal error bars depict the *estimated* temporal uncertainty in assigning a data point to a certain delay time. Vertical error bars and red-shaded area refer to the 95% confidence interval of data (black dots) and fit (red solid line), respectively. b) Simulated temporal evolution of the number of photoelectrons for certain kinetic energy values, but restricted to the FC point only. The curves associated with 80 eV (black solid line), 86 eV (brown solid line) and 88 eV (green solid line) can be interpreted with the temporal evolution of the ground X state population. c) shows ground X state-related nuclear wave packet density plots (blue isolines with contour values  $1e0$ ,  $1e-1$ ,  $1e-2$  and  $1e-3$ ) for four instants of time ( $-20$  fs (*i*), 14 fs (*ii*), 21 fs (*iii*) and 30 fs (*iv*)). Adapted with courtesy of Ágnes Vibók and Gábor J. Halász.

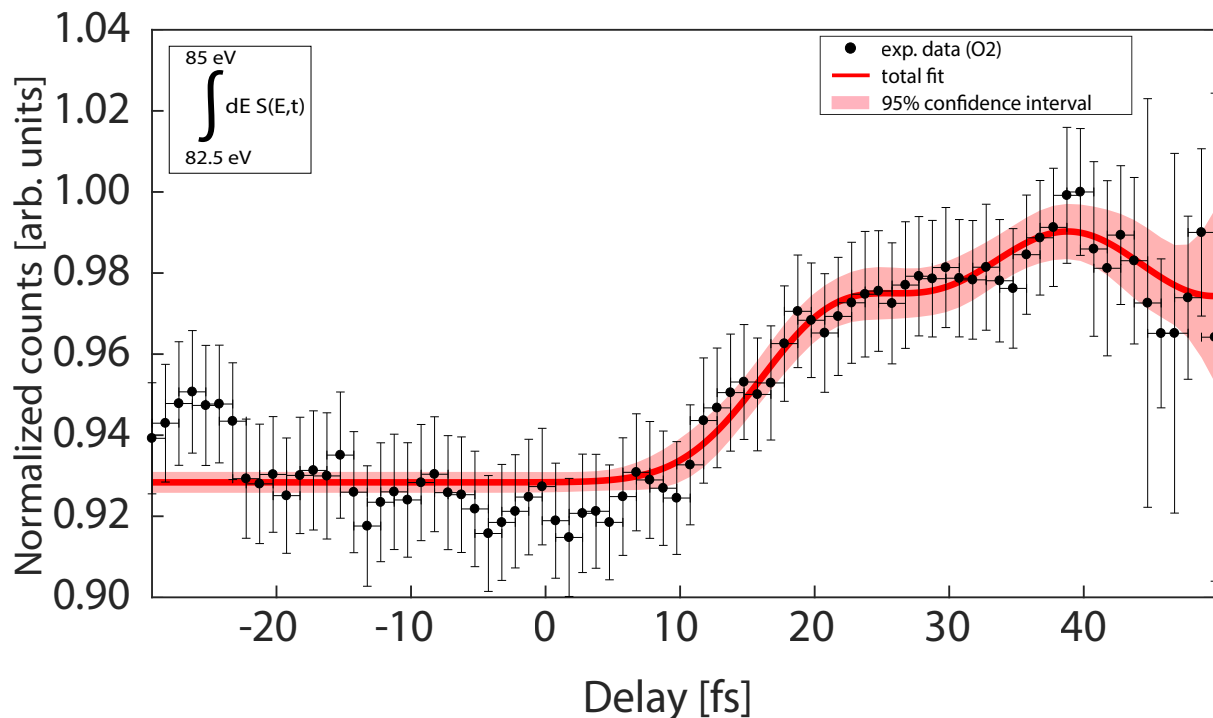


**Figure 4.26:** Experimentally attained temporal evolution of the integrated number of  $O_2$ -related photoelectrons from the spectrogram  $S(E, t)$  as a function of delay time. Integration is performed over its respective energy domain (82.5 eV – 85 eV). Horizontal error bars stand for the *estimated* temporal uncertainty in assigning a data point to a certain delay time  $t$ . Vertical error bars and red-shaded area refer to the 95% confidence interval of data (black dots) and fit (red solid line), respectively.

is another increase in the number of  $O_2$ -related photoelectrons between 30 fs and 40 fs, though with decreasing amplitude, as compared to the first  $O_2$  rise. We will see later on that the second jump has a physical origin with respect to nuclear wave packet motion on the excited B state PES and is accompanied by nuclear wave packet recurrences (section 4.9).

#### 4.8.5 Temporal Evolution of the Transiently Populated B State

Now, we look into the intermediate dynamics showing up between ground X state depletion and  $O_2$ -formation. They take place on the excited B state PES and this is why we pay our attention to this process. Unlike the previous treatment, we combine the B state-related temporal evolution profiles (Figure 4.24), reorder all the data points in ascending order of delay times, and bin those data points together, that fall within one-femtosecond, just as we did before, but with one crucial difference. Since the signal strength, i.e. the absolute number of B state-associated photoelectrons is way smaller than those of the ground X state or  $O_2$  due to a smaller B-state population and squared *Dyson norm*, we pursuit a different *ansatz*. Prior to temporal binning,

we subtract their constant background and normalized each trace with respect to its maximum value. These steps have already been accomplished in the plots shown in Figure 4.24. This proceeding makes sure that the B state-related data is corrected for potential deviations among different measurements in terms of DUV intensity. Remember that all of the six measurements were recorded on different days with slightly varying DUV pump pulse parameters. The idea behind this *ansatz* is that the B state-associated dynamics evolve independently of the exact strength of the DUV intensity and are exclusively dictated by the B state PES topography and wavelength of the DUV pump pulse. The latter is kept constant for all measurements. The result is displayed in Figure 4.27 a). Once again, horizontal error bars denote the estimated temporal uncertainty in assigning a single data point to a specific delay time. Vertical error bars and the red-shaded area refer one more time to the 95% confidence interval, respectively. The fit parameters amount to  $(9.6 \pm 0.9)$  fs for the Gaussian part,  $(19.6 \pm 1.8)$  fs for the oscillating part and  $(16.5 \pm 2.7)$  fs for the exponential decay constant of equation (4.18). The specified errors refer to the 95% confidence interval. Figure 4.27 b) shows an energy-integrated, simulated trace of the very same B state dynamics with DUV pump pulse parameters, as defined in subsection 4.8.3. The simulation explicitly takes the angle  $\theta$  between detection axis and XUV probe pulse polarization into account. It shows exactly the angle dependence in the number of detected photoelectrons derived from a group theoretical viewpoint (section 4.3). Figures 4.27 a) and b) agree qualitatively well with each other. We monitor a build-up of the B state excitation between  $-20$  fs and  $0$  fs. By  $t = 0$  fs, the DUV pump pulse has already passed the ozone molecule, meaning that everything that happens after this moment is due to the molecular dynamics. These, in turn, are exclusively steered by the topography of the B state PES. Except for a sole exponential decay of the B state excitation, we clearly observe an oscillatory behavior in both plots with maxima located around  $0$  fs,  $20$  fs and  $40$  fs, while traversing a minimum around  $34$  fs, where the B state-related photoelectron yield nearly drops to zero. The reason for that will be unveiled in the next section.

## 4.9 Interpretation

Finally, we give a physical interpretation of all the differently evolving temporal profiles, discussed in subsections 4.8.3 – 4.8.5. We will recognize that they foot on a common ground. The qualitatively good agreement between Figures 4.27 a) and b) allows us to interpret the molecular dynamics by looking at the simulated evolution of the nuclear wave packet density on the ground X and excited B state PESs, respectively.

We will start describing the X state dynamics in subsection 4.9.1 first, before we will look more deeply into the excited B state dynamics in subsection 4.9.2. Density plots of the X state-associated nuclear wave packet are depicted as blue contours<sup>15</sup> in Figure 4.25 c) and those corresponding to the B state (colormap) are displayed in Figure 4.27 c) as colormap plots. In the former case, they refer to the times indicated by gray lines in Figure 4.25 b) ( $-20$  fs (*i*),  $14$  fs (*ii*),  $21$  fs (*iii*) and  $30$  fs (*iv*)), while in the latter case, they belong to the gray lines in Figures 4.27 a) and b) ( $-20$  fs (I),  $0$  fs (II),  $20$  fs (III),  $34$  fs (IV) and  $40$  fs (V)).

<sup>15</sup>contours correspond to values of  $1e0$ ,  $1e-1$ ,  $1e-2$  and  $1e-3$



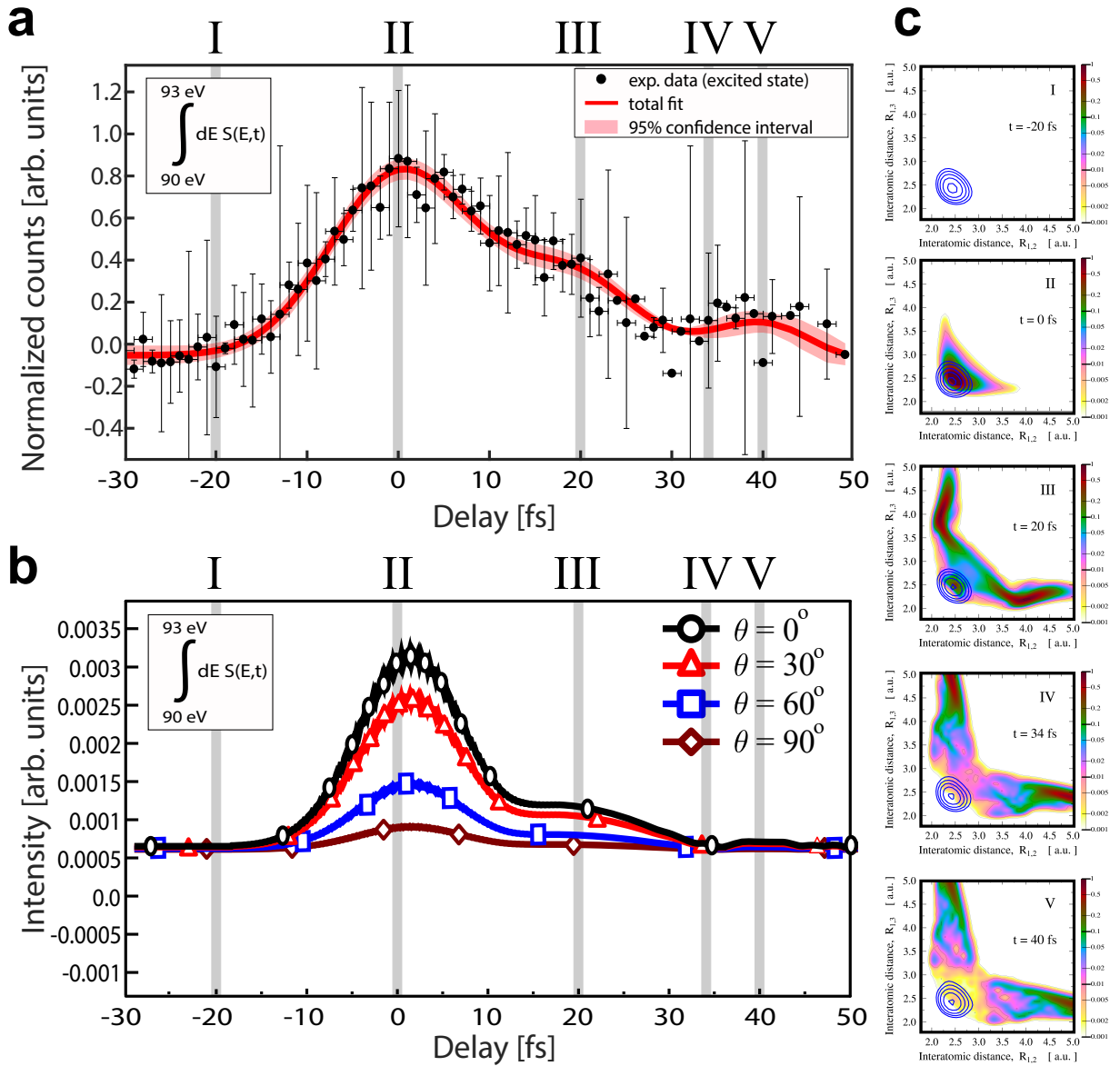


**Figure 4.27:** a) Experimentally attained and b) simulated temporal evolution of the integrated number of B state-related photoelectrons from the spectrogram  $S(E, t)$  as a function of delay time. Integration is performed over its respective energy domain (90 eV – 93 eV). Horizontal error bars depict the *estimated* temporal uncertainty in assigning a data point to a certain delay time  $t$ . Vertical error bars and red-shaded area refer to the 95% confidence interval of data (black dots) and fit (red solid line), respectively. The simulation in b) assumes interaction of a randomly oriented ozone molecule ensemble with a 10 fs Gaussian DUV pump pulse, centered around 268 nm, and carrying a pulse energy of  $(2.0 \pm 0.5) \mu\text{J}$ . Photoemission is simulated for four angles  $\theta$ , defined as the angle between detection axis and XUV probe pulse ionization. Here, only wave functions at the FC point are considered in the calculation. c) shows snapshots of the evolving nuclear wave packet on the excited B state PES (colored contour plots) for five instants of time ( $-20$  fs (I),  $0$  fs (II),  $20$  fs (III),  $34$  fs (IV) and  $40$  fs (V)). *Adapted with courtesy of Ágnes Vibók and Gábor J. Halász.*

### 4.9.1 X State-related Nuclear Wave Packet Motion

The overall temporal evolution of the ground X state dynamics is very subtle and depicted in Figure 4.25 c). However, we will provide a physical interpretation, explaining the origin of the oscillations showing up in the temporal evolution of the ground X state-related photoelectron yield. The following discussion always refers to Figures 4.25 b) and c). At  $t = -20$  fs, the nuclear wave packet of the molecule is solely located on the X state PES at its equilibrium position, that is the FC point ( $R_{1,2} = R_{1,3} = 2.42$  a.u.). Its shape serves as a reference from now on (Figure 4.25 c) (*i*:  $-20$  fs)). By  $t = 14$  fs, the DUV pump pulse has already interacted with the ozone molecule and has partially depleted the ground X state, preferably at the FC point, and consequently leads to less X state population at this point. This so-called *R-selective* depletion triggers vibrational motion of the ground state nuclear wave packet. By *R-selective* depletion, we mean that depletion heavily depends on the position of the ground X state nuclear wave packet, with respect to the nuclear coordinate space, and favors depletion at the FC point, whereas it inhibits depletion for other nuclear configurations. Since our DUV pump pulse is on resonance with the  $X \rightarrow B$  transition at the FC point and due to the fact that the transition energy changes with the nuclear configuration — attributed to different evolving topographies of the X and B state PESs with nuclear configuration — it is not surprising that there might be an *R-selectivity*. As recently discussed in [96], though for strong-field ionization, *R-selective* depletion may indeed lead to nuclear motion, as the nuclear wave packet is not in a steady state any more afterwards. Consequently, by  $t = 14$  fs (position of first minimum in Figure 4.25 b)), the center of the nuclear wave packet has been displaced upon depopulation of the ground X state at the FC point towards increasing interatomic distances ( $R_{1,2} = R_{1,3} \approx 2.5$  a.u.). This is equivalent to nuclear motion of the ground X state-associated nuclear wave packet. Because our colleagues solely focus on the FC point when calculating the photoelectron yield from the ground X state, their simulations predict a minimum at  $t = 14$  fs owing to a decreasing nuclear wave packet density at that point. By  $t = 21$  fs, the nuclear wave packet had enough time to move back to the FC point, therefore increasing its density there again. This, in turn, makes the simulated photoelectron yield grow (first maximum in Figure 4.25 b) (*iii*: 21 fs)). One remark on the shape of the nuclear wave packet. Obviously, it is squeezed symmetrically along the diagonal of the nuclear coordinate space at this moment and differs to some extent from the shapes, which the nuclear wave packet takes on at  $t = 14$  fs or  $t = 30$  fs, respectively. By  $t = 30$  fs, one full vibrational motion of the nuclear wave packet on the ground X state PES is completed, explaining why we observe another decrease in the photoelectron yield (Figure 4.25 b) (*iv*: 30 fs)) and why the shape of the wave packet again resembles that of (Figure 4.25 b) (*ii*: 14 fs)) once again and keeps repeating.

Now, the question arises, why do we not see these oscillations (Figure 4.25 b)) in our measurements as well (Figure 4.25 a)))? We attribute this to the circumstance that XUV-mediated photoionization from the ground X state does not exclusively probe the nuclear wave packet density at the FC point alone, as the simulations suggest, but rather probes the density of multiple nuclear configurations in its near vicinity all at once. Nonetheless, we find evidence in subsection 4.9.2 that photoionization in ozone, from either ground X or excited B state, is restricted to probing the *near vicinity* of the FC point. Thanks to the fact that the displacement

of the ground X state-associated nuclear wave packet is small in terms of absolute units and — as we believe — due to insufficient *R-selectivity* of the ozone photoionization cross section itself, the ground X state-related nuclear wave packet motion is smeared out in our measurements and thus not resolvable.

#### 4.9.2 B State-related Nuclear Wave Packet Motion

After having interpreted the ground X state-related molecular dynamics in subsection 4.9.1 by comparison with MCTDH-simulated nuclear wave packet density plots, we want to apply these to the excited B state dynamics as well. The following discussion always refers to Figures 4.27 a) to c). At  $t = -20$  fs, the B state PES stays unpopulated, because the DUV pump pulse has not interacted with the ozone molecule yet. By  $t = 0$  fs, the situation has changed and part of the X state-related nuclear wave packet has coherently been excited from the X to the B state PES, which is now located around the FC point. The latter is still coherent with the nuclear wave packet part being left on the X state PES (Figure 4.4 b)). As mentioned earlier, we determine by fit a sub-10 fs pulse duration of the DUV pump pulse of  $(9.6 \pm 0.9)$  fs, that can be considered as an average value, and where the error refers to the 95% confidence interval. However, part of the B state-associated nuclear wave packet has already started leaving the FC point towards increasing interatomic distances ( $R_{1,2}$  and  $R_{1,3}$ ) indicated by the symmetric wings in Figure 4.25 c) (II: 0 fs). As before, the simulations predict a high photoelectron yield from the B state, since the nuclear wave packet density is high at the FC point. From this moment on ( $t = 0$  fs), the propagation of the nuclear wave packet on the B state PES is solely steered by the topography of its respective PES. This PES is quite different from the X state PES, since it possesses two minima in nuclear space and a valley-ridge inflection point midway between these minima and close to the increasing potential barrier (Figure 4.3). By  $t = 20$  fs, the nuclear wave packet density has increased at those nuclear configurations, that are far away from the FC point, indicating that dissociation of ozone into atomic ( $R_{1,3} = R_{1,2} = 4.0 a.u.$ ) and diatomic oxygen ( $R_{1,2} = R_{1,3} = 2.25 a.u.$ ) has completed. Moreover, this explains the rise in  $O_2$ -related photoelectrons from Figure 4.26 at  $t = 20$  fs, but even more interesting is the fact that the nuclear wave packet density is still high in the vicinity of the FC point. Also the simulations suggest a non-vanishing B state-related photoelectron yield at the very same moment (Figures 4.27 a) and b) (III: 20 fs)) and manifests itself as a shoulder between  $t = 10$  fs and  $t = 30$  fs. We interpret its appearance in the following way: After excitation the nuclear wave packet on the B state PES leaves the FC point quite quickly along the path midway between the two minima of the B state PES towards the valley-ridge inflection point. There, it segregates into three parts, where two parts keep dissociating and finally lead to ozone photodissociation, while the remaining part returns to the FC point and arrives there at  $t = 20$  fs. At  $t = 34$  fs, however, the nuclear wave packet density around the FC point has dropped to nearly zero, since the nuclear wave packet repeats its motion along the same trajectory, giving rise to zero photoelectron yield at this instant of time (IV in Figures 4.27 a) and b)). Nonetheless, at  $t = 40$  fs, the nuclear wave packet trifurcates once again on its motion towards the valley-ridge inflection point, where two parts keep dissociating again, while another part revisits the FC point for a second time, though with reduced amplitude due to the preceding wave packet segregation. Regarding the

two dissociating parts of the nuclear wave packet, we find evidence for this assumption in the nuclear wave packet density subplot (V) at  $R_{1,3} = 4.0 \text{ a.u.}$  and  $R_{1,2} = 2.25 \text{ a.u.}$  (and vice versa). These features resemble those of subplot (III) of Figure 4.27 c), though with reduced amplitude as well. Moreover, by comparison with Figure 4.26, we monitor another rise of  $\text{O}_2$ -related photoelectrons around  $t = 40 \text{ fs}$ , also with reduced amplitude, as compared to its counterpart at  $t = 20 \text{ fs}$ , validating our interpretation. Considering the returning part of the nuclear wave packet density, both the simulation and the experiment show another non-vanishing photoelectron yield at  $t = 40 \text{ fs}$ , also with more reduced amplitude than compared to  $t = 20 \text{ fs}$ .

Now, one might wonder, why the experiment agrees so well with theory, since we already know that the simulation is restricted to photoionization at the FC point only and neglects photoionization arising from other nuclear configurations. As pointed out at the end of subsection 4.9.1, the ozone photoionization is — by accident — only sensitive to the B state-associated nuclear wave packet density in the near vicinity of the FC point. We refer this circumstance to a transition dipole strength between neutral ozone  $\text{O}_3$  and its cation  $\text{O}_3^+$  that is localized around the FC point. Therefore, only those nuclear wave packets are released into the continuum that have reasonable overlap with the nuclear wave packet of its cation, and hamper those having little overlap. Other than in the case of the ground X state-associated oscillations in the photoelectron yield, where the motion of its nuclear wave packet takes place on small length scales around the FC point, the B state-related nuclear wave packet motion evolves on bigger length scales. This is attributed to excited B state population inevitably leading to photodissociation, where the latter is concomitant with a tremendous increase of interatomic distances.

## 4.10 Excited B State-Related Dyson Orbitals of $\text{O}_3$ and $\text{O}_2 + \text{O}$

In order to verify the assumption brought up at the end of the preceding section, which claims that the excited state-related photoionization of ozone preferentially takes place at the FC point (subsequently referred to as case (I)) and which is suppressed far away from it (subsequently referred to as case (II)), we calculated the Dyson orbitals at these distinct molecular configurations given in detail by:

- (I) :  $R_{1,2} = 2.43 \text{ a.u.}$ ;  $R_{1,3} = \mathbf{2.43} \text{ a.u.}$  ;  $\alpha = 116.9^\circ$ ,
- (II) :  $R_{1,2} = 2.43 \text{ a.u.}$ ;  $R_{1,3} = \mathbf{5.00} \text{ a.u.}$  ;  $\alpha = 116.9^\circ$ ,

where  $R_{1,2}$ ,  $R_{1,3}$  and  $\alpha$  denote the nuclear coordinates of the ozone molecule, as defined previously. In this way, we show why oscillations occur in the B state-associated photoelectron yield during the ozone-photodissociation and relate these to different Dyson norms for divergent nuclear coordinates. Therefore, we performed post-Hartree-Fock quantum mechanical electronic structure calculations of ozone, similar to those that were run by our colleagues *Ágnes Vibók*, *Gábor J. Halász*, *Piero Declava* and *Fabien Gatti*. Unlike them, we ran such simulations on a

single workstation, but at the same level of theory, though using a smaller basis set<sup>16</sup>.

Technically speaking, we ran CASSCF(18,12)<sup>17</sup>/aug-cc-pVDZ simulations for the electronic wave function of the neutral ozone molecule and CASSCF(17,12)/aug-cc-pVDZ simulations for that of its cation with the *GAMESS quantum chemistry package* [97]. As always, we focus on the most intense excited B state-related photoionization channel into the B-3 cation state with a squared Dyson norm of  $I_{jk} = 0.41$  (Table 4.3), namely  $B(3^1A') \rightarrow B^+(1^2A'')$ , where the states are labeled to conform with the irreducible representations of the  $C_s$  point group. Here, we restrict our calculations to the few lowest singlet states of  $^1A'$  symmetry for the neutral ozone molecule and to the few lowest doublet states of  $^2A''$  symmetry for the cation, respectively. Since *GAMESS* does not only provide singlet and doublet states during the CASSCF-calculation, we are forced to calculate the ten lowest states in case (I) and the 20 lowest states in case (II) to guarantee that the set of calculated states contains those that are relevant to describe the currently considered photoionization channel. Usually, CASSCF-calculations yield different converged molecular orbitals for the neutral and the cation, respectively, since *Koopmans' theorem*<sup>18</sup> [98] does not apply due to electronic relaxation upon photoionization [83]. In this case, evaluation of the overlap integral between the electronic wave functions of the neutral molecule and of the cation, expressed as a linear combination of Slater determinants, enforces a *biorthonormalization* of their molecular orbitals [99], which would be quite cumbersome. Therefore, we choose another *ansatz* and use the molecular orbitals obtained for the neutral molecule to express the electronic wave function of the cation. Then, the overlap integral, that occurs in the calculation of the Dyson orbitals according to equation (4.6), becomes quite simple, as one forgoes the otherwise required *biorthonormalization* step.

Figure 4.28 depicts the Dyson orbitals, calculated according to the above description, and the squared Dyson norms (displayed above the Dyson orbitals) for the molecular geometry (I), that is O<sub>3</sub> at the FC point (Figure 4.28 a)), and for dissociated ozone (II), namely O<sub>2</sub> + O far away from the FC point (Figures 4.28 b) – d)). Both molecular geometries are run through at some time during the evolution of the ozone-photodissociation. All orbitals in Figure 4.28 are plotted using the *MOLDEN electronic and molecular visualization tool* [100] using a contour value of 0.05 in each case. Apart from the mere illustration of the Dyson orbitals, Figure 4.28 shows the two most important molecular orbitals (white-rimmed insets) contributing to the appropriate Dyson orbital, the latter belonging to the photoionization channel that is indicated at the bottom of each subplot.

While the excited B state is well-defined as the third electronic state of  $^1A'$ -symmetry at the FC point (case (I)), it is not unambiguously identifiable for dissociated ozone (case (II)), since three

<sup>16</sup>Our colleagues use the *aug-cc-pVQZ* basis set [70].

<sup>17</sup>CASSCF(m,n) stands for *complete active space self-consistent field* and means that one considers all possible electron-hole excitations (and multiples thereof), which can be constructed from the Hartree-Fock Slater determinant. There, m electrons are distributed among n orbitals. Then, all Slater determinants arising from this procedure are employed in a *configuration interaction* calculation, where the molecular orbitals, which comprise the Slater determinants, are iteratively determined in a self-consistent fashion.

<sup>18</sup>*Koopmans' theorem* argues that the energy levels do not change with the transition from a neutral molecule to its ionized version, but remain almost constant. Consequently, this assumption implies that the molecular orbitals of the neutral molecule and of the cation are identical.

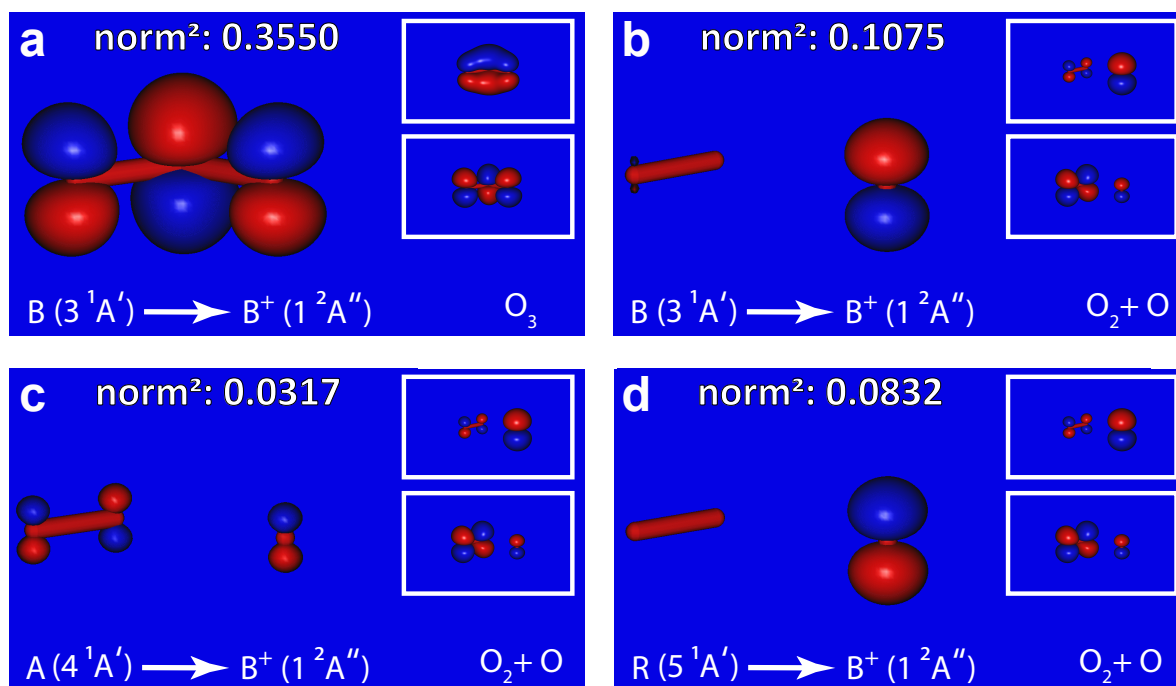


**Figure 4.28:** Dyson orbitals (blue- and red-shaded object) for the most intense excited B state-related photoionization channel  $B(3^1A') \rightarrow B^+(1^2A'')$ . **a)** Dyson orbital and squared Dyson norm at the FC point ( $R_{1,2} = 2.43 a.u.$ ;  $R_{1,3} = 2.43 a.u.$ ;  $\alpha = 116.9^\circ$ ) **b) – d)** Dyson orbital and squared Dyson norm far away from the FC point for already dissociated ozone ( $R_{1,2} = 2.43 a.u.$ ;  $R_{1,3} = 5.00 a.u.$ ;  $\alpha = 116.9^\circ$ ). **b)** photoionization from  $3^1A'$ , **c)** from  $4^1A'$  and **d)** from  $5^1A'$  into the same final electronic state  $1^2A''$  as in **a)**. We choose a contour value of 0.05 for visualization of the Dyson orbitals and for the two most strongly contributing molecular orbitals (white-rimmed insets). All orbitals are plotted using the *MOLDEN electronic and molecular visualization tool* [100]. For more information regarding the calculations, see main text.

singlet states of  $^1A'$ -symmetry are nearly degenerate in energy. Therefore, we calculated three Dyson orbitals for case (II) to ensure that the relevant photoionization channel is covered by our simulation (Figures 4.28 b) – d)). The state labeling (either *A*, *B* or *R* for neutral ozone) is guided by the state labeling used in Figure 4.2 b) for  $R_1 = 5.00 a.u.$ . Therefore, we identify the B state with  $3^1A'$ , the A state with  $4^1A'$  and the R state with  $5^1A'$ . However, more elaborated electronic structure calculations might propose a state labeling that deviates from ours due to state reordering.

However, the squared Dyson norms in case (II) (Figures 4.28 b) – d)) are smaller than the squared Dyson norm in case (I) (Figures 4.28 a)) and differ from it by a factor of approximately three to ten (3 – 10). Moreover, the squared Dyson norm that we calculated for case (I), almost reproduces that obtained by our colleagues (squared Dyson norm (present calculation): 0.355 vs. squared Dyson norm calculated by our colleagues [70]: 0.41). Since the photoionization

---

cross section is nearly proportional to the squared Dyson norm (equation (4.12)), it is this circumstance that can be considered as an indication for why oscillations in the excited B state-associated photoelectron yield is detectable after all, although the simulated TRPES-spectra of our colleagues are known to exclusively apply to the FC point of ozone. Nonetheless, our results suggest that photoionization from molecular geometries far away from the FC point tend to be suppressed in comparison with photoionization around the FC point. This allows one to probe the nuclear wave packet density on the excited B state PES almost exclusively in the vicinity of the FC point.





## Chapter 5

# Conclusion

The goal of the present thesis was to develop an as compact as possible, ultrafast radiation source in the DUV spectral range, that provides *wavelength-tunable, short and intense* pure-UV pump pulses. Its application in a TRPES-experiment has eventually paved the way for the *first experimental, few-femtosecond study* of the molecular dynamics of ozone ( $\text{O}_3$ ), which are inextricably linked to the temporal evolution of its photodissociation.

The most decisive step towards a successful measurement of molecular dynamics in ozone on a few-femtosecond timescale is achieved by discarding the previously used DUV generation scheme, that is based upon THG in neon-filled ceramic targets, and to replace it with a setup relying on SHG in freestanding  $20\ \mu\text{m}$  thin BBO crystals, instead. By doing so, it is shown in the course of this work that SHG-based DUV pulses can be created, that are characterized by a sub-10 fs pulse duration (*THG*: sub-6 fs) (measured via a self-built DUV-capable TG-FROG), carry  $(2.0 \pm 0.5)\ \mu\text{J}$  pulse energy on target (*THG*:  $0.15\ \mu\text{J}$ ) and are wavelength-tunable around approximately 268 nm (*THG*: no wavelength-tunability) by changing the crystal axis orientation. The latter assumes that the DUV-generating spectrum of our few-femtosecond laser possesses appropriate spectral components. To some extent, its spectral broadening can be enforced by SPM and plasma-blueshifting effects in a neon-filled HHG gas target during XUV pulse generation and without compromising the XUV flux too much. Moreover, as we use type-I SHG for DUV generation, the DUV transmission through the silicon wafer chicane is more efficient and yields  $>83\%$  (*THG*: 15%), while still maintaining an NIR attenuation of  $10^4$  during DUV/NIR-filtering. This circumstance naturally enhances the total DUV transmission from the place of generation down to the place, where the experiment is performed. On the whole, we have proven that DUV pulses created via SHG outperform those generated from THG and experience a more than one order of magnitude improvement in terms of usable pulse energy on target.

Another interesting and, regarding the observability of the electronic and nuclear dynamics during the ozone-photodissociation process, important aspect is represented by the angular distribution of XUV-probe-pulse-mediated photoemission in TRPES-experiments. By application of molecular symmetry considerations, borrowed from *group theory*, on the qualitative evalua-

tion of photoionization dipole transition integrals, we showed for the example of ozone that the excited state-related photoelectron yield can be optimized when using a cross-polarized DUV-pump / XUV-probe pulse train geometry. In addition, we exemplified why the photoelectron yield is heavily suppressed for the opposite case of identically polarized pulses.

The experimental results of our TRPES-experiment on the molecular dynamics in ozone agree qualitatively well with the most prominent features of simulated time-resolved photoelectron spectra. The underlying nuclear wave packet evolution of the latter is computed with the *MOL-PRO quantum chemistry software package* [74], while photoionization cross sections around an XUV photon energy of 99.5 eV are estimated via a Dyson orbital approach [70, 76]. The good accordance between *theory* and *experiment* allowed us to relate the results to snapshots of the ground and excited state-associated nuclear wave packet motion. The thus obtained results provide evidence for the ozone-photodissociation of being accompanied by multiple recurrences of a nuclear wave packet along closed trajectories on the excited B state PES. The oscillation period is determined to  $(19.6 \pm 1.8)$  fs, while the ozone photodissociation itself is completed after approximately 20 fs. Both can be regarded as a manifestation of ultrafast coherent photochemistry. At the same time, our approach marks the very first DUV-pump / XUV-probe experiment in a neutral polyatomic molecule with few-femtosecond time resolution. Beyond this, our setup basically allows for few-femtosecond or even attosecond investigation of other DUV-sensitive molecules, thus pushing the frontier of ultrafast pump-probe experiments towards the DUV spectral domain.

## Chapter 6

# Outlook

Apart from the ground X and excited B state, which are considered within the scope of this work, ozone possesses even more electronic states. For example, the weakly binding A state, that is responsible for the formation of cyclic ozone [17], but also the repulsive R state, that leads to ground X state-related photofragments, should be named (Figure 4.2). Some of the electronic states of ozone partially cross each other in the form of so-called *conical intersections* in the space spanned by the nuclear degrees of freedom of the molecule. These conical intersections may be considered as funnels for radiation-less energy relaxation pathways of the B state-associated nuclear wave packet after absorption of a single DUV-photon. Thereby, the nuclear wave packet changes from one PES onto other adjacent PESs in an energy-descending cascade. This process keeps going until the amount of energy, that is stored in the electronic system, is converted into kinetic energy of the nuclei, eventually resulting in electronically de-excited photofragments. Although these nonadiabatic effects can be neglected in first order approximation, they are of uttermost importance for a more thorough understanding of, for instance, the photostability of DNA against DUV radiation. After DUV excitation, the molecule relaxes along pathways comprising conical intersections, but may also decay along pathways leading to DNA-photodamage in the form of thymine-dimerization on a femtosecond timescale [101, 102]. By adaption of the scheme introduced by *Kowalewski et al.* [103], that relies on extracting information on nonadiabatic couplings via a three-color streaking approach, one should in principle be able to study these nonadiabatic effects, not only in ozone, but also in biomolecules, like *amino acids* [104], *peptides* [62, 105], *proteins* [63] or even *DNA* [106].

Due to usually weaker DUV absorption cross sections of these biomolecules than compared to ozone, a more refined and even more intense DUV radiation source is indispensable to compensate for this issue. Some schemes have already been published in this direction and promise to be capable of creating many- $\mu$ J-level, few-femtosecond DUV pulses without aversing from the single-pass configuration, but suffer from being highly sophisticated and bulky, as chromatic dispersion effects have to be taken into account explicitly. Right now, steps are being taken to boost our DUV pump pulses towards higher pulse energy, while maintaining or even reducing their pulse duration at the same time. It mainly follows the ideas of *angular phase-matching*

discussed in, for example, [107–110] and make use of thicker BBO crystals. Using these thicker crystals would solve the problem of degrading long-term mechanical integrity that come along with ultrathin BBO crystals. In order to make up for the expectedly reduced phase-matching bandwidth of thicker crystals, the incident beam of the fundamental laser is spectrally dispersed by either a grating pair [110] or a prism pair [109] such that each spectral component is incident on the crystal at its respective phase-matching angle. After DUV generation in these crystals, the dispersion is reversed by a suitable DUV optical grating or prism pair to form a collimated DUV beam and compressed DUV pulse. Thus, it was already shown that the achievable phase-matching bandwidth can be increased by a factor of roughly 80, compared to the case where the incident beam remains undispersed [108]. Alternatively, one could also think of creating a line-focus in a 4-f-configuration, along which the components of the fundamental laser spectrum are spatially dispersed, and where a battery of mutually twisted crystals is used to meet the phase-matching condition for each component individually. This promises to minimize the risk of crystal damage and increases the phase-matching bandwidth tremendously [111].

## Appendix A

# Pulse Characterization Techniques

Owing to the development of ever shorter pulse generation techniques, a complete temporal characterization of these ultrashort pulses turned out to be problematic, since their electric field usually oscillates more rapidly than what even the fastest electronic devices can resolve. By complete temporal characterization we denote the measurement of both spectral amplitude and spectral phase of the pulse, that yields the unambiguous reconstruction of its electric field evolution. So with the advent of femtosecond or even attosecond pulses, new or at least more refined pulse characterization techniques had to be invented. This section does not claim to give a complete summary of all known pulse characterization methods, but to provide an overview of the two concepts relevant within the scope of this work. We will in brief address the notion of *Attosecond Streaking* in order to show its scaling with electric field strengths, wavelength and detection angle, but also with respect to polarization. Especially the latter must be accounted for in order to rule out its contribution to the ozone TRPES-experiment. After this, we will quickly introduce the method of *Frequency Resolved Optical Gating* (FROG), because it is used for the temporal characterization of the DUV pulses, utilized for triggering ozone photodissociation. However, *Attosecond Streaking* can be interpreted in the framework of *FROG* as well.

### Appendix A.1. Attosecond Streaking

The concept of *Attosecond Streaking* [112–114] is based on a similar technique that has been employed for the characterization of pulses in the picosecond domain, namely, the *Streak Camera* [115]. The basic idea is to map the temporal pulse profile onto a spatially dependent intensity distribution, using an appropriate experimental setup. There, the pulse is shone onto a target, followed by ionization of electrons. The released electron bunches will then propagate towards a detector (screen) and on their journey towards it, they will be deflected by a steadily increasing, time-varying electric field. This field is called the *streaking field* and is applied perpendicularly to the propagation direction of the ionized electrons. Depending on the electron time of arrival at the streaking field transit zone, they experience more or less deflection, depending on the applied instantaneous electric field strength and hit the detector at different places. Thus, the

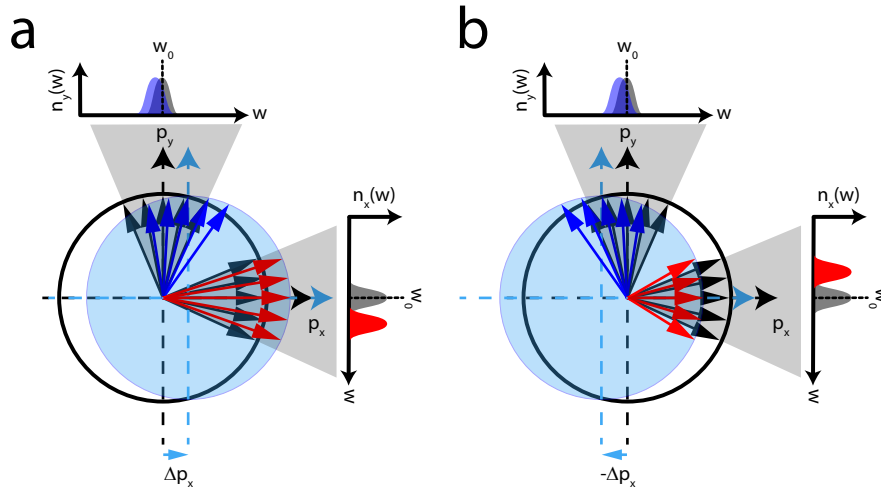


**Figure A.1:** a),b) Illustration of attosecond streaking for a x-polarized and non-vanishing electric field at two different instants of time, separated by half an oscillation period. *Gray cones:* acceptance angle of TOF for photoelectron detection. *Black circle:* unmodified (unstreaked) momentum distribution of released photoelectrons. *Blue-shaded circle:* modified (streaked) momentum distribution. In both cases a),b), the unstreaked electron momenta (*black arrows*) acquire a net momentum transfer along the x-direction (a)  $+\Delta p_x$ , b)  $-\Delta p_x$ ). Momenta that are measured alongside the polarization direction (x-axis) are shown as *red arrows*, while perpendicularly detected momenta (y-axis) are transferred into those shown as *blue arrows*. For parallel streaking (detection along x-direction) the streaked momentum distributions experience an up or down shift, respectively, depending on the sign of the electric field, while for transverse streaking (detection along y-direction) the momentum distribution gets broadened to either sides, but more strongly to lower momenta. Figure adapted from [112].

space–time mapping is completed. Obviously, this approach will only work, if the temporal variation of the streaking field and the electrons time of arrival are properly synchronized to each other.

As discussed in subsection 2.2.4.1, the created attosecond pulses and their corresponding driving fields are inherently phase-locked to each other as a consequence of the generation process itself. Consequently, both pulses are predestined to be used for pump–probe experiments, because their proper synchronization is guaranteed and since they propagate collinearly. Let us omit the driving field for now and assume that a gaseous target sample is subjected to the attosecond pulse in a way that it undergoes photoionization. Photoelectrons which escape from the target have got a momentum distribution that resembles the spectral distribution<sup>1</sup> of the attosecond pulse. The same is valid for their temporal profile. On the whole, the electron bunch

<sup>1</sup>Naturally, this will only be true, if the bound–continuum transition dipole moment can be regarded independent of momentum so that the spectrum does not get modified by this additional impact. This assumption is made throughout the attosecond community.

carries information about the temporal and spectral properties of the attosecond pulse and can be considered to be a replica of the attosecond pulse itself. Now, if we added the driving pulse to the attosecond pulse and managed to delay it in a reliable fashion with respect to the latter on an attosecond timescale, the initial electron momentum distribution, induced by the attosecond pulse just after photoionization, would be modified by the presence of the driving field, serving as the streaking field here. The influence of the streaking field can be understood as follows: As long as photoionization has not set in yet, the electrons will not feel the presence of the streaking field much, but as soon as they get ionized by the attosecond pulse, they undergo a transition from a bound state into the continuum. As they are not shielded against this streaking field anymore after entering the continuum, they start to follow the evolution of the electric field. Hence, they gain or lose momentum periodically, depending on the instant of ionization. Then, the electron bunches will either have been accelerated, decelerated or will not have been modified at all at the end of the pulse with regard to their unmodified spectra. If the attosecond pulse duration was way shorter than an optical half-cycle of the streaking field, we would expect to obtain a streaked spectrum that was displaced as an entity. If the condition above was violated, we would expect the momentum distribution to split up as a consequence of different parts of the momentum distribution, being exposed to different phases of the streaking field. This, in turn, leads to alternating gain or loss of momentum, once the streaking pulse has passed by and results in the occurrence of spectral sidebands which are separated by one quantum of the laser frequency,  $\hbar\omega$  [113]. Anyway, for the remainder of this section, we assume a short attosecond pulse fulfilling the above condition.

Figure A.1 illustrates the underlying effect and its impact on the spectra measured alongside (spectra on the right hand side of the gray cones, x-axis) or perpendicularly (spectra above the gray cone, y-axis) to the polarization direction. Additionally, for the remainder of this section, we restrict ourselves to the case of linear polarization, but it can be extended easily to the case of circular or elliptical polarization. Furthermore, we make use of the *strong field approximation*<sup>2</sup> (SFA), the *single active electron approximation*<sup>3</sup> (SAE) and suppose that the Coulomb potential of the parent ions does not influence the temporal evolution of the photoelectrons much, since they enter the continuum with high initial velocity. In this framework we can describe the released electron trajectory semi-classically and make use of Newton's law and write the equation of motion down as (in atomic units)

$$\ddot{x}(t) = -E(t), \tag{A.1}$$

where  $\ddot{x}(t)$  is the second time-derivative of the electron position and  $E(t)$  is the x-component of the streaking field polarization. We now integrate equation (A.1) directly from the moment of ionization until infinity when the pulse has already passed by. Hence, we get (after some

---

<sup>2</sup>Here, we assume that the applied streaking field strength outweighs the atomic potential in a way that the electron motion is mainly governed by the streaking field.

<sup>3</sup>This approximation presumes that only the outermost valence electron is influenced by the streaking field as well as by the attosecond pulse.

maths [116,117]) an expression for the final electron kinetic energy

$$\frac{v_f(t, \theta)^2}{2} = \frac{v_0^2}{2} + \frac{A(t)^2 \cos(2\theta)}{2} - A(t) \cos(\theta) \sqrt{v_0^2 - A(t)^2 \sin^2(\theta)}, \quad (\text{A.2a})$$

$$\approx W_0 + 2U_p(t) \cos(2\theta) \sin^2(\omega t) + \alpha \sqrt{8W_0 U_p(t)} \cos(\theta) \sin(\omega t), \quad (\text{A.2b})$$

where  $\alpha = \sqrt{1 - 2(U_p(t)/W_0) \sin^2(\theta) \sin^2(\omega t)}$ . The final photoelectron velocity  $v_f$  is a function of the moment of ionization  $t$  and of the detection angle  $\theta$  with respect to the streaking field polarization. But besides that, we can analyze equations (A.2a) – (A.2b) for two separate cases:

- *Parallel streaking*: Detection alongside the polarization ( $\theta = 0$ )
- *Transverse streaking*: Detection that is perpendicular to the polarization ( $\theta = \pi/2$ ).

In the first case, the final velocity distribution closely follows the time evolution of the streaking field and is proportional to the vector potential  $A(t)$ , weighted with some nearly constant expression for  $A(t) \ll W_0$ . This is equivalent to being proportional to the square root of the ponderomotive energy  $U_p(t) = \frac{E^2(t)}{4\omega^2}$ , which clearly shows the wavelength and intensity scaling of the modified velocity distribution. Therefore, it is perfectly suited to rasterize the streaking field for different time delays. Moreover, a spectrogram obtained in this way even carries information about the attosecond pulse itself, as stated above, but is beyond the scope of this work. For further information see, for example, [116, 117]. In the second case, that is more closely connected with the experimental setup used in this thesis, we observe a different behavior inasmuch as the momentum distribution oscillates at twice the fundamental angular frequency. This behavior is represented by the term  $\sin^2(\omega t) = 1/2(1 - \cos(2\omega t))$  in equation (A.2b) and mainly leads to broadened velocity distributions and, additionally, to those being downshifted in energy with regard to the unstreaked velocity distribution  $W_0$ . Moreover, it scales linearly with the ponderomotive energy (equation (A.2b)) and is usually smaller in absolute values than the third term in equations (A.2a) – (A.2b) due to the absence of the weighting factor  $\sqrt{W_0}$ , where  $W_0$  is on the order of 100 eV. Let us assume to have two laser pulses, one centered around angular frequency  $\omega$  and the other one centered around its third harmonic  $3\omega$  in a transverse streaking geometry. According to equation (A.2b), we would expect a streaking amplitude that scales linearly with the ponderomotive energy  $U_p(t) = \frac{E^2(t)}{4\omega^2}$ . If both pulses had identical intensity  $I(t) \propto E^2(t)$ , it would imply that the streaking amplitude of the third harmonic is almost one order of magnitude smaller than compared to its fundamental. In contrast to this, it is simply a factor of three less in case of parallel streaking (equation (A.2b)).

## Appendix A.2. FROG

As pointed out in the introduction of this section, attosecond streaking itself can be described as a manifestation of FROG. Here, we would like to introduce the basic idea of FROG and give at least a mathematical formulation that is universal, because there is quite a number



of different implementations of FROG, resting upon various nonlinear effects. Common to all implementations is the following mathematical formulation of FROG [118]

$$S(\omega, \tau) = \left| \int_{-\infty}^{\infty} dt E(t) \cdot g(t - \tau) \exp(-i\omega t) \right|^2, \quad (\text{A.3})$$

where  $\omega$  and  $\tau$  denote the angular frequency and time delay between a gate function  $g(t)$  and the electric field  $E(t)$ , respectively, in which one is interested to reconstruct and  $S(\omega, \tau)$  is a so-called spectrogram of the nonlinear response. The latter is triggered by the unknown pulse  $E(t)$  and is resolved spectrally as a function of the time delay  $\tau$ . The gate function  $g(t)$  itself is responsible for sampling parts of the laser pulse and its temporal spread is on the order of the laser pulse duration. As a matter of fact, it is usually a function of the electric field to be measured. In the case of attosecond-streaking, the gate-function is provided by an integral function of the streaking-field vector potential, while  $E(t)$  represents the attosecond pulse used for ionization [113]. Depending on the explicit form of the gate function, one distinguishes between several types of FROG, which are best suited for different demands [118]. In this thesis, we make use of TG-FROG [119] in particular, where the prefix stands for *transient grating*. The name arises from a nonlinear refractive index grating, transiently created by two replica of the pulse that is intended to be measured and which contributes to the gate function at the same time. The gate function can be written as  $g(t - \tau) = |E(t - \tau)|^2$  and is a manifestation of the nonlinear optical Kerr effect.

The setup is as follows: We illuminate a mask that comprises three regularly arranged and equally sized holes. The latter, in turn, are located on three corners of a square. This is the so-called *BOXCARS*-geometry. Hence, we generate three replica of the very same laser pulse, which we want to characterize temporally. If we focus these beams onto a common spot of a nonlinear medium with  $\chi^{(3)}$ -nonlinearity, they will form a checkered interference pattern in the focal plane, depending on the time delay that is introduced between the single and the two remaining pulses by a retardable double mirror. This leads to the generation of a fourth beam, diffracted off this transiently generated grating and which emerges from the fourth corner of the *BOXCARS*-geometry in the far field. As the latter provides a signal at the fundamental angular frequency in case of the TG-FROG, this setup is inherently phase-matched. Once the spectrogram for different time delays has been recorded, the task is to reconstruct the underlying pulse, making use of iterative retrieval algorithms that are either based upon *generalized projections* [120] or *ptychography* [121]. These algorithms are commonly used techniques for the solution of phase-retrieval problems like those formulated in equation (A.3).



## Appendix B

# Group Theory and Group Representations

Group theory and representation theory proved themselves valuable as easy to handle tool-boxes for the qualitative evaluation of certain electronic transition integrals in photoelectron spectroscopy experiments, as molecular states can be attributed to certain, so-called *irreducible representations*. Therefore, we will quickly walk through the definitions of a group in a mathematical sense, of a class, of group representations (encompassing irreducible representations) and relations between them. It should be stated that the upcoming discussion does not claim to give a rigorously derived and mathematically complete introduction to group theory, but to provide an overview that is relevant within the scope of this work and which lets the reader recognize the most important concepts. For a more detailed discussion concerning groups and their application in molecular physics see, for example [79].

### Appendix B.1. Groups

A group  $G$  in a mathematical sense is defined as a set of elements with a mathematical operation " $\bullet$ ", defined between any two elements. Besides this,  $(G, \bullet)$  must fulfill the so-called *group axioms* for all elements:

- **Closure:** For all elements  $a, b \in G$ , the newly formed element  $a \bullet b$  must reside in the set  $G$ .
- **Associativity:** For all elements  $a, b, c \in G$ , the following equality must hold true:  $(a \bullet b) \bullet c = a \bullet (b \bullet c)$ .
- **Identity element:** For all elements  $a \in G$ , there is a unique element  $\mathbb{1} \in G$ , such that:  $a \bullet \mathbb{1} = \mathbb{1} \bullet a = a$ .
- **Inverse element:** For all elements  $a \in G$ , there is a corresponding inverse element  $a^{-1} \in G$  such that:  $a \bullet a^{-1} = a^{-1} \bullet a = \mathbb{1}$ .

If additionally the following condition is satisfied, the group is called an *Abelian* or *commutative* group:

- **Commutativity:** For all elements  $a, b \in G$ :  $a \bullet b = b \bullet a$ .

Thereby, it is irrelevant what is used as elements as long as these axioms apply. Elements can simply be numbers, but could also be functions or even more complex objects, but in our case turn out to be symmetry operations / geometrical transformations, which are applied to the ozone molecule in its molecular coordinate system. Accordingly, the operation " $\bullet$ " is not specified at all, it just has to combine any two elements in order to result in another element that still resides in the set  $G$  and fulfills the above axioms.

## Appendix B.2. Classes

Moreover, one can subdivide a group  $G$  — or more generally a set of elements — into more subsets which are known as *classes*  $\mathcal{C}$ . A class  $\mathcal{C} \subset G$  is a set of elements  $a, b \in G$  for which the following condition is fulfilled and which can be considered an *equivalence relation*

$$\exists t \in G : t^{-1} \bullet a \bullet t = b. \quad (\text{B.1})$$

Elements satisfying this condition are said to be *conjugated* or *equivalent* to each other. Without evidence, we state that every group can be decomposed into disjoint classes. We are going to encounter this notion once more when addressing representations of groups.

## Appendix B.3. Group Representations

In general, set elements are not specified further and can be considered abstract, so one endeavors to find matrix representatives for them, still fulfilling the group axioms. The map between these abstract group elements is usually referred to as an *isomorphism* or *homomorphism*, according to whether the map is bijective<sup>1</sup> or not. An  $n$ -dimensional matrix group, homomorph to a group  $G$ , is said to be an  *$n$ -dimensional group representation*. The circumstance that there is an infinite number of representations, which are linked to each other via similarity transformations like those defined by equation (B.1), one is usually interested in finding those representations of the very same group  $G$  that are not equivalent to each other. Moreover, one distinguishes between *reducible* and *irreducible* representations. A representation that can be brought to diagonal block form for every group element  $R \in G$  is said to be *reducible*. Without proof we state that there are as many irreducible representations  $n$  as classes within the group, which in turn is a finite number for groups of non-infinite order<sup>2</sup>. The remaining representations are known as *irreducible* and these are the ones we are basically interested in, because the reducible

<sup>1</sup>In this context, *bijection* means a one-to-one-correspondence between group elements and matrix representatives

<sup>2</sup>By *order* we mean the number of group elements.

$G$	$R_1$	$R_2$	$\dots$	$R_k$
$R_1$	$R_1 \bullet R_1$	$R_2 \bullet R_1$	$\dots$	$R_k \bullet R_1$
$R_2$	$R_1 \bullet R_2$	$R_2 \bullet R_2$	$\dots$	$R_k \bullet R_2$
$\vdots$	$\vdots$	$\vdots$	$\ddots$	$\vdots$
$R_k$	$R_1 \bullet R_k$	$R_2 \bullet R_k$	$\dots$	$R_k \bullet R_k$

**Table B.1:** Group multiplication table of an arbitrary group,  $G$ . The result of such a concatenation refers to the case where the symmetry operations, shown as columns, are applied before those from the rows.

representations can be expressed as a *direct sum*  $\oplus$  of the irreducible representations and is formally written as:

$$\Gamma(R) = \bigoplus_i c_i \Gamma^{(i)}(R) \quad (\text{B.2})$$

where  $\Gamma(R)$  denotes a reducible representation for group element  $R \in G$  and the set of  $\Gamma^{(i)}(R)$  denotes an irreducible representations and where  $c_i$  are contraction coefficients. In matrix notation it is written as follows:

$$\Gamma(R) = \begin{pmatrix} c_1 \Gamma^{(1)}(R) & 0 & \dots & \dots & 0 \\ 0 & c_2 \Gamma^{(2)}(R) & 0 & \dots & 0 \\ \vdots & 0 & \ddots & 0 & \vdots \\ \vdots & \vdots & 0 & \ddots & 0 \\ 0 & 0 & \dots & 0 & c_n \Gamma^{(n)}(R) \end{pmatrix}. \quad (\text{B.3})$$

Concerning the exact knowledge of a representation, it turns out that it is unnecessary in most cases and what does really matter are the *characters*  $\chi^{(i)}(R)$  of a certain irreducible representation for all group elements  $R \in G$ . The character of a representation is defined as the sum along the diagonal elements of a certain representation matrix and is thus identical with the trace of a matrix:

$$\chi^{(i)}(R) = \sum_k^{g_i} \left( \Gamma^{(i)}(R) \right)_{kk}, \quad (\text{B.4})$$

where  $\Gamma^{(i)}(R)$  is once more an irreducible matrix representation of a certain group element  $R \in G$  and  $g_i$  is its dimension. The advantage of the character over the exact form of a representation matrix lies in its invariance with respect to similarity transformations and thus stays constant for all group elements  $R \in G$  within a class  $\mathcal{C}$ . Their output is usually summarized in form of a *group multiplication table* like the one in Table B.1.

$G$	$h_1 R_1$	$h_2 R_2$	$\dots$	$h_k R_k$
$\Gamma^{(1)}$	$\chi^{(1)}(R_1)$	$\chi^{(1)}(R_2)$	$\dots$	$\chi^{(1)}(R_k)$
$\Gamma^{(2)}$	$\chi^{(2)}(R_1)$	$\chi^{(2)}(R_2)$	$\dots$	$\chi^{(2)}(R_k)$
$\vdots$	$\vdots$	$\vdots$	$\ddots$	$\vdots$
$\Gamma^{(k)}$	$\chi^{(k)}(R_1)$	$\chi^{(k)}(R_2)$	$\dots$	$\chi^{(k)}(R_k)$

**Table B.2:** Group character table of an arbitrary group  $G$ . The irreducible representation  $\Gamma^{(1)}$  is present in all group character tables and exclusively consists of "1"s and is therefore known as the *totally-symmetric representation*. The numbers  $h_k$  in front of the group elements  $R_k$  in the topmost row of this table count the number of equivalent group elements within each class and where each class is labeled by one of their representatives  $R_k$ . The set  $\Gamma^{(k)}$  denotes the different irreducible representations.

In order to make use of the characters  $\chi^{(i)}(R_k)$  of any irreducible representation  $\Gamma^{(i)}$  and for a specific group element  $R_k$ , one strives for finding the so-called *character table*. It summarizes all these characters, depending on the irreducible representation (rows) and for all group elements (columns), as displayed in Table B.2.

It is not a trivial task to get characters from generally unknown matrix representations. Fortunately, there are strategies on how to obtain the character tables from simple symmetry considerations, even without the exact knowledge of their matrix representation. With the help of the following orthogonality relation, which is given without proof, it is possible to determine these:

$$\sum_k h_k \chi^{(i)}(R_k)^* \chi^{(j)}(R_k) = h \delta_{ij}, \quad (\text{B.5})$$

where the summation runs across all classes, represented by  $R_k$ , and  $h_k$  is the number of elements within a class of conjugated elements and  $h$  is the order of the underlying group. The symbol "\*" denotes the complex conjugate of the character  $\chi$ . As we have already seen, any representation can be written as a direct sum of irreducible representations. This and equation (B.5) enable us to find the contraction coefficients  $c_i$  according to

$$c_i = \frac{1}{h} \sum_k h_k \chi^{(i)}(R_k)^* \chi(R_k), \quad (\text{B.6})$$

where  $\chi(R_k)$  is the character of any (reducible) representation. Finally and for the sake of completeness, we want to introduce the concept of the *direct product*  $\otimes$  of representations. If we define the direct product as the *Kronecker product* in terms of characters, it will be converted into a simple product between characters. The Kronecker product  $\otimes$  for matrices  $A, B$  and  $C$  is defined as

$$C = A \otimes B = \begin{pmatrix} a_{11}B & \dots & a_{1n}B \\ \vdots & \ddots & \vdots \\ a_{m1}B & \dots & a_{mn}B \end{pmatrix}, \quad (\text{B.7})$$

where  $a_{ij}$  is the  $i$ -th row and  $j$ -th column element of the  $m \times n$ -matrix  $A$  and for any  $o \times p$ -matrix  $B$  so that the dimension of the resulting matrix is  $mo \times np$ . For an  $m \times m$ -matrix  $A$  and an  $n \times n$ -matrix  $B$ , it immediately follows for the character of their direct product  $A \otimes B$  from equation (B.7) and equation (B.4):

$$\chi(A \otimes B) \stackrel{(\text{B.4})}{=} \sum_{k=1}^{m \cdot n} (A \otimes B)_{kk} \stackrel{(\text{B.7})}{=} \sum_{s=1}^m \sum_{t=1}^n (a_{ss}b_{tt}) = \left( \sum_{s=1}^m a_{ss} \right) \left( \sum_{t=1}^n b_{tt} \right) = \chi(A) \cdot \chi(B). \quad (\text{B.8})$$





# Bibliography

- [1] Brian Clegg and Eadweard Muybridge. *The man who stopped time: The illuminating story of Eadweard Muybridge - pioneer photographer, father of the motion picture, murderer*. Joseph Henry Press, Washington, D.C, 2007.
- [2] Ahmed H. Zewail. Femtochemistry: Atomic-scale dynamics of the chemical bond †. *The journal of physical chemistry. A*, 104(24):5660–5694, 2000.
- [3] M. Ossiander, F. Siegrist, V. Shirvanyan, R. Pazourek, A. Sommer, T. Latka, A. Guggenmos, S. Nagele, J. Feist, J. Burgdörfer, R. Kienberger, and M. Schultze. Attosecond correlation dynamics. *Nature Physics*, 13(3):280–285, 2016.
- [4] M. Schultze, M. Fiess, N. Karpowicz, J. Gagnon, M. Korbman, M. Hofstetter, S. Neppl, A. L. Cavalieri, Y. Komninos, Th Mercouris, C. A. Nicolaides, R. Pazourek, S. Nagele, J. Feist, J. Burgdörfer, A. M. Azzeer, R. Ernstorfer, R. Kienberger, U. Kleineberg, E. Goulielmakis, F. Krausz, and V. S. Yakovlev. Delay in photoemission. *Science (New York, N.Y.)*, 328(5986):1658–1662, 2010.
- [5] Hiromichi Niikura, F. Légaré, R. Hasbani, Misha Yu Ivanov, D. M. Villeneuve, and P. B. Corkum. Probing molecular dynamics with attosecond resolution using correlated wave packet pairs. *Nature*, 421(6925):826–829, 2003.
- [6] A. L. Cavalieri, N. Müller, Th Uphues, V. S. Yakovlev, A. Baltuska, B. Horvath, B. Schmidt, L. Blümel, R. Holzwarth, S. Hendel, M. Drescher, U. Kleineberg, P. M. Echenique, R. Kienberger, F. Krausz, and U. Heinzmann. Attosecond spectroscopy in condensed matter. *Nature*, 449(7165):1029–1032, 2007.
- [7] Florentin Reiter, Ulrich Graf, Martin Schultze, Wolfgang Schweinberger, Hartmut Schroder, Nicholas Karpowicz, Abdallah Mohammed Azzeer, Reinhard Kienberger, Ferenc Krausz, and Eleftherios Goulielmakis. Generation of sub-3 fs pulses in the deep ultraviolet. *Optics letters*, 35(13):2248–2250, 2010.
- [8] Yuichiro Kida and Takayoshi Kobayashi. Generation of sub-10 fs ultraviolet gaussian pulses. *Journal of the Optical Society of America B*, 28(1):139, 2011.

- [9] Ka Fai Mak, John C. Travers, Philipp Hölzer, Nicolas Y. Joly, and Philip St J. Russell. Tunable vacuum-uv to visible ultrafast pulse source based on gas-filled kagome-pcf. *Optics express*, 21(9):10942–10953, 2013.
- [10] Ryan Hossaini, Martyn P. Chipperfield, Stephen A. Montzka, Amber A. Leeson, Sandip S. Dhomse, and John A. Pyle. The increasing threat to stratospheric ozone from dichloromethane. *Nature communications*, 8:15962, 2017.
- [11] Martyn P. Chipperfield, Slimane Bekki, Sandip Dhomse, Neil R. P. Harris, Birgit Hassler, Ryan Hossaini, Wolfgang Steinbrecht, Rémi Thiéblemont, and Mark Weber. Detecting recovery of the stratospheric ozone layer. *Nature*, 549(7671):211–218, 2017.
- [12] Zheng-Wang Qu, Hui Zhu, and Reinhard Schinke. The ultra-violet photodissociation of ozone revisited. *Chemical Physics Letters*, 377(3-4):359–366, 2003.
- [13] Zheng-Wang Qu, Hui Zhu, Motomichi Tashiro, Reinhard Schinke, and Stavros C. Farantos. The huggins band of ozone: unambiguous electronic and vibrational assignment. *The Journal of chemical physics*, 120(15):6811–6814, 2004.
- [14] Zheng-Wang Qu, Hui Zhu, Sergy Yu Grebenshchikov, Reinhard Schinke, and Stavros C. Farantos. The huggins band of ozone: a theoretical analysis. *The Journal of chemical physics*, 121(23):11731–11745, 2004.
- [15] L. Rosenqvist, K. Wiesner, A. Naves de Brito, M. Bässler, R. Feifel, I. Hjelte, C. Miron, H. Wang, M. N. Piancastelli, S. Svensson, O. Björneholm, and S. L. Sorensen. Femtosecond dissociation of ozone studied by the auger doppler effect. *The Journal of chemical physics*, 115(8):3614–3620, 2001.
- [16] R. Schinke and G. C. McBane. Photodissociation of ozone in the hartley band: Potential energy surfaces, nonadiabatic couplings, and singlet/triplet branching ratio. *The Journal of chemical physics*, 132(4):044305, 2010.
- [17] S. Yu Grebenshchikov, Z-W Qu, H. Zhu, and R. Schinke. New theoretical investigations of the photodissociation of ozone in the hartley, huggins, chappuis, and wulf bands. *Physical chemistry chemical physics : PCCP*, 9(17):2044–2064, 2007.
- [18] Robert W. Boyd. *Nonlinear optics*. Elsevier, Amsterdam, third edition edition, 2008.
- [19] Bahaa E. A. Saleh and Malvin Carl Teich. *Fundamentals of Photonics*. Wiley Series in Pure and Applied Optics. Wiley, Chicester, 2nd ed. edition, 2013.
- [20] R. Clark Jones. A new calculus for the treatment of optical systems iii the sohncke theory of optical activity. *Journal of the Optical Society of America*, 31(7):500, 1941.
- [21] Henry Hurwitz and R. Clark Jones. A new calculus for the treatment of optical systems ii proof of three general equivalence theorems. *Journal of the Optical Society of America*, 31(7):493, 1941.
- [22] R. Clark Jones. A new calculus for the treatment of optical systems i description and discussion of the calculus. *Journal of the Optical Society of America*, 31(7):488, 1941.

- 
- [23] R. Clark Jones. A new calculus for the treatment of optical systems iv. *Journal of the Optical Society of America*, 32(8):486, 1942.
- [24] J. N. Eckstein, A. I. Ferguson, and T. W. Hänsch. High-resolution two-photon spectroscopy with picosecond light pulses. *Physical review letters*, 40(13):847–850, 1978.
- [25] J. H. Poynting. On the transfer of energy in the electromagnetic field. *Philosophical Transactions of the Royal Society of London*, 175(0):343–361, 1884.
- [26] John David Jackson, Kurt Müller, Christopher Witte, and Martin Diestelhorst. *Klassische Elektrodynamik*. De Gruyter Studium. De Gruyter, Berlin, 5., überarb. Aufl. edition, 2014.
- [27] E. Schrödinger. Quantisierung als eigenwertproblem. *Annalen der Physik*, 385(13):437–490, 1926.
- [28] A. Einstein. Die grundlage der allgemeinen relativitätstheorie. *Annalen der Physik*, 354(7):769–822, 1916.
- [29] Robert E. Newnham. *Properties of materials: Anisotropy, symmetry, structure*. Oxford Univ. Press, Oxford, repr edition, 2006.
- [30] R. de L. Kronig. On the theory of dispersion of x-rays. *Journal of the Optical Society of America*, 12(6):547, 1926.
- [31] D. A. Kleinman. Nonlinear dielectric polarization in optical media. *Physical Review*, 126(6):1977–1979, 1962.
- [32] Christopher A. Dailey, Brian J. Burke, and Garth J. Simpson. The general failure of kleinman symmetry in practical nonlinear optical applications. *Chemical Physics Letters*, 390(1-3):8–13, 2004.
- [33] P. A. Franken, A. E. Hill, C. W. Peters, and G. Weinreich. Generation of optical harmonics. *Physical review letters*, 7(4):118–119, 1961.
- [34] J. E. Midwinter and J. Warner. The effects of phase matching method and of uniaxial crystal symmetry on the polar distribution of second-order non-linear optical polarization. *British Journal of Applied Physics*, 16(8):1135–1142, 1965.
- [35] G. H. C. New and J. F. Ward. Optical third-harmonic generation in gases. *Physical review letters*, 19(10):556–559, 1967.
- [36] R. Y. Chiao, E. Garmire, and C. H. Townes. Self-trapping of optical beams. *Physical review letters*, 13(15):479–482, 1964.
- [37] Gadi Fibich and Alexander L. Gaeta. Critical power for self-focusing in bulk media and in hollow waveguides. *Optics letters*, 25(5):335, 2000.
- [38] M. Lewenstein, Ph. Balcou, M. Yu. Ivanov, Anne L’Huillier, and P. B. Corkum. Theory of high-harmonic generation by low-frequency laser fields. *Physical Review A*, 49(3):2117–2132, 1994.

- 
- [39] L’Huillier and Balcou. High-order harmonic generation in rare gases with a 1-ps 1053-nm laser. *Physical review letters*, 70(6):774–777, 1993.
- [40] Maciej Lewenstein, Pascal Salières, and Anne L’Huillier. Phase of the atomic polarization in high-order harmonic generation. *Physical Review A*, 52(6):4747–4754, 1995.
- [41] Shambhu Ghimire, Anthony D. DiChiara, Emily Sistrunk, Pierre Agostini, Louis F. DiMauro, and David A. Reis. Observation of high-order harmonic generation in a bulk crystal. *Nature Physics*, 7(2):138–141, 2010.
- [42] Georges Ndabashimiye, Shambhu Ghimire, Mengxi Wu, Dana A. Browne, Kenneth J. Schafer, Mette B. Gaarde, and David A. Reis. Solid-state harmonics beyond the atomic limit. *Nature*, 534(7608):520–523, 2016.
- [43] F. Langer, M. Hohenleutner, U. Huttner, S. W. Koch, M. Kira, and R. Huber. Symmetry-controlled temporal structure of high-harmonic carrier fields from a bulk crystal. *Nature Photonics*, 2017.
- [44] A. McPherson, G. Gibson, H. Jara, U. Johann, T. S. Luk, I. A. McIntyre, K. Boyer, and C. K. Rhodes. Studies of multiphoton production of vacuum-ultraviolet radiation in the rare gases. *Journal of the Optical Society of America B*, 4(4):595, 1987.
- [45] Corkum. Plasma perspective on strong field multiphoton ionization. *Physical review letters*, 71(13):1994–1997, 1993.
- [46] Armelle de Bohan, Bernard Piraux, Lino Ponce, Richard Taieb, Valerie Veniard, and Alfred Maquet. Direct and indirect pathways in strong field atomic ionization dynamics. *Physical review letters*, 89(11):113002, 2002.
- [47] L. V. Keldysh. Ionization in the field of a strong electromagnetic wave. *J. Exptl. Theoret. Phys. (U.S.S.R)*, (47):1945–1957, November, 1964.
- [48] N. B. Delone and Vladimir P. Krainov. Tunneling and barrier-suppression ionization of atoms and ions in a laser radiation field. *Physics-Uspekhi*, 41(5):469–485, 1998.
- [49] A. Baltuska, Th Udem, M. Uiberacker, M. Hentschel, E. Goulielmakis, Ch Gohle, R. Holzwarth, V. S. Yakovlev, A. Scrinzi, T. W. Hansch, and F. Krausz. Attosecond control of electronic processes by intense light fields. *Nature*, 421(6923):611–615, 2003.
- [50] Kenneth J. Schafer and Kenneth C. Kulander. High harmonic generation from ultrafast pump lasers. *Physical review letters*, 78(4):638–641, 1997.
- [51] Alessandro Averchi, Daniele Faccio, Ricardo Berlasso, Miroslav Kolesik, Jerome V. Moloney, Arnaud Couairon, and Paolo Di Trapani. Phase matching with pulsed bessel beams for high-order harmonic generation. *Physical Review A*, 77(2), 2008.
- [52] L. G. Gouy. Sur une propriété nouvelle des ondes lumineuses. *C. R. Acad. Sci. Paris*, (110):1251–1253, 1890.

- [53] I. J. Sola, E. Mével, L. Elouga, E. Constant, V. Strelkov, L. Poletto, P. Villorosi, E. Benedetti, J.-P. Caumes, S. Stagira, C. Vozzi, G. Sansone, and M. Nisoli. Controlling attosecond electron dynamics by phase-stabilized polarization gating. *Nature Physics*, 2(5):319–322, 2006.
- [54] T. J. Hammond, Graham G. Brown, Kyung Taec Kim, D. M. Villeneuve, and P. B. Corkum. Attosecond pulses measured from the attosecond lighthouse. *Nature Photonics*, 10(3):171–175, 2016.
- [55] H. W. Schweinberger. *A Laser Source for the Generation of Intense Attosecond Pulses and its First Applications*. Phd thesis, Ludwig-Maximilians-Universität, München, 2014.
- [56] Michael J. Jobst. *Attosecond Dynamics in Molecules and on Interfaces*. Phd thesis, Technische Universität München, München, 2014.
- [57] Pierre Tournois. Acousto-optic programmable dispersive filter for adaptive compensation of group delay time dispersion in laser systems. *Optics Communications*, 140(4-6):245–249, 1997.
- [58] Rick K. Nubling. Launch conditions and mode coupling in hollow-glass waveguides. *Optical Engineering*, 37(9):2454, 1998.
- [59] E. A. J. Marcatili and R. A. Schmeltzer. Hollow metallic and dielectric waveguides for long distance optical transmission and lasers. *Bell System Technical Journal*, 43(4):1783–1809, 1964.
- [60] Vahe Shirvanyan. *Erzeugung von sub-4-fs, mJ Pulsen mittels nichtlinearer Hohlkernfaser-Pulskompression mit konjugierten Druckgradienten*. Master’s thesis, Technische Universität München, May 15th, 2015.
- [61] Wolfgang Domcke, David Roy Yarkony, and Horst Köppel, editors. *Conical intersections: Theory, computation and experiment*, volume 17 of *Advanced series in physical chemistry*. World Scientific, Singapore, 2011.
- [62] Edward W. Schlag, Sheh-Yi Sheu, Dah-Yen Yang, Heinrich L. Selzle, and Sheng Hsien Lin. Distal charge transport in peptides. *Angewandte Chemie (International ed. in English)*, 46(18):3196–3210, 2007.
- [63] Jin Yang, Luyuan Zhang, Lijuan Wang, and Dongping Zhong. Femtosecond conical intersection dynamics of tryptophan in proteins and validation of slowdown of hydration layer dynamics. *Journal of the American Chemical Society*, 134(40):16460–16463, 2012.
- [64] Susanne Ullrich, Thomas Schultz, Marek Z. Zgierski, and Albert Stolow. Direct observation of electronic relaxation dynamics in adenine via time-resolved photoelectron spectroscopy. *Journal of the American Chemical Society*, 126(8):2262–2263, 2004.
- [65] Mario Barbatti, Adélia J. A. Aquino, Jaroslaw J. Szymczak, Dana Nachtigallová, Pavel Hobza, and Hans Lischka. Relaxation mechanisms of uv-photoexcited dna and rna nucle-

- obases. *Proceedings of the National Academy of Sciences of the United States of America*, 107(50):21453–21458, 2010.
- [66] Brantley A. West, Jordan M. Womick, and Andrew M. Moran. Interplay between vibrational energy transfer and excited state deactivation in dna components. *The journal of physical chemistry. A*, 117(29):5865–5874, 2013.
- [67] Gilbert N. Lewis. The atom and the molecule. *Journal of the American Chemical Society*, 38(4):762–785, 1916.
- [68] Z-W Qu, H. Zhu, S. Yu Grebenshchikov, and R. Schinke. The photodissociation of ozone in the hartley band: a theoretical analysis. *The Journal of chemical physics*, 123(7):074305, 2005.
- [69] F. Bloch. Nuclear induction. *Physical Review*, 70(7-8):460–474, 1946.
- [70] Piero Decleva, Nicola Quadri, Aurelie Perveaux, David Lauvergnat, Fabien Gatti, Benjamin Lasorne, Gabor J. Halasz, and Agnes Vibok. Attosecond electronic and nuclear quantum photodynamics of ozone monitored with time and angle resolved photoelectron spectra. *Scientific reports*, 6:36613, 2016.
- [71] H.-D. Meyer, U. Manthe, and L. S. Cederbaum. The multi-configurational time-dependent hartree approach. *Chemical Physics Letters*, 165(1):73–78, 1990.
- [72] Beck, M. H., Jäckle A., Worth G. A., Meyer H.-D. The multiconfiguration time-dependent hartree (mctdh) method: A highly efficient algorithm for propagating wavepackets. *Physics Reports*, 324(1):1–105, 2000.
- [73] Worth G. A., Beck M. H., Jäckle A., and Meyer H.-D. The mctdh package, version 8.2, (2000). meyer h.-d., version 8.3 (2002), version 8.4 (2007). current version: 8.4.12 (2016). see <http://mctdh.uni-hd.de/>.
- [74] Hans-Joachim Werner, Peter J. Knowles, Gerald Knizia, Frederick R. Manby, and Martin Schütz. Molpro: A general-purpose quantum chemistry program package. *Wiley Interdisciplinary Reviews: Computational Molecular Science*, 2(2):242–253, 2012.
- [75] Aurelie Perveaux, David Lauvergnat, Fabien Gatti, Gabor J. Halasz, Agnes Vibok, and Benjamin Lasorne. Monitoring the birth of an electronic wavepacket in a molecule with attosecond time-resolved photoelectron spectroscopy. *The journal of physical chemistry. A*, 118(38):8773–8778, 2014.
- [76] A. Perveaux, D. Lauvergnat, B. Lasorne, F. Gatti, M. A. Robb, G. J. Halász, and Á. Vibók. Attosecond electronic and nuclear quantum photodynamics of ozone: Time-dependent dyson orbitals and dipole. *Journal of Physics B: Atomic, Molecular and Optical Physics*, 47(12):124010, 2014.
- [77] G. J. Halász, A. Perveaux, B. Lasorne, M. A. Robb, F. Gatti, and Á. Vibók. Simulation of laser-induced quantum dynamics of the electronic and nuclear motion in the ozone molecule on the attosecond time scale. *Physical Review A*, 86(4), 2012.

- [78] G. J. Halász, A. Perveaux, B. Lasorne, M. A. Robb, F. Gatti, and Á. Vibók. Coherence revival during the attosecond electronic and nuclear quantum photodynamics of the ozone molecule. *Physical Review A*, 88(2), 2013.
- [79] Joachim Reinhold. *Quantentheorie der Moleküle: Eine Einführung*. Studienbücher Chemie. Springer Spektrum, Wiesbaden, 5., überarb. Aufl. edition, 2015.
- [80] Arthur Schoenflies. *Krystallsysteme und Krystallstruktur*. Springer, Berlin, 1984.
- [81] Á. Vibók. Qualitative molecular-frame photoelectron angular distributions (1/2): unpublished. unpublished, 2014.
- [82] C. Melania Oana and Anna I. Krylov. Dyson orbitals for ionization from the ground and electronically excited states within equation-of-motion coupled-cluster formalism: theory, implementation, and examples. *The Journal of chemical physics*, 127(23):234106, 2007.
- [83] Gilbert Grell, Sergey I. Bokarev, Bernd Winter, Robert Seidel, Emad F. Aziz, Saadullah G. Aziz, and Oliver Kühn. Multi-reference approach to the calculation of photoelectron spectra including spin-orbit coupling. *The Journal of chemical physics*, 143(7):074104, 2015.
- [84] Juan Ramón Ruíz-Tolosa and Enrique Castillo. *From Vectors to Tensors*. Universitext. Springer-Verlag Berlin Heidelberg, Berlin, Heidelberg, 2005.
- [85] U. Graf, M. Fieß, M. Schultze, R. Kienberger, F. Krausz, and E. Goulielmakis. Intense few-cycle light pulses in the deep ultraviolet. *Optics express*, 16(23):18956, 2008.
- [86] S. P. Le Blanc and R. Sauerbrey. Spectral, temporal, and spatial characteristics of plasma-induced spectral blue shifting and its application to femtosecond pulse measurement. *Journal of the Optical Society of America B*, 13(1):72, 1996.
- [87] Corkum, Rolland, and Srinivasan-Rao. Supercontinuum generation in gases. *Physical review letters*, 57(18):2268–2271, 1986.
- [88] S. P. Le Blanc, S. C. Rae, K. Burnett, and R. Sauerbrey. Spectral blue shifting of a femtosecond laser pulse propagating through a high-pressure gas. *Journal of the Optical Society of America B*, 10(10):1801, 1993.
- [89] M. Kolesik, J. V. Moloney, and M. Mlejnek. Unidirectional optical pulse propagation equation. *Physical review letters*, 89(28 Pt 1):283902, 2002.
- [90] Peter Rentrop. *A generalized runge-kutta method of order 3 - 4 for stiff systems of ordinary differential equations*, volume 7808 of *TUM-MATH / Technische Universität München, Institut für Mathematik*. TUM Inst. für Mathematik, München, 1978.
- [91] Rick Trebino and Daniel J. Kane. Using phase retrieval to measure the intensity and phase of ultrashort pulses: Frequency-resolved optical gating. *Journal of the Optical Society of America A*, 10(5):1101, 1993.

- [92] Kenneth W. DeLong and Rick Trebino. Improved ultrashort pulse-retrieval algorithm for frequency-resolved optical gating. *Journal of the Optical Society of America A*, 11(9):2429, 1994.
- [93] Roger L. DeKock and Harry B. Gray. *Chemical structure and bonding*. Univ. Science Books, Mill Valley, Calif., 1989.
- [94] C. R. Brundle and A. D. Baker, editors. *Electron spectroscopy: Theory, techniques and applications*. Acad. Pr, London, 1977.
- [95] Joris J. Snellenburg, Sergey P. Laptinok, Ralf Seger, Katharine M. Mullen, and Ivo H. M. van Stokkum. Glotaran: A java -based graphical user interface for the r package timp. *Journal of Statistical Software*, 49(3), 2012.
- [96] Zhengrong Wei, Jialin Li, Lin Wang, Soo Teck See, Mark Hyunpong Jhon, Yingfeng Zhang, Fan Shi, Minghui Yang, and Zhi-Heng Loh. Elucidating the origins of multimode vibrational coherences of polyatomic molecules induced by intense laser fields. *Nature communications*, 8(1):735, 2017.
- [97] Michael W. Schmidt, Kim K. Baldridge, Jerry A. Boatz, Steven T. Elbert, Mark S. Gordon, Jan H. Jensen, Shiro Koseki, Nikita Matsunaga, Kiet A. Nguyen, Shujun Su, Theresa L. Windus, Michel Dupuis, and John A. Montgomery. General atomic and molecular electronic structure system. *Journal of Computational Chemistry*, 14(11):1347–1363, 1993.
- [98] T. Koopmans. Über die zuordnung von wellenfunktionen und eigenwerten zu den einzelnen elektronen eines atoms. *Physica*, 1(1-6):104–113, 1934.
- [99] Per ke Malmqvist. Calculation of transition density matrices by nonunitary orbital transformations. *International Journal of Quantum Chemistry*, 30(4):479–494, 1986.
- [100] G. Schaftenaar and J. H. Noordik. Molden: a pre- and post-processing program for molecular and electronic structures\*. *Journal of Computer-Aided Molecular Design*, 14(2):123–134, 2000.
- [101] Wolfgang J. Schreier, Tobias E. Schrader, Florian O. Koller, Peter Gilch, Carlos E. Crespo-Hernández, Vijay N. Swaminathan, Thomas Carell, Wolfgang Zinth, and Bern Kohler. Thymine dimerization in dna is an ultrafast photoreaction. *Science (New York, N. Y.)*, 315(5812):625–629, 2007.
- [102] Chris T. Middleton, Kimberly de La Harpe, Charlene Su, Yu Kay Law, Carlos E. Crespo-Hernández, and Bern Kohler. Dna excited-state dynamics: From single bases to the double helix. *Annual review of physical chemistry*, 60:217–239, 2009.
- [103] Markus Kowalewski, Benjamin P. Fingerhut, Konstantin E. Dorfman, Kochise Bennett, and Shaul Mukamel. Simulating coherent multidimensional spectroscopy of nonadiabatic molecular processes: From the infrared to the x-ray regime. *Chemical reviews*, 2017.
- [104] H. Kang, C. Jouvét, C. Dedonder-Lardeux, S. Martrenchard, G. Grégoire, C. Desfrancois, J.-P. Schermann, M. Barat, and J. A. Fayeton. Ultrafast deactivation mechanisms of



- protonated aromatic amino acids following uv excitation. *Physical Chemistry Chemical Physics*, 7(2):394–398, 2005.
- [105] Dorit Shemesh, Andrzej L. Sobolewski, and Wolfgang Domcke. Efficient excited-state deactivation of the gly-phe-ala tripeptide via an electron-driven proton-transfer process. *Journal of the American Chemical Society*, 131(4):1374–1375, 2009.
- [106] Benjamin P. Fingerhut, Konstantin E. Dorfman, and Shaul Mukamel. Probing the conical intersection dynamics of the rna base uracil by uv-pump stimulated-raman-probe signals; ab initio simulations. *Journal of chemical theory and computation*, 10(3):1172–1188, 2014.
- [107] Teruto Kanai, Xiangyu Zhou, Taro Sekikawa, Shuntaro Watanabe, and Tadashi Togashi. Generation of subterawatt sub-10-fs blue pulses at 1–5khz by broadband frequency doubling. *Optics letters*, 28(16):1484, 2003.
- [108] Peter Baum, Stefan Lochbrunner, and Eberhard Riedle. Tunable sub-10-fs ultraviolet pulses generated by achromatic frequency doubling. *Optics letters*, 29(14):1686, 2004.
- [109] P. Baum, S. Lochbrunner, and E. Riedle. Generation of tunable 7-fs ultraviolet pulses: Achromatic phase matching and chirp management. *Applied Physics B*, 79(8):1027–1032, 2004.
- [110] Teruto Kanai, Xiangyu Zhou, Tingting Liu, Atsushi Kosuge, Taro Sekikawa, and Shuntaro Watanabe. Generation of terawatt 10-fs blue pulses by compensation for pulse-front distortion in broadband frequency doubling. *Optics Letters*, 29(24):2929, 2004.
- [111] Bruno E. Schmidt, Nicolas Thiré, Maxime Boivin, Antoine Laramée, François Poitras, Guy Lebrun, Tsuneyuki Ozaki, Heide Ibrahim, and François Légaré. Frequency domain optical parametric amplification. *Nature communications*, 5:3643, 2014.
- [112] M. Hentschel, R. Kienberger, Ch. Spielmann, G. A. Reider, N. Milosevic, T. Brabec, P. Corkum, U. Heinzmann, M. Drescher, and F. Krausz. Attosecond metrology. *Nature*, 414(6863):509–513, 2001.
- [113] J. Itatani, F. Quere, G. L. Yudin, M. Yu Ivanov, F. Krausz, and P. B. Corkum. Attosecond streak camera. *Physical review letters*, 88(17):173903, 2002.
- [114] R. Kienberger, M. Hentschel, M. Uiberacker, Ch Spielmann, M. Kitzler, A. Scrinzi, M. Wieland, Th Westerwalbesloh, U. Kleineberg, U. Heinzmann, M. Drescher, and F. Krausz. Steering attosecond electron wave packets with light. *Science (New York, N.Y.)*, 297(5584):1144–1148, 2002.
- [115] D. J. Bradley, B. Liddy, and W. E. Sleat. Direct linear measurement of ultrashort light pulses with a picosecond streak camera. *Optics Communications*, 2(8):391–395, 1971.
- [116] F. Quéré, Y. Mairesse, and J. Itatani. Temporal characterization of attosecond xuv fields. *Journal of Modern Optics*, 52(2-3):339–360, 2005.
- [117] Ferenc Krausz and Misha Ivanov. Attosecond physics. *Reviews of Modern Physics*, 81(1):163–234, 2009.

- [118] Rick Trebino, Kenneth W. DeLong, David N. Fittinghoff, John N. Sweetser, Marco A. Krumbügel, Bruce A. Richman, and Daniel J. Kane. Measuring ultrashort laser pulses in the time-frequency domain using frequency-resolved optical gating. *Review of Scientific Instruments*, 68(9):3277–3295, 1997.
- [119] John N. Sweetser, David N. Fittinghoff, and Rick Trebino. Transient-grating frequency-resolved optical gating. *Optics letters*, 22(8):519, 1997.
- [120] Kenneth W. DeLong, Bern Kohler, Kent Wilson, David N. Fittinghoff, and Rick Trebino. Pulse retrieval in frequency-resolved optical gating based on the method of generalized projections. *Optics letters*, 19(24):2152, 1994.
- [121] D. Spangenberg, E. Rohwer, M. H. Brugmann, and T. Feurer. Ptychographic ultrafast pulse reconstruction. *Optics letters*, 40(6):1002–1005, 2015.

---

# Curriculum Vitae

**Tobias Thomas Latka**

*born in Dusseldorf on September 6th, 1985*

---

## *Education*

03/2012 - 01/2018	PhD Student at the Max Planck Institute of Quantum Optics (MPQ) and at the Technical University of Munich (TUM) in the group of Prof. Dr. Reinhard Kienberger
11/2010 - 11/2011	Diploma thesis at the Max Planck Institute of Quantum Optics (MPQ) under supervision of Prof. Dr. Gerhard Rempe
10/2006 - 11/2011	Studies of Physics at the Technical University of Munich (TUM)
2005	Abitur at Michael-Ende-Gymnasium, Tönisvorst

---

## *Teaching*

2014-2018	Supervision of advanced laboratory course "Laser & Non-linear Optics"
-----------	---

---



# List of Publications and Conference Contributions

## Publications of the Author Directly Related to Current Thesis

- **T. Latka**, V. Shirvanyan, M. Ossiander, O. Razskazovskaya, A. Guggenmos, M. Jobst, M. FieSS, S. Holzner, A. Sommer, M. Schultze, C. Jakubeit, J. Riemensberger, B. Bernhardt1, W. Helml, F. Gatti, B. Lasorne, D. Lauvergnat, P. Decleva, G. J. Halász, Á. Vibók, R. Kienberger. *Few-Femtosecond Wave Packet Revivals in Ozone*. *Submitted*.

## Further Publications of the Author

- M. Ossiander, F. Siegrist, V. Shirvanyan, R. Pazourek, A. Sommer, **T. Latka**, A. Guggenmos, S. Nagele, J. Feist, J. Burgdörfer, R. Kienberger, M. Schultze. *Attosecond correlation dynamics*. *Nature Physics*, vol. **13**, pp. 280-286 (2016)
- A. Sommer, E. Bothschafter, S. A. Sato, C. Jakubeit, **T. Latka**, O. Razskazovskaya, H. Fattahi, M. Jobst, W. Schweinberger, V. Shirvanyan, V. Yakovlev, R. Kienberger, K. Yabana, N. Karpowicz, M. Schultze, F. Krausz. *Attosecond nonlinear polarization and lightmatter energy transfer in solids*. *Nature*, vol. **534**, pp. 86-90 (2016)

## Conference Contributions

- **T. Latka**, V. Shirvanyan, M. Ossiander, O. Razskazovskaya, B. Bernhardt, W. Helml, B. Lasorne, P. Decleva, G. J. Halász, Á. Vibók, R. Kienberger. *Probing Electronic and Nuclear Dynamics in Ozone on a Femtosecond Timescale*. FEMTO 13 - The 13th Femtochemistry Conference, Cancun, Mexiko, Poster Presentation (2017)



# Danksagung

An dieser Stelle möchte ich mich bei allen Menschen bedanken, die zum Gelingen dieser Dissertation beigetragen haben, als auch bei jenen, die stets auSSerhalb der Arbeit eine Stütze waren und nach wie vor sind.

Allen voran gilt mein besonderer Dank meinem Doktorvater Professor Reinhard Kienberger, der mir das Vertrauen und die Möglichkeit gab, mich unter besten Forschungsbedingungen an einem hochinteressanten, sowie — über viele Jahre hinweg — hoch anspruchsvollen Projekt zu versuchen. Mit seiner ruhigen, fröhlichen und optimistischen Art, die immer wieder Hoffnung gab, gerade wenn mal alles aus den Fugen zu geraten drohte, trägt er maßgeblich zum Erfolg dieser Arbeit bei.

Ebenso geht mein Dank an Birgitta Schultze-Bernhardt, Martin Schultze und Wolfram Helml, die teils bis spät in die Nacht bei den Strahlzeiten geholfen haben, aber auch sonst immer ein offenes Ohr für mich hatten, wenn es scheinbar unüberbrückbare Probleme gab. Wolfram Helml danke ich darüber hinaus für seine bedingungslose Hilfsbereitschaft, das Korrekturlesen dieser Arbeit und die stets aufmunternden Worte.

Des Weiteren möchte ich Vage Shirvanyan, Marcus Ossiander und Johann Riemensberger für ihren unermüdlichen Einsatz während der kräftezehrenden Strahlzeiten, ihre hilfreichen Ideen und Denkanstöße innerhalb wie auSSerhalb der Arbeit meinen Dank aussprechen.

Das gleiche gilt für meine Vorgänger Markus FieSS, Simon Holzner, Annkatrin Sommer und Michael Jobst, auf dessen Vorarbeiten sich sehr gut aufbauen lieSS. Sie tragen ebenso zum Gelingen dieser Arbeit bei.

Ebenso wären die Experimente nicht möglich gewesen ohne die hervorragenden, speziell für dieses Projekt entwickelten optischen Beschichtungen, die ihresgleichen suchen. Im Speziellen sind hier Olga Razskazovskaya und Alexander Guggenmos zu nennen, die auch kurzfristig immer hervorragende Spiegel lieferten.

Im besonderen Maße danke ich auch meinen Kollegen aus Ungarn, Frankreich und Italien, die die Simulationen zu den experimentellen Ergebnissen beisteuerten und damit einen wesentlichen Beitrag zum Verständnis und Interpretation der beobachteten Dynamik im Ozon-Molekül leisteten. Hier sind insbesondere Ágnes Vibók, Gábor J. Halász, Fabien Gatti, Benjamin Lasorne, David Lauvergnat und Piero Decleva zu nennen, aber auch jene namentlich nicht genannten

Personen aus den jeweiligen Gruppen, die im Hintergrund zur Theorie beitrugen.

Trotz alledem wären die Experimente ohne entsprechende technische Unterstützung vermutlich gescheitert. Daher richte ich meinen Dank auch an Harald Haas, Anton Horn, Alois Böswald, Manfred Fischer sowie Tobias Kleinhenz. Gleiches gilt für die Werkstatt sowohl am Max-Planck-Institut für Quantenoptik, stellvertretend in Person von Michael Rogg, als auch für jene am Lehrstuhl für Laser- und Röntgenphysik der Fakultät für Physik an der TUM, in Person von Wolfgang Dürichen.

AuSSerdem zolle ich weiteren Personen meinen Dank. Namentlich sollen hier genannt werden: Elisabeth Bothschafter, Wolfgang Schweinberger, Clemens Jakubeit, Nicholas Karpowicz, Vladislav Yakovlev und Florian Siegrist.

Alle bereits genannten Personen zeichnen sich dadurch aus, als dass sie mit ihrem Charakter, ihrem Humor und ihrer Expertise ein angenehmes und produktives Arbeitsumfeld geschaffen haben.

Zu guter Letzt, geht mein tiefster Dank an meine engsten Freunde, meine Eltern, meine Schwester und natürlich Jenny, die mich alle in jeder Lebenslage, in guten, aber vor allem auch in schlechten Zeiten immer unterstützen, mir unaufhörlich den Rücken stärken und freihalten, sowie in den vergangenen Jahren einiges mit mir mitmachen mussten.

Danke!